

**The first 9 Ma years in the life of an  
East Pacific Rise segment**

**Burkhard Schramm**

**Dissertation for the doctorate degree  
of the Department of Geoscience at the  
University of Bremen**

## **Erklärung**

Hiermit versichere ich, dass ich

1. die Arbeit ohne unerlaubte fremde Hilfe angefertigt habe,
2. keine anderen als die von mir angegebenen Quellen und Hilfsmittel benutzt habe und
3. die den benutzten Werken wörtlich oder inhaltlich entnommenen Stellen als solche kenntlich gemacht habe.

Bremen, den

**The first 9 Ma years in the life of an East  
Pacific Rise segment**

**Dissertation for the doctorate degree  
of the Department of Geoscience at the  
University of Bremen**

**submitted by**

**Burkhard Schramm**

**Bremen, 2003**

Tag des Kolloquiums:

19.12.2003

Gutachter:

1. Prof. Dr. C. W. Devey
2. Prof. Dr. O. Brockamp

Prüfer:

1. Prof. Dr. H. Villinger
2. Prof. Dr. J. Peckmann

## **Danksagung**

Das größte Dankeschön geht natürlich an Prof. Colin W. Devey der dieses Projekt überhaupt erst ermöglichte und das Vertrauen in mich gesetzt hat diese Arbeit umzusetzen. Darüber hinaus hat er mich stets gefördert an Forschungsfahrten teilzunehmen, was für mich unglaublich wichtige Erfahrungen waren. Die Zusammenarbeit war immer hervorragend, egal ob es sich um die Fertigstellung der Veröffentlichungen oder etwas anderes handelte. DANKE !

Special thanks to Prof. Kathryn M. Gillis for the unforgettable time during my visit in Victoria, Canada. She introduced me to the fascinating world of alteration. I have never learned so much in just a short time. She improved the alteration part of this thesis more than I have ever believed. And of course – thanks for the bike !  
THANK YOU VERY MUCH !

Ein weiteres Dankeschön geht natürlich an Prof. Olaf Brockamp, der sich netterweise bereit erklärt hat bei meiner Arbeit als zweiter Gutachter zu fungieren.

Danke natürlich auch an Dr. Klas Lackschewitz, der immer alles stehen und liegen ließ um meine Fragen zu beantworten, die Veröffentlichungen korrigierte, super hilfreich bei der Analyse der Proben in Zusammenarbeit mit der Uni / GEOMAR Kiel war und auch sonst immer bereit war zu helfen.

Tausend Dank natürlich auch an Dr. Andreas Klügel, der mit seiner Hilfsbereitschaft immer zur Stelle war um Probleme beiseite zu räumen und für alle Tips und Tricks, die es galt im Laufe der letzten Jahre zu lernen.

Gar nicht oft genug erwähnen kann ich hier das phantastische, außergewöhnlich gute Arbeitsklima in unserer kleinen Arbeitsgruppe. Danke an alle: Aloys Deeken, Heike Anders, Jutta Ait Majdari, Imme Martelock, Stefanie Schwarz und Karsten Galipp.

Ein ganz spezielles Dankeschön geht natürlich an Anette von der Handt, für eine unvergeßlich schöne Zeit und natürlich auch als Mikrosondenspezialistin.

Vielen Dank fürs Korrigieren, besorgen von unauffindbarer Literatur und vor allen Dingen für moralische Unterstützung an Valérie Epplé, Anna Ksienzyk, Katrin Monecke und Silke Steph.

Natürlich auch ein Dankeschön für die Finanzierung der Arbeit durch das BMBF projekt 03G0145A.

## Contents

Abstract .....	1
Introduction .....	2
Aims of the project .....	6
References .....	7

### **I. The fourth dimension in spreading axis activity: Magmatic evolution along the Southern East Pacific Rise at 14°S during the last 9 Ma**

*Burkhard Schramm and Colin W. Devey*

*Submitted to Earth and Planetary Science Letters, 29 September 2003*

Abstract .....	13
Introduction .....	14
EXCO field area .....	15
Geologic setting, sampling and previous work .....	15
Major element chemistry of axial basalts .....	16
Analytical methods .....	17
Results .....	22
Major elements .....	22
Trace elements .....	23
Discussion .....	23
How old is the magmatic border and how stable is the magmatic evolution ? .....	23
On- and Off-axis eruptions ? .....	24
Can crystal fractionation explain the differences between the EXCO basalts ? .....	26
Summary and conclusions .....	28
Acknowledgements .....	30
References .....	31

### **II. A multibeam-sonar, magnetic and geochemical flowline survey at 14°14'S on the southern East Pacific Rise: Insights into the fourth dimension of ridge crest segmentation**

*Ingo Grevemeyer, Burkhard Schramm, Colin W. Devey, Douglas S. Wilson, Birgit Jochum, Jan Hauschild, Kay Aric, Heinrich W. Villinger, Wilfried Weigel*

*Earth and Planetary Science Letters 199 (2002) 359-372, accepted 11 March 2002*

Abstract .....	37
1. Introduction .....	38
2. Geological background .....	38
3. Data collections and processing .....	39
3.1. Magnetics .....	41
3.2. Bathymetry .....	41
3.3. Geochemical analytical methods .....	41

4. Results and discussion .....	44
4.1. Asymmetric spreading and segmentation .....	44
4.2. Tectonic and geochemical segmentation .....	46
5. Conclusions .....	48
Acknowledgements .....	49
References .....	49

### **III. Quantitative assessment of chemical and mineralogical changes due to progressive low temperature alteration of East Pacific Rise basalts from 0-9 Ma**

*Burkhard Schramm, Colin W. Devey, Kathryn M. Gillis and Klas Lackschewitz*

*Submitted to Chemical Geology, 19 May 2003*

Abstract .....	52
1. Introduction .....	53
2. EXCO field area .....	56
Sampling .....	56
3. Analytical Methods .....	56
4. Results .....	58
4.1. Petrology of the sample suite .....	60
Ridge axis - 21DS, 18DS, 20DS .....	60
0.12 Ma – 22DS .....	60
0.65 Ma – 28DS .....	61
1.16 and 2.56 Ma – 29DS and 35DS .....	61
2.92 Ma – 9DS .....	61
4.6 Ma – 36DS .....	63
6.84 Ma – 42DS .....	64
8.64 Ma – 43DS .....	65
4.3. Mineral Chemistry .....	65
Celadonite .....	65
Saponite .....	67
Phillipsite .....	67
4.4. Geochemical fluxes .....	68
5. Discussion .....	72
5.1. Evolution of low temperature alteration .....	72
5.2. Fluid circulation in the crust .....	74
5.3. Geochemical fluxes .....	75
5.3.1. K <sub>2</sub> O, P <sub>2</sub> O <sub>5</sub> , Rb and Cs .....	75
5.3.2. Ba and U .....	76
5.2.3. Global importance .....	76
6. Summary & conclusions .....	79
Acknowledgements .....	80
Appendices .....	81

References .....	84
------------------	----

#### **IV. Colored atlas of low temperature alteration features in basalts**

*Burkhard Schramm*

1. Introduction .....	92
2. Preliminary work .....	92
3. Problems .....	93
4. Photomicrographs .....	93
4.1 Glass / palagonite (Pic.1-4) .....	93
4.2 Alteration haloes (Pic.5-8) .....	94
4.3 Void filling (Pic.9-12) .....	94
4.4 Vein filling (Pic.13-20) .....	95
4.5 Secondary Minerals .....	96
4.5.1 FeOOH (Pic.21, 22) .....	96
4.5.2 Celadonite and saponite (Pic.23-32) .....	96
4.5.3 Phillipsite (Pic.33-42) .....	97
Pictures .....	98
Appendix – Thin sections .....	119
References .....	126

#### **V. Producing melts of crystalline basaltic groundmass for analysis with the electron microprobe**

*Burkhard Schramm and Colin W. Devey*

*Submitted to European Journal of Mineralogy, 3 September 2003*

Abstract .....	128
Introduction .....	129
Experiment .....	130
Running procedure .....	130
Material and Methods .....	130
Results .....	131
Summary .....	134
Acknowledgments .....	134
References .....	134

<b>Conclusions</b> .....	136
--------------------------	-----

## **Abstract**

The understanding of mid-ocean ridge processes is dominated by the results of studies on zero-age basalts from the present-day axes. Little is known about the processes that occur as the crust moves off-axis in terms of the influence of low temperature alteration on the mineralogical and chemical composition of the rocks, as well as the magmatic evolution of the spreading axis during the past on a several million year time scale. This thesis is focused on basalts dredged within a narrow flow-line corridor perpendicular to the present day ridge axis extending 9 Ma eastward of the East Pacific Rise. Backtracking these samples to their original on-axis eruption location and comparison of their geochemical data with samples from the present day ridge axis, results in a report of the first 9 Ma in the life of an East Pacific Rise segment.

The backtracked samples show a surprisingly good and significant agreement with samples from the present day ridge axis and can be divided into two geographical groups separated by a magmatic border at 14°24'S. Modeling of the trace element variations from samples north of the magmatic border shows that they can be related by differences in the amount of garnet present in the melting residue and that variation in the degree of crystal fractionation are negligible, in contrast to samples south of the border, which are related to one another by crystal fractionation, suggesting that they are derived from the same long-lived magma chamber. Samples collected close to seamounts show trace-element depleted signatures characteristic of off-axis volcanism that all backtrack to the same eruption latitude, suggesting a magmatic system which is characterized by stability on the several million year scale.

Information about the influence of low temperature alteration over several million years on the geochemical composition of the oceanic crust, is of fundamental importance when examining the changes on the surface of the upper crust, for crust-ocean mass balances and for an understanding of the input to the subduction factory. Fresh rocks were sampled at the present day ridge axis, whereas off-axis rocks contain features of seawater dominated low temperature alteration. Secondary minerals, sealing of fractures and the occurrence of more intense alteration rinds on older rocks show evidence for a slight change in redox conditions from an oxidizing, water dominated to a more reducing, rock-dominated environment with time. Iron-oxyhydroxide and celadonite (main alteration component in 0.12-4.6 Ma old rocks) are the first alteration products, partly replaced by saponite under more reducing conditions. Phillipsite is present in fractures and veins and is the main alteration product in rocks older than 4.6 Ma. Mass balance calculations show that off-axis basalts show significant uptake of Rb, Cs and Ba which are supplied by seawater and incorporated in or on secondary minerals. An enrichment of U appears to be especially strong under oxidative conditions. The enrichment of K<sub>2</sub>O in all off-axis basalts is

connected to the formation of celadonite. The element movement during alteration affects the composition of the oceanic crust significantly and has an important influence on the evolution of mantle, crust, and biosphere.

## **Introduction**

The composition of mid-ocean ridge basalts (MORB) provides important information about their geochemical history, magmatic evolution, mantle source and degree of alteration. Axial magma chamber (AMC) processes beneath mid-ocean ridges are responsible for creation of the oceanic crust that covers about  $\frac{2}{3}$  of the Earth's surface. Although most of the oceanic crust is mapped, less than 1 % of these remote areas have been studied by rock samples. Previous studies have been concentrated mainly along active spreading centers to study spatial magmatic variations along the ridge axis (e.g. Schilling et al., 1983; Sinton et al., 1991; Bach et al., 1994; Mahoney et al., 1994) or off-axis collecting dredged samples from topographic highs or seamounts or as part of the Ocean Drilling Program. Magmatic provinces along axis can be defined by the geochemical composition of the erupted magmas. The magmatic segmentation sometimes coincide with different kinds of bathymetric or tectonic ridge axis discontinuities. Based on their age and longevity these boundaries have been classified into first to fourth order as: Transform faults (last for  $10^7$  years); overlapping spreading centers (OSC) ( $10^6$  years); small offset OSC ( $10^4 - 10^5$  years) and minor deviations in axial linearity (devals) ( $<10^4$  years) (MacDonald et al., 1988; MacDonald, 1998). It has been suggested that the magmatic and tectonic segmentation of the ridge axis are related (e.g. Langmuir et al., 1986; MacDonald et al., 1988; Batiza, 1996; Perfit and Chadwick, 1998), so sampling along mid-ocean ridges provides ideal locations to study the relationships of magmatic evolution and its mantle source with bathymetric or tectonic segmentation.

All MORB are generally believed to be derivative liquids that have undergone at least some degree of fractional crystallization and magma mixing, as first proposed by O'Hara (1968; 1977). The major element chemistry of the magma is also influenced by degree of melting (e.g. Klein and Langmuir, 1987). Many studies have shown that the AMC beneath the East Pacific Rise (EPR) consists of crystal-liquid mush, even most portions of the melt lens, but the composition of the magma lens is still uncertain and it is unclear whether the melt lens contains melt of average composition or is more primitive or more fractionated than the average (Sinton and Detrick, 1992; Natland and Dick, 1996; Singh et al., 1998). Klein and Langmuir (1987; 1989) and Langmuir et al. (1992) defined global and local trends in the chemical variation of magmas from the spreading axis. The global trends represent averages of ~100 km long ridge segments to focus on the large scale trends. To

avoid the effects of shallow magma crystallization, element concentrations are corrected to a constant degree of differentiation. These correlations are controlled by differences in thermal regime between major mantle segments much more than by differences in mantle composition (Langmuir et al., 1992). The authors suggest that the thermal regime beneath a ridge segment exerts a major control on the quantity and composition of MORB and therefore on crustal thickness and depth below sea level of the ridge axis. Local trends can vary from the broadly averaged global trends, e.g. the mean degree of melting varies inversely with the pressure of melting, opposite to the global trend. They concluded that local trends on slow-spreading ridges must be controlled by mantle melting processes and low thermal stability of the hydrothermal cooled crust, whereas those on fast-spreading ridges such as the EPR are best modeled by small-scale mantle heterogeneities associated with an enriched component that is independent of depth. Fast-spreading ridges are more homogeneous in terms of topography, morphology and chemical variability, probably the result of more efficient mantle melting due to fast replenishment, resulting in less temperature variation.

Since geochemical variations between different segments of a ridge axis may reflect differences in MORB source composition (Niu and Batiza, 1991; Sinton et al., 1991; Bach et al., 1994), geochemical studies can give important information about the magmatic segmentation along the ridge. Enriched MORB from the Pacific generally have higher  $\text{Al}_2\text{O}_3$  and lower FeO contents than typical N-MORB, reflecting different liquid lines of descent for N- and E-MORB (Michael and Chase, 1987). Major element compositions reflect the physical conditions of mantle melting and magma evolution (Hanson and Langmuir, 1978; Niu et al., 1996), whereas radiogenic isotopes and incompatible trace elements reflect the nature and history of the fertile mantle material, because shallow level cooling and fractionation cannot change K/Ti element ratios and  $^{87}\text{Sr}/^{86}\text{Sr}$  significantly without evidence for obvious assimilation (Niu et al., 2002). U-series disequilibria show that axial N-MORB reflects an efficient mixing process that integrates and homogenizes melts derived from heterogeneous sources, consisting a mixture of 5-10 % E-MORB and 90-95 % depleted MORB. Variations in the composition of MORB are most easily reconciled with a lherzolite source consisting of small amounts of mafic veins and can occur over small spatial scales (Lundstrom et al., 2000). Other workers suggest that MORB are produced by melting of a mixed garnet pyroxenite / spinel peridotite source identified as the “garnet signature” leading to low Lu/Hf and high Sm/Yb ratios (Hirschmann and Stolper, 1996).

Most MORB studies of the EPR have focused on samples collected within 10 km of the ridge axis (e.g. Hékinian and Walker, 1987; Reynolds et al., 1992; Perfit et al., 1994) and therefore provide only little information about the magmatic evolution in the past. A study of samples dredged near the EPR up to 50 km off the ridge axis at  $10^{\circ}30'N$  provides information about the temporal geochemical changes of lavas erupted over

the past 800 ka (Regelous et al., 1999). These authors showed that changes in the major element composition of lavas over a few thousand years are related to changes in the rate at which melt is supplied beneath the ridge axis. Other studies showed that the melt lens of the AMC does not play a significant role in controlling the crystal content and characters of erupted lavas (Pan and Batiza, 2002). Geochemical heterogeneity also occurs within individual lava flows, caused either by variations in low-pressure equilibrium fractional crystallization or required by multiple parent magmas or complex crystallization conditions (Rubin et al., 2001). Other studies showed that changes in melt composition along the ridge axis can result from differences between on and off-axis volcanism. Perfit et al. (1994) reported young-looking lava fields and pillow ridges and suggest that recent volcanic activity occurred up to 4 km off the EPR axis. They suggest compositional heterogeneities of the off-axis volcanism, compared to samples from on-axis eruptions, can be taken as an indication for several small, spatially and temporally distinct magma chambers with lifespans of 5000 years or less during the last 80000 years at the EPR. Off-axis volcanism can also be identified by its more depleted nature compared to samples erupted at the ridge axis (Spiegelman and Reynolds, 1999).

The convective cooling of the lithosphere as the crust moves off-axis is responsible for the passive fluid circulation, which has significant effects on the chemistry of the oceanic crust. Most of the heat (~70 %) is lost in the ocean basins rather than on-axis (Stein and Stein, 1994; Mottl, 2003) and as a consequence most of the fluid flux and geochemical exchange occurs off-axis (Mottl and Wheat, 1994; Alt et al., 1996; Mottl and Wheat, 2000). The convective heat loss from ocean crust ceases on average at about 65 Ma (Stein and Stein, 1994). The cooling causes hydrothermal metamorphism for up to several tens of million years, from very low-grade to amphibolite facies conditions. However, the fluid flow in oceanic crust is limited by the degree of rock permeability and occurs mostly in the uppermost few hundred meters of basement (e.g. Fisher et al., 1990; Fisher et al., 1994; Davis et al., 1996; Fisher, 1998; Fisher and Becker, 2000). The nature of water circulation will evolve with time as the crust is buried by sediments and fractures are sealed with secondary minerals. The resulting alteration influences significantly the chemical and physical conditions of the off-axis lavas and therefore the global geochemical budget, as the crust is one of the major inputs to subduction zones.

Alteration takes place as the crust ages, as documented by weathering of primary minerals, glass and the groundmass, and the precipitation of secondary minerals. Rocks from the ridge axis are fresh or less altered, whereas off-axis rocks are generally characterized by features of more intense alteration. Nevertheless, no specific alteration stage can be related to a specific crustal age, because alteration is not only affected by time. Local parameters such as basement topography, permeability and porosity of the oceanic crust, rate and nature of sedimentation, water-rock interaction and hydrothermal vents are important factors influencing alteration.

Investigators have attempted to quantify how alteration varies with age by comparing samples from geographically unrelated DSDP/ODP sites. These studies document how alteration proceeds through progressive alteration stages, from oxidizing to reducing conditions and from seawater- to hydrothermal fluid-dominated alteration and provide quantitative constraints for geochemical fluxes (e.g. Alt et al., 1992; Staudigel et al., 1996; Teagle et al., 1998; Laverne et al., 2001; Bach et al., 2003).

Seawater–ocean crust hydrothermal fluxes and budgets of chemical alteration of ocean crust are still poorly constrained. A reference section of upper oceanic crust was drilled at ODP Hole 504B, 200 km south of the Costa Rica Rift in the eastern Pacific in 6 Ma old crust and is the only section penetrating through the volcanic section to near the base of the sheeted dyke complex (e.g. Alt et al., 1996). The alteration stratigraphy indicates that processes change with depth and varying alteration effects in the oceanic crust of different ages show a sequence of very low-grade metamorphic processes (Alt, 1999). The chemical and petrographic data identify the upper crust as a significant sink for K and Mg and a source of Ca and Si to the oceans. However, the low core recovery, the unusually depleted nature of the mantle source and the remarkably high sedimentation rate in the area raise the question of how representative 504B is for ‘normal’ ocean crust (Bach et al., 2003).

Other investigations focused on a section of the Juan de Fuca Ridge, where ten sites were drilled during ODP Leg 168 along a 120 km (up to ~3.5 Ma) linear transect perpendicular to the spreading axis. The flank flux experiment is the only study where processes of hydrothermal metamorphism and how these evolve with time and space were studied. The observed ranges in secondary mineral composition across the flank are directly related to changes in the geochemical and textural characteristics of the basement, to interaction between fluids and phases from increasing stages of alteration, changes from oxidizing to reducing conditions, as well as strongly modified seawater derived fluids (Elderfield et al., 1999; Hunter et al., 1999; Buatier et al., 2001). Nevertheless, the sediment thickness in the flank flux area increases to about 600 m, exceptionally high for only 3.5 Ma old crust, therefore the results of these studies do not represent the norm for ocean crust which is buried by pelagic sediments at much slower rates (4-5 cm / 1000 years at the EPR (Kennett, 1982)).

For a complete understanding of the mid-ocean ridge system and the oceanic crust, it is important to study MORB systematics and alteration features over spatial as well as temporal scales at localities representing “normal” oceanic crust. Only this combination provides the possibility to decipher the magmatic evolution along the ridge axis and the alteration history of the fluid rock interaction in the crust.

## **Aims of the project**

The study is based on rocks dredged from the East Pacific Rise at 14°S during the EXCO (**E**xchange between **C**rust and **O**cean) cruises. For the first time magmas from a single spreading segment at the southern East Pacific Rise (SEPR) at 14°S were sampled along a flow line perpendicular to the ridge axis. In contrast to previous studies along mid-ocean ridges which concentrated on regional variations of zero-age basalts, the sampling program was conducted over short distances and a time period of 9 Ma to decipher the following questions:

- Is the magmatic evolution on a single spreading segment affected by variations in spreading rate ?
- Is there a homogeneous mantle source along this part of the EPR ?
- Was the MORB source homogeneous during the last 9 Ma ?
- Are there any systematic variations in degree of crystal fractionation with time ?
- Experimental petrological investigations have shown that it is possible to calculate the depth and degree of melting through Na, Fe, Ca and Al concentrations corrected for fractionation processes (Klein and Langmuir, 1987; Niu and Batiza, 1991; Langmuir et al., 1992). Is there any dependence between degree and/or depth of melting and spreading rate ? Is it possible to calculate the degree of melting with trace element analyses ?
- How are the low temperature altered rocks characterized (secondary minerals, alteration features) ?
- Can the water-rock interaction and geochemical fluxes be quantified ?
- How has the style of alteration changed during the last 9 Ma, and what kind of different alteration stages can be identified ?

In order to answer these questions, analyses of fresh glass compositions were necessary, because they reflect the pristine composition of MORB. Due to the limited presence of glass in a few dredges the thesis also focused on the problem of producing glass from crystalline basaltic groundmass in the laboratory that could be analyzed by electron microprobe. During the intense study of the altered rock samples, many mineralogical features of secondary minerals at the EXCO area were characterized under the microscope and cataloged in form of photomicrographs. These pictures were used to create a colored atlas of low temperature alteration features in basalts as an helpful tool for the novice alteration petrographer.

## References

- Alt, J.C., 1999. Very Low Grade Metamorphism of Basic Igneous Rocks. In: M. Frey and D. Robinson (Editors), *Low Grade Metamorphism*. Blackwell Scientific, pp. 169-201.
- Alt, J.C., France-Lanord, C., Floyd, P.A., Castillo, P. and Galy, A., 1992. Low-temperature hydrothermal alteration of Jurassic ocean crust, Site 801. *Proceedings of the Ocean Drilling Program, Scientific Results*, 129: 415-427.
- Alt, J.C., Teagle, D.A.H., Laverne, C., Vanko, D.A., Bach, W., Honnorez, J., Becker, K., Ayadi, M. and Pezard, P.A., 1996. Ridge flank alteration of upper ocean crust in the eastern Pacific; synthesis of results for volcanic rocks of holes 504B and 896A. *Proceedings of the Ocean Drilling Program, Scientific Results*, 148: 435-450.
- Bach, W., Hegner, E., Erzinger, J. and Satir, M., 1994. Chemical and isotopic variations along the superfast spreading East Pacific Rise from 6° - 30°. *Contr. Min. Petrology*, 116: 365-380.
- Bach, W., Peucker-Ehrenbrink, B., Hart, S.R. and Blusztajn, J.S., 2003. Geochemistry of hydrothermally altered oceanic crust: DSDP/ODP Hole 504B - Implications for seawater-crust exchange budgets and Sr- and Pb-isotopic evolution of the mantle. *Geochemistry, Geophysics, Geosystems, G<sup>3</sup>*, an electronic journal of the earth sciences, 4(3): (29).
- Batiza, R., 1996. Magmatic segmentation of mid-ocean ridges: A review. In: C.J. MacLeod, P.A. Tyler and C.L. Walker (Editors), *Tectonic, Magmatic, Hydrothermal and Biological Segmentation of Mid-Ocean Ridges*. Geological Society Special Publications, pp. 103-130.
- Buatier, M.D., Monnin, C., Früh-Green, G.L. and Karpoff, A.-M., 2001. Fluid-sediment interactions related to hydrothermal circulation in the Eastern Flank of the Juan de Fuca Ridge. *Chemical Geology*, 175: 343-360.
- Davis, E.E., Chapman, D.S. and Forster, C.B., 1996. Observations concerning the vigor of hydrothermal circulation in young oceanic crust. *Journal of Geophysical Research*, 101(2): 2927-2942.
- Elderfield, H., Wheat, C.G., Mottl, M.J., Monnin, C. and Spiro, B., 1999. Fluid and geochemical transport through oceanic crust: A transect across the eastern flank of the Juan de Fuca Ridge. *Earth and Planetary Science Letters*, 172: 151-165.
- Fisher, A.T., 1998. Permeability within basaltic oceanic crust. *Reviews of Geophysics*, 36(2): 143-182.
- Fisher, A.T. and Becker, K., 2000. Channelized fluid flow in oceanic crust reconciles heat-flow and permeability data. *Nature*, 403(6765): 71-74.

- Fisher, A.T., Becker, K. and Narasimhan, R.N., 1994. Off-axis hydrothermal circulation: Parametric tests of a refined model of processes at Deep Sea Drilling Project/Ocean Drilling Program Site 504. *Journal of Geophysical Research*, 99: 3097-3123.
- Fisher, A.T., Becker, K., Narasimhan, T.N., Langseth, M.G. and Mottl, M.J., 1990. Passive off-axis convection through the southern flank of the Costa Rica Rift. *Journal of Geophysical Research*, 95: 9343-9370.
- Hanson, G.N. and Langmuir, C.H., 1978. Modelling of major elements in mantle systems using trace element approaches. *Geochemica et Cosmochimica Acta*, 42: 725-741.
- Hékinian, R. and Walker, D., 1987. Diversity and spatial zonation of volcanic rocks from the East Pacific Rise near 21°N. *Contributions to Mineralogy and Petrology*, 96: 265-280.
- Hirschmann, M.M. and Stolper, E.M., 1996. A possible role for garnet pyroxenite in the origin of the "garnet signature" in MORB. *Contributions to Mineralogy and Petrology*, 124(2): 185-208.
- Hunter, A.G., Kempton, P.D. and Greenwood, P., 1999. Low-temperature fluid-rock interaction: An isotopic and mineralogical perspective of upper crustal evolution, eastern flank of the Juan de Fuca Ridge (JdFR), ODP Leg 168. *Chemical Geology*, 155(1-2): 3-28.
- Kennett, J., 1982. *Marine Geology*. Prentice-Hall, 752 pp.
- Klein, E.M. and Langmuir, C.H., 1987. Global correlations of oceanic ridge basalt chemistry with axial depth and crustal thickness. *Journal of Geophysical Research*, 92(B8): 8089-8115.
- Klein, E.M. and Langmuir, C.H., 1989. Local Versus Global Variations in Ocean Ridge Basalt Composition: A Reply. *Journal of Geophysical Research*, 94(B4): 4241-4252.
- Langmuir, C.H., Bender, J.F. and Batiza, R., 1986. Petrological segmentation of the East Pacific Rise, 5°30' - 14°30'N. *Nature*, 322: 422-429.
- Langmuir, C.H., Klein, E.M. and Plank, T., 1992. Petrological Systematics of Mid-Ocean Ridge Basalts: Constraints on Melt Generation Beneath Ocean Ridges. In: J.P. Morgan, D.K. Blackman and J.M. Sinton (Editors), *Mantle Flow and Melt Generation at Mid-Ocean Ridges*. Geophysical Monograph. American Geophysical Union, pp. 183-280.
- Laverne, C., Agrinier, P., Hermitte, D. and Bohn, M., 2001. Chemical fluxes during hydrothermal alteration of a 1200-m long section of dikes in the oceanic crust, DSDP/ODP Hole 504B. *Chemical Geology*, 181: 73-98.
- Lundstrom, C.C., Gill, J. and Williams, Q., 2000. A geochemically consistent hypothesis for MORB generation. *Chemical Geology*, 162(2): 105-126.

- MacDonald, K.C., 1998. Linkages between faulting, volcanism, hydrothermal activity and segmentation on fast spreading centers. In: W.R. Buck, P.T. Delaney, J.A. Karson and Y. Lagabrielle (Editors), *Faulting and Magmatism at Mid-Ocean Ridges*. Geophysical Monograph, pp. 27-58.
- MacDonald, K.C., Fox, P.J., Perram, L.J., Eisen, M.F., Hayman, R.M., Miller, S.P., Carbotte, S.M., Cormier, M.H. and Shor, A.N., 1988. A new view of the mid-ocean ridge from the behaviour of ridge-axis discontinuities. *Nature*, 335: 217-225.
- Mahoney, J.J., Sinton, J.M., Kurz, M.D., Macdougall, J.D., Spencer, K.J. and Lugmair, G.W., 1994. Isotope and trace element characteristics of a super-fast spreading ridge: East Pacific Rise, 13-23 degrees S. *Earth and Planetary Science Letters*, 121(1-2): 173-193.
- Michael, P.J. and Chase, R.L., 1987. The influence of primary magma composition, H<sub>2</sub>O and pressure on mid-ocean ridge basalt differentiation. *Contributions to Mineralogy and Petrology*, 96: 245-263.
- Mottl, M.J., 2003. Partitioning of Energy and Mass Fluxes between Mid-ocean Ridge Axes and Flanks at High and Low Temperature. In: P.E. Halbach, V. Tunnicliffe and J.R. Hein (Editors), *Dahlem Workshop Report 89, Energy and Mass Transfer in Marine Hydrothermal Systems*. Dahlem University Press, Berlin, pp. 271-286.
- Mottl, M.J. and Wheat, C.G., 1994. Hydrothermal circulation through mid-ocean ridge flanks: Fluxes of heat and magnesium. *Geochimica et Cosmochimica Acta*, 58(10): 2225-2237.
- Mottl, M.J. and Wheat, C.G., 2000. Hydrothermal Fluxes on Mid-Ocean Ridge Flanks: EXCO II on the Eastern Flank of the East Pacific Rise near 14°S. *Eos Trans. AGU*, 81(48): F458 Fall Meeting.
- Natland, J.H. and Dick, H.J.B., 1996. Melt migration through high-level gabbroic cumulates of the East Pacific Rise at Hess Deep; the origin of magma lenses and the deep crustal structure of fast-spreading ridges. *Proceedings of the Ocean Drilling Program, Scientific Results*, 147: 21-58.
- Niu, Y. and Batiza, R., 1991. An empirical method for calculating melt composition produced beneath mid-ocean ridges: Application for axis and off-axis (Seamount) melting. *Journal of Geophysical Research*, 96: 21753-21777.
- Niu, Y., Regelous, M., Wendt, I.J., Batiza, R. and O'Hara, M.J., 2002. Geochemistry of near-EPR seamounts: importance of source vs. process and the origin of enriched mantle component. *Earth and Planetary Science Letters*, 199(3-4): 327-345.
- Niu, Y., Waggoner, D.G., Sinton, J.M. and Mahoney, J.J., 1996. Mantle source heterogeneity and melting processes beneath seafloor spreading centers: The East Pacific Rise, 18°-19°S. *Journal of Geophysical Research*, 101: 27711-27733.

- O'Hara, M.J., 1968. Are ocean floor basalts primary magmas ? *Nature*, 220: 683-686.
- O'Hara, M.J., 1977. Geochemical evolution during fractional crystallisation of a periodically refilled magma chamber. *Nature*, 266: 503-507.
- Pan, Y. and Batiza, R., 2002. Mid-ocean ridge magma chamber processes: Constraints from olivine zonation in lavas from the East Pacific Rise at 9°30'N and 10°30'N. *Journal of Geophysical Research*, 107(B1): 10.1029/2001JB000435.
- Perfit, M.R. and Chadwick, W.W., 1998. Magmatism at Mid-Ocean Ridges: Constraints from Volcanological and Geochemical Investigations. In: W.R. Buck, P.T. Delaney, J.A. Karson and Y. Lagabriele (Editors), *Faulting and magmatism at mid-ocean ridges*. *Geophysical Monograph*, pp. 59-115.
- Perfit, M.R., Fornari, D.J., C, S.M., Bender, J.F., Langmuir, C.H. and Haymon, R.M., 1994. Small-scale spatial and temporal variations in mid-ocean ridge crest magmatic processes. *Geology*, 22(4): 375-379.
- Regelous, M., Niu, Y., Wendt, J.I., Batiza, R., Greig, A. and Collerson, K.D., 1999. Variations in the geochemistry of magmatism on the East Pacific Rise at 10°30'N since 800 ka. *Earth and Planetary Science Letters*, 168(1-2): 45-63.
- Reynolds, J.R., Langmuir, C.H., Bender, J.F., Kastens, K.A. and Ryan, W.B.F., 1992. Spatial and temporal variability in the geochemistry of basalts from the East Pacific Rise. *Nature*, 359: 493-499.
- Rubin, K.H., Smith, M.C., Bergmanis, E.C., Perfit, M.R., Sinton, J.M. and Batiza, R., 2001. Geochemical heterogeneity within mid-ocean ridge lava flows: Insights into eruption, emplacement and global variations in magma generation. *Earth and Planetary Science Letters*, 188(3-4): 349-367.
- Schilling, J.G., Zajac, M., Evans, R., Johnson, T., White, W., Devine, J.D. and Kingsley, R., 1983. Petrologic and geochemical variations along the Mid-Atlantic Ridge from 29°N to 73°N. *American Journal of Science*, 283(6): 510-586.
- Singh, S.C., Kent, G.M., Collier, J.S., Harding, A.J. and Orcutt, J.A., 1998. Melt to mush variations in crustal magma properties along the ridge crest at the southern East Pacific Rise. *Nature*, 394(6696): 874-878.
- Sinton, J.M. and Detrick, R.S., 1992. Mid-Ocean Ridge magma chambers. *Journal of Geophysical Research*, 97(B1): 197-216.
- Sinton, J.M., Smaglik, S.M. and Mahoney, J.J., 1991. Magmatic processes at superfast Mid-Ocean Ridges: Glass compositional variations along the East Pacific Rise 13°-23°S. *Journal of Geophysical Research*, 96(B4): 6133-6155.
- Spiegelman, M. and Reynolds, J.R., 1999. Combined dynamic and geochemical evidence for convergent melt flow beneath the East Pacific Rise. *Nature*, 402: 282-285.

- Staudigel, H., Plank, T., White, B. and Schmincke, H.-U., 1996. Geochemical fluxes during seafloor alteration of the basaltic upper oceanic crust: DSDP Sites 417 and 418. In: G.E. Bebout, D.W. Scholl, S.H. Kirby and J.P. Platt (Editors), Subduction top to bottom. Geophysical Monograph, pp. 19-38.
- Stein, C.A. and Stein, S., 1994. Constraints on hydrothermal heat flux through the oceanic lithosphere from global heat flow. *Journal of Geophysical Research*, 99: 3081-3095.
- Teagle, D.A.H., Alt, J.C. and Halliday, A.N., 1998. Tracing the evolution of hydrothermal fluids in the upper oceanic crust: Sr-isotopic constraints from DSDP/ODP Holes 504B and 896A. In: R.A. Mills and K. Harrison (Editors), Modern ocean floor processes and the geological record. Geological Society Special Publications, pp. 81-97.

**The fourth dimension in spreading axis activity:  
Magmatic evolution along the Southern East Pacific  
Rise at 14°S during the last 9 Ma**

Burkhard Schramm and Colin W. Devey



*Submitted to Earth and Planetary Science Letters, 29 September 2003*

## **The fourth dimension in spreading axis activity: Magmatic evolution along the Southern East Pacific Rise at 14°S during the last 9 Ma**

Burkhard Schramm<sup>1\*</sup> and Colin W. Devey<sup>1</sup>

<sup>1</sup> *Fachbereich Geowissenschaften, Universität Bremen, Klagenfurter Str., 28359 Bremen, Germany*

\* *Corresponding author. Phone: +49-421-2187766 Fax: +49-421-218 9460; E-mail: bschramm@uni-bremen.de*

*Submitted to Earth and Planetary Science Letters, 29 September 2003*

### **Abstract**

Our conception of mid-ocean ridge processes is dominated by the results of studies on the present-day axes. Spreading systems are envisaged to be highly dynamic, fluctuating environments, with both tectonic and magmatic features varying over relatively short (< 1Ma) time scales. Here we present geochemical results on basalts dredged within a narrow flow-line corridor extending 9 Ma eastward of the East Pacific Rise at 14°S. Backtracking these samples to their original on-axis eruption location, and comparison of their geochemical data with samples from the present-day axis shows a surprisingly good and significant agreement. The samples can be divided into two geographical groups, separated by a magmatic border at 14°24'S. Samples erupted over the last 2.9 Ma south of the border can be related to one another by crystal fractionation, suggesting they are derived from the same, long-lived magma chamber. All samples erupted on-axis north of the magmatic border have, on the other hand, MgO contents within the range  $7.3 \pm 0.4$  wt. %. Modeling of the trace-element variations in these samples shows that they can be related by differences in the amount of garnet present in the melting residue and that variation in the degree of crystal fractionation are negligible. Samples collected close to small seamounts covering the age range 2.56 – 4.6 Ma show trace-element depleted signatures characteristic of off-axis volcanism and also all back-track to the same ( $\pm 3.6$  km) eruption latitude. These observation taken together suggest a magmatic system both on- and off-axis which is characterized by stability on the several million year scale.

Keywords: East Pacific Rise, major elements, trace elements, off-axis volcanism

## Introduction

To understand the history of magmatic evolution on mid-ocean ridges (MOR), it is important to study them over large spatial and temporal length scales. The chemical composition of MOR-basalt provides information on their complex geochemical history, from initial processes in the mantle to the eruption at the narrow fissure zone of the ridge axis.

Variation in the composition of the erupted magmas along axis allows magmatic provinces to be defined. These in turn suggest a magmatic segmentation of the ridge which can sometimes be associated with bathymetric or tectonic ridge axis discontinuities. Structural and petrological considerations allow the different forms of tectonic segmentation to be divided into first to fourth order discontinuities based on their age and longevity. From first to fourth order segmentation boundaries are defined respectively by: Transform faults (last for  $10^7$  years); overlapping spreading centers (OSC) ( $10^6$  years); small offset OSC ( $10^4 - 10^5$  years) and minor deviations in axial linearity (devals) ( $<10^4$  years) [1, 2]. Even very small offsets such as devals or discontinuities in the axial magma chamber which maybe appear insignificant morphologically can define important magmatic boundaries [e.g. 3-6].

The East Pacific Rise (EPR) is the fastest spreading ridge along the 70000 km long MOR system. Spreading rates span a range of 80-160 mm/years, with the fastest rates along the Southern EPR (SEPR). Fast-spreading ridges are more homogeneous in terms of topography, morphology and chemical variability than slow-spreading ridges [7]. This may reflect a more stable crust and mantle temperature regime, in turn related to more efficient mantle processing [8]. Characteristic differences in sources and melting parameters have been shown to control the compositions of MORB on a global and regional scale. Local trends in the chemistry from fast-spreading ridges are probably caused by small but frequent eruptions of magmas that have undergone differing degrees of partial melting, mixing and fractional crystallization as they rise towards the surface [7-10].

Off-axis volcanism occurs outside the neovolcanic zone in the form of volcanic edifices and seamounts and adds only minor amounts to the crustal volume (edifices 0.02-0.03 %, seamounts 0.3-1 %) but covers 7-11 % (edifices) or ~6 % (seamounts) of the mature seafloor [11-13]. Investigations from the EPR between 12°N and 12°30'N suggest that off-axis lavas cover ~20 % of the seafloor around the EPR [14]. The off-axis volcanism can take the form of young-looking lava fields, prominent pillow ridges or ideally near-axis seamounts [9, 15, 16]. At fast spreading ridges seamounts form within a zone 5-15 km away from the axis [12, 13]. Many near-axis seamount lavas show a geochemical depleted nature, derived from mantle sources more depleted than MOR basalt [9, 15]. In addition, off-axis volcanism identified by lava fields or pillow ridges also exhibit a more depleted nature and can therefore be distinguished from magmas erupted at the ridge crest [17].

Due to the concentration of sampling efforts along the present-day ridge axis, little is known about the behaviour of the axis through time. The limited information available comes from, for example, a transect focused on alteration, e.g. dredged samples from the Mid-Atlantic that are up to 57 Ma old [18], or from the Flank Flux experiment during ODP Leg 168 off the Juan de Fuca Ridge that provides information about ten sites, drilled along a 120 km (up to ~3.5 Ma) linear transect perpendicular to the spreading axis [e.g. 19, 20].

In this paper we will present geochemical data from basalts collected along a crustal flow line east of the SEPR up to 8.64 Ma and compare them with samples from the same eruption latitudes erupting on the present day ridge axis. For the first time it is possible to discuss the geochemical history of a single spreading segment in terms of major and trace elements over several million years. We provide information about tectonic and geochemical segmentation, fractionation, mantle sources and the signature of off-axis volcanism near the ridge crest.

## **EXCO field area**

### *Geologic setting, sampling and previous work*

The EXCO (**Ex**change processes between **C**rust and **O**cean) investigations are carried out in an area located between 14-16°S on the SEPR between the Easter microplate near 23°S and the right-stepping Garrett Transform Fault (GTF) boundary near 13°30'S (Fig.1). The field area is characterized by spreading at ultrafast rates, ranging from 143mm/year to 150 mm/year [21, 22] and a current axis which is remarkably linear and devoid of any transform fault boundaries [23].

The area was first studied in 1995 during Sonne cruise SO105 [24]. The cruise consisted of seismic, topographic, magnetic and heat flow studies of a strip of seafloor extending from the spreading axis out to 9 Ma old crust [25]. The EXCO II cruises (SO145 Legs 1 & 2, Spring 2000) were carried out to build on this earlier work and focus in more detail on the variations in heat flow (Leg1) and explore the chemical and magmatic variations in the Layer 2 rocks (Leg 2) in this ageing crust. The geophysical and rock sampling program followed a flow line east of the EPR within a single first-order spreading segment. The age of the samples could be determined by linear interpolation between the age of picked magnetic reversals [4]. Within this 720 km long and 20-45 km wide corridor the migration of at least five overlapping spreading centers (OSC) has left discordant bathymetric zones consisting of hummocky basins and motley texture of curved lineations [4]. Previous investigations on the samples studied here show that the major element composition of the magmas is stable and independent of tectonic events (OSCs) during the last 9 Ma [4]. These authors suggest that the

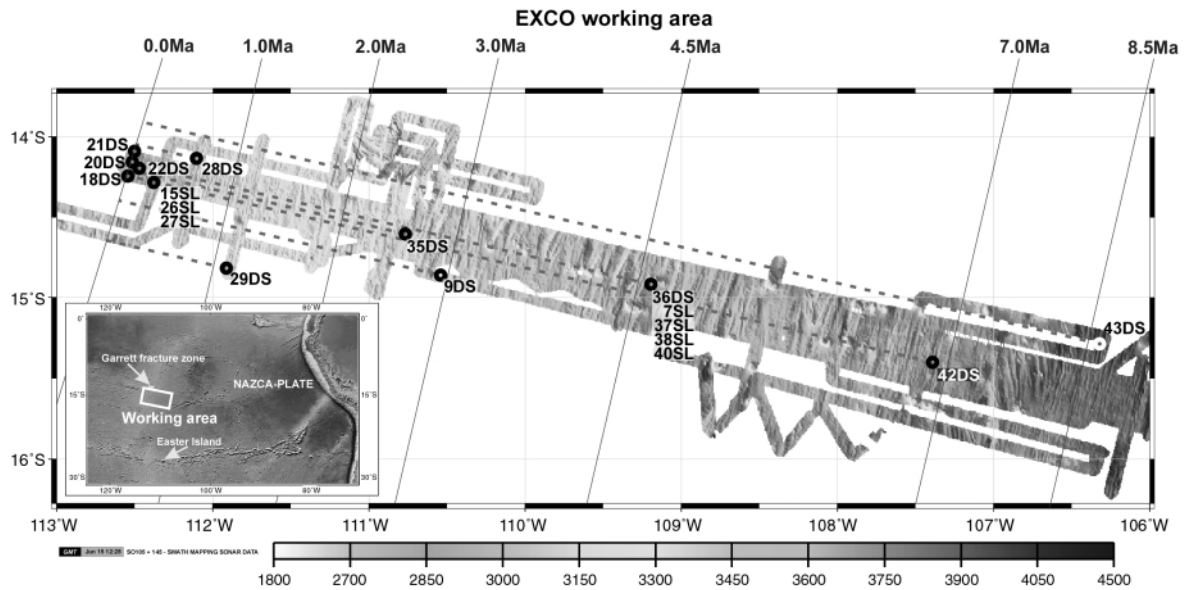


Figure 1. The EXCO working area east of the East Pacific rise, south of the Garrett transform fault after Grevemeyer et al. [4]. The map shows the sample locations of dredges (DS) and core catchers (SL). Diagonal lines indicate the age of the ocean crust based on magnetic anomalies. Dashed lines indicate the trace of the backtracked positions to the ridge axis. Samples 18DS, 20DS, and 21DS are directly from the present day ridge axis. Small image taken from Ridge Multibeam Synthesis (<http://ocean-ridge.ldeo.columbia.edu/>).

magmatic variations along the ridge axis are coming from the mantle. Features of progressive low temperature alteration on the samples have been investigated by comparing the mineralogical and chemical changes that occur at the ridge- and off-axis, showing a progressive alteration sequence over the last 9 Ma [26].

Rock samples were recovered by dredging on topographic highs (~100 – 200 m above the surrounding sedimented seafloor) or close to seamounts (35DS and 36DS). Three dredges were collected at the present day ridge axis; the remaining eight dredges were collected on a flow-line east of the ridge. Two sampling areas are located close to seamounts (and hence close to locations of off-axis magmatic activity), in case of the other flow-line locations we were not able to classify the morphological features sampled as being the result of on- or off-axis volcanism. We also collected glass pieces from the core catcher of 7 gravity corers. By projecting all samples along the flow line from their present day locations back to the ridge axis, we get eruption latitudes for all samples of between 13°54'S to 14°38'S. We can therefore use the samples to investigate the long-term activity of this 80 km of ridge axis.

### *Major element chemistry of axial basalts*

The nearby GTF is dominantly characterized by olivine and plagioclase phyric and picritic basalts [27-29]. Compared to lavas of the SEPR ridge axis, the Garrett lavas are generally less evolved, contain lower concentrations of incompatible minor and trace elements and have lower  $\text{TiO}_2$ ,  $\text{FeO}$ ,  $\text{Na}_2\text{O}$  and  $\text{P}_2\text{O}_5$ , and higher  $\text{CaO}$  and  $\text{Al}_2\text{O}_3$  [29]. Samples collected on the ridge axis in the EXCO area south of the GTF [3, 27, 28, 30-34], show a smaller range in  $\text{Mg\#}$  ( $\text{Mg\#} = \text{Mg}/(\text{Mg}+\text{Fe})$ ) down to  $\sim 14^\circ 30'\text{S}$  and then a clear decrease and wider range in  $\text{Mg\#}$  south of this (Fig.2). This change in magma composition is close to a deval identified at  $14^\circ 30'\text{S}$  (Fig.3).

The  $14^\circ 30'$  deval has been explained as corresponding to a magmatic border, with samples from opposing sides of the deval being related by variable extents of crystal fractionation from similar parental magmas. The deval, therefore, was suggested to a significant boundary in extent of fractionation within a single magma chamber [3]. Generally, published analytical work has focused on major elements, so only few trace element analyses are reported for the ridge axis of the EXCO area.

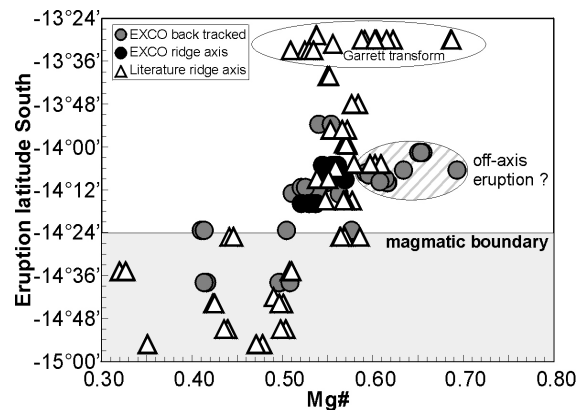


Figure 2. Geochemical data backtracked to the ridge axis crest with the magmatic boundary at  $14^\circ 24'\text{S}$  (Figure taken from Grevenmeyer et al. [4]). Note the significant compositional variations of samples from the ridge crest with latitude. The composition of samples in the striped area with a somewhat higher  $\text{Mg\#}$  is probably related to off-axis eruptions (see text for discussion).

### Analytical methods

This study is based on investigations carried out on 50 basalt samples from 11 dredge locations (DS) and glass pieces select from the core catcher of a gravity corer (SL) at 7 locations. Analyses are given in Table 1 (major elements) and 2 (trace elements). Glass samples from each dredge and core catcher were prepared for examination of their geochemical history. Fresh glass chips were carefully handpicked under the binocular and washed in an ultrasonic bath to provide material for the determination of pristine magmatic compositions. All samples appear unaltered both under the microscope and at high magnification under the electron microprobe.

Major element analyses were carried out on five spectrometer JEOL JXA 8900 RL electron microprobes at the University of Göttingen and University of Mainz, Germany on the hand picked glass pieces. Analytical conditions were 15kV accelerating voltage and 11-13 nA sample current. The electron beam was slightly defocused ( $10\ \mu\text{m}$  diameter) to avoid the volatilization of alkalis. Calibration was performed using international

Sample	Ma	Latitude	Longitude	Eruption	SiO <sub>2</sub>	TiO <sub>2</sub>	Al <sub>2</sub> O <sub>3</sub>	FeO	MnO	MgO	CaO	Na <sub>2</sub> O	K <sub>2</sub> O	P <sub>2</sub> O <sub>5</sub>	Cr <sub>2</sub> O <sub>3</sub>	Total	Mg#	K/Ti	n
21DS1	0.000	-14°05	-112°30	-14°05	50.9	1.8	14.4	10.7	0.20	7.5	11.7	2.9	0.11	0.15	0.03	100.4	0.56	0.08	10
21DS2	0.000	-14°05	-112°30	-14°05	50.9	1.8	14.4	10.6	0.21	7.6	11.7	2.9	0.11	0.15	0.06	100.4	0.56	0.09	10
21DS3	0.000	-14°05	-112°30	-14°05	50.5	1.8	14.4	10.7	0.19	7.5	11.7	3.0	0.11	0.14	0.04	100.0	0.56	0.09	10
21DS4	0.000	-14°05	-112°30	-14°05	50.5	1.8	14.2	11.0	0.21	7.4	11.3	3.1	0.13	0.16	0.03	99.9	0.54	0.10	10
21DS5	0.000	-14°05	-112°30	-14°05	50.6	1.8	14.4	10.6	0.20	7.5	11.7	3.0	0.11	0.15	0.04	100.1	0.56	0.08	10
21DS6	0.000	-14°05	-112°30	-14°05	50.6	1.8	14.3	10.7	0.20	7.5	11.7	3.0	0.10	0.15	0.04	100.1	0.56	0.08	10
21DS7	0.000	-14°05	-112°30	-14°05	50.6	1.8	14.4	10.5	0.19	7.6	11.6	3.0	0.11	0.15	0.05	99.9	0.56	0.08	10
18DS1	0.015	-14°16	-112°33	-14°16	51.1	1.9	13.8	11.3	0.20	7.4	11.3	2.9	0.12	0.15	0.03	100.2	0.54	0.09	10
18DS2	0.015	-14°16	-112°33	-14°16	50.2	1.8	13.8	11.4	0.18	7.4	11.4	2.9	0.13	0.13	0.02	99.2	0.54	0.10	5
18DS3	0.015	-14°16	-112°33	-14°16	50.3	1.9	14.0	11.5	0.20	7.0	11.1	2.9	0.14	0.16	0.03	99.1	0.52	0.10	5
18DS5	0.015	-14°16	-112°33	-14°16	50.3	1.8	13.9	11.3	0.22	7.1	11.3	2.9	0.13	0.13	0.02	99.1	0.53	0.10	7
18DS6	0.015	-14°16	-112°33	-14°16	50.5	1.8	13.8	11.3	0.21	7.3	11.4	2.9	0.13	0.13	0.04	99.5	0.54	0.10	7
18DS7	0.015	-14°16	-112°33	-14°16	51.1	1.9	13.9	11.4	0.22	7.2	11.5	2.9	0.11	0.13	0.03	100.5	0.53	0.08	10
18DS9	0.015	-14°16	-112°33	-14°16	51.0	1.9	13.9	11.3	0.21	7.3	11.3	2.9	0.11	0.15	0.02	100.1	0.54	0.09	10
20DS1	0.015	-14°09	-112°31	-14°09	50.4	1.7	14.0	11.0	0.21	7.6	11.6	2.7	0.11	0.13	0.04	99.3	0.55	0.09	7
20DS3	0.015	-14°09	-112°31	-14°09	49.9	1.7	14.7	10.3	0.18	7.6	11.8	2.8	0.19	0.15	0.05	99.4	0.57	0.16	5
20DS4	0.015	-14°09	-112°31	-14°09	50.6	1.7	14.1	11.0	0.20	7.5	11.7	2.7	0.10	0.12	0.04	99.7	0.55	0.09	7
20DS5	0.015	-14°09	-112°31	-14°09	50.8	1.7	14.0	11.0	0.20	7.5	11.7	2.7	0.11	0.10	0.04	99.7	0.55	0.09	7
22DS1	0.120	-14°12	-112°28	-14°10	49.6	1.7	14.0	10.8	0.20	7.3	11.0	2.7	0.12	0.16	0.04	97.8	0.55	0.09	32
22DS2	0.120	-14°12	-112°28	-14°10	49.8	1.7	14.0	11.0	0.19	7.3	11.1	2.7	0.12	n.d.	0.04	98.0	0.54	0.09	25
27SL	0.360	-14°17	-112°19	-14°13	50.1	2.0	13.5	11.7	0.22	6.8	11.0	2.8	0.11	0.16	0.03	98.3	0.51	0.08	37
15SL	0.360	-14°16	-112°19	-14°13	50.3	1.7	13.8	11.1	0.21	7.3	11.6	2.7	0.07	0.11	0.03	98.8	0.54	0.06	17
26SL	0.360	-14°17	-112°19	-14°13	49.5	1.7	14.0	10.2	0.20	7.4	11.4	2.7	0.09	0.16	0.04	97.3	0.56	0.08	22
28DS1	0.650	-14°09	-112°07	-14°02	48.9	0.92	16.7	9.6	0.18	10.1	11.6	2.2	0.07	0.06	0.06	100.5	0.65	0.11	10
28DS2	0.650	-14°09	-112°07	-14°02	49.2	0.95	16.7	9.6	0.17	10.0	11.5	2.2	0.07	0.06	0.06	100.5	0.65	0.11	10
28DS3	0.650	-14°09	-112°07	-14°02	49.0	0.92	16.6	9.6	0.17	10.2	11.5	2.2	0.08	0.06	0.07	100.4	0.66	0.11	10
28DS4	0.650	-14°09	-112°07	-14°02	48.9	0.91	16.7	9.6	0.17	10.1	11.6	2.1	0.06	0.05	0.06	100.3	0.65	0.10	9
28DS5	0.650	-14°09	-112°07	-14°02	49.0	0.92	16.7	9.6	0.18	10.1	11.5	2.2	0.07	0.06	0.06	100.2	0.65	0.10	10
29DS1	1.160	-14°49	-111°54	-14°38	50.3	2.3	13.7	12.0	0.21	6.7	10.9	3.0	0.19	0.23	0.03	99.6	0.50	0.12	10
29DS10	1.160	-14°49	-111°54	-14°38	53.9	1.9	13.4	12.3	0.22	4.9	9.0	3.4	0.34	0.37	0.02	99.8	0.42	0.25	10
29DS2	1.160	-14°49	-111°54	-14°38	53.8	1.9	13.2	12.1	0.22	4.8	8.7	3.7	0.35	0.38	0.02	99.1	0.41	0.25	10
29DS3	1.160	-14°49	-111°54	-14°38	50.5	2.3	13.8	12.0	0.21	6.6	11.0	3.1	0.19	0.21	0.02	99.8	0.50	0.12	10
29DS4	1.160	-14°49	-111°54	-14°38	50.6	2.2	13.8	11.8	0.21	6.9	11.2	3.1	0.17	0.19	0.02	100.2	0.51	0.11	10
35DS2	2.560	-14°36	-110°46	-14°10	50.1	1.2	15.1	9.5	0.17	8.5	12.8	2.4	0.04	0.06	0.05	99.9	0.62	0.05	9
35DS4	2.560	-14°36	-110°46	-14°10	49.7	1.1	14.5	9.5	0.20	8.6	12.7	2.5	0.04	0.09	0.07	99.0	0.62	0.06	13
9DS2	2.920	-14°52	-110°32	-14°23	50.0	2.8	12.6	14.6	0.25	5.7	9.9	3.2	0.17	0.25	0.01	99.5	0.41	0.08	11
9DS4	2.920	-14°52	-110°32	-14°23	49.8	2.2	13.7	12.0	0.21	6.8	11.0	3.0	0.17	0.18	0.04	99.2	0.50	0.11	9
9DS8	2.920	-14°52	-110°32	-14°23	49.7	1.6	14.9	10.1	0.18	7.7	12.0	3.0	0.15	0.13	0.06	99.4	0.58	0.13	10
9DS11	2.920	-14°52	-110°32	-14°23	49.6	2.8	12.7	14.5	0.26	5.8	9.7	3.1	0.19	0.22	0.01	99.0	0.41	0.09	7
37SL	4.590	-14°57	-109°12	-14°09	49.7	1.1	14.7	9.5	0.18	8.4	12.4	2.4	0.02	0.08	0.05	98.6	0.61	0.03	36
36DS7	4.600	-14°54	-109°11	-14°06	48.1	0.89	16.7	7.8	0.14	9.8	12.4	2.4	0.03	0.07	0.07	98.4	0.69	0.04	17
36DS8	4.600	-14°54	-109°11	-14°06	49.6	1.1	15.6	9.4	0.17	9.1	12.7	2.4	0.04	0.06	0.07	100.2	0.63	0.05	7
38SL	4.610	-14°55	-109°11	-14°07	50.2	1.2	14.3	9.8	0.19	8.0	12.4	2.6	0.02	0.07	0.03	98.9	0.59	0.02	41
40SL	4.610	-14°56	-109°11	-14°08	49.3	1.4	14.7	9.9	0.18	8.1	11.9	2.5	0.05	0.10	0.05	98.2	0.60	0.05	40
7SL	4.620	-14°55	-109°10	-14°10	49.7	1.1	14.6	9.5	0.18	8.3	12.4	2.5	0.02	0.07	0.04	98.4	0.61	0.02	30
42DS2	6.840	-15°23	-107°22	-14°11	50.3	2.0	13.8	11.6	0.20	7.1	11.5	2.8	0.13	0.15	0.03	99.7	0.52	0.09	10
42DS10	6.840	-15°23	-107°22	-14°11	49.7	1.9	13.9	11.5	0.21	7.1	11.4	2.8	0.14	0.14	0.02	98.8	0.53	0.10	7
43DS4	8.640	-15°18	-106°18	-13°54	50.3	2.0	14.0	11.2	0.21	7.4	11.4	2.8	0.11	0.13	0.04	99.6	0.54	0.08	7
43DS13	8.640	-15°18	-106°18	-13°54	50.7	1.8	14.2	10.8	0.20	7.5	11.8	2.8	0.09	0.14	0.03	100.1	0.55	0.07	10
Analytical error (1 S.D. relative %)					1.7	4.1	2.2	2.5	9.2	2.6	2.1	3.6	17.3	19.9	51.7				

Table 1. Average major element microprobe analyses of glassy MORB pieces. In contrast to our previous work [4] we group all core catcher analyses of one sampling location and present all analyses of each dredge haul. All analyses are taken from Grevemeyer et al. [4], only in the case of sample 22DS do we present new analyses. Note that analyses of sample 27SL and 38SL show small differences to the previous published data due to discrepancies during standard normalization of the earlier study. Eruption latitude is discussed in the text; DS = dredge; SL = core catcher; n = number of analyses used to build the mean.

Sample	21DS1	21DS3	21DS4	18DS9	18DS10	20DS3	20DS4	22DS2	27SL	15SL	26SL	28DS1	28DS2	28DS3	28DS4	29DS10	29DS2	29DS3	29DS4
Ma	0.000	0.000	0.000	0.015	0.015	0.015	0.015	0.120	0.360	0.360	0.360	0.650	0.650	0.650	0.650	1.160	1.160	1.160	1.160
Latitude	-14°05	-14°05	-14°05	-14°16	-14°16	-14°09	-14°09	-14°12	-14°17	-14°16	-14°17	-14°09	-14°09	-14°09	-14°09	-14°49	-14°49	-14°49	-14°49
Longitude	-112°30	-112°30	-112°30	-112°33	-112°33	-112°31	-112°31	-112°28	-112°19	-112°19	-112°19	-112°07	-112°07	-112°07	-112°07	-111°54	-111°54	-111°54	-111°54
Eruption	-14°05	-14°05	-14°05	-14°16	-14°16	-14°09	-14°09	-14°10	-14°13	-14°13	-14°13	-14°02	-14°02	-14°02	-14°02	-14°38	-14°38	-14°38	-14°38
Li	6.2	6.2	5.2	5.7	5.4	5.8	5.7	5.5	7.6	6.3	7.4	3.5	2.7	3.0	2.7	13.0	15.8	6.2	5.7
Sc	41.4	41.9	42.4	42.6	43.4	41.7	46.7	39.2	43.4	41.6	42.0	38.3	34.6	36.8	34.3	32.9	32.1	40.5	38.4
V	311	310	315	344	337	301	356	340	391	381	370	183	171	186	177	237	219	372	320
Cr	238	243	246	160	140	261	204	193	142	127	118	458	485	459	384	109	90.7	112	140
Co	37.6	37.7	37.3	39.0	38.4	39.7	40.9	38.0	40.3	37.7	39.0	56.8	44.8	48.9	44.3	29.5	29.6	37.1	32.4
Ni	63.4	64.9	60.5	52.2	52.5	78.5	64.2	70.0	61.7	50.8	55.6	339	207	229	183	33.4	33.0	46.2	44.7
Cu	61.6	62.4	59.7	58.3	65.3	73.0	68.8	56.8	55.1	51.3	55.5	85.0	76.1	84.1	80.7	40.5	41.1	52.8	47.3
Ga	15.2	15.2	17.7	17.9	18.0	16.9	18.4	17.4	16.7	18.2	16.9	12.7	13.4	14.4	13.9	21.7	20.5	18.8	16.7
Rb	1.20	1.17	1.18	1.25	2.6	2.5	1.02	1.19	1.21	1.24	1.79	1.06	0.87	0.98	0.88	3.6	4.1	2.2	1.94
Sr	122	121	124	111	128	150	99.9	92.5	106	102	116	125	120	125	121	94.6	100	121	112
Y	31.9	31.6	34.8	32.7	31.9	31.2	38.0	33.9	40.7	39.8	39.6	17.0	15.7	16.5	15.9	84.9	88.7	39.2	36.5
Zr	102	101	130	102	108	104	115	103	119	125	120	38.2	33.5	37.1	35.0	337	363	141	116
Nb	2.7	2.6	2.7	2.7	4.6	4.6	2.3	2.7	2.9	2.9	3.6	2.0	1.87	2.0	1.99	6.8	7.5	4.9	3.8
Cs	0.02	0.02	0.02	0.02	0.04	0.03	0.01	0.02	0.02	0.01	0.02	0.04	0.01	0.02	0.01	0.04	0.06	0.03	0.02
Ba	11.2	11.0	11.4	11.5	23.0	23.8	9.6	11.0	11.2	11.5	15.9	9.8	9.3	9.8	9.6	23.9	27.4	20.8	17.9
La	3.6	3.6	3.6	3.4	4.4	4.6	3.0	3.3	4.0	4.0	4.4	1.87	1.74	1.81	1.79	10.2	11.7	5.4	4.8
Ce	11.6	11.5	11.2	10.4	12.3	13.2	9.3	10.2	12.9	12.2	13.5	5.5	4.9	5.1	5.0	30.9	36.6	15.5	13.8
Pr	2.0	2.0	1.97	1.85	2.0	2.2	1.67	1.82	2.3	2.2	2.3	0.92	0.84	0.88	0.86	5.3	6.2	2.6	2.4
Nd	10.8	10.7	10.6	10.0	10.7	11.2	9.3	10.0	12.5	12.0	12.7	5.1	4.6	4.8	4.7	27.5	32.2	13.6	12.5
Sm	3.8	3.7	3.7	3.5	3.7	3.8	3.5	3.7	4.6	4.3	4.5	1.85	1.69	1.76	1.74	9.0	10.6	4.6	4.3
Eu	1.34	1.34	1.31	1.27	1.29	1.34	1.23	1.26	1.57	1.48	1.56	0.77	0.70	0.73	0.72	2.4	2.8	1.56	1.45
Gd	4.9	4.9	4.9	4.7	4.7	4.9	4.8	4.9	6.1	5.8	6.0	2.5	2.3	2.4	2.3	11.2	13.5	5.9	5.5
Tb	0.89	0.88	0.90	0.87	0.87	0.88	0.91	0.90	1.12	1.08	1.09	0.46	0.42	0.44	0.43	2.1	2.4	1.08	1.00
Dy	6.0	6.0	6.1	5.8	5.7	5.9	6.3	6.1	7.6	7.2	7.5	3.2	2.9	3.0	2.9	13.7	16.4	7.2	6.7
Ho	1.28	1.26	1.33	1.26	1.23	1.26	1.38	1.31	1.63	1.57	1.59	0.67	0.62	0.64	0.63	3.0	3.5	1.54	1.44
Er	3.7	3.6	3.9	3.6	3.5	3.5	4.0	3.7	4.6	4.5	4.5	1.93	1.77	1.84	1.80	8.5	10.0	4.4	4.1
Tm	0.53	0.53	0.59	0.52	0.51	0.52	0.60	0.55	0.68	0.66	0.66	0.29	0.26	0.27	0.27	1.26	1.50	0.64	0.60
Yb	3.5	3.4	3.9	3.4	3.3	3.5	4.0	3.6	4.5	4.3	4.4	1.89	1.71	1.79	1.75	8.3	10.0	4.2	3.9
Lu	0.52	0.51	0.59	0.51	0.50	0.51	0.60	0.54	0.67	0.65	0.65	0.28	0.26	0.27	0.26	1.23	1.49	0.62	0.59
Hf	2.8	2.8	3.3	2.6	2.7	2.9	3.1	2.7	3.4	3.3	3.5	1.15	0.97	1.10	1.05	8.3	10.1	3.6	3.1
Ta	0.19	0.19	0.19	0.18	0.29	0.32	0.15	0.19	0.21	0.20	0.25	0.14	0.13	0.14	0.14	0.44	0.52	0.32	0.26
Th	0.18	0.18	0.32	0.19	0.32	0.34	0.31	0.19	0.20	0.24	0.26	0.12	0.12	0.13	0.12	0.62	0.72	0.37	0.32
U	0.06	0.06	0.17	0.07	0.10	0.11	0.14	0.06	0.07	0.09	0.09	0.04	0.04	0.06	0.04	0.21	0.25	0.12	0.10

Table 2. Trace element ICP-MS analyses of glassy MORB pieces.

Sample	35DS2 <sup>*</sup>	9DS2 <sup>*</sup>	9DS4 <sup>*</sup>	9DS8 <sup>*</sup>	37SL	36DS8 <sup>*</sup>	38SL	40SL	7SL	42DS2	42DS10 <sup>*</sup>	43DS4	43DS13 <sup>*</sup>
Ma	2.560	2.920	2.920	2.920	4.590	4.600	4.610	4.610	4.620	6.840	6.840	8.640	8.640
Latitude	-14°36	-14°52	-14°52	-14°52	-14°57	-14°54	-14°55	-14°56	-14°55	-15°23	-15°23	-15°18	-15°18
Longitude	-110°46	-110°32	-110°32	-110°32	-109°12	-109°11	-109°11	-109°11	-109°10	-107°22	-107°22	-106°18	-106°18
Eruption	-14°10	-14°23	-14°23	-14°23	-14°09	-14°06	-14°07	-14°08	-14°10	-14°11	-14°11	-13°54	-13°54
Li	4.8	10.1	5.7	4.0	4.0	4.0	4.3	4.6	4.4	6.0	6.1	5.9	6.6
Sc	39.1	45.5	40.5	34.9	38.7	38.0	41.1	37.5	37.5	42.4	42.2	43.2	43.9
V	257	498	358	234	257	251	285	242	260	355	356	357	335
Cr	353	38.6	205	262	339	374	199	309	292	196	190	241	208
Co	42.0	44.0	36.6	32.1	43.4	44.0	40.9	43.8	35.2	38.2	39.2	39.1	38.9
Ni	81.8	33.9	56.6	59.6	75.3	57.2	59.5	86.7	65.9	49.4	55.3	64.6	68.2
Cu	83.2	54.1	59.8	58.6	91.0	98.8	76.5	90.9	65.7	63.7	60.7	61.5	66.5
Ga	13.4	19.3	18.2	15.0	16.0	15.5	16.3	13.6	16.1	18.2	18.4	18.8	15.3
Rb	0.26	1.66	1.63	1.06	0.16	0.14	0.13	0.18	1.11	1.31	1.35	0.86	0.91
Sr	85.2	118	117	131	93.9	88.9	87.2	98.0	135	112	114	117	110
Y	21.7	54.8	39.1	24.7	22.2	20.1	24.4	21.3	25.3	35.2	35.2	37.9	33.7
Zr	48.5	176	136	81.7	54.1	45.9	52.5	49.5	87.9	116	115	126	101
Nb	0.72	4.2	3.6	2.5	0.56	0.51	0.47	0.52	2.7	2.9	2.9	2.4	2.1
Cs	0.00	0.02	0.02	0.01	0.00	0.00	0.00	0.00	0.01	0.02	0.02	0.01	0.02
Ba	2.9	14.9	14.1	11.3	2.4	1.7	1.6	2.3	11.6	11.5	11.5	7.9	7.0
La	1.36	6.1	4.8	3.5	1.37	1.25	1.31	1.35	3.6	3.9	3.9	3.9	3.3
Ce	4.9	19.4	14.0	10.4	4.9	4.5	5.0	5.0	10.6	11.7	11.7	12.4	10.9
Pr	0.96	3.3	2.4	1.76	0.95	0.88	1.02	0.95	1.78	2.0	2.0	2.2	1.94
Nd	5.6	17.9	13.1	9.1	5.6	5.1	6.1	5.5	9.2	10.9	10.8	12.2	10.6
Sm	2.2	6.4	4.6	3.1	2.2	2.0	2.5	2.2	3.1	3.8	3.8	4.3	3.9
Eu	0.87	2.1	1.55	1.10	0.84	0.79	0.94	0.86	1.11	1.33	1.33	1.48	1.36
Gd	3.1	8.3	5.9	3.9	3.0	2.8	3.5	3.1	3.9	5.0	5.1	5.6	5.1
Tb	0.59	1.52	1.08	0.70	0.58	0.53	0.65	0.58	0.70	0.93	0.93	1.04	0.94
Dy	4.1	10.1	7.2	4.6	4.0	3.6	4.4	4.0	4.7	6.3	6.3	6.9	6.4
Ho	0.87	2.2	1.56	0.98	0.88	0.77	0.96	0.87	0.99	1.35	1.36	1.49	1.35
Er	2.5	6.2	4.4	2.8	2.5	2.2	2.7	2.5	2.8	3.9	3.8	4.3	3.8
Tm	0.37	0.91	0.65	0.41	0.38	0.33	0.39	0.36	0.40	0.57	0.57	0.63	0.56
Yb	2.4	6.0	4.3	2.6	2.5	2.1	2.6	2.4	2.7	3.7	3.7	4.1	3.7
Lu	0.36	0.89	0.63	0.39	0.38	0.31	0.39	0.35	0.39	0.55	0.55	0.61	0.55
Hf	1.57	4.9	3.5	2.2	1.69	1.43	1.70	1.54	2.3	2.9	3.0	3.3	2.9
Ta	0.06	0.28	0.25	0.17	0.04	0.04	0.04	0.06	0.22	0.19	0.19	0.17	0.15
Th	0.04	0.28	0.27	0.19	0.09	0.03	0.03	0.03	0.19	0.22	0.24	0.17	0.14
U	0.02	0.10	0.10	0.06	0.04	0.01	0.01	0.02	0.07	0.07	0.08	0.06	0.05

Table 2 (continued). Trace element ICP-MS analyses of glassy MORB pieces.

rock standards. The raw major element data from each measured spot were corrected to the KL2-G MPI-DING reference glass [35]. Representative errors are given in Table 1 together with the number of individual spots measured and used to calculate the mean values. We note that samples from the gravity corer (samples labeled SL) have analytical totals lower than the acceptable  $99.6 \pm 0.5\%$ . We attribute this to hydration of the glasses. We see no evidence that the trace element compositions of the gravity core samples are systematically different from those of dredge samples and so conclude that this hydration has not significantly affected the trace element signatures of the samples.

Glass chips were also crushed in a steel mortar and pulverized with an agate mortar to provide material for analyzing trace elements by inductively coupled plasma-mass spectrometry (ICP-MS) using a VG Plasma-Quad PQ1 (University of Kiel, Germany). Total dissolution was performed by pressurized HF-HClO<sub>4</sub>-aqua regia attack [36]. The accuracy of the analytical results was assessed by measuring the international standard reference material BHVO-1, BHVO-2 and BIR-1 [37, 38]. Precision was estimated from repeat sample and standard

measurements. The relative standard deviation of repeat measurements of sample 21DS1 and BHVO-2 is below 7% and for different dissolutions of the same standards below 12% for most elements. The results of blank measurements show significant blank values for Zn and Pb presumably indicating contamination problems in the dissolution procedure, therefore these elements are not considered in this paper.

In some cases we could identify multiple compositions in one dredge, possibly a hint for different lava flows having been sampled (20DS, 29DS, 9DS). In the case of core-catcher samples it was not possible with our analytical methods to analyze trace elements on individual grains and we had to perform trace element analyses on multiple grains. We have therefore, contrary to our previous work which reported only major elements [4], averaged the major element compositions of samples from the core catcher even if major elements of different grains show different composition. This is however not a problem for the conclusion drawn here, as the trace element differences between the chemical groups we will examine in this paper are large and we can always check by mixing calculations whether a core-catcher trace element signature could in fact be the result of mixing between other magma types.

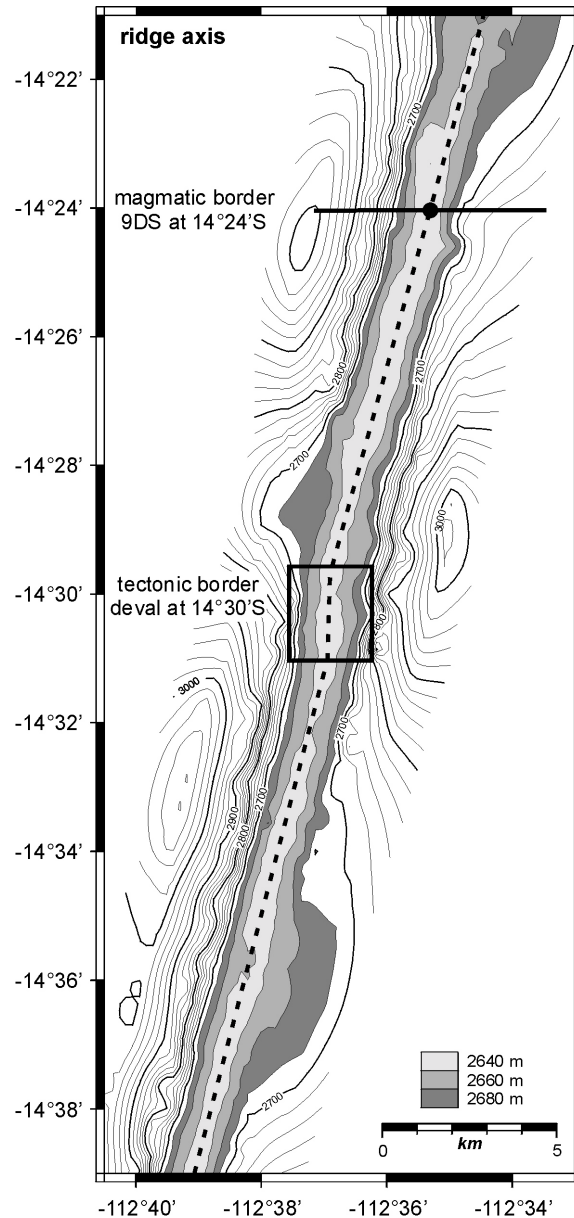


Figure 3. Topographic map of the present day ridge axis in the EXCO area, indicating the position of the magmatic border (backtracked position of sample 9DS) at 14°24'S, not correlating with the position of the tectonic border (left stepping deval) at 14°30'S.

## Results

The EXCO basalts from the eastern flank of the SEPR provide important information about temporal variations in magma geochemistry. All dredge samples are characterized by the presence of glassy margins, small amounts of vesicles (3 %), are plagioclase-phyric (1-5 %) with minor olivine (1-2 %) and pyroxene (<1%) and are part of pillows or sheet flows. Samples from the core catcher contain only glass pieces. Fig.1 shows sample locations and their positions backtracked to the ridge axis. The results of the backtracked positions are presented in a plot of eruption latitude vs. Mg# together with literature data from the present day ridge axis (Fig.2). As shown by Grevenmeyer et al. [4] the EXCO data show a surprisingly good and significant agreement with the present-day geochemical variation from literature data along axis. In other words, every EXCO sample backtracked to the ridge axis shows nearly the same magmatic composition as the closest present day sample, so the composition of glass chips from every off-axis sample can be linked to the according sample from the ridge axis.

### *Major elements*

The EXCO basalts are characterized by a wide range of chemical composition, even within a single dredge, for example 29DS (1.16 Ma) shows magmas varying from N- to E-MORB as defined by their K/Ti ratios [39]. Analyses show that samples with backtracked positions in the north are Mg-richer (Mg# 0.51 – 0.66) and from the south Mg-poorer (Mg# 0.41 – 0.58). The transition from Mg-rich to Mg-poor compositions occurs on the present-day ridge axis at the deval at around 14°30'S noted by Sinton et al. [3]. The depth of the present day ridge axis in the EXCO area is relative homogeneous (~2640 m) and no dependence between magma composition and axial depth has been observed. Unfortunately only one dredge (29DS, 1.16 Ma) was taken south of the 14°30'S deval, but even the more heterogeneous geochemical composition of single samples in this dredge corresponds very well with literature data from this southern part of the ridge (Fig.2).

The least evolved volcanics are characterized by enriched Mg# (>0.6), high CaO and low Na<sub>2</sub>O and K/Ti values. Nearly all of these basalts are sampled close to seamounts (35DS, 36DS, 7SL, 37SL, 38SL, 40SL) and show eruption latitudes between 14°06'S and 14°10'S (see shaded ellipse, Fig.2). In this area samples from the present day ridge axis (20DS at 14°09'S and 21DS at 14°05'S) show a more evolved and homogeneous composition and therefore plot with Mg# <0.57. Only one high-Mg# sample (28DS) was not sampled close to a seamount. Its backtracked position on the axis (14°02'S) is further north than the other samples, but its composition is also one of the most depleted.

**Trace elements**

By comparing the trace elements we are able to discern four different rock types. This is best illustrated in a chondrite normalized [40] plot of the rare earth elements (REE) (Fig.4). The most trace element enriched rocks are E-MORBs from 29DSE (1.16 Ma), clearly indicated as Type 1. The rest of 29DS plots in Type 2, which comprises all N-MORB collected over the flow line and representing 9 Ma of axial history. The striped area shows the heterogeneous composition in 9DS (2.92 Ma) located at the magmatic boundary, which develops most clearly towards the less incompatible REE. Type 3 is characterized by a more depleted composition, especially towards the LREE and comprises all samples collected close to seamounts. Only one sample, 7SL, also collected in this area, shows higher concentrations in the

LREE and MREE and is therefore not grouped in Type 3. Type 4 is clearly indicated by its very homogeneous and also depleted composition and comprises all samples of 28 DS (0.65 Ma). These differences are also apparent in an extended trace element plot normalized to N-MORB (Fig.5) [41]. Type 3 and 4 are clearly separated from the rest of the EXCO samples, showing their more depleted nature, especially Type 3 is most depleted in K, Rb, Ba, Th, Ta and Nb. All samples from the EXCO area have similar patterns in the more compatible elements and heterogeneous in the more incompatible elements.

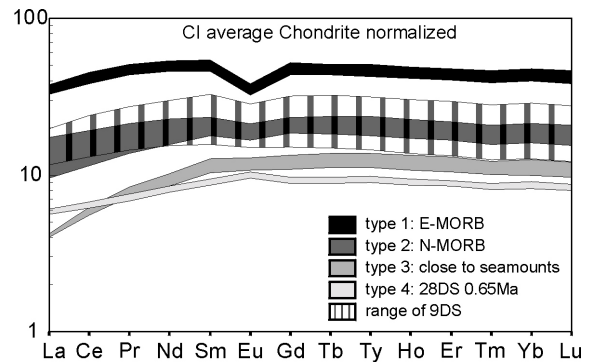


Figure 4. Comparison of the chondrite normalized (average CI [40]) REE patterns of EXCO basalts. Type 1 and 2 define all samples erupted on-axis, Type 3 and 4 are erupted off-axis (see text for discussion). Note the heterogeneous composition of dredge 9DS (bold striped field), erupted at the magmatic boundary at 14°24'S.

**Discussion**

The data presented above raise the following different questions.

**How old is the magmatic border and how stable is the magmatic evolution ?**

The very good agreement of the backtracked major element data with both the EXCO ridge axis

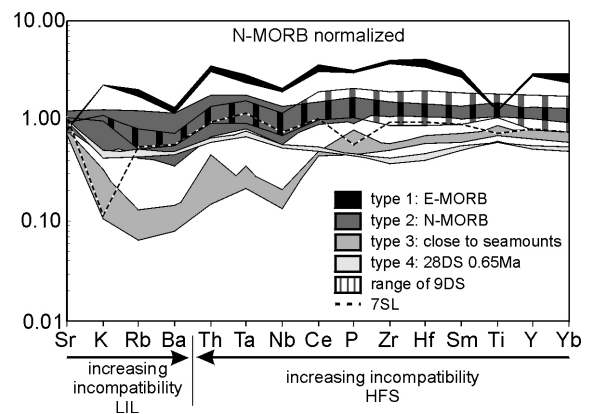


Figure 5. EXCO trace element composition normalized to N-MORB [41]. Samples collected close to small seamounts (Type 3) show trace-element depleted signatures characteristic of off-axis volcanism.

and literature data was first observed by Grevenmeyer et al. [4], suggesting that the system controlling the magmatic evolution has been stable since 8.64 Ma. Based on the deval and the abrupt change in Mg# from high (north) to low (south) on the axis in the EXCO area today, Sinton et al. [3] set the magmatic and tectonic boundary at 14°30'S (note that [24, 42, 43] gave the location of this boundary in their geophysical papers as 14°27'S). In contrast to Sinton et al. [3], we observe no change in axial depth at 14°30'S, but we find a left stepping deval at the ridge axis at this location (Fig.3). Such small ridge axis discontinuities together with abrupt changes in MgO-variations have been suggested to be related to shallow magma chamber processes and to last for only  $10^2 - 10^4$  years [2]. Sample 9DS at 14°24'S shows the most heterogeneous composition of all EXCO samples and we believe that this marks the position of both the transition from high Mg# in the north to low Mg# in the south and so the magmatic border. The large age of sample 9DS (relative to the supposed age of the deval of  $10^2 - 10^4$  years) implies that the geochemical signature of the magmatic border has lasted for at least 2.92 Ma. The deval at 14°30'S does not coincide with the magmatic border at 14°24'S, therefore the change in magmatic composition along the ridge axis is not related to tectonic features.

### ***On- and Off-axis eruptions ?***

On the basis of Fig.2 the EXCO samples can be divided, as discussed, into two groups across the 14°24'S magmatic boundary based on high and low Mg#. Nevertheless, the REE define four rock types (Fig.4), independent of their eruption latitude or age. Type 1 and 2 correspond to the geochemical compositions of E- and N-MORBs respectively and have similar composition to those found in the heterogeneous dredge 9DS (striped field). Type 3 and 4 show a more depleted nature in their incompatible elements. Samples from mid-ocean ridges with such depletions have been reported from off-axis eruptions and have been linked to off-axis morphological features [e.g. 14, 17]. In case of the backtracked EXCO samples, we are not able to identify features such as flows or pillow mounds that cover abyssal hill faults which have been used near the modern axis to identify off-axis activity, but all samples of Type 3 are located close to seamounts (Fig.6), the largest and most obvious manifestation of off-axis volcanism. Observations indicate that most seamounts in the eastern Pacific form in a remarkably narrow range of distance from the axis, about 6–15 km [44]. Trace element composition of individual seamount magmas are reported to span a wider range than MOR magmas [45]. However, off-axis EXCO samples show a homogeneous depletion in their incompatible elements and significant differences in their major element compositions relative to N-MORB from the axis, with gains in  $\text{Al}_2\text{O}_3$ , MgO, and CaO and losses in  $\text{TiO}_2$ , FeO,  $\text{Na}_2\text{O}$ ,  $\text{K}_2\text{O}$  and  $\text{P}_2\text{O}_5$ . Nevertheless, the presence of seamounts and the depleted

geochemical signature of the trace elements suggests that samples of Type 3 erupted off-axis. Spiegelman [46] suggested that the trace element depletion of such magmas results from an under representation of the deepest-formed, least depleted melts in the off-axis magmas. These deep melts are more strongly focused to the ridge axis and so do not enter the off-axis magmatic system. Sample 7SL, also collected close to the seamount at 4.6 Ma (Fig.6) (and in fact the closest to the seamount of all samples collected at this age), shows a distinctive composition but is very similar to the MORBs of types 1 and 2. It is possible that the core catcher hit an on-axis lava flow which was not covered by later erupted off-axis flows and therefore sample 7SL is more enriched than the trace elements as the other near seamount samples. Therefore we have not grouped sample 7SL into Type 3.

We normalized the composition of Type 3 and 4 averages to samples from the present day ridge axis (18DS, 20DS, 21DS) to show their difference in geochemical composition (Fig.7). Off-axis samples show similar signatures in the major elements and are characterized by low abundances of incompatible trace elements, with a depletion of on average 40 % (Type 3) and 35 % (Type 4) (c.f. 20% depletion in the study of Spiegelman and Reynolds [17]). Only Sr, which behaves compatibly during low pressure plagioclase fractionation, shows about the same concentrations in all three averages. Samples from the EPR at 12°N show a very similar geochemical signature and have been explained by convergent melt flow towards the ridge axis [17]. Although there are no seamounts located in the environment of Type 4, the chemical signature indicate that these samples also erupted off-axis [14, 17].

The occurrence of depleted off-axis magmas can best be explained by a passive as opposed to an active spreading model [14, 17]. As such these magmas provide further support for the crack-controlled passive spreading model for the EXCO area proposed independently to account for both geophysical and geochemical back-tracking evidence [4].

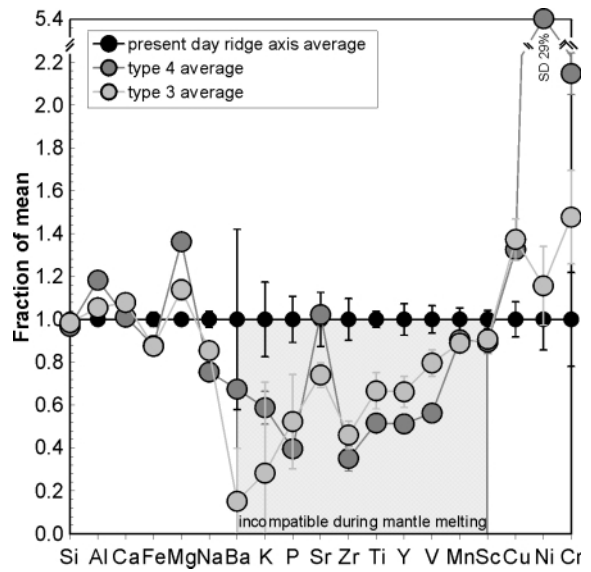


Figure 7. Comparison of on- and off-axis EXCO magmas. Black circles are the mean of all present day ridge axis samples (18DS, 20DS, 21DS), grey circles indicate the mean of Type 3 and 4. Elements from Ba to Cr are shown roughly in order of compatibility. The shaded area indicates the incompatible elements during mantle melting. Off-axis rocks are characterized by a mean depletion of incompatible elements of ~35-40 %. Error bars show  $\pm 1\sigma$  standard variation.

Seismic reflection and refraction studies under mid-ocean ridges have shown that the crust forms within 1 to 2 km of the axis [47, 48]. In the EXCO area the width of the neovolcanic zone (and axial magma chamber (AMC)) is between 1.5 km (AMC = ~400 m) at the magmatic border and 3.4 km at about 14°09'S (AMC = ~750 m) [42]. Other studies confine the neovolcanic zone only to the inner valley floor or the axial summit graben and define the typical width of fast spreading ridges as only <250 m [9]. In the area of our backtracked off-axis eruptions, the AMC is 375 – 400 m width, suggesting that “off-axis” eruptions could occur very close to the ridge-axis. Seamount type volcanism starts within only 1-2 km of the axis [14]. We are not able to determine how far Type 3 and 4 rocks erupted off-axis, but by comparing the homogeneous geochemical signature of the EXCO ridge-axis basalts which are up to 15000 years old (based on magnetic data), the distance over which accretion directly related to the AMC occurs has to be at least 1.1 km (based on a total spreading rate of 150 mm/year). Only precise dating of these rocks, however, will bring out the exact position of the off-axis eruption.

The occurrence at 2.56 and 4.6 Ma, of geochemically very similar off-axis type samples which back-track to the same latitude, may imply that preferential long term sites of off-axis activity exist and that the off-axis magmatic plumbing system is also very stable through time.

### ***Can crystal fractionation explain the differences between the EXCO basalts ?***

When observing the geochemical plots we have to interpret the trends of the off-axis rocks (Type 3 and 4) separately to those of on-axis samples. Therefore we have to take care when interpreting trends from samples collected on mid-ocean ridges and we have to test the possibility of off-axis eruptions.

By testing the possibility that crystal fractionation is responsible for chemical differences in the EXCO area we calculate Rayleigh crystal fractionation for a constant low pressure (1kbar) and temperature:

$$C_L/C_0 = F^{(D-1)} \text{ Rayleigh Crystal Fractionation}$$

where  $C_L$  is the residual liquid,  $C_0$  the concentration of the element in the original magma,  $F$  the fraction of melt remaining after removal of crystals as they form and  $D$  the bulk distribution coefficient of the fractionating assemblage during crystal fractionation [49]. By modeling the fractionation trends for the magmatic composition we choose an assemblage of 20 % olivine, 15 % clinopyroxene and 65 % plagioclase for our calculation. Considering the different rock types and samples north and south of the magmatic border separately, we find that fractionation can only explain the range in composition south of the magmatic border, where the calculated liquid line of descent overlaps with the geochemical composition (Fig. 8). By plotting both Rb and Ba in ratio to the highly incompatible Th versus MgO, we observe that Ba/Th shows a positive correlation for rocks south of

the magmatic border, whereas the Rb/Th ratio does not change. Ba substitutes for Ca during plagioclase fractionation and therefore we conclude that the Ba/Th ratio is decreasing due to crystallization. The on-axis EXCO samples north of the magmatic border show no correlation between Ba and MgO and therefore follow no liquid lines of descent and can not be explained by fractionation, a situation which also applies to the off axis samples (Type 3 and 4), which in fact show a negative trend. Former studies described the two sides of the magmatic boundary as showing different liquid lines of descent and concluded that they resulted from mixture boundaries within the continuous magma chamber [3]. To explain the differences amongst the back-tracked samples we need different mantle sources, because fractionation can only explain the variation in trace element concentration south of the magmatic border. Our conclusions are in agreement with Grevenmeyer et al. [4] who described the latitudinal variations in magma composition as features of the sublithospheric magma supply and relatively independent of crustal processes.

The large high Rb/Th variation for a constant (narrow range) MgO-value is a unique feature of the EXCO rocks backtracked to north of the magmatic boundary (Fig.8). Both Rb and Th are highly incompatible elements and so their ratio will not be affected by crystal fractionation in a basaltic system. Because the northern samples show negligible MgO differences we can use not only trace element ratios but also trace element concentration to investigate the origin of these rocks. By plotting trace elements in order of compatibility against Rb/Th we observe a positive trend for the incompatible elements, changing to a negative correlation for elements more

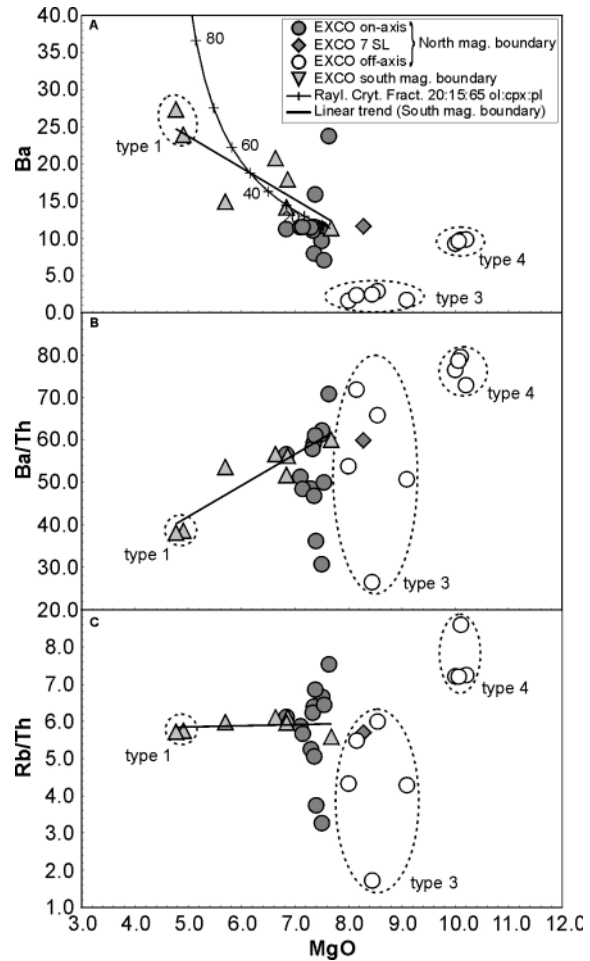


Figure 8. MgO variation diagrams indicating on- and off-axis eruptions and all different types of EXCO rocks. A. Modelling of crystal fractionation as a possible explanation for the chemical variations in samples from south of the magmatic border. Illustrated is a calculated curve for Rayleigh crystal fractionation with an assemblage of 20 % olivine, 15 % clinopyroxene and 65 % plagioclase. Numbers close to the curve indicate the amount of melt crystallized. B and C shows the unique Ba/Th and Rb/Th variation for a constant MgO-value (see text for discussion).

compatible than Gd (Fig.9). We argue that garnet is responsible for the change in correlation, because the mineral melt partition coefficients for garnet correlate with the slopes of the element vs. Rb/Th diagrams. Compatible trace elements with a partition coefficient  $>1$  show a negative correlation, whereas incompatible trace elements ( $<1$ ) show a positive correlation, changing at Gd with a partition coefficient of 0.97 and a slope of -0.01. Salters and Hart [50] found that garnet affects the Lu-Hf and Sm-Nd systematics of MORBs during the initial stage of melting. Hirschmann and Stolper [51] suggested that MORBs are produced by melting of mixed garnet pyroxenite/spinel peridotite sources and that some or all of the “garnet signature” in MORB is contributed by partial melting of garnet pyroxenite, rather than partial melting of spinel peridotite. This then leads to high Sm/Yb and low Lu/Hf ratios [51]. The influence of garnet pyroxenite during the initial stage of melting of EXCO rocks can be seen in Fig.10. Off-axis rocks show high Lu/Hf and low Sm/Yb<sub>DM</sub> (average of 1.29) ratios, whereas on-axis rocks show low Lu/Hf and higher Sm/Yb<sub>DM</sub> (1.40) ratios, therefore the influence of pyroxenite in off-axis rocks is lower. The on-axis Sm/Yb<sub>DM</sub> values are well within the range of typical MORB ( $1.45 \pm 0.15$  [52, 53]) indicating the presence of partial melting of a mixed (95% / 5%) spinel peridotite/garnet pyroxenite source [51]. The large and correlated variations in Rb/Th and Sm/Yb (Fig.10) suggest that the trace element signatures of the samples from north of the magmatic boundary are dominated by low degree partial melts formed deep in the melting column [54, 55]. We do not observe any dependence between the back-tracked geographical position of the on-axis samples north of the magmatic border along the ridge axis and the amount of garnet pyroxenite influence or the degree of melting.

### Summary and conclusions

1. Magmatic evolution in the EXCO area has remained stable throughout the last 8.64 Ma. When backtracked along a relative spreading vector, data on off-axis samples show similar compositions to samples from the present-day spreading axis. In particular the significant and systematic variations of the major and trace elements along-axis is a striking long-term feature, with homogeneous and high MgO in the north and more heterogeneous and low MgO in the south. This shows that small scale spatial variations in chemistry are a robust feature along the SEPR.

2. The EXCO samples can be divided into two geographical groups, separated by a magmatic boundary at 14°24'S. The age and geochemical signature of samples from south of the boundary suggest that they are derived by crystal fractionation from the same, long-lived magma chamber during the last 2.9 Ma. The magmatic boundary does not coincide with the left stepping deval at 14°30'S, therefore magmatic boundaries along the SEPR can be independent of ridge axis discontinuities.

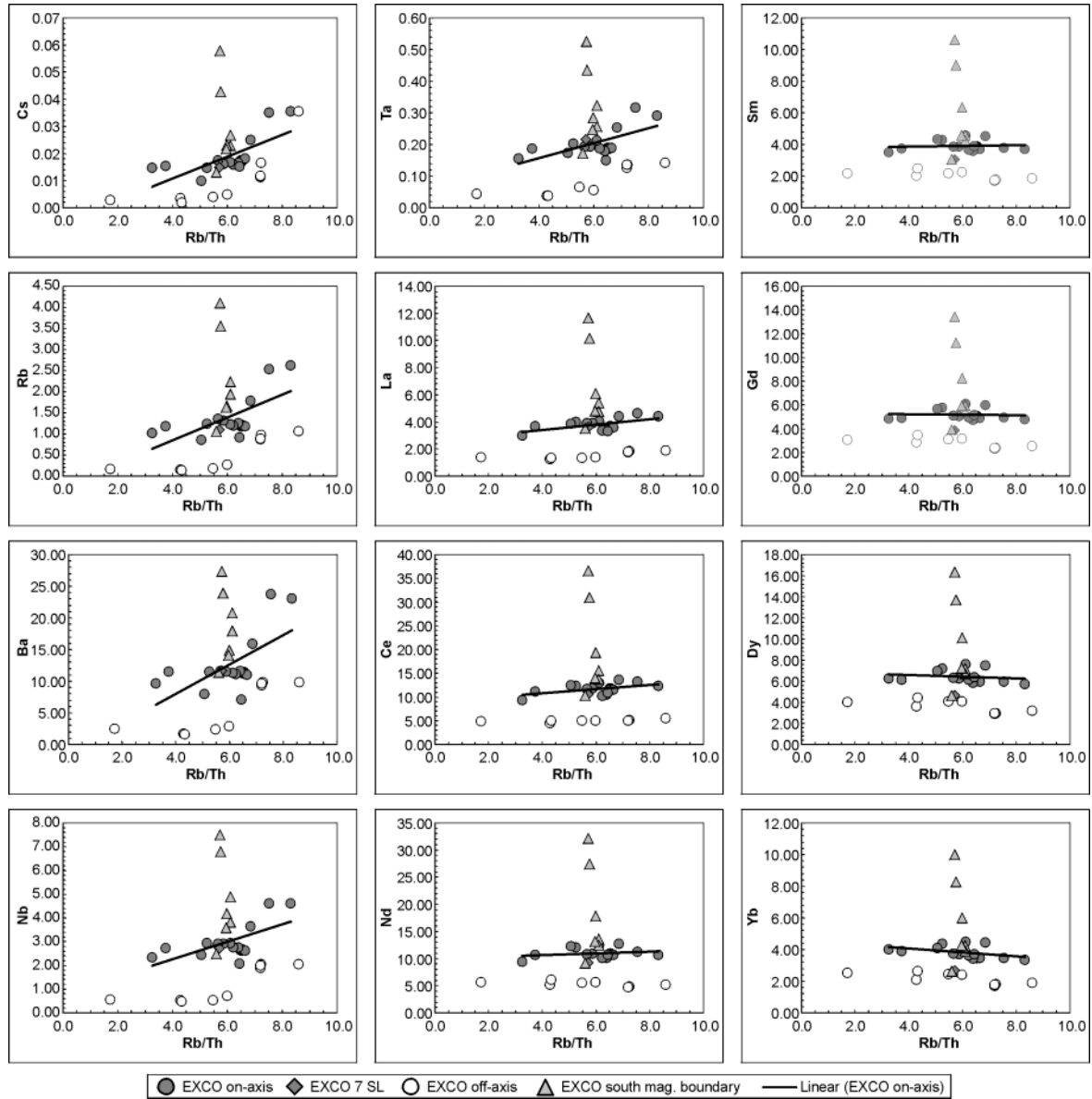


Figure 9. Element plots versus Rb/Th ratio in order of compatibility (in columns, read from top left to bottom right). Note the gradual change in slope from positive (elements Cs – Ce) to negative (clearly seen for Yb) for the samples from north of the magmatic boundary, with Gd in particular showing a horizontal array.

3. Samples erupted at the spreading axis north of the magmatic border during the last 8.64 Ma show a very homogeneous magmatic composition with MgO contents within the range of  $7.3 \pm 0.4$  wt.%. Despite negligible variations in the degree of crystal fractionation that this implies, incompatible trace element contents and ratio vary significantly in these samples. Modeling of the trace element variation shows that they are dominated by low degrees of partial melts deep in the melting column, related by differences in the amount of garnet in the melting residue. The very restricted MgO range of the samples imply an exceptionally long-lived steady-state on-axis magma plumbing system during the last 8.64 Ma.

4. Samples collected close to small seamounts show trace-element depleted signatures characteristic of off-axis volcanism, that all back-track to the same eruption latitude. The age of the sampling locations of 2.56 and 4.6 Ma, implies the presence of an off-axis magmatic system characterized by stability on the several million year scale.

### Acknowledgements

The authors wish to thank Captain Papenhagen and his crew for the excellent support during the SO145/2 sampling work. Anette von der Handt (MPI Mainz), Burkhard Schulz-Dobrick (Univ. Mainz) and Andreas Kronz (Univ. Göttingen) are thanked for assistance with the microprobe analyses, Dieter Garbe-Schönberg (Univ. Kiel) kindly provided ICP-MS analyses. Marion Pfender is thanked for assistance with the topographical maps. This study was supported by BMBF grant 03G0145A.

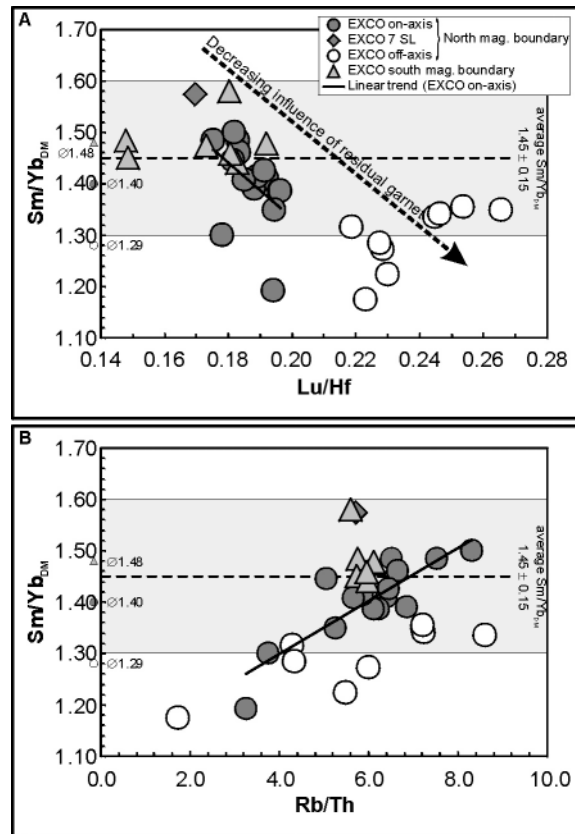


Figure 10. Depleted mantle normalized Sm/Yb ratio plotted against Lu/Hf (A) and Rb/Th (B). The depleted mantle normalized Sm/Yb<sub>DM</sub> ratio is used as an indicator for the influence of garnet pyroxenite during partial melting of the spinel peridotite mantle source [51]. The shaded area indicates the range of typical MORB (1.45 ± 0.15 [52, 53]). Small symbols and values on the left side of the diagram indicate the average of the rock samples.

## References

- [1] K.C. MacDonald, Linkages between faulting, volcanism, hydrothermal activity and segmentation on fast spreading centers, in: *Faulting and Magmatism at Mid-Ocean Ridges*, W.R. Buck, P.T. Delaney, J.A. Karson and Y. Lagabriele, eds. 106, *Geophysical Monograph*, 1998, pp. 27-58.
- [2] K.C. MacDonald, P.J. Fox, L.J. Perram, M.F. Eisen, R.M. Hayman, S.P. Miller, S.M. Carbotte, M.H. Cormier and A.N. Shor, A new view of the mid-ocean ridge from the behaviour of ridge-axis discontinuities, *Nature* 335 (1988) 217-225.
- [3] J.M. Sinton, S.M. Smaglik and J.J. Mahoney, Magmatic processes at superfast Mid-Ocean Ridges: Glass compositional variations along the East Pacific Rise 13°-23°S, *Journal of Geophysical Research* 96 (1991) 6133-6155.
- [4] I. Grevemeyer, B. Schramm, C.W. Devey, B. Jochum, D.S. Wilson, J. Hauschild, K. Aric, H. Villinger and W. Weigel, A multibeam-sonar, magnetic and geochemical flow-line survey at 14°14'S on the southern East Pacific Rise - insights into the fourth dimension of ridge crest segmentation, *Earth and Planetary Science Letters* 199 (2002) 359-372.
- [5] C.H. Langmuir, J.F. Bender and R. Batiza, Petrological segmentation of the East Pacific Rise, 5°30' - 14°30'N, *Nature* 322 (1986) 422-429.
- [6] S.M. White, R.M. Haymon, D.J. Fornari, M.R. Perfit and K.C. MacDonald, Correlation between volcanic and tectonic segmentation of fast-spreading ridges: Evidence from volcanic structures and lava flow morphology on the East Pacific Rise at 9°–10°N, *Journal of Geophysical Research*, B, *Solid Earth and Planets* 107 (2002) 10.1029/2001JB000571.
- [7] C.H. Langmuir, E.M. Klein and T. Plank, Petrological Systematics of Mid-Ocean Ridge Basalts: Constraints on Melt Generation Beneath Ocean Ridges, in: *Mantle Flow and Melt Generation at Mid-Ocean Ridges*, J.P. Morgan, D.K. Blackman and J.M. Sinton, eds., *Geophysical Monograph* 71, American Geophysical Union, 1992, pp. 183-280.
- [8] E.M. Klein and C.H. Langmuir, Global correlations of oceanic ridge basalt chemistry with axial depth and crustal thickness, *Journal of Geophysical Research* 92 (1987) 8089-8115.
- [9] M.R. Perfit and W.W. Chadwick, Magmatism at Mid-Ocean Ridges: Constraints from Volcanological and Geochemical Investigations, in: *Faulting and magmatism at mid-ocean ridges*, W.R. Buck, P.T. Delaney, J.A. Karson and Y. Lagabriele, eds. 106, *Geophysical Monograph*, 1998, pp. 59-115.

- [10] E.M. Klein and C.H. Langmuir, Local Versus Global Variations in Ocean Ridge Basalt Composition: A Reply, *Journal of Geophysical Research* 94 (1989) 4241-4252.
- [11] R.T. Alexander and K.C. MacDonald, Small off-axis volcanoes on the East Pacific Rise, *Earth and Planetary Science Letters* 139 (1996) 387-394.
- [12] D.S. Scheirer and K.C. Macdonald, Near-axis seamounts on the flanks of the East Pacific Rise, 8°N to 17°N, *Journal of Geophysical Research* 100 (1995) 2239-2259.
- [13] Y. Shen, D.W. Forsyth, D.S. Scheirer and K.C. Macdonald, Two forms of volcanism: Implications for mantle flow and off-axis crustal production on the west flank of the Southern East Pacific Rise, *Journal of Geophysical Research* 98 (1993) 17875-17889.
- [14] J.R. Reynolds and C.H. Langmuir, Identification and implications of off-axis lava flows around the East Pacific Rise, *Geochemistry, Geophysics, Geosystems*, an electronic journal of the earth sciences 1 (2000) paper number 1999GC000033.
- [15] S.J. Goldstein, M.R. Perfit, R. Batiza, J. Fornari and M.T. Murell, Off-axis volcanism at the East Pacific Rise detected by uranium-series dating of basalts, *Nature* 367 (1994) 157-159.
- [16] T.A. Russ and K.C. Macdonald, Small off-axis volcanoes on the East Pacific Rise, *Earth and Planetary Science Letters* 139 (1996) 387-394.
- [17] M. Spiegelman and J.R. Reynolds, Combined dynamic and geochemical evidence for convergent melt flow beneath the East Pacific Rise, *Nature* 402 (1999) 282-285.
- [18] J.N. Ludden and G. Thompson, Behaviour of rare earth elements during submarine weathering of tholeiitic basalt, *Nature* 274 (1978) 147-149.
- [19] M.D. Buatier, C. Monnin, G.L. Früh-Green and A.-M. Karpoff, Fluid-sediment interactions related to hydrothermal circulation in the Eastern Flank of the Juan de Fuca Ridge, *Chemical Geology* 175 (2001) 343-360.
- [20] A.G. Hunter, P.D. Kempton and P. Greenwood, Low-temperature fluid-rock interaction; an isotopic and mineralogical perspective of upper crustal evolution, eastern flank of the Juan de Fuca Ridge (JdFR), ODP Leg 168, *Chemical Geology* 155 (1999) 3-28.
- [21] C. DeMets, R.G. Gordon, D.F. Argus and S. Stein, Effect of recent revisions to the Geomagnetic Reversal Time Scale on estimates of current plate motions, *Geophysical Research Letters* 21 (1994) 2191-2194.

- [22] M.H. Cormier, D.S. Scheirer and K.C. MacDonald, Evolution of the East Pacific Rise at 16°-19°S Since 5 Ma: Bisection of Overlapping Spreading Centers by New, Rapidly Propagating Ridge Segments, *Marine Geophysical Researches* 18 (1996) 53-84.
- [23] P. Lonsdale, Segmentation of the Pacific-Nazca spreading center, 1°N-20°S, *Journal of Geophysical Research* 94 (1989) 12197-12225.
- [24] W. Weigel, I. Grevemeyer, N. Kaul, H. Villinger, T. Lüdman and H.K. Wong, Aging of oceanic crust at the southern East Pacific Rise, *EOS Trans. AGU* 77 (1996) 504.
- [25] I. Grevemeyer, N. Kaul, H. Villinger and W. Weigel, Hydrothermal activity and the evolution of the seismic properties of upper oceanic crust, *Journal of Geophysical Research* 104 (1999) 5069-5079.
- [26] B. Schramm, C.W. Devey, K.M. Gillis and K. Lackschewitz, Quantitative assessment of chemical and mineralogical changes due to progressive low temperature alteration of East Pacific Rise basalts from 0-9 Ma, *Chemical Geology* (submitted).
- [27] R. Hékinian, D. Bideau and M. Cannat, Volcanic activity and crust-mantle exposure in the ultrafast Garrett transform fault near 13°28'S in the Pacific, *Earth and Planetary Science Letters* 108 (1992) 259-275.
- [28] R. Hékinian and D. Bideau, Magmatism in the Garrett transform fault (East Pacific Rise near 13°27'S), *Journal of Geophysical Research* 100 (1995) 10163-10185.
- [29] J.I. Wendt, M. Regelous, Y. Niu, R. Hékinian and K.D. Collerson, Geochemistry of lavas from the Garrett Transform Fault: insights into mantle heterogeneity beneath the eastern Pacific, *Earth and Planetary Science Letters* 173 (1999) 271-284.
- [30] W. Bach, E. Hegner, J. Erzinger and M. Satir, Chemical and isotopic variations along the superfast spreading East Pacific Rise from 6° - 30°, *Contr. Min. Petrology* 116 (1994) 365-380.
- [31] H. Puchelt and R. Emmermann, Petrogenetic implications of tholeiitic basalt glasses from the East Pacific Rise and the Galapagos spreading center, *Chemical Geology* 38 (1983) 39-56.
- [32] J.J. Mahoney, J.M. Sinton, M.D. Kurz, J.D. Macdougall, K.J. Spencer and G.W. Lugmair, Isotope and trace element characteristics of a super-fast spreading ridge; East Pacific Rise, 13-23 degrees S, *Earth and Planetary Science Letters* 121 (1993) 173-193.
- [33] D. Laschek, Geochemische Untersuchungen an Basalten vom Galapagos Spreading Center und vom East Pacific Rise, *Fortschritte der Mineralogie* 64 (1986) 95.
- [34] K.F. Scheidegger and J.B. Corliss, Petrogenesis and secondary alteration of upper layer 2 basalts of the Nazca Plate, *Geological Society American Memoir* 154 (1981) 77-107.

- [35] K.P. Jochum, D.B. Dingwell, A. Rocholl, B. Stoll and A.W. Hofmann, The preparation and preliminary characterisation of eight geological MPI-DING reference glasses for in-situ microanalysis, *Geostandards Newsletter* 24 (2000) 87-133.
- [36] D. Garbe-Schönberg, Simultaneous determination of 37 trace elements in 28 international rock standards by ICP/MS, *Geostandards Newsletter* 17 (1993) 81-97.
- [37] K. Govindaraju, 1994 compilation of working values and descriptions for 383 geostandards, *Geostandards Newsletter* 118 (1994) 1-158.
- [38] S.A. Wilson, Data compilation for USGS reference material BHVO-2, Hawaiian Basalt, U.S. Geological Survey Open-File Report, 1997.
- [39] R. Hékinian, J. Francheteau, R. Armijo, J.P. Cogné, M. Constantin, J. Girardeau, R. Hey, D.F. Naar and R. Searle, Petrology of the Easter microplate in the South Pacific, *Journal of volcanology and geothermal research* 72 (1996) 259-289.
- [40] W.V. Boynton, Cosmochemistry of the rare earth elements; meteorite studies, in: Rare earth element geochemistry, P. Henderson, ed., In the collection: *Developments in geochemistry*. 1984, Elsevier, 1984, pp. 63-114.
- [41] J.A. Pearce, Role of the sub-continental lithosphere in magma genesis at active continental margins, in: *Continental basalts and mantle xenoliths; papers prepared for a UK Volcanic Studies Group meeting at the University of Leicester*, C.J. Hawkesworth and M.J. Norry, eds., In the collection: *Shiva geology series*. 1983, 1983, pp. 230-249.
- [42] G.M. Kent, A.J. Harding, J.A. Orcutt, R.S. Detrick, J.C. Mutter and P. Buhl, Uniform accretion of oceanic crust south of the Garrett Transform at 14 degrees 15'S on the East Pacific Rise, *Journal of Geophysical Research*, B, *Solid Earth and Planets* 99 (1994) 9097-9116.
- [43] I. Grevemeyer and W. Weigel, Increase of seismic velocities in upper oceanic crust: The "superfast" spreading East Pacific Rise at 14°14'S, *Geophysical Research Letters* 24 (1997) 217-220.
- [44] D.S. Wilson, Focused mantle upwelling beneath mid-ocean ridges: Evidence from seamount formation and isostatic compensation of topography, *Earth and Planetary Science Letters* 113 (1992) 41-55.
- [45] Y. Niu and R. Batiza, Trace element evidence from seamounts for recycled oceanic crust in the Eastern Pacific mantle, *Earth and Planetary Science Letters* 148 (1997) 471-483.
- [46] M. Spiegelman, Geochemical consequences of melt transport in 2-D: The sensitivity of trace elements to mantle dynamics, *Earth and Planetary Science Letters* 139 (1996) 115-132.

- [47] E.E. Vera, J.C. Mutter, P. Buhl, J.A. Orcutt, A.J. Harding, M.E. Kappus, R.S. Detrick and T.M. Brocher, The structure of 0- to 0.2-m.y.-old oceanic crust at 9 degrees N on the East Pacific Rise from expanded spread profiles, *Journal of Geophysical Research, B, Solid Earth and Planets* 95 (1990) 15529-15556.
- [48] R.S. Detrick, P. Buhl, E.E. Vera, J.C. Mutter, J.A. Orcutt, J.A. Madsen and T.M. Brocher, Multi-channel seismic imaging of a crustal magma chamber along the East Pacific Rise, *Nature* 326 (1987) 35-41.
- [49] H.R. Rollinson, *Using Geochemical Data: Evaluation, Presentation, Interpretation*, Longman Group UK Limited, 1993, 352 pp.
- [50] V.J.M. Salters and S.R. Hart, The hafnium paradox and the role of garnet in the source of mid-ocean-ridge basalts, *Nature* 342 (1989) 420-422.
- [51] M.M. Hirschmann and E.M. Stolper, A possible role for garnet pyroxenite in the origin of the "garnet signature" in MORB, *Contributions to Mineralogy and Petrology* 124 (1996) 185-208.
- [52] R.S. White, D. McKenzie and R.K. O'Nions, Oceanic crustal thickness from seismic measurements and rare earth element inversions, *Journal of Geophysical Research* 97 (1992) 19683-19715.
- [53] Y. Shen and D.W. Forsyth, Geochemical constraints on initial and final depths of melting beneath mid-ocean ridges, *Journal of Geophysical Research* 100 (1995) 2211-2237.
- [54] C.W. Devey, C.D. Garbe-Schönberg, P. Stoffers, C. Chauvel and D.F. Mertz, Geochemical effects of dynamic melting beneath ridges: Reconciling major and trace element variations in Kolbeinsey (and global) mid-ocean ridge basalt, *Journal of Geophysical Research* 99 (1994) 9077-9095.
- [55] D. McKenzie and R.K. O'Nions, Partial Melt Distributions from Inversion of Rare Earth Element Concentrations, *Journal of Petrology* 32 (1991) 1021-1091.

**A multibeam-sonar, magnetic and geochemical  
flowline survey at 14°14'S on the southern East  
Pacific Rise: insights into the fourth dimension of  
ridge crest segmentation**

Ingo Grevemeyer, Burkhard Schramm, Colin W. Devey, Douglas S. Wilson,  
Birgit Jochum, Jan Hauschild, Kay Aric, Heinrich W. Villinger, Wilfried Weigel



*Earth and Planetary Science Letters, accepted 11 March 2002*



ELSEVIER

Earth and Planetary Science Letters 199 (2002) 359–372

EPSL

www.elsevier.com/locate/epsl

## A multibeam-sonar, magnetic and geochemical flowline survey at 14°14'S on the southern East Pacific Rise: insights into the fourth dimension of ridge crest segmentation

Ingo Grevemeyer<sup>a,\*</sup>, Burkhard Schramm<sup>a</sup>, Colin W. Devey<sup>a</sup>,  
Douglas S. Wilson<sup>b</sup>, Birgit Jochum<sup>c</sup>, Jan Hauschild<sup>a</sup>, Kay Aric<sup>c</sup>,  
Heinrich W. Villinger<sup>a</sup>, Wilfried Weigel<sup>d</sup>

<sup>a</sup> Department of Earth Sciences, University of Bremen, Klagenfurter Straße, 28359 Bremen, Germany

<sup>b</sup> Department of Geological Sciences and Marine Institute, University of California, Santa Barbara, CA 93106, USA

<sup>c</sup> Institute of Meteorology and Geophysics, University of Vienna, Althanstraße, 1000 Vienna, Austria

<sup>d</sup> Institute of Geophysics, University of Hamburg, Bundesstraße 55, 20146 Hamburg, Germany

Received 4 February 2002; received in revised form 6 March 2002; accepted 11 March 2002

### Abstract

A detailed bathymetric and magnetic survey of the eastern flank of the East Pacific Rise at 14°14'S covering seafloor ages of 0–10 Ma has been carried out and used, along with a flowline profile on the conjugate western ridge flank, to reveal the spreading history and the temporal ridge crest segmentation. Additional information from basaltic lavas is included to study the relationship between physical and magmatic segment boundaries. The sequence of magnetic reversals indicates a total spreading rate of 150 mm/yr since 10 Ma. Symmetric spreading, however, occurred only since 2.8 Ma. Between 7 and 2.8 Ma spreading was asymmetric, with a higher spreading rate toward the east. Migration events of at least five overlapping spreading centres (OSC) left discordant zones on the Nazca plate consisting of hummocky basins and motley texture of curved lineations striking a few degrees oblique to the strike of the ridge crest. Four of the OSCs were right-stepping and migrated northward and one was left-stepping and migrated southward. By transferring Pacific lithosphere to the Nazca plate, these migration events may account for most of the asymmetric accretion observed. The basaltic samples from the eastern flank have been analysed and back tracked to the position of eruption on the ridge crest. In terms of their geochemical signature (Mg# 0.41–0.68) the samples reveal that the magmatic segment boundary between the Garrett transform and 14°30'S has remained stationary over the last 10 Myr and therefore provide no evidence for a link between magmatic and physical segmentation. We therefore propose that migrating non-transform ridge axis discontinuities are governed by propagating giant cracks; as a crack front advances a melt reservoir is tapped and magma rises passively into the crack and erupts subsequently on the seafloor. Some of the OSCs seem to have originated close to transform faults and therefore argue that far-field stresses, perhaps caused by the evolution of the Bauer microplate, rather than mantle upwelling create non-transform ridge axis discontinuities. © 2002 Elsevier Science B.V. All rights reserved.

\* Corresponding author. Tel.: +49-421-218-4511; Fax: +49-421-218-7163.

E-mail address: ingo@geophys2.uni-bremen.de (I. Grevemeyer).

*Keywords:* East Pacific Rise; mid-ocean ridges segmentation; bathymetry; reversals; major elements

## 1. Introduction

Observations along the approximately 70 000 km long mid-ocean ridge system support the concept of a hierarchy in the segmentation of spreading ridges [1–3]. Discontinuities that define first-order segments are rigid and long-lived transform faults, whereas finer scales of segmentation occur between transform faults. At fast spreading ridges, lateral offsets of 1–30 km occur at second- and third-order discontinuities and are accommodated by overlapping spreading centres (OSC). Fourth-order discontinuities are minor deviations in axial linearity (DEVAL) with offsets of less than 1 km. At higher orders, segments are shorter, more short-lived, and unstable [4].

Off-axis traces of ridge axis discontinuities are created at first- and second-order segment boundaries. Transverse ridges and fracture zone valleys of transform fault boundaries have even been imaged by satellite-borne altimeters [5]. Recent multibeam-sonar surveys of mid-ocean ridges reveal off-axis discordant zones related to non-transform ridge axis discontinuities at both slow and fast spreading ridges [4,6,7]. The off-axis discordant zones of second-order discontinuities reveal the history of segment evolution and magmatic activity. At fast spreading ridges many show a pattern of abandoned ridge tips and fossil overlap basins caused by repeated decapitation of ridge tips. Such propagation and decapitation events have a recurrence interval of  $2 \times 10^4$ – $2 \times 10^5$  yr with an average interval of  $\sim 5 \times 10^4$  yr [4,8]. The lack of any off-axis discordant zone documents the short-lived nature of third- and fourth-order segments relative to the larger, longer-lived discontinuities.

Seismic measurements along the axis of the East Pacific Rise (EPR) reveal an axial magma chamber (AMC) whose shape and position correlate with the shape of the rise [8]. The AMC disappears near transform faults, is deeper and commonly discontinuous near second-order discontinuities, and it shows only small variations at third- and some fourth-order discontinuities [9].

These observations suggest a linkage between tectonic segmentation and the axial melt reservoir. Langmuir et al. [1] show that volcanic rocks at broader and hence magmatically robust segments [8] have higher MgO content than those from the narrower parts of segments, generally near discontinuities. The data are, however, sparse and noisy. Nevertheless, they suggest a tendency for hotter magmas to erupt near the middle of segments and cooler magmas to erupt near segment ends. Within the resolution of sampling, virtually all segments of order 1–3 have distinct geochemical signatures, as do at least 30% of the fourth-order segments [1,10]. Some authors argue that spreading segments behave like giant cracks in the plate [4,11], however. In this case tectonic segment boundaries are not necessarily prone to coincide with magmatic segment boundaries which may explain why the correspondence between geochemical and geophysical segmentation is imperfect.

Flowline studies crossing abandoned ridge tips have the potential to be able to tell us more about the linkage between physical and magmatic segmentation of ridge crests. During the EXCO surveys in 1995 and 2000 [12–15] the German research vessel *Sonne* investigated a flowline corridor centred at 14°14'S on the southern East Pacific Rise (SEPR) (Fig. 1). This portion of the SEPR is known to be among the most robust and magmatically active portions of the world's mid-ocean ridge system [8,16,17]. Here we use HYDROSWEEP multibeam bathymetry and magnetic coverage of a 40–80 km wide and 720 km long tectonic corridor on the eastern ridge flank along with a conjugate flowline profile on the western flank and geochemical information on basaltic lavas from the eastern flank to reveal the tectonic and magmatic evolution of the SEPR at 14°14'S since 10 Ma.

## 2. Geological background

The Southern East Pacific Rise between the



Fig. 1. Location map showing the survey area of research vessel *Sonne* in 1995 and 2000 in the south-east Pacific ocean on the East Pacific Rise.

Easter Microplate near 23°S and the Garrett transform fault boundary near 13°30'S is spreading at ultrafast rates, ranging from 143 mm/yr to 150 mm/yr [18,19]. Between the Garrett fracture zone and a large duelling OSC at 20°40'S the SEPR is remarkably linear and devoid of any transform fault boundaries [20]. On a finer scale, however, the ridge crest is offset en echelon by a series of small, left stepping discontinuities [7,20]. These discontinuities range in offset from 1 to 7 km, and the intervening ridge segments consistently strike within a few degrees of 013°, normal to the spreading direction predicted by the NUVEL-1A model of current plate motions [18,19]. In addition, all second-order physical ridge offsets seem to correspond to magmatic segment boundaries defined by the ratio of K/P and K/Ti of glass [10]. Along this portion of the ridge crest five regions with relatively smooth variation in MgO contents are apparent [10]. Most of the boundaries of these regions correspond to major physical or secondary magmatic boundaries. Nevertheless, two occur within secondary magmatic segments near small offset non-transform ridge axis discontinuities.

Between 16°S and 21°S the SEPR has been intensively studied by combined multibeam, side

scan and magnetic surveys. Off-axis discordant zones reveal that between 1 and 5 Ma several left-stepping OSCs offset the ridge axis between 16°S and 19°S. Since 1 Ma these OSCs were bisected into smaller OSCs by new spreading segments forming within their overlap basins [19,21]. The smaller OSCs migrated rapidly southward and were further bisected until the present segmentation was achieved. By transferring lithosphere from one plate to the other, these migration and reorientation events account remarkably well for the spreading asymmetry along the SEPR. The large OSC at 20°40'S has remained stationary since 1 Ma, but its history involves duelling propagation with a great deal of variation in the amount of overlap of the two ridges as well as inward and outward cutting and abandonment of tips of both ridges [22,23].

In general, along axis variations of several physical and chemical parameters in this area suggest that the melt supply to the ridge is robust between the Garrett transform fault and the duelling OSC at 20°40'S. At 14°14'S the ridge crest is characterized by a prominent bathymetric high with smooth flanks and a relatively flat summit [8,20]. Seismic reflection imaging provides evidence for an axial magma chamber reflector [16,17]. Both the blocky crestal ridge and the prominent AMC reflector are consistent with a magmatically active ridge segment [8,16]. Moreover, the seismic data indicate a very uniform process of crustal accretion along axis [16,17]. Off-axis, Grevemeyer et al. [13] investigated the seafloor morphology and found that changes in seafloor roughness and abundance and height of seamounts correlate with temporal changes in spreading rate. Over the last 10 Myr, however, crustal accretion has produced a quite uniform crustal thickness [24] which argues for only minor changes in melt supply.

### 3. Data collection and processing

Most of the bathymetric and magnetic data have been acquired during leg 105 of the *Sonne* in 1995. Data covering a 20–45 km wide and 720 km long corridor on the eastern flank were ini-

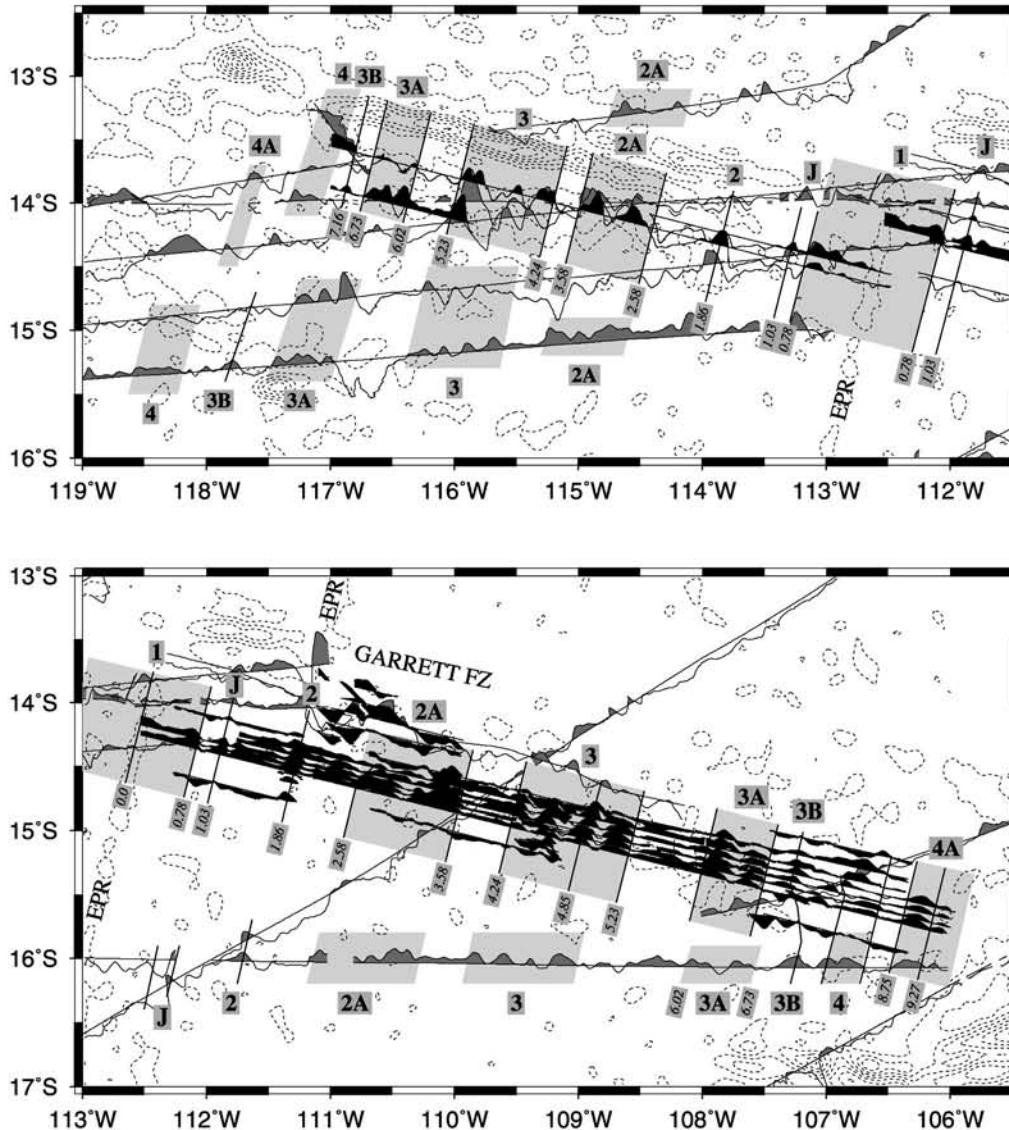


Fig. 2. Wiggle plot of magnetic data acquired on the East Pacific Rise south of the Garrett transform fault. Annotation above the surveyed corridors indicates the identified magnetic anomalies and numbers below give the seafloor age in million years [28–30]. Black wiggles are from the *Sonne* cruises and grey wiggles are from previous cruises. Isolines are gravity anomalies derived from satellite altimetry [5] (contour interval: 15 mGal).

tially interpreted by Grevemeyer et al. [13] who documented a correlation between changes in spreading rate and profound changes in the seafloor fabric as expressed by the rms height of abyssal hills. To verify whether these patterns are related to asymmetric spreading, a conjugate profile on the western flank was surveyed in 2000

during *Sonne* leg 145-1. However, because of the Sojourn Ridge [25] the profile had to be shifted by 30–40 km to the south. Additionally, the corridor on the eastern flank has been extended by flowline profiles to the north and south. Rock samples were dredged during *Sonne* leg 145-2 and provided basaltic lavas from 10 dredges on oceanic

crust and one dredge on a seamount. A further seven samples were recovered in the core catcher of a gravity corer.

### 3.1. Magnetism

Total magnetic field intensity was measured using a proton precession magnetometer. On the eastern flank up to seven flowline profiles allow an unambiguous identification of the sequence of reversals; coverage reaches 710 km off-axis. On the western flank only two profiles are available out to ~500 km in the spreading direction. For each survey the appropriate International Geomagnetic Reference Field (IGRF), which describes the long wavelength magnetic field for 5 yr intervals, has been removed from the observed magnetic field data. Unfortunately, the survey area is located close to the magnetic equator where daily variations are reasonably high [26]. We therefore calculated synthetic Sq variations and removed those from the field data. In addition, we tried to assess magnetic storms by using the worldwide DST index. Variations were calculated and removed. This procedure provided crossover errors for the corrected data, which are generally smaller than 25 nT [27]. In addition, we included magnetic tracks collected previously to our cruises to further constrain the spreading rate to the west and to the south of the survey area. The top and bottom panels of Fig. 2 show wiggle plots of the residual magnetic anomaly. Geomagnetic polarity reversals of Cande and Kent [28] were generally used to derive the crustal age. However, ages of anomaly #C3A and anomalies #C3B to #C4A are from Krijgsman et al. [29] and Hilgen et al. [30], respectively. The oldest anomaly on the western flank is #C4A (8.75 Ma) at 533 km off-axis and on the eastern flank #C4Ar1 (9.27 Ma) at 708 km off-axis. In Fig. 3 the age of the identified magnetic anomalies is plotted as a function of offset from the ridge axis, hence showing the half spreading rate.

### 3.2. Bathymetry

The multibeam-sonar data are from a HY-

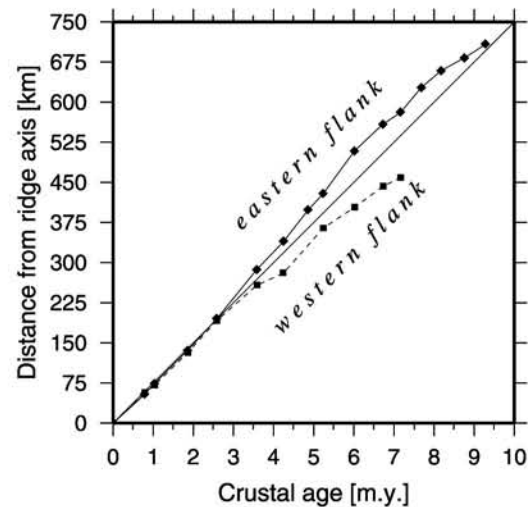


Fig. 3. Distance versus age plot of the picked magnetic reversals for the eastern and western ridge flank. The straight line indicates a half spreading rate of 75 mm/yr; thus, before 2.7 Ma seafloor spreading was asymmetric with faster spreading to the east.

DROSWEEP swathmapping echosounder [31]. The 59 beams fired within an angle of 90° survey a stripe on the seabed with a width about twice the water depth. These data have been processed and edited with the MB Software from the Lamont-Doherty Earth Observatory [32]. The resulting digital terrain models (DTM) were displayed and imaged with the GMT Software [33]. In total, about 15 000 line km of swath bathymetry covered about 35 000 km<sup>2</sup> of seafloor. On the eastern flank nearly full coverage extends up to 720 km off-axis. The width of the corridor is between 50 and 80 km. Detailed maps are shown in Fig. 4.

### 3.3. Geochemical analytical methods

The geochemistry study is based on investigations carried out on more than 50 samples of mid-ocean ridge basalt (MORB) from 17 locations. Sample locations are shown in Fig. 4 and mean major element compositions are summarized in Table 1. The samples were recovered either by dredging or in the core catcher of a gravity corer. Major element analyses were carried out on a five

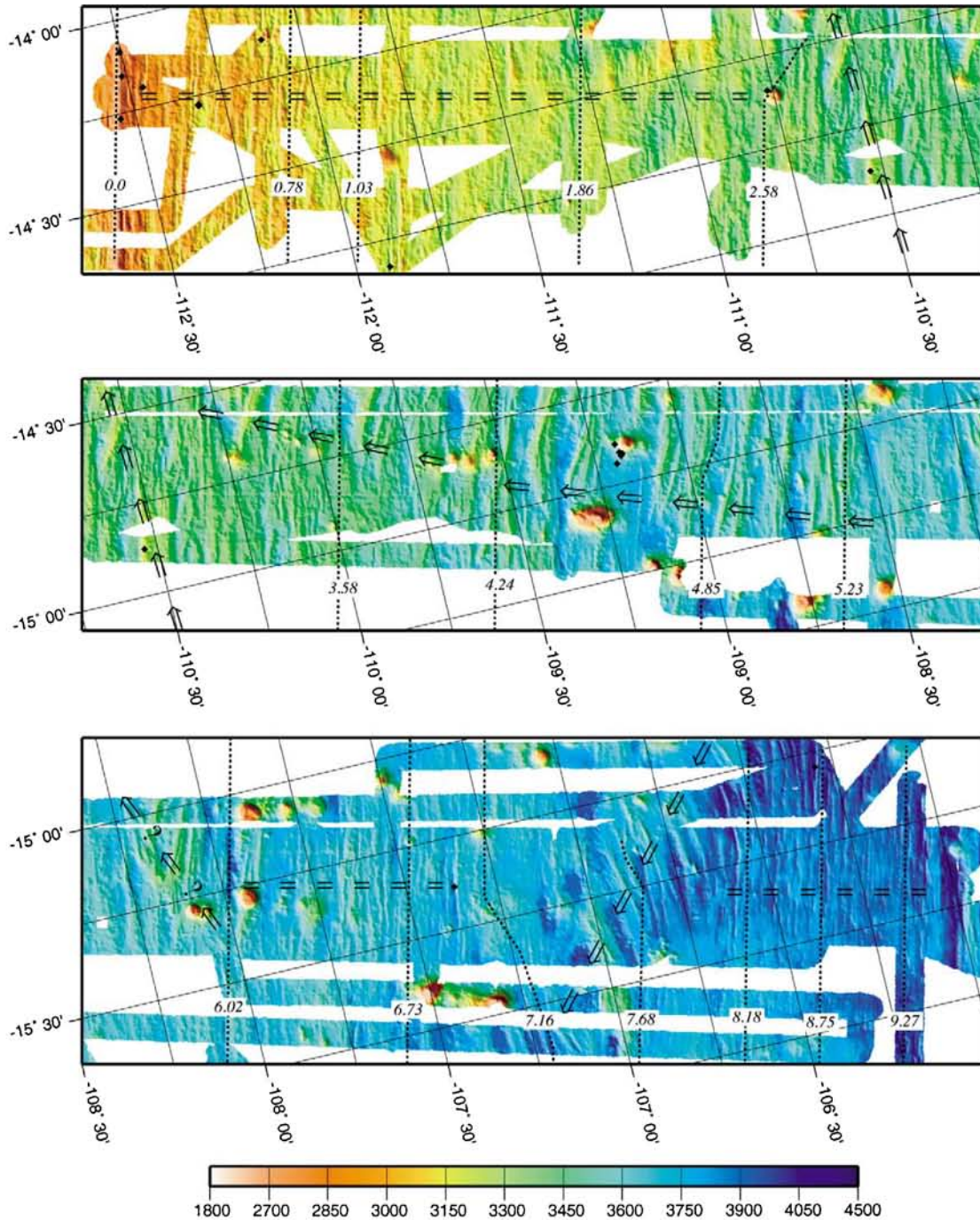


Fig. 4. Oblique projection of the bathymetry derived from the multibeam-sonar data. Data are displayed with artificial illumination. Seafloor fabric which plot vertically in the figure runs parallel to the strike of the ridge crest. Hummocky basins and motley texture of curved lineations striking oblique to the ridge axis are caused by at least five migration events of overlapping spreading centres. Broken horizontal lines mark times characterized by stable spreading condition at the ridge crest. Arrows show the migration paths of non-transform ridge axis discontinuities. Dotted lines are chrons in million years. Sample locations are shown by diamonds.

Table 1  
Average microprobe analyses of glassy MORB pieces from *Somme* leg 145-2 (wt%)

Sample	Ma	Latitude	Longitude	Eruption latitude	SiO <sub>2</sub>	TiO <sub>2</sub>	Al <sub>2</sub> O <sub>3</sub>	FeO	MnO	MgO	CaO	Na <sub>2</sub> O	K <sub>2</sub> O	P <sub>2</sub> O <sub>5</sub>	Cr <sub>2</sub> O <sub>3</sub>	Total	n	Mg#
21DS all	0.000	-14°05'	-112°30'	-14.086	50.64	1.80	14.36	10.69	0.20	7.51	11.63	2.98	0.13	0.15	0.04	100.13	70	0.56
18DS all	0.015	-14°16'	-112°33'	-14.264	50.63	1.85	13.86	11.35	0.20	7.25	11.32	2.90	0.13	0.14	0.03	99.66	54	0.53
20DS rest	0.015	-14°09'	-112°31'	-14.154	50.58	1.68	14.04	10.97	0.20	7.52	11.65	2.69	0.11	0.12	0.04	99.58	21	0.55
20DS3	0.015	-14°09'	-112°31'	-14.154	49.88	1.68	14.71	10.29	0.18	7.63	11.79	2.83	0.19	0.15	0.05	99.39	5	0.55
22DS all	0.120	-14°12'	-112°28'	-14.167	49.50	2.16	13.09	11.97	0.21	6.77	10.87	2.71	0.11	0.19	0.02	97.60	83	0.50
27SL all	0.360	-14°17'	-112°19'	-14.216	50.04	2.03	13.63	11.75	0.22	6.88	11.01	2.77	0.12	0.16	0.02	98.63	37	0.51
15SL rest	0.360	-14°16'	-112°19'	-14.215	50.50	2.16	13.54	12.30	0.23	6.78	11.00	2.80	0.14	0.15	0.02	99.61	7	0.50
15SL3	0.360	-14°16'	-112°19'	-14.215	50.09	1.33	13.94	10.24	0.20	7.66	12.07	2.55	0.02	0.09	0.03	98.23	10	0.57
26SL all	0.360	-14°17'	-112°19'	-14.219	49.50	1.67	13.98	10.21	0.20	7.38	11.37	2.73	0.09	0.16	0.04	97.33	22	0.56
28DS all	0.650	-14°09'	-112°07'	-14.026	49.00	0.92	16.68	9.59	0.18	10.09	11.57	2.16	0.09	0.06	0.06	100.40	49	0.65
29DS rest	1.160	-14°49'	-111°54'	-14.632	50.46	2.23	13.78	11.94	0.21	6.72	11.04	3.06	0.20	0.21	0.02	99.87	30	0.50
29DSE	1.160	-14°49'	-111°54'	-14.632	53.86	1.92	13.30	12.16	0.22	4.84	8.84	3.54	0.36	0.37	0.02	99.43	20	0.41
35DS all	2.560	-14°36'	-110°46'	-14.167	50.13	1.17	15.13	9.46	0.17	8.54	12.77	2.38	0.04	0.06	0.05	99.91	9	0.62
9DS rest	2.920	-14°52'	-110°32'	-14.389	49.84	2.79	12.68	14.57	0.25	5.72	9.83	3.15	0.19	0.24	0.01	99.27	18	0.41
9DS4	2.920	-14°52'	-110°32'	-14.389	49.83	2.23	13.70	11.97	0.21	6.84	11.04	2.97	0.17	0.18	0.04	99.17	9	0.50
9DS8	2.920	-14°52'	-110°32'	-14.389	49.67	1.64	14.92	10.05	0.18	7.68	11.98	2.96	0.15	0.13	0.06	99.42	10	0.58
37SL rest	4.590	-14°57'	-109°12'	-14.143	49.96	1.39	13.92	10.47	0.20	7.85	12.18	2.61	0.04	0.09	0.03	98.71	14	0.57
37SL1	4.600	-14°57'	-109°12'	-14.143	49.51	1.01	15.28	8.87	0.17	8.82	12.56	2.30	0.02	0.07	0.06	98.66	22	0.64
36DS all	4.600	-14°54'	-109°11'	-14.108	49.58	1.09	15.61	9.35	0.17	9.09	12.67	2.45	0.04	0.06	0.07	100.16	7	0.63
38SL all	4.610	-14°55'	-109°11'	-14.121	50.24	1.24	14.41	9.91	0.19	8.03	12.42	2.65	0.02	0.07	0.03	99.21	41	0.59
40SL rest	4.610	-14°56'	-109°11'	-14.130	49.17	1.02	15.49	8.94	0.16	8.94	12.61	2.33	0.02	0.06	0.06	98.81	27	0.64
40SL3	4.610	-14°56'	-109°11'	-14.130	49.87	2.09	13.23	11.92	0.22	6.63	10.62	2.78	0.11	0.18	0.03	97.68	13	0.50
7SL1+3	4.620	-14°55'	-109°10'	-14.162	49.34	1.00	15.23	8.88	0.17	8.87	12.52	2.33	0.02	0.05	0.06	98.45	13	0.64
7SL2+3	4.620	-14°55'	-109°10'	-14.162	49.94	1.21	14.20	10.02	0.19	7.82	12.34	2.58	0.02	0.08	0.04	98.43	17	0.58
42DS all	6.840	-15°23'	-107°22'	-14.189	50.03	1.94	13.85	11.57	0.21	7.12	11.43	2.83	0.13	0.15	0.03	99.28	17	0.52
43DS all	8.640	-15°18'	-106°18'	-13.895	50.52	1.91	14.09	10.99	0.20	7.45	11.59	2.81	0.11	0.14	0.03	99.85	17	0.55
		<i>Analytical error (1 S.D. relative %)</i>			<i>0.64</i>	<i>3.70</i>	<i>1.17</i>	<i>1.57</i>	<i>9.22</i>	<i>1.80</i>	<i>1.23</i>	<i>3.20</i>	<i>23.82</i>	<i>24.80</i>	<i>59.39</i>	<i>0.48</i>		<i>0.87</i>

Averages are either of single samples (in the cases where the letters in the sample names are followed by numbers) or of many or all samples from a dredge haul (shown by the word rest or all in the sample names). Sample 22DS is an analysis of bulk rock powder fused to a glass. Eruption latitude is discussed in the text; n, number of analyses used to build the mean. The age of the samples was derived by linear interpolation between the age of magnetic reversals (Fig. 2).

Table 2  
Summary of results and interpretation of seafloor fabric generated at the EPR near 14°14'S over the last 10 Myr

Time interval	Magnetic lineations	Strike of seafloor fabric	Advance of discordant zones	Interpretation
0.0–2.5 Ma	ridge parallel	013°	none	stable system
2.5–~2.7 Ma	right lateral offset by 20–30 km	oblique, curving SW	northward	northward migrating right-stepping OSC
~2.7–4.2 Ma	ridge parallel	oblique, curving SW	slowly northward	slowly northward migrating right-stepping OSC
4.2–5.3 Ma	right lateral offset	oblique, curving SW, fossil overlap basin	none?	duelling OSC
5.3–5.5 Ma	–	smooth seafloor	–	stable system
5.5–6.0 Ma	–	oblique, curving SW	northward	northward migrating right-stepping OSC
6.0–7.2 Ma	ridge parallel	013°	none	stable system
7.2–~7.8 Ma	left lateral offset by 20–30 km	oblique, curving NW	southward	southward migrating left-stepping OSC
~7.8–~9.4 Ma	ridge parallel	013°	none	stable system

spectrometer JEOL JXA 8900 RL electron microprobe (University of Göttingen, Germany) either on natural glass pieces from pillow rinds or, in the case of sample 22DS, on glasses produced by melting powdered groundmass on a platinum wire in the laboratory. Analytical conditions were 15 kV accelerating voltage and 11–13 nA sample current. Representative errors on the analyses are shown in Table 1 together with the number of individual spots measured and used to calculate the mean values. The electron beam was slightly defocused (10  $\mu$ m diameter) to avoid the volatilization of alkalis. The raw major element data from each measured spot have been corrected to the KL2-G MPI-DING reference glass [34]. We note that the samples from the gravity corer (samples labelled SL) and from the melted powdered groundmass (22DS) have analytical totals lower than the acceptable  $99.6 \pm 0.5\%$  found for all other samples. We attribute this to hydration of the glasses in the case of gravity corer samples and to the inclusions of microbubbles of air during the melting of the powder in the case of 22DS. We do not expect either of these effects to alter the Mg/Fe ratio of the measurement; their effects are therefore unimportant for the conclusions of the paper.

## 4. Results and discussion

### 4.1. Asymmetric spreading and segmentation

Since 10 Ma, seafloor spreading rates derived from the magnetic data indicate an average total separation rate of the Nazca plate and Pacific plate of 150 mm/yr (Fig. 3), which is in reasonable agreement with the NUVEL-1A spreading model of current plate motions [18]. However, symmetric spreading has occurred only since about 3 Ma. In Early Pliocene and Late Miocene times the spreading rate was profoundly asymmetric. In general, faster spreading rates of the Nazca plate to the east of the rise axis are compensated by slower spreading rates of the Pacific plate to the west. It is important to note that magnetic data immediately to the south of the survey corridor show a right-lateral offset of the magnetic spreading anomalies on both ridge flanks. Unfortunately, these profiles do not follow the flowline. Nonetheless, they clearly suggest that spreading was asymmetric and faster to the east. However, this asymmetry is not as pronounced as immediately to the north.

In a statistical study of seafloor fabric Grevemeyer et al. [13] show a change in seafloor fea-

tures at about 225 km off-axis. This offset corresponds to the 3 Ma isochron derived from the magnetic data. The high-resolution bathymetric maps in Fig. 4 show that within 225 km of the rise axis (out to about 110°45'S) abyssal hills strike parallel to the ridge axis and therefore imply a spreading system similar to the present configuration of the ridge at 14°14'S. Beyond 110°45'W, however, the seafloor fabric is orientated obliquely to the 013° strike of the ridge axis. In addition, the magnetic anomaly #C2ay (2.58 Ma) indicates a right-lateral offset of 20–30 km. Such features are generally taken as evidence for off-axis discordant zones of migrating OSC [4,19,21]. This interpretation is supported by bathymetric studies within the adjacent MELT study area. Immediately to the south, Cormier et al. [25] found similar features, which they interpreted as the trace of a right-stepping northward migrating OSC.

East of 110°20'W the surveyed corridor indicates a wedge of rough terrain in the northern part of the swath. This zone is comprised of hummocky basins and motley lineaments, interpreted as abandoned curvilinear ridge tips of OSCs. In terms of Wilson's [35] model for overlapping rift propagation, we would interpret the curvature and the trace of the discordant zone (or inner pseudofault) to result from a right-stepping northward migrating OSC. This idea is supported by a right-stepping offset of the magnetic anomaly #C3.3 (4.85 Ma) and seafloor younger than anomaly #C3.1 (4.24 Ma) indicates a northward shift of the discordant zone. Other features resemble fossil overlap basins, for example the seafloor fabric near 109°20'W. Nonetheless, features are not consistent; the curved abandoned tips between anomaly #C3.3 (4.85 Ma) and #C3o (5.23 Ma) seem to indicate only a small or no northward shift. Unfortunately, seafloor coverage is not complete. However, to explain the seafloor fabric we propose a model including a northward migrating right-stepping OSC, which was active between ~2.7 Ma and 4.24 Ma; features between chron ~4.24 and ~5.3 Ma are interpreted to result from a right-stepping duelling OSC.

Immediately to the east of 108°30'W the seafloor is very smooth for about 30 km. Features

between 108°15'W and 108°00'W are not very clear. Some structural elements, such as the curvature of abyssal hills, may indicate a northward migrating right-stepping OSC. However, the magnetic anomaly #C3Ay (6.02 Ma) does not indicate any right-lateral step.

East of chron 6.02 Ma the seafloor is smooth and the abyssal hill fabric strikes parallel to the present trend of the ridge axis until magnetic anomaly #C3B (7.16 Ma) is reached. This suggests a stable spreading regime similar to the present situation at 14°14'S. Nevertheless, to the north and south several large seamounts have been surveyed. Swathmapping data suggest, however, that seamount volcanism on the eastern ridge flank at 14°14'S has been relatively scarce during the last 3 Myr.

The ridge axis was offset by another OSC between 107°15'W and 106°45'W. The orientation of abandoned ridge tips indicates a left-stepping OSC. This fact is supported by the magnetic data, which indicate a left-lateral offset of 20–30 km of anomaly #C4n.1r (7.68 Ma). In addition, the seafloor fabric shows an inner pseudofault and suggests that the OSC migrated southward. This fact is important to note and will be discussed below.

At the end of the survey area, i.e., east of 106°40'W, the seafloor is remarkably smooth. Additionally, the swathmapping revealed no seamounts. Seafloor in this area is between ~7.8 and ~9.4 Ma and may have been formed by a crustal accretion process similar to that typical for the rise axis since ~3 Ma.

A summary of the Late Miocene to Pleistocene segmentation of the SEPR at 14°14'S is given in Table 2. The features detected in the seafloor fabric provide a reasonable explanation for the degree of asymmetric spreading detected in the magnetic data. Both northward migrating right-stepping and southward migrating left-stepping overlapping spreading centres transfer lithosphere from the Pacific plate to the Nazca plate and may therefore account for the spreading asymmetry. With respect to previous studies of the ridge flanks immediately to the south [19,21], it seems reasonable to suggest that between the Garrett fracture zone and the OSC at 20°40'S the majority of the spreading asymmetry is accommodated

by migrating OSC. Immediately to the south of the detailed study area our interpretation of magnetic tracks (Fig. 2) suggests a less prominent degree of asymmetric spreading. On the western flank, about two degrees to the south, magnetic anomaly #C4n.1r was identified approximately 580 km away from the ridge crest. Back tracking of the anomaly suggests that this crust was created where the SEPR intersected latitude 16°S. Its distance from the ridge axis indicates a spreading half rate of about 75 mm/yr, which is exactly the rate predicted by the NUVEL-1A spreading model [18]. Consequently, the existing data may argue that the spreading asymmetry observed at 14°14'S is a local feature primarily related to the tectonic evolution of the rise axis north of 16°S. However, the identification of the magnetic anomalies south of the flowline corridor may not be entirely reliable. Therefore, additional profiles will be necessary to constrain the tectonic evolution of the 14.5°S to 16°S area between 5 and 10 Ma.

#### 4.2. Tectonic and geochemical segmentation

The underlying principle of ridge segmentation presented by Macdonald et al. [3] is the along axis migration of melt away from the shallowest portions of the rise axis which coincide with localized regions of asthenospheric upwelling. Thus, gravitational spreading forces due to excess ridge topography cause a segment to lengthen and force a discontinuity to migrate [36]. Because magma supply beneath the ridge axis will tend to be enhanced over loci of partial melting in the upper mantle, this model works well where hot spot magmatism has produced extraordinary ridge axis elevation and significant variations in near-field stresses. It may also work if focused mantle upwelling occurs [37]. However, at ~7.3–7.8 Ma a southward migrating OSC dominated the rise axis at 14°14'S and must have originated close to the Garrett transform fault. Although the primary segmentation of the southern EPR around ~8 Ma is largely unconstrained, work of Goff and Cochran [38] suggest that the Garrett transform already offset the EPR between 8 and 10 Ma. Near first-order discontinuities, a small cross-sectional area and a deepening of the ridge

crest towards the transform fault is generally interpreted as evidence for a starved magma supply at the ends of a spreading segment [8]. Consequently, an OSC migrating away from a transform fault is inconsistent with a model where the migration of non-transform ridge axis discontinuities is controlled by the along axis distribution of melt. In addition, the few existing magnetic profiles to the south of the detailed study area suggest a less prominent degree of asymmetric spreading near 16°S, which makes it unlikely that all of the detected OSCs have been created in the middle of the first-order segment near 18–19°S, but instead somewhere north of 16°S. Therefore, forces other than mantle upwelling and melting may control the creation and migration of overlapping spreading centres.

Wilson et al. [39] proposed a model which suggested that migration events of non-transform ridge axis discontinuities are caused by far-field stresses related to the reorientation of a plate boundary and Macdonald et al. [4] suggested that crack propagation caused by such far-field stresses might cause discontinuities to migrate. Such models appeal to us because they may explain how an OSC can originate close to a magmatically starved first-order discontinuity. Following the breakup of the Farallon plate a major reorientation of the plate boundary configuration occurred in the southern East Pacific Ocean about 20 Myr ago and included the formation of the Bauer microplate [20,38]. Goff and Cochran [38] investigated the evolution of the Bauer microplate and a now extinct spreading ridge: the Galapagos Rise. Between ~17 and ~6 Ma two spreading centres were active between latitudes ~2°S and ~16°S. Because the Galapagos Rise was orientated obliquely to the EPR, it is reasonable to assume that the resulting stress field affected the on-axis stress field of the southern EPR and perhaps forced the migration of the OSC. Therefore, the southward migrating OSC, which was generated at or near the Garrett transform fault, was perhaps forced by far-field stresses caused by the plate boundary reorientation and evolution of the Bauer microplate. In addition, back tracking of the OSCs dominating the SEPR at 14°14'S between magnetic chron #C3.1

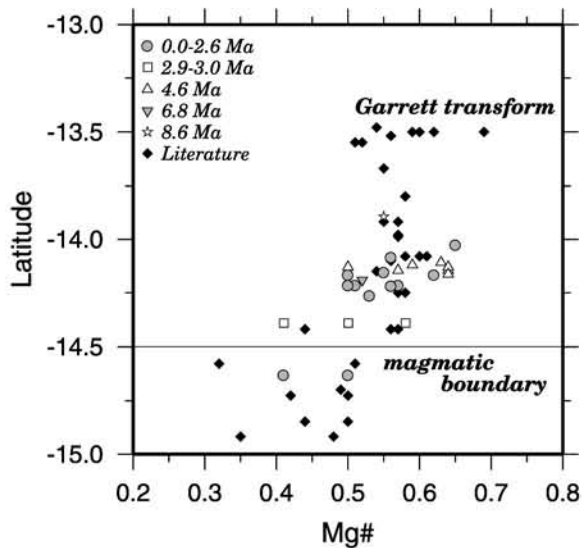


Fig. 5. Geochemical data (Mg#) back tracked to the ridge crest. The common trend of samples (labelled literature) from the ridge crest [10,40,41] and off-axis samples argues that the latitudinal variations in magma composition are a robust feature of the sub-lithospheric magmatic system and independent of the shallow processes controlling the propagation of non-transform ridge axis discontinuities.

(4.24 Ma) and #C3Ay (6.02 Ma) points toward the fossil Bauer fracture zone (Fig. 2, gravity anomaly in the lower right hand corner), which marked the southern terminus of the Bauer microplate [38]. The birth of both OSCs was probably related to a change of the regional stress pattern as spreading at the Galapagos Rise ceased and the EPR-Bauer-microplate ridge-ridge-transform triple junction became inactive  $\sim 6$  Ma ago.

Additional support for a crack model rather than a melt migration model is provided by the geochemical data from the seafloor samples. The works of Langmuir et al. [1] and Sinton et al. [10] suggest that the tectonic and chemical segment boundaries are linked. They suggest that all first-, second- and third-order ridge offsets correspond to secondary magmatic segment boundaries, although some secondary magmatic boundaries may even occur at small, fourth-order discontinuities. Secondary magmatic segments are believed to define the length scale of mantle melting variations, which are mainly variations in extent of melting, but are not necessarily the scale

of melt extraction processes that feed the axis. Melt extraction is suggested to correspond to the length scale of fourth-order physical segments [10]. The samples collected on the eastern flank are sparse but still define an important dataset, because they provide the means to study temporal variations in magma geochemistry. In this paper, we report only some initial results of the geochemistry. In Fig. 5, all samples have been projected back to their eruption latitude and plotted together with data from samples taken on the present day axis [10,40,41]. A striking feature of the present day axis is a significant and systematic variation of Mg# with latitude, characterized by high Mg# of about 0.6 for lavas north of a DEVAL at 14°30'S. South of this DEVAL all magmas show Mg# lower than ca. 0.5. In general, Sinton et al. [10] found that most secondary magmatic boundaries defined by K/Ti and K/P ratios correspond to boundaries apparent in MgO content. The prominent Mg# boundary at 14°30'S, however, occurred within a secondary magmatic segment and hence defines a tertiary magmatic and fourth-order physical segment boundary. Sinton et al. [10] attributed this type of magmatic segmentation to mixture boundaries within the continuous magma chambers. Therefore, it is surprising that the back tracked data show exactly the same patterns of Mg# variations with latitude, despite the fact that they cover a range of ages back to ca. 10 Ma. The bathymetric data clearly show that up to five OSCs dominated the ridge morphology for various amounts of time in the period 2.6–7.8 Ma. In total, we have sampled six locations from two sites affected by OSCs and 14 locations (including one on-axis and three at  $\sim 15$  ka) from sites, which, based on the bathymetric data, were characterized by stable spreading conditions similar to those of the present day (Fig. 4). Unfortunately, only one dredge provided two samples to the south of the 14°30'S magmatic boundary on 1 Myr old crust. Nevertheless, DEVALs are generally believed to last only for  $10^2$ – $10^4$  yr [8]; thus, it is remarkable that its geochemical signature lasted for at least 1 Myr and maybe even longer. Because all the data from our survey, irrespective of tectonic setting, plot within the Mg# vs. Latitude trend seen at the present day

on the axis, we believe that magmatic segmentation defined by the change in Mg# at 14°30'S has been stationary over the last  $\sim 10$  Myr.

In an overview of the East Pacific Rise morphology, Macdonald [8] quantified the commonly noted observations that primitive basalts tend to be found on the shallower and broader parts of the ridge axis and emphasized the 14°30'S discontinuity as a place where basalt chemistry correlates much better with cross-sectional area of the ridge axis than with simple axial depth. The more evolved lavas to the south are associated with a cross-section of 3–4 km<sup>2</sup>, while the more primitive lavas to the north are associated with an area of 4–5 km<sup>2</sup>. Axial depth is nearly uniform at 2620–2660 m. If the chemical discontinuity has been persistent, as we suggest, then one speculative interpretation is that the broad cross-section reflects an extremely stable and robust site of upwelling that has neither influenced nor been influenced by small ridge offsets that have propagated through the area. Although the causes of variation in magma fractionation along ridge axes remain poorly understood, it is widely accepted that frequent replenishment of shallow crustal magma chambers would generally dilute any evolved magmas that may form there.

We conceive of two plausible mechanisms to explain the observation of a stationary chemical segmentation defined by Mg#. Either (1) the magmas being supplied from the mantle have similar Mg# over the whole area and the extent of crystal fractionation occurring in the sub-axial magma chamber is consistently higher (and by implication the rate of magma supply consistently lower [10]) towards the south of the 14°30'S discontinuity or (2) the Mg# of the parental magmas decreases systematically southward and the extent of fractionation stays constant. In view of the fact that total crustal thickness (as indicated by axial depths) appears to be constant over the area, the former option would imply a systematic change in the Layer 2/Layer 3 thickness from north to south (assuming that Layer 3 represents the cumulates and Layer 2 the residual liquids from fractionation). Data from Hooft et al. [9] show constant Layer 2A thickness throughout the region studied here and appear to provide

some evidence against changing extents of crystal fractionation. We therefore must conclude that the latitudinal variations in magma composition are principally a feature of the sub-lithospheric magma supply and relatively independent of crustal processes.

The fact that the composition of the lavas between the Garrett transform and 14°30'S appears to remain constant over the last 10 Myr and the lack of correlation of compositional boundaries with off-axis discordant zones provide important implications for the processes controlling the segmentation of mid-ocean ridges. We propose that these observations provide further support for a crack model. As a cracking front advances along the ridge axis, it is likely to intersect and tap a number of separate mantle melt sources. Magmas would rise passively into the open crack and erupt on the seafloor. Thus, such a model would be dominantly plate- and crack-controlled and hence a passive spreading model. Nevertheless, focused mantle upwelling [37] would result in an increased melt supply toward the middle of a first-order segment and in the presence of magma, crustal failure can occur at much lower deviatoric stresses [42]. It therefore seems likely that overlapping spreading centres will generally tend to originate near the middle of a first-order segment and may support a feedback between passive and active driving forces, as proposed by Macdonald et al. [4]. However, four out of five OSCs imaged in our dataset are probably linked to far-field stresses related to the evolution of the now extinct Bauer microplate and originated somewhere near 16°S and hence well to the north of the middle of the first-order segment.

## 5. Conclusions

A combined geophysical mapping and geochemical sampling approach provided a unique dataset from a flowline corridor out to a seafloor age of  $\sim 10$  Ma on the eastern flank of the East Pacific Rise at 14°14'S. In addition to multibeam-sonar data and magnetic anomalies from the eastern flank, magnetic and bathymetric data were obtained on the conjugate western flank to esti-

mate the degree of asymmetric spreading. Seafloor spreading was generally asymmetric with a faster spreading to the east, although since  $\sim 2.8$  Ma crustal accretion occurs symmetrically. The seafloor characterized by symmetric spreading did not show any evidence for discordant zones, while seafloor indicating asymmetric spreading suffered from at least five overlapping spreading centre migration events. One was a left-stepping southward migrating discontinuity, which was created close to the Garrett transform fault. The other four were right-stepping and northward migrating OSCs and originated somewhere near 16°S. Both right-stepping northward and left-stepping southward migrating OSC transfer lithosphere from the Pacific plate to the Nazca plate and may therefore account for the spreading asymmetry. The fact that the birth of four of the five OSCs seems to be initially related to the evolution of the Bauer microplate between  $\sim 9$  and 6 Ma suggests that in addition to mantle upwelling other forces – like far-field stresses – can create non-transform ridge axis discontinuities. Furthermore, the geochemical data seem to support a crack-controlled rather than upwelling-controlled model for higher-order ridge crest segmentation. They suggest that the magmatic segment boundary near 14°30'S has remained stationary for at least the last 10 Myr. Moreover, the geochemistry of samples does not show any correlation with off-axis discordant zones of fossil OSCs. This observation suggests that advancing cracks tap underlying melt reservoirs and melts rise passively into the crack to build the seafloor. Thus, to explain all observations we favour a feedback mechanism between active and passive plate- and crack-controlled spreading mechanisms. Magma, however, is not distributed along axis by propagating segment tips.

#### Acknowledgements

We are grateful to Milene Cormier, Jennifer Reynolds and Maurice Tivey for their reviews, which led to substantial improvements in the manuscript. This work was supported by the German Ministry of Education, Science, Research

and Technology (grants 03G0105A and 03G0145A). We would particularly like to thank the masters, crews and shipboard scientific parties of research vessel *Sonne* cruises 105 and 145 for their efficiency and cooperation at sea. [AC]

#### References

- [1] C.H. Langmuir, J.F. Bender, R. Batiza, Petrological segmentation of the East Pacific Rise, 5°30'–14°30'N, *Nature* 322 (1986) 422–429.
- [2] H. Schouten, K.D. Klitgord, J.A. Whitehead, Segmentation of mid-ocean ridges, *Nature* 317 (1985) 225–229.
- [3] K.C. Macdonald, P.J. Fox, L.J. Perram, M.F. Eisen, R.M. Haymon, S.P. Miller, S.M. Carbotte, M.-H. Cormier, A.N. Shor, A new view of the mid-ocean ridge from the behaviour of ridge axis discontinuities, *Nature* 335 (1988) 217–225.
- [4] K.C. Macdonald, D.S. Scheirer, S.M. Carbotte, Mid-ocean ridges: discontinuities, segments and giant cracks, *Science* 253 (1991) 986–994.
- [5] D.T. Sandwell, W.H.F. Smith, Marine gravity anomaly from Geosat and ERS-1 satellite altimetry, *J. Geophys. Res.* 102 (1997) 10039–10054.
- [6] B.E. Tucholke, J. Lin, M.C. Kleinrock, M.A. Tivey, T.B. Reed, J. Goff, G.E. Jaroslow, Segmentation and crustal structure of the western Mid-Atlantic Ridge flank, 25°25'–27°10'N and 0–29 m.y., *J. Geophys. Res.* 102 (1997) 10203–10223.
- [7] D.S. Scheirer, K.C. Macdonald, D.W. Forsyth, S.P. Miller, D.J. Wright, M.-H. Cormier, C.M. Weiland, A map series of the southern East Pacific Rise and its flanks, *Mar. Geophys. Res.* 18 (1996) 1–12.
- [8] K.C. Macdonald, Linkages between faulting, volcanism, hydrothermal activity and segmentation on fast spreading centers, in: W.R. Buck, P.T. Delaney, J.A. Karson, Y. Lagabriele (Eds.), *Faulting and Magmatism at Mid-Ocean Ridges*, *Geophys. Monogr.* 106 (1998) 27–58.
- [9] E.E.E. Hooft, R.S. Detrick, G.M. Kent, Seismic structure and indicators of magma budget along the Southern East Pacific Rise, *J. Geophys. Res.* 102 (1997) 27319–27340.
- [10] J.M. Sinton, S.M. Smaglik, J.J. Mahoney, K.C. Macdonald, Magmatic processes at the superfast spreading mid-ocean ridges: glass compositional variations along the East Pacific Rise 13°–23°S, *J. Geophys. Res.* 96 (1991) 6133–6155.
- [11] J.-C. Sempéré, K.C. Macdonald, Overlapping spreading centers: implications from crack growth simulation by the displacement discontinuity methods, *Tectonics* 5 (1986) 151–163.
- [12] W. Weigel, I. Grevemeyer, N. Kaul, H. Villinger, T. Lüdman, H.K. Wong, Aging of oceanic crust at the southern East Pacific Rise, *EOS Trans. Am. Geophys. Un.* 77 (1996) 504.

- [13] I. Grevemeyer, V. Renard, C. Jennrich, W. Weigel, Seamount abundances and abyssal hill morphology on the eastern flank of the East Pacific Rise at 14°S, *Geophys. Res. Lett.* 24 (1997) 1955–1958.
- [14] I. Grevemeyer, N. Kaul, H. Villinger, W. Weigel, Hydrothermal activity and the evolution of the seismic properties of upper oceanic crust, *J. Geophys. Res.* 104 (1999) 5069–5079.
- [15] C.W. Devey, H. Villinger, I. Grevemeyer, J. Hauschild, K. Lackschewitz, N. Kaul, M. Mottl, M. Pfender, B. Schramm, G. Wheat, and scientific party EXCOII legs 1 and 2, The fourth dimension in ridge studies: sampling along a flow-line corridor 0–9 Ma at 14°S on the EPR, *InterRidge News* 9 (2000) 34–36.
- [16] R.S. Detrick, A.J. Harding, G.M. Kent, J.A. Orcutt, J.C. Mutter, P. Buhl, Seismic structure of the southern East Pacific Rise, *Science* 259 (1993) 499–503.
- [17] G.M. Kent, A.J. Harding, J.A. Orcutt, R.S. Detrick, J.C. Mutter, P. Buhl, Uniform accretion of oceanic crust south of the Garrett transform at 14°15'S on the East Pacific Rise, *J. Geophys. Res.* 99 (1994) 9097–9116.
- [18] C. DeMets, R.G. Gordon, D.F. Argus, S. Stein, Effect of recent revisions to the Geomagnetic Reversal Time Scale on estimates of current plate motions, *Geophys. Res. Lett.* 21 (1994) 2191–2194.
- [19] M.-H. Cormier, D.S. Scheirer, K.C. Macdonald, Evolution of the East Pacific Rise at 16°–19° S since 5 Ma: bisection of overlapping spreading centers by new, rapidly propagating segments, *Mar. Geophys. Res.* 18 (1996) 53–84.
- [20] P. Lonsdale, Segmentation of the Pacific-Nazca spreading center, 1°N–20°S, *J. Geophys. Res.* 94 (1989) 12197–12225.
- [21] M.-H. Cormier, K.C. Macdonald, East Pacific Rise 18°–19°S: asymmetric spreading and ridge reorientation by ultrafast migration of axial discontinuities, *J. Geophys. Res.* 99 (1994) 543–564.
- [22] K.C. Macdonald, R.M. Haymon, S.P. Miller, J.-C. Sempéré, P.J. Fox, Deep-tow and SeaBeam studies of dueling propagating ridges on the East Pacific Rise near 20°40'S, *J. Geophys. Res.* 93 (1988) 2875–2898.
- [23] L.J. Perram, M.-H. Cormier, K.C. Macdonald, Magnetic and tectonic studies of the dueling propagating spreading centers at 20°40'S on the East Pacific Rise: evidence for crustal rotations, *J. Geophys. Res.* 98 (1993) 13835–13850.
- [24] I. Grevemeyer, W. Weigel, C. Jennrich, Structure and ageing of oceanic crust at 14°S on the East Pacific Rise, *Geophys. J. Int.* 135 (1998) 573–584.
- [25] M.-H. Cormier, D.S. Scheirer, K.C. Macdonald, S. White, R.M. Haymon, and the Sojourn Leg 1 Scientific Party, Sojourn, Leg 1: detailed study of the asymmetries about the East Pacific Rise, 15°30'–20°S, *Ridge Events* 8 (1997) 1–5.
- [26] A.P. Hitchman, F.E.M. Lilley, W.H. Campbell, The quite daily variation in the total magnetic field: global curves, *Geophys. Res. Lett.* 25 (1998) 2007–2010.
- [27] B. Jochum, Geomagnetische Untersuchungen am Ostpazifischen Rücken unter Benutzung simulierter magnetischer Variationen, M.Sc. thesis, Inst. Meteorology and Geophysics, Univ. Vienna, Vienna, 1996, 70 pp.
- [28] S.C. Cande, D.V. Kent, Revised calibration of the geomagnetic polarity timescale for the Late Cretaceous and Cenozoic, *J. Geophys. Res.* 100 (1995) 6093–6095.
- [29] W. Krijgsman, F.J. Hilgen, I. Raffi, F.J. Sierro, D.S. Wilson, Chronology, causes and progression of the Messinian salinity crisis, *Nature* 400 (1999) 652–655.
- [30] F.J. Hilgen, W. Krijgsman, C.G. Langereis, L.J. Lourens, A. Santarelli, W.J. Zachariasse, Extending the astronomical (polarity) time scale into the Miocene, *Earth Planet. Sci. Lett.* 136 (1995) 495–510.
- [31] J.A. Grant, R. Schreiber, Modern swathe sounding and sub-bottom profiling technology for research applications: the Atlas Hydrosweep and Parasound systems, *Mar. Geophys. Res.* 12 (1990) 9–19.
- [32] D.W. Caress, D.N. Chayes, Improved processing of Hydrosweep DS multibeam data on the R/V Maurice Ewing, *Mar. Geophys. Res.* 18 (1996) 631–650.
- [33] P. Wessel, W.H.F. Smith, Free software helps map and display data, *EOS Trans. Am. Geophys. Un.* 72 (1991) 441, 445–446.
- [34] K.P. Jochum, D.B. Dingwell, A. Rocholl, B. Stoll, A.W. Hofmann, The preparation and preliminary characterisation of eight geological MPI-DING reference glasses for in-situ microanalysis, *Geostand. Newslett.* 24 (2000) 87–133.
- [35] D.S. Wilson, Kinematics of overlapping rift propagation with cyclic rift failure, *Earth Planet. Sci. Lett.* 96 (1990) 384–392.
- [36] J. Phipps Morgan, E.M. Parmentier, Causes and rate-limiting mechanisms of ridge propagation: a fracture mechanics model, *J. Geophys. Res.* 90 (1985) 8603–8612.
- [37] J. Lin, J. Phipps Morgan, The spreading rate dependence of three-dimensional mid-ocean ridge gravity structure, *Geophys. Res. Lett.* 19 (1992) 13–16.
- [38] J.A. Goff, J.R. Cochran, The Bauer scarp ridge jump: a complex tectonic sequence revealed in satellite altimetry, *Earth Planet. Sci. Lett.* 141 (1996) 21–33.
- [39] D.S. Wilson, R.N. Hey, C. Nishimura, Propagation as a mechanism of reorientation of the Juan de Fuca Ridge, *J. Geophys. Res.* 89 (1984) 9215–9225.
- [40] W. Bach, E. Hegner, J. Erzinger, M. Satir, Chemical and isotopic variations along the superfast spreading East Pacific Rise from 6°–30°S, *Contr. Min. Petr.* 116 (1994) 365–380.
- [41] H. Puchelt, R. Emmermann, Petrogenetic implications of tholeiitic basalt glasses from the East Pacific Rise and Galapagos spreading center, *Chem. Geol.* 38 (1983) 39–56.
- [42] A.L. Rubin, D.D. Pollard, Dike-induced faulting in rift zones of Iceland and Afar, *Geology* 16 (1988) 413–416.

**Quantitative assessment of chemical and  
mineralogical changes due to progressive low  
temperature alteration of East Pacific Rise basalts  
from 0-9 Ma**

Burkhard Schramm, Colin W. Devey, Kathryn M. Gillis and Klas Lackschewitz



*Submitted to Chemical Geology, 19 May 2003*

## **Quantitative assessment of chemical and mineralogical changes due to progressive low temperature alteration of East Pacific Rise basalts from 0-9 Ma**

Burkhard Schramm<sup>1\*</sup>, Colin W. Devey<sup>1</sup>, Kathryn M. Gillis<sup>2</sup>, Klas Lackschewitz<sup>1</sup>

<sup>1</sup> *Fachbereich Geowissenschaften, Universität Bremen, Klagenfurter Str., 28359 Bremen, Germany*

<sup>2</sup> *School of Earth and Ocean Sciences, University of Victoria, Victoria, B.C., Canada*

\* *Corresponding author. Fax: +49-421-218 9460; E-mail: bschramm@uni-bremen.de*

*Submitted to Chemical Geology, 19 May 2003*

### **Abstract**

Little is known about the influence of low temperature alteration on the mineralogical and chemical composition of the oceanic crust once it leaves the spreading axis, although such information is of fundamental importance not only for crust-ocean mass balances but also to characterize an important input to the subduction factory. We have studied dredged basalts from the eastern flank of the East Pacific Rise at 14°15'S, concentrating on the products of a single spreading segment in a corridor perpendicular to the spreading axis and covering a range of crustal ages from 0 to 9 Ma. Electron microprobe, X-ray fluorescence, X-ray diffraction and ICP-MS analyses have been carried out to examine the mineralogical and chemical changes on the surface of the upper crust caused by low temperature alteration.

Fresh rocks were sampled at the ridge axis; off-axis basalts contain features of seawater-generated alteration. Celadonite is the main alteration component in 0.12-4.6 Ma old rocks, whereas phillipsite is more abundant in rocks older than 4.6 Ma. Secondary minerals, sealing of fractures and the occurrence of more intense alteration rinds on older rocks show evidence for a slight change in redox conditions, from oxidizing, water-dominated to more reducing, rock-dominated environment with time. Iron-oxyhydroxide and celadonite are the first alteration products, partly replaced or dissolved by saponite under more reducing conditions. The Fe necessary for the formation of these minerals is furnished by the dissolution of glass and the breakdown of olivine. Phillipsite is present in fractures and veins in rocks older than 1 Ma. Analyses also indicate an illite-smectite mixed layer which is believed to be an intermediate between saponite and celadonite and small amounts of a chlorite/smectite

mixed layer. All samples are characterized by the lack of minerals formed by hydrothermal processes. We conclude that the alteration took place under seawater dominated conditions at low temperature.

A comparison of trace element analyses from altered whole rock samples and their appendant fresh glass chips provides a record of element movement during alteration. Off-axis basalts show significant uptakes of Rb, Cs and Ba which are supplied by seawater and incorporated in or on secondary minerals. An enrichment of U is also apparent and appears to be especially strong when alteration conditions are oxidative.  $K_2O$  is also gained in all altered off-axis basalts, believed to be the result of the formation of celadonite. However, the volume of rock being altered is so small relative to the volume of the oceans that this scavenging has no noticeable effect on the composition of the oceans. The composition of the oceanic crust, on the other hand, is affected significantly.

*Keywords:* Low temperature alteration, East Pacific Rise, secondary minerals, mineral chemistry, clay minerals, phillipsite

## **1. Introduction**

Seawater circulation in oceanic crust plays an important role in the interaction between hydrosphere and lithosphere. Passive fluid circulation is driven by the cooling of the lithosphere as the crust moves off-axis. The global geochemical budget is affected by this convection, as both ocean and crustal compositions are buffered by fluid rock interaction. The effects of off-axis heat transfer are important because most of the heat (~70 %) is lost in the ocean basins rather than on-axis (Stein and Stein, 1994; Mottl, 2003) and as a consequence most of the fluid flux and geochemical exchange occurs off-axis (Mottl and Wheat, 1994; Alt et al., 1996b; Mottl and Wheat, 2000). The crust is also one of the major inputs to subduction zones, its composition following off-axis alteration is therefore relevant for the evolution of mantle, crust and biosphere. Hence this is a critical environment to study.

Alteration takes place as the crust ages, as documented by weathering of primary minerals, glass and the groundmass, and the precipitation of secondary minerals. Alteration processes are affected by changing fluid-rock ratios and redox conditions. During this low-temperature metamorphism of the volcanic section, most major elements (Si, Al, Mg, Ca and Na) and many trace elements (Sr, Ba) experience substantial large scale redistribution (Staudigel et al., 1981; Staudigel et al., 1996). The crust also takes up large amounts of water and  $CO_2$ , a large fraction of which resides in veins and disseminated alteration minerals, much within the zone of oxidative alteration in the upper part of the oceanic basement. The nature of water circulation will evolve with

time as the crust is buried by sediments and fractures are sealed with secondary minerals. The cementation of fractures will act to increase density and decrease porosity and permeability (Wilkens et al., 1991). Seismic data illustrate that porosity decreases (by a factor of 0.5) within <10 Ma, presumably due to the infilling of porosity by secondary minerals (Grevemeyer and Weigel, 1996; Carlson, 1998; Grevemeyer et al., 1999). The convective heat loss from ocean crust ceases on average at about 65 Ma (Stein and Stein, 1994).

Although the intensity of crustal alteration varies from place to place and no specific alteration state can be related to a specific crustal age, rocks from on or near the ridge axis are generally fresh, whereas off-axis rocks contain features of more intense alteration. The first systematic study to address how the crustal alteration varies with age focused on a 57 Ma transect of dredged samples from the Mid-Atlantic (Ludden and Thompson, 1978). Results from this and other (e.g. Hart, 1973; Hékinian, 1973; Thompson, 1973) studies show that the upper crust is progressively oxidized and hydrated with age, and that mobile elements such as K, Rb, Cs, Li, B, light rare earth elements (LREE), and  $^{18}\text{O}$  are progressively taken up by low-temperature alteration, starting within the first 5 Ma (Ludden and Thompson, 1978; Thompson, 1983). Other investigators have attempted to quantify how alteration varies with age by comparing samples from geographically unrelated DSDP/ODP sites. These studies document how alteration proceeds through progressive alteration stages, from oxidizing to reducing conditions and from seawater- to hydrothermal fluid-dominated alteration and provide quantitative constraints for geochemical fluxes (e.g. Alt et al., 1992; Alt et al., 1996a; Staudigel et al., 1996; Teagle et al., 1998; Laverne et al., 2001; Bach et al., 2003). However, we have to consider that alteration is also strongly influenced by local parameters such as rate and nature of sedimentation and basement topography, therefore we cannot use these data explicitly to examine how age influences alteration processes and to calculate meaningful, global-scale geochemical fluxes.

The flank flux experiment during ODP Leg 168 off the Juan de Fuca Ridge provides information about ten sites, drilled along a 120 km (up to ~3.5 Ma) linear transect perpendicular to the spreading axis, where the glacial turbiditic sediment thickness increases from 40 (~1.4 Ma) to ~600 m. Heat flow data show that all lithospheric heat is conserved at about 40 km (~1.4 Ma) from the ridge axis and sediment-basement interface temperatures increase from 16-64 °C along the transect. The degree of alteration in the basalts varies from <1 to 16 % or even 100 % in the breccias (Hunter et al., 1998). Across the flank the observed ranges in secondary mineral composition are directly related to changes in the geochemical and textural characteristics of the basement, as well as to interaction between fluids and phases from increasing stages of alteration. The secondary mineral assemblage formed from chlorite and chlorite/smectite in the earliest stages of alteration to iron oxyhydroxides and celadonite; saponite  $\pm$  pyrite; ending with the formation of carbonate  $\pm$  zeolites  $\pm$  quartz (Hunter et al.,

1999). The systematic shifts in alteration are related to changes from oxidizing to reducing conditions and to strongly modified seawater derived fluid (Elderfield et al., 1999; Hunter et al., 1999; Buatier et al., 2001). Although the results of these studies are very important, they do not represent the norm for ocean crust, which is buried by pelagic sediments at much slower rates.

The EXCO (**EX**change processes between **C**rust and **O**cean) investigations are an integrated series of field programs similar to those conducted at the Juan de Fuca Ridge but in a more typical setting. The area (Fig.1) was first studied in 1995 during Sonne cruise SO105 (Weigel et al., 1996). This initial cruise consisted of seismic, topographic, magnetic, and heat flow studies of a strip of seafloor extending from the spreading axis out to 8 Ma old crust (Grevemeyer et al., 1999). The EXCO II cruises (SO145 Legs 1 & 2, Spring 2000) were designed to build on this earlier work and explore in more detail the variations in heat flow (Leg 1) and to sample the Layer 2 rocks (Leg 2) in an effort to establish the chemical changes which are occurring in this ageing crust. The focus of this paper is the low temperature alteration of lavas recovered by dredging at topographic highs. While dredging is not the ideal sampling tool, it is our best opportunity to obtain an age transect in fast-spreading crust in the foreseeable future. Additionally, the geochemical and mineralogical trends documented for long cores into altered basement show that the style of alteration persists from the top of the cores to tens to hundreds of meters depth into the hole depending on the specific history of the drill sites. Therefore, dredged samples provide a reasonably representative view of the altered parts of the upper crust.

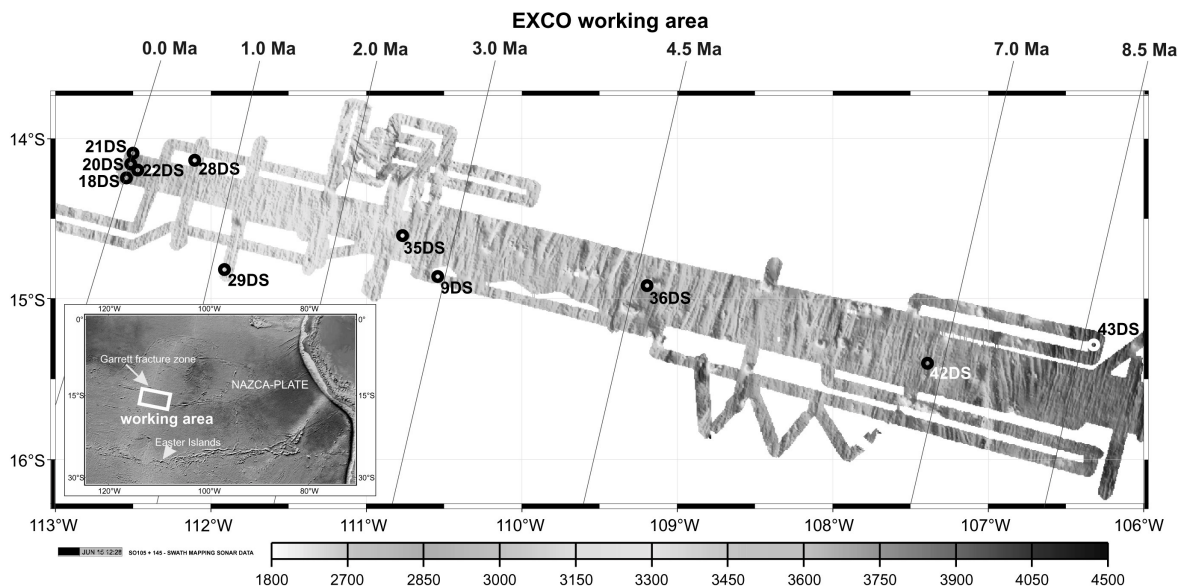


Figure 1. The EXCO working area east of the East Pacific rise, south of the Garrett transform fault. The map shows the sample positions of dredges (DS). Diagonal lines indicate the age of the ocean crust based on magnetic anomalies. The ages of the samples are derived by linear interpolation between the age of magnetic reversals (Grevemeyer et al., 2002). Samples 18DS, 20DS, and 21DS are from the ridge axis. Small image taken from Ridge Multibeam Synthesis (<http://ocean-ridge.ldeo.columbia.edu/>).

## **2. EXCO field area**

The Southern East Pacific Rise (SEPR) between the Easter Microplate near 23°S and the Garrett transform fault boundary near 13°30'S is spreading at ultrafast rates, ranging from 143mm/yr to 150mm/yr (DeMets et al., 1994; Cormier et al., 1996). The EXCO field area is located between 14-16°S (Fig.1), where on a larger scale the SEPR is remarkably linear and devoid of any transform fault boundaries (Lonsdale, 1989). The EXCO geophysical and rock sampling programs followed a flow line east of the EPR within a single first-order spreading segment (720 km long and 20-45km wide corridor, 0-9 Ma) (age of the samples are derived by linear interpolation between the age of magnetic reversals, Grevemeyer et al., 2002). Migration events of at least five overlapping spreading centers (OSC) left discordant zones consisting of hummocky basins and motley texture of curved lineations (Grevemeyer et al., 2002). Heat flow data show low values close to the ridge, associated with vigorous hydrothermal circulation of cold seawater through the upper volcanic crust, and a fast recovery to lithospheric conductive cooling values at a crustal age of 9.3 Ma. Heat flow is high in areas with an almost flat and sedimented basement, and low within ~10-20 km of seamounts or rough basement relief (Villinger et al., 2002). Seismic data show a large increase in velocity in Layer 2 away from the ridge axis (~2.2 – 4.9 km/s, Grevemeyer and Weigel, 1997). Sediment thickness increases only slowly with distance from the spreading axis to about 15m on 4.5 Ma old crust and 30 m on 7 Ma old crust (Hauschild et al., 2003).

### ***Sampling***

Rock samples were recovered by dredging at 11 sites at topographic highs (~100 – 200 m above the surrounding sedimented seafloor) which are believed to be discharge areas for circulating fluids (Devey et al., 2000). Three dredges were located at the present-day ridge axis; the remaining dredges were collected along a flow-line east of the ridge. Extrapolation of each dredge site from its present location back to the ridge yields eruption latitudes between 13°54 S and 14°38 S. Due to the relative inexact method of dredging we cannot be sure if dredge 36DS (targeted on a seamount) recovered material from the oceanic crust or seamount.

## **3. Analytical Methods**

This study is based on investigations carried out on 42 basalt samples from 11 locations spanning an age of 0 to 8.64 Ma. Representative samples from each dredge were prepared for examination of their mineralogical and geochemical alteration history.

Whole rock samples excluding vein material were crushed in a steel mortar and pulverized with an agate mortar. Major element compositions were determined by X-ray fluorescence (XRF) using a Philips PW 1400 spectrometer at the University of Kiel. Powders were dried at 900°C and melted using lithiumtetraborate ( $\text{Li}_2\text{B}_4\text{O}_7$ ) in a mixture consisting of 600 mg sample and 3600 mg lithiumtetraborate. For calibration of the XRF determinations, 44 international rock standards were used. Loss on ignition was not determined. The accuracy of the analytical results was controlled by measuring the international standard reference material BHVO-1 (Appendix 3). Trace elements were analyzed by inductively coupled plasma-mass spectrometry (ICP-MS) using a VG Plasma-Quad PQ1 (University of Kiel, Germany). Total dissolution was performed by pressurized  $\text{HF-HClO}_4$ -aqua regia attack (Garbe-Schönberg, 1993). The accuracy of the analytical results was assessed by measuring the international standard reference material BHVO-1, BHVO-2 and BIR-1. Precision was estimated from repeat sample and standard measurements (Appendix 1). The relative standard deviation of repeat measurements of sample 21DS1 and BHVO-2 is below 7% and for different dissolutions of the same standards below 12% for most elements. Only for Li and Ta, are the deviations in accuracy higher (-24% and -23%). Most of the element concentrations measured in BHVO-2 lie 6-11% below the accepted values (Wilson, 1997). For BHVO-1 standard measurements, the accuracy deviation of Ga, Cs, Pb and Th is higher than for other elements. Zr and Dy show higher accuracy deviation in BIR-1 measurements (Govindaraju, 1994). The results of blank measurements show significant blank values for Zn, Zr and Pb presumably indicating contamination problems in the dissolution procedure.

Fresh glass chips were carefully separated and washed in an ultrasonic bath to provide material for the determination of pristine magmatic compositions. The glass chips appear unaltered both in thin section and at high magnification (1.200x) under the electron microprobe. Major element analyses were determined by electron microprobe. Analytical conditions were 15kV accelerating voltage and 11-13 nA sample current. Representative errors are given in Appendix 2 together with the number of individual spots measured and used to calculate the mean values. The electron beam was slightly defocused (10  $\mu\text{m}$  diameter) to avoid the volatilization of alkalis. The raw major element data from each measured spot have been corrected to the KL2-G MPI-DING reference glass (Jochum et al., 2000). The analyses also yield totals of ~100%, implying that little or no extraneous water has been incorporated due to incipient alteration.

Secondary mineral compositions were also determined by electron microprobe. Five-spectrometer JEOL JXA 8900 RL electron microprobes (University of Göttingen and Mainz, Germany) were utilized to analyze clay minerals and zeolites. For zeolite analyses, an accelerating voltage of 15 kV, a beam current of 12 nA, and a 2

$\mu\text{m}$  beam diameter were used. Clay minerals were analyzed with a 5  $\mu\text{m}$  beam diameter. Element counting times vary between 10/5 s and 30/15 s (peak/background). Calibration was performed using mineral standards.

Attempts were made to determine the secondary mineralogy using a Philips X-ray diffractometer PW 1710 with monochromatic Cu-K $\alpha$  radiation. Oriented samples were produced by vacuum filtration through a 0.15  $\mu\text{m}$  filter. Due to the relative rarity of clay minerals, measurements ( $2^\circ$ - $75^\circ 2\theta$ ) were carried out on air-dried whole rock samples from altered zones of the rock (oxidation haloes). Glycol-saturated samples were also measured ( $2^\circ$ - $35^\circ 2\theta$ ) in an attempt to identify the smectitic clay minerals.

#### 4. Results

An overview of all identified minerals and the main alteration features is given in Table 1a, 1b and Fig.2. Representative chemical analyses with mean elemental compositions of clay minerals are listed in Table 2.

dredge	21DS	18DS	20DS	22DS	28DS	29DS	35DS	9DS	36DS	42DS	43DS
Ma	0	0,015	0,015	0,12	0,65	1,16	2,56	2,92	4,6	6,84	8,64
total alteration	0.5%	0.3%	0.3%	2.5%	2.6%	2.4%	3.2%	4.2%	4.8%	6.1%	5.3%
phillipsite						--	--	--	+	++	++
celadonite				++	+	++	++	++	+	-	+
saponite-celadonite				-				-	-		--
saponite				--				-	--	--	--
nontronite				--				--	--	--	--
chlorite/smectite				--	--			--	--	--	--
Fe-oxyhydroxide	+	-	+	-	--	+	-	--	--	--	-

**Table 1a. Abundance** of secondary mineralogical assemblages determined by electron microprobe X-ray diffraction and thin section observations. Total alteration (average) determined by petrographic observation of all samples in each dredge (++ high, -- low).

secondary mineral	main location	filling	replacing	main association
Fe-oxyhydroxide	oxidation halo	voids, pervasive	-	celadonite
celadonite	oxidation halo	voids, veins	Fe-oxyhydroxide, olivine	Fe-oxyhydroxide
saponite-celadonite	oxidation halo	voids	celadonite	celadonite
saponite	oxidation halo	voids	celadonite, saponite-celadonite	celadonite
phillipsite	oxidation halo, glassy margin	voids, veins	palagonite	celadonite

**Table 1b.** Summary of the alteration phases identified by electron microprobe, illustrating variations in occurrence, distribution and mineralogical assemblages.

ridge axis	0.12 - 4.6 Ma	6.84 - 8.64 Ma
	<i>alteration</i>	
0 %	2 - 5 %	> 5 %
iron oxyhydroxide	<i>main alteration component</i> celadonite	phillipsite
	<i>oxidation state</i>	
more oxidizing		less oxidizing

Figure 2. Overview of the main alteration features as a function of distance from the spreading axis.

Dredge Ma	22DS1 0.12	22DS2 0.12	22DS3 0.12	28DS1 0.65	29DS2 1.16	29DS3 1.16	35DS4 2.56	9DS4 2.92	9DS8 2.92	36DS7 4.6	43DS13 8.64	22DS2 0.12	9DS8 2.92	36DS8 4.6	9DS8 2.92	9DS8 2.92	36DS8 4.6
mineral	celadonite	celadonite	celadonite	celadonite	celadonite	saponite- celadonite	saponite- celadonite	saponite- celadonite	saponite	saponite	saponite						
SiO <sub>2</sub>	46.5	46.9	49.3	45.8	44.9	44.8	46.8	47.2	49.2	44.0	44.7	42.7	49.6	42.4	46.9	46.1	37.4
TiO <sub>2</sub>	0.05	0.02	0.05	0.05	0.05	0.04	0.11	0.10	0.02	0.08	0.02	0.06	0.04	0.83	0.03	0.05	0.56
Al <sub>2</sub> O <sub>3</sub>	1.7	0.11	1.6	1.6	3.2	4.2	3.3	4.6	1.5	3.9	2.4	3.5	2.1	6.9	3.0	3.2	3.1
FeO	32.0	31.4	29.8	31.9	35.0	33.4	28.4	29.9	28.8	30.2	37.3	21.9	25.1	16.6	23.4	14.5	17.3
MnO	0.04	0.03	0.21	0.05	0.15	0.08	0.17	0.03	0.06	0.08	0.22	0.08	0.05	0.12	0.06	0.02	0.16
MgO	3.2	3.4	3.4	3.7	1.3	1.6	4.0	1.8	4.7	2.9	1.7	11.1	9.4	13.8	13.8	17.1	27.5
CaO	0.18	0.21	0.08	0.28	0.24	0.13	0.14	0.15	0.13	0.25	0.30	0.08	0.25	0.36	0.23	0.13	0.34
Na <sub>2</sub> O	1.4	1.5	0.9	1.8	1.5	1.3	1.2	1.1	0.9	1.9	1.7	0.8	1.4	1.5	1.6	0.9	0.7
K <sub>2</sub> O	5.0	4.7	2.5	4.1	3.4	3.7	5.6	4.3	5.8	4.6	2.7	1.9	2.2	2.1	1.4	0.7	1.0
P <sub>2</sub> O <sub>5</sub>	n.d.	0.03	n.d.	0.06	0.06	0.13	0.05	n.d.	0.03	0.08	0.11	0.01	0.02	0.04	0.00	0.02	0.07
Cr <sub>2</sub> O <sub>3</sub>	n.d.	0.02	n.d.	0.05	0.03	0.03	0.08	0.00	0.03	0.04	0.03	0.08	0.01	0.10	0.02	0.05	0.11
total	90.1	88.4	87.9	89.4	89.9	89.4	89.9	89.2	91.1	88.0	91.1	82.3	90.2	84.8	90.6	82.8	88.1
Number of ions on the basis of 20 (O) and 4 (OH)																	
Si	7.726	7.925	8.077	7.657	7.525	7.477	7.652	7.721	7.899	7.451	7.472	7.290	7.733	6.844	7.255	7.397	5.942
Al	0.338	0.022	0.307	0.315	0.639	0.811	0.639	0.876	0.285	0.785	0.460	0.710	0.383	1.312	0.554	0.603	0.575
tetrahedral	8.000	7.947	8.000	7.973	8.000	8.000	8.000	8.000	8.000	8.000	7.931	8.000	8.000	8.000	7.809	8.000	6.516
Al	0.064	0.000	0.307	0.000	0.164	0.288	0.290	0.597	0.184	0.236	0.000	0.000	0.115	0.156	0.000	0.000	0.000
Ti	0.007	0.002	0.006	0.006	0.006	0.006	0.013	0.012	0.003	0.009	0.003	0.007	0.004	0.100	0.004	0.006	0.067
Fe	4.440	4.431	4.089	4.459	4.948	4.731	3.892	4.110	3.874	4.277	5.248	3.130	3.274	2.251	3.030	1.946	2.293
Mn	0.006	0.005	0.028	0.007	0.021	0.012	0.024	0.004	0.008	0.012	0.032	0.012	0.006	0.017	0.007	0.003	0.021
Mg	0.799	0.866	0.836	0.922	0.326	0.388	0.970	0.448	1.118	0.726	0.420	2.826	2.184	3.325	3.191	4.084	6.503
P		0.004		0.008	0.008	0.019	0.007		0.004	0.012	0.016	0.001	0.002	0.006	0.000	0.002	0.009
Cr		0.003		0.006	0.004	0.004	0.010	0.000	0.004	0.005	0.004	0.011	0.001	0.012	0.002	0.006	0.013
octahedral	5.316	5.312	5.266	5.408	5.478	5.447	5.205	5.172	5.195	5.277	5.722	5.988	5.587	5.867	6.234	6.048	8.907
Ca	0.033	0.038	0.013	0.050	0.043	0.024	0.025	0.026	0.022	0.045	0.053	0.014	0.042	0.062	0.039	0.022	0.058
Na	0.437	0.498	0.288	0.587	0.493	0.430	0.375	0.358	0.279	0.617	0.557	0.262	0.434	0.472	0.490	0.295	0.206
K	1.062	1.016	0.524	0.878	0.734	0.793	1.167	0.905	1.181	0.992	0.571	0.414	0.446	0.439	0.273	0.141	0.198
interlayer	1.532	1.553	0.826	1.515	1.270	1.247	1.566	1.289	1.482	1.654	1.182	0.690	0.922	0.973	0.802	0.458	0.462
standard deviation																	
n	13	46	62	10	43	58	31	35	170	9	31	1	2	5	2	3	1
SiO <sub>2</sub>	1.13	0.85	1.91	1.44	3.57	4.35	2.26	2.57	1.39	1.98	3.48		0.72	2.82	0.19	0.34	
TiO <sub>2</sub>	0.03	0.02	0.03	0.03	0.05	0.05	0.05	0.07	0.03	0.05	0.03		0.01	0.22	0.00	0.04	
Al <sub>2</sub> O <sub>3</sub>	0.53	0.19	0.50	0.33	1.28	1.98	0.76	1.83	1.03	0.63	1.24		0.46	1.34	0.17	0.12	
FeO	1.08	1.61	1.09	3.58	4.21	5.68	1.83	3.14	1.76	1.96	3.76		1.17	0.63	2.02	0.40	
MnO	0.03	0.03	0.05	0.03	0.32	0.05	0.17	0.02	0.09	0.07	0.16		0.06	0.03	0.01	0.02	
MgO	0.22	0.36	0.37	0.51	0.68	0.34	0.66	0.29	0.54	0.25	0.31		1.70	2.58	1.54	0.51	
CaO	0.05	0.10	0.04	0.09	0.06	0.07	0.06	0.05	0.05	0.07	0.04		0.07	0.11	0.03	0.02	
Na <sub>2</sub> O	0.38	0.39	0.18	0.49	0.18	0.25	0.34	0.20	0.32	0.42	0.23		0.02	0.29	0.11	0.05	
K <sub>2</sub> O	0.85	0.59	0.34	0.27	0.50	0.67	0.87	0.95	0.87	1.11	0.57		0.47	0.30	0.57	0.07	
P <sub>2</sub> O <sub>5</sub>		0.03		0.03	0.04	0.07	0.04		0.03	0.03	0.05		0.01	0.03	0.00	0.02	
Cr <sub>2</sub> O <sub>3</sub>		0.03		0.03	0.03	0.03	0.05	0.01	0.03	0.02	0.02		0.01	0.03	0.02	0.03	

**Table 2.** Average major element compositions and calculated formulae for celadonite and saponite from EXCO rocks (wt%), n = number of analyses. Standard deviation is given in wt%. The formula for celadonite and saponite has been calculated on the basis of the ideal O<sub>20</sub>(OH)<sub>4</sub> anion content. Tetrahedral sites (Si+Al) are calculated on the basis of 8 cations, the excess Al is added to the octahedral site. Due to the very small size of individual occurrences, the ferric iron content was not determined. It is however well known that celadonites, in contrast to saponites, are characterized by high contents of ferric iron, although small amounts of trivalent Fe in saponite may also be present (Andrews, 1980).

#### ***4.1. Petrology of the sample suite***

All recovered rocks are part of pillows, lava or sheet flows. Most of the younger rocks are characterized by the presence of glassy margins, whereas older rocks (> 4 Ma) exhibit minor glass with larger amounts of palagonite, a more strongly developed Mn-crust and alteration haloes, and increasing amounts of secondary minerals. All basalts are vesicular (up to 3 % vesicles, mostly concentrated near the margin) and plagioclase-phyric (1-5 %) with minor olivine (1-2 %) and pyroxene (<1 %). A few samples contain spinel (<1%) and magnetite (<1%).

EXCO basalts show a general trend of increasing pervasive alteration with distance from the ridge axis and crustal age. Alteration is most prevalent within alteration haloes (mostly dark grey or brownish) that occur at the outer rims of the samples or are associated with fractures (Fig.3.1a). Rock interiors are generally characterized by low abundances of secondary minerals (<1 %), giving this part of the rock a lighter grey color (Fig.3.1a). Fractures and vesicles in the interior remain open and are lined with celadonite or small amounts of iron oxyhydroxides. In some cases a transition zone separates the glassy rim and the oxidation halo. This black transition zone consists of variolites, giving the rock an aphanatic texture (Fig.3.1b). Determination of the degree of alteration, described below, is based on petrographic observations (abundance of alteration haloes, palagonite and other secondary minerals) from all rocks of each dredge.

##### Ridge axis - 21DS, 18DS, 20DS

Samples from the ridge axis are pillow fragments, lava flows and lava tubes, all are very fresh with glassy margins and show only minor indications of alteration (trace amounts of palagonite). Samples contain only small numbers of fractures which are either open or lined with iron oxyhydroxide. Voids and cavities also remain open or are in rare cases lined with iron oxyhydroxide.

##### 0.12 Ma – 22DS

Rocks from this dredge are somewhat different to all the other dredges. Basalts are fully crystalline, contain alteration haloes, a thin manganese crust and only small amounts of glass. The general degree of alteration is about 2.5 %. Trace palagonisation occurs only at the outer glassy margin. Fractures and voids are very rare and remain open or lined with trace amounts of iron oxyhydroxide or celadonite. Iron oxyhydroxide and celadonite, with trace saponite, nontronite and a mixed layered chlorite/smectite, are distributed throughout the groundmass, altering small amounts of the present primary minerals (~2 %, probably olivine), with higher abundances within

alteration haloes (~5 %). An illite/smectite mixed-layer phase was also identified, indicating the occurrence of saponite-celadonite.

#### 0.65 Ma – 28DS

Pillows and fragments of lava flows have up to 5 mm thick glass rind (only minor amounts are altered to palagonite) and are coated with a thin (1mm) manganese crust. Fractures and cavities are rare and lined with celadonite in the interior of the rocks or remain open towards the rim. Celadonite occurs only in the interior of the sample throughout the groundmass, beneath the oxidation halo. Also, trace amounts of a chlorite/smectite mixed layer are identified in the oxidation halo.

#### 1.16 and 2.56 Ma – 29DS and 35DS

Basalts from 29DS contain N- and E-MORB and therefore show variations in their magmatic composition (Table 3). Samples are aphyric with glassy margins (1-4 mm) and 1-10 mm thick manganese crust. The general degree of alteration is about 2-3 %. Fractures and cavities in the glassy margins remain open. Within oxidation haloes, veins are filled with celadonite, iron oxyhydroxide and trace amounts (identified by XRD) of phillipsite, none of which are found in the interior of the rock. Phillipsite is very fine-grained, implying that these samples are just beginning to form zeolites. Celadonite occurs predominantly in alteration haloes, which occur adjacent to fractures and veins, giving this part of the rock a darker color (Fig.3.1a). Glass is partly altered to palagonite along fractures or at the outer rim of the glassy margins.

#### 2.92 Ma – 9DS

Most of the basalts are aphyric with a thin (<2 mm) glass crust partly altered to palagonite beneath the margin and at the rim of fractures. Degree of alteration is about 4 %. Veins and voids within oxidation haloes are filled with celadonite, whereas adjacent to the haloes they are only lined with trace amounts of celadonite and saponite in the interior of the rocks. In some vesicles, celadonite is replaced along the outer rim by saponite (Fig.3.2). In other cases it replaces olivine, beginning at intramineral fissures and progressing to complete replacement of olivine where only the pseudomorph gives a clue to the nature of the primary mineral (Fig.3.3). All samples are characterized by the very small amount or lack of iron oxyhydroxides.

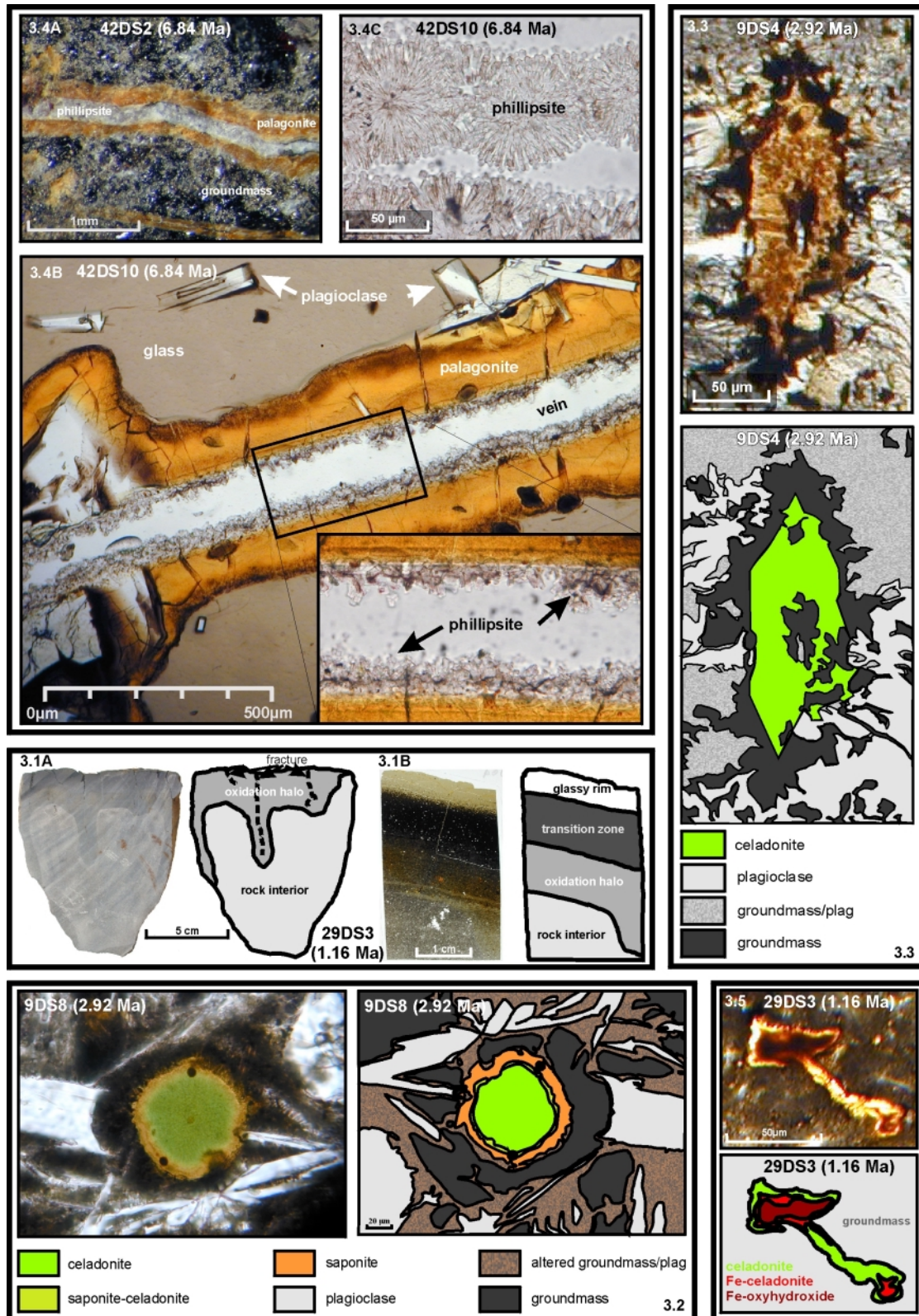


Figure 3. Photomicrographs of EXCO samples. **3.1.** Oxidation halo in sample 29DS3 (1.16 Ma). 3.1A. Rock sample with an oxidation halo connected to small fractures. 3.1B. Thin section containing glass at the outer rim, a transition zone (black halo), an oxidation halo and a part of the rock interior. The occurrence of clay minerals is limited to the oxidation halo; fractures, veins and voids in the outer part and the rock interior remain open. The thin section is taken from a different part of the sample shown in A. **3.2.** Photograph of celadonite and saponite in a vesicle. The vesicle is filled by celadonite and later replaced at the outer rim by saponite, indicating a redox change towards more reducing conditions. The yellow-green transition zone is characterized by a mixture of saponite and celadonite. More reducing conditions would have caused the celadonite to be totally replaced by saponite. **3.3.** Photograph of a completely replaced primary mineral (olivine ?) by celadonite. **3.4.** Photographs of phillipsites in 6.84 Ma rocks. 3.4A. Photograph (from sample 42DS2) of phillipsite completely filling a vein lined by palagonite. 3.4B. Photomicrograph (from sample 42DS10) of an altered part of the glassy rim. Formation of phillipsite at the inner wall of a vein, bounded by palagonite. 3.4C. Close up photomicrograph of vein-filling, fibrous phillipsite in 42DS10. **3.5.** Iron oxyhydroxide associated with celadonite in a cavity, maybe replacing olivine. Iron oxyhydroxide occur at the center, whereas celadonite lines the outer rim. The red transition zone is characterized by celadonite with a high Fe content.

Sample	0		0.015		0.015		0.12		0.65		0.65		1.16		1.16	
	21DS4 bulk	21DS4 glass	18DS9 bulk	18DS9 glass	20DS3 bulk	20DS3 glass	22DS2 bulk	22DS2 glass	28DS1 bulk	28DS1 glass	28DS3 bulk	28DS3 glass	29DS2 bulk	29DS2 glass	29DS3 bulk	29DS3 glass
alt %	0.3	0.0	0.0	0.0	0.5	0.0	3.0	0.0	2.7	0.0	2.5	0.0	2.7	0.0	2.0	0.0
SiO <sub>2</sub>	49.9	50.5	50.1	51.0	49.1	49.9	49.2	49.8	47.3	48.9	47.8	49.0	52.2	53.8	48.4	50.5
TiO <sub>2</sub>	1.7	1.8	1.7	1.9	1.5	1.7	1.9	1.7	0.76	0.92	0.77	0.92	1.8	1.9	2.1	2.3
Al <sub>2</sub> O <sub>3</sub>	14.4	14.2	13.8	13.9	14.8	14.7	13.1	14.0	15.7	16.7	15.6	16.6	12.9	13.2	13.3	13.8
Fe <sub>2</sub> O <sub>3</sub>	11.4	12.3	12.2	12.6	10.8	11.4	13.6	12.2	10.5	10.7	10.6	10.6	13.8	13.4	14.4	13.3
MnO	0.18	0.21	0.19	0.21	0.17	0.18	0.19	0.19	0.16	0.18	0.17	0.17	0.32	0.22	0.22	0.21
MgO	7.3	7.4	7.1	7.3	7.5	7.6	6.6	7.3	11.6	10.1	11.7	10.2	4.7	4.8	6.4	6.6
CaO	11.8	11.3	11.4	11.3	11.9	11.8	10.9	11.1	11.1	11.6	11.0	11.5	8.7	8.7	10.8	11.0
Na <sub>2</sub> O	2.7	3.1	2.8	2.9	2.8	2.8	2.7	2.7	2.1	2.2	2.0	2.2	3.4	3.7	2.7	3.1
K <sub>2</sub> O	0.15	0.13	0.13	0.11	0.18	0.19	0.27	0.12	0.10	0.07	0.08	0.08	0.40	0.35	0.32	0.19
P <sub>2</sub> O <sub>5</sub>	0.15	0.16	0.15	0.15	0.15	0.15	0.16	n.d.	0.08	0.06	0.08	0.06	0.35	0.38	0.21	0.21
Cr <sub>2</sub> O <sub>3</sub>	n.d.	0.03	n.d.	0.02	n.d.	0.05	n.d.	0.04	n.d.	0.06	n.d.	0.07	n.d.	0.02	n.d.	0.02
total	99.6	101.1	99.5	101.4	99.0	100.5	98.6	99.2	99.4	101.6	99.7	101.4	98.6	100.4	98.8	101.2
Li	4.6	5.2	4.3	5.7	4.8	5.8	5.3	5.5	2.8	3.5	3.3	3.0	6.8	15.8	6.5	6.2
Sc	42.7	42.4	42.3	42.6	41.5	41.7	42.9	39.2	35.0	38.3	37.8	36.8	33.0	32.1	41.5	40.5
V	330	315	343	344	309	301	365	340	179	183	190	186	234	219	377	372
Cr	273	246	161	160	277	261	174	193	490	458	474	459	104	91	103	112
Co	38.6	37.3	38.7	39.0	39.2	39.7	38.5	38.0	47.8	56.8	51.7	48.9	28.6	29.6	37.4	37.1
Ni	63.5	60.5	55.3	52.2	69.1	78.5	59.2	70.0	258	339	228	229	32.1	33.0	46.1	46.2
Cu	63.9	59.7	61.0	58.3	67.2	73.0	42.0	56.8	67.9	85.0	82.1	84.1	37.6	41.1	53.0	52.8
Zn	110	73.1	90.1	80.9	791	91.1	88.0	86.3	59.1	65.1	57.1	60.6	122	101	85.9	91.9
Ga	18.3	17.7	17.7	17.9	17.4	16.9	17.5	17.4	13.3	12.7	14.5	14.4	22.9	20.5	17.6	18.8
Rb	1.49	1.18	1.12	1.25	2.3	2.5	5.1	1.19	0.96	1.06	1.05	0.98	11.4	4.1	2.5	2.2
Sr	128	124	110	111	141	150	104	92.5	118	125	127	125	119	100	125	121
Y	32.5	34.8	32.0	32.7	28.5	31.2	35.3	33.9	15.3	17.0	16.4	16.5	92.2	88.7	40.6	39.2
Zr	111	130	97.3	102	94.3	104	111	103	33.5	38.2	36.5	37.1	362	363	136	141
Nb	2.8	2.7	2.7	2.7	4.2	4.6	2.8	2.7	1.91	2.0	2.1	2.0	7.5	7.5	4.8	4.9
Cs	0.02	0.02	0.02	0.02	0.03	0.03	0.33	0.02	0.01	0.04	0.03	0.02	0.62	0.06	0.04	0.03
Ba	12.5	11.4	11.0	11.5	78.0	23.8	11.9	11.0	10.0	9.8	77.9	9.8	35.7	27.4	30.0	20.8
La	3.7	3.6	3.3	3.4	4.1	4.6	3.6	3.3	1.71	1.87	1.84	1.81	11.3	11.7	5.6	5.4
Ce	11.3	11.2	10.2	10.4	11.4	13.2	10.8	10.2	4.7	5.5	5.2	5.1	34.5	36.6	16.4	15.5
Pr	1.99	1.97	1.79	1.85	1.90	2.2	1.93	1.82	0.82	0.92	0.88	0.88	5.9	6.2	2.7	2.6
Nd	10.7	10.6	9.8	10.0	9.8	11.2	10.7	10.0	4.4	5.1	4.8	4.8	30.7	32.2	14.2	13.6
Sm	3.7	3.7	3.5	3.5	3.3	3.8	3.8	3.7	1.62	1.85	1.75	1.76	10.0	10.6	4.9	4.6
Eu	1.32	1.31	1.23	1.27	1.18	1.34	1.32	1.26	0.67	0.77	0.72	0.73	2.6	2.8	1.65	1.56
Gd	4.8	4.9	4.6	4.7	4.3	4.9	5.1	4.9	2.2	2.5	2.3	2.4	12.4	13.5	6.3	5.9
Tb	0.88	0.90	0.85	0.87	0.78	0.88	0.94	0.90	0.40	0.46	0.44	0.44	2.26	2.43	1.13	1.08
Dy	5.9	6.1	5.7	5.8	5.1	5.9	6.4	6.1	2.7	3.2	2.9	3.0	15.1	16.4	7.6	7.2
Ho	1.25	1.33	1.22	1.26	1.10	1.26	1.37	1.31	0.59	0.67	0.64	0.64	3.2	3.5	1.62	1.54
Er	3.6	3.9	3.5	3.6	3.1	3.5	3.9	3.7	1.69	1.93	1.83	1.84	9.4	10.0	4.6	4.4
Tm	0.52	0.59	0.51	0.52	0.45	0.52	0.58	0.55	0.25	0.29	0.27	0.27	1.39	1.50	0.68	0.64
Yb	3.4	3.9	3.3	3.4	3.0	3.5	3.8	3.6	1.63	1.89	1.77	1.79	9.1	10.0	4.4	4.2
Lu	0.51	0.59	0.50	0.51	0.44	0.51	0.56	0.54	0.25	0.28	0.27	0.27	1.35	1.49	0.66	0.62
Hf	2.8	3.3	2.6	2.6	2.4	2.9	2.9	2.7	0.98	1.15	1.06	1.10	9.2	10.1	3.7	3.6
Ta	0.19	0.19	0.18	0.18	0.26	0.32	0.19	0.19	0.13	0.14	0.14	0.14	0.49	0.52	0.33	0.32
Pb	0.46	0.47	0.39	0.40	0.52	0.64	0.40	0.45	0.23	0.22	0.21	0.18	1.26	1.21	0.55	0.57
Th	0.20	0.32	0.19	0.19	0.29	0.34	0.20	0.19	0.12	0.12	0.13	0.13	0.68	0.72	0.36	0.37
U	0.10	0.17	0.07	0.07	0.10	0.11	0.09	0.06	0.06	0.04	0.05	0.06	0.35	0.25	0.12	0.12

**Table 3.** Electron microprobe (major elements, glass, wt%), XRF (major elements, bulk, wt%) and ICP-MS (trace elements, ppm) analyses of glassy MORB pieces and the respective altered part of the rock (bulk) from EXCO rocks. Analyses from the same hand specimen are marked by  $\square$ . DS = dredge, alt % = alteration of individual sample in percent.

#### 4.6 Ma – 36DS

These rocks were dredged along the flank of a seamount (Fig.1). Some of the recovered samples have a higher percentage of voids (3%) with diameters up to 2mm. Most of the glass remains fresh, with only minor palagonite along fractures. Vesicles and cavities at the glassy margins remain open or are lined with sediment and phillipsite, whereas within oxidation haloes they are lined with celadonite and rare spotted iron oxyhydroxide. Most fractures remain open, only a few are lined with secondary minerals. The main alteration product celadonite is also distributed within the groundmass, where it occurs with trace saponite and nontronite.

Ma	2.56		2.92		2.92		2.92		4.6		6.84		8.64	
Sample	35DS2 bulk	35DS2 glass	9DS2 bulk	9DS2 glass	9DS4 bulk	9DS4 glass	9DS8 bulk	9DS8 glass	36DS8 bulk	36DS8 glass	42DS10 bulk	42DS10 glass	43DS13 bulk	43DS13 glass
alt %	3.3	0.0	4.5	0.0	3.0	0.0	4.0	0.0	4.0	0.0	7.0	0.0	7.0	0.0
SiO <sub>2</sub>	49.6	50.1	49.5	50.0	48.8	49.8	49.3	49.7	49.2	49.6	49.5	49.7	50.0	50.7
TiO <sub>2</sub>	1.0	1.2	2.7	2.8	2.2	2.2	1.5	1.6	1.0	1.1	1.8	1.9	1.7	1.8
Al <sub>2</sub> O <sub>3</sub>	15.3	15.1	12.5	12.6	14.0	13.7	15.3	14.9	16.4	15.6	14.0	13.9	14.3	14.2
Fe <sub>2</sub> O <sub>3</sub>	10.4	10.5	16.1	16.2	13.3	13.3	10.8	11.2	10.5	10.4	12.6	12.8	12.0	12.0
MnO	0.17	0.17	0.24	0.25	0.23	0.21	0.19	0.18	0.17	0.17	0.21	0.21	0.20	0.20
MgO	8.7	8.5	5.5	5.7	6.6	6.8	7.7	7.7	6.8	9.1	7.2	7.1	7.4	7.5
CaO	12.8	12.8	9.9	9.9	11.3	11.0	11.6	12.0	13.2	12.7	11.6	11.4	11.8	11.8
Na <sub>2</sub> O	2.4	2.4	2.8	3.2	2.8	3.0	2.8	3.0	2.6	2.4	3.4	2.8	2.5	2.8
K <sub>2</sub> O	0.07	0.04	0.18	0.17	0.31	0.17	0.25	0.15	0.07	0.04	0.19	0.14	0.14	0.09
P <sub>2</sub> O <sub>5</sub>	0.07	0.06	0.24	0.25	0.20	0.18	0.14	0.13	0.12	0.06	0.16	0.14	0.14	0.14
Cr <sub>2</sub> O <sub>3</sub>	n.d.	0.05	n.d.	0.01	n.d.	0.04	n.d.	0.06	n.d.	0.07	n.d.	0.02	n.d.	0.03
total	100.5	101.0	99.6	101.1	99.7	100.5	99.6	100.5	100.1	101.2	100.6	100.1	100.3	101.3
Li	5.0	4.8	7.8	10.1	6.3	5.7	4.4	4.0	6.0	4.0	7.0	6.1	6.3	6.6
Sc	38.0	39.1	41.1	45.5	42.8	40.5	33.1	34.9	36.6	38.0	43.8	42.2	43.7	43.9
V	260	257	456	498	382	358	230	234	245	251	358	356	346	335
Cr	372	353	182	39	218	205	261	262	350	374	184	190	218	208
Co	38.6	42.0	41.3	44.0	35.1	36.6	41.6	32.1	42.1	44.0	39.6	39.2	48.7	38.9
Ni	68.0	81.8	1207	33.9	54.2	56.6	76.0	59.6	50.4	57.2	53.8	55.3	100	68.2
Cu	82.2	83.2	50.7	54.1	68.2	59.8	64.3	58.6	95.3	98.8	51.5	60.7	105	66.5
Zn	68.4	84.1	108	270	94.4	104	91.3	62.2	66.0	61.3	82.6	95.4	109	83.8
Ga	15.3	13.4	20.2	19.3	18.9	18.2	14.5	15.0	15.3	15.5	16.3	18.4	16.6	15.3
Rb	0.49	0.26	1.70	1.66	6.9	1.63	1.67	1.06	0.35	0.14	2.1	1.35	4.9	0.91
Sr	85.3	85.2	111	118	128	117	129	131	92.5	88.9	114	114	95.9	110
Y	21.0	21.7	54.0	54.8	38.5	39.1	23.4	24.7	20.2	20.1	38.8	35.2	35.6	33.7
Zr	49.1	48.5	179	176	138	136	86.4	81.7	46.1	45.9	114	115	130	101
Nb	0.74	0.72	3.9	4.2	3.7	3.6	2.5	2.5	0.54	0.51	2.8	2.9	2.6	2.1
Cs	0.01	0.00	0.02	0.02	0.37	0.02	0.03	0.01	0.01	0.00	0.03	0.02	0.07	0.02
Ba	4.8	2.9	16.1	14.9	21.8	14.1	16.3	11.3	4.0	1.70	11.4	11.5	50.4	7.0
La	1.50	1.36	5.5	6.1	4.7	4.8	3.9	3.5	1.41	1.25	4.4	3.9	5.0	3.3
Ce	4.5	4.9	16.8	19.4	13.9	14.0	11.0	10.4	4.5	4.5	12.7	11.7	12.2	10.9
Pr	0.91	0.96	2.9	3.3	2.4	2.4	1.70	1.76	0.92	0.88	2.3	2.0	2.2	1.94
Nd	5.3	5.6	15.8	17.9	12.9	13.1	8.7	9.1	5.3	5.1	12.3	10.8	11.8	10.6
Sm	2.1	2.2	5.6	6.4	4.4	4.6	2.8	3.1	2.0	2.0	4.4	3.8	4.0	3.9
Eu	0.80	0.87	1.85	2.1	1.50	1.55	1.01	1.10	0.80	0.79	1.55	1.33	1.33	1.36
Gd	2.9	3.1	7.2	8.3	5.7	5.9	3.6	3.9	2.9	2.8	5.9	5.1	5.2	5.1
Tb	0.55	0.59	1.32	1.52	1.05	1.08	0.65	0.70	0.54	0.53	1.08	0.93	0.95	0.94
Dy	3.8	4.1	8.9	10.1	7.0	7.2	4.3	4.6	3.7	3.6	7.4	6.3	6.3	6.4
Ho	0.82	0.87	1.93	2.2	1.51	1.56	0.91	0.98	0.78	0.77	1.55	1.36	1.37	1.35
Er	2.3	2.5	5.6	6.2	4.3	4.4	2.6	2.8	2.2	2.2	4.4	3.8	3.9	3.8
Tm	0.35	0.37	0.83	0.91	0.63	0.65	0.38	0.41	0.33	0.33	0.66	0.57	0.57	0.56
Yb	2.3	2.4	5.4	6.0	4.2	4.3	2.5	2.6	2.1	2.1	4.3	3.7	3.7	3.7
Lu	0.34	0.36	0.80	0.89	0.62	0.63	0.37	0.39	0.32	0.31	0.64	0.55	0.55	0.55
Hf	1.50	1.57	4.4	4.9	3.5	3.5	2.2	2.2	1.41	1.43	3.3	3.0	3.0	2.9
Ta	0.05	0.06	0.26	0.28	0.24	0.25	0.16	0.17	0.04	0.04	0.22	0.19	0.15	0.15
Pb	0.30	0.24	0.78	0.94	0.56	0.54	2.5	0.42	0.22	0.21	0.48	0.46	2.7	0.65
Th	0.06	0.04	0.33	0.28	0.27	0.27	0.21	0.19	0.04	0.03	0.25	0.24	0.20	0.14
U	0.06	0.02	0.18	0.10	0.11	0.10	0.12	0.06	0.05	0.01	0.09	0.08	0.17	0.05

Table 3. (continued)

6.84 Ma – 42DS

Samples contain up to 5 mm thick glassy margins, a 1-10 mm thick manganese crust and up to 4 cm thick alteration haloes. At the glassy margins palagonite is present along the rim of fractures, which are mainly filled with the main secondary mineral phillipsite (Fig.3.4) or in rare cases a mixture of phillipsite and celadonite. Fractures within rock interiors remain open. Olivine phenocrysts are partly altered by celadonite. Very minor amounts of iron oxyhydroxide, saponite and nontronite are also present within the groundmass. Phillipsite is the dominant secondary mineral in veins, whereas finely dispersed celadonite dominates the alteration products in the groundmass.

### 8.64 Ma – 43DS

The oldest rocks in the working area are characterized by alteration haloes, glassy margins (up to 10 mm), manganese crusts (up to 7 mm) and the presence of iron oxyhydroxide, chlorite/smectite, celadonite, saponite, nontronite and phillipsite as secondary minerals. Palagonite is present in the glassy margins at the outer rim of fractures. As in the 6.84 Ma old rocks, fractures at the outer rim are mainly filled with the main alteration product phillipsite and a mixture of phillipsite and celadonite, in the interior of the rocks they remain open. Cavities occurring in the interior are filled with celadonite or remain open. We suppose that the lack of olivine is controlled by the magmatic composition because there is no evidence for replaced olivine in thin sections.

### **4.3. Mineral Chemistry**

Described are only minerals identified by microprobe analyses (celadonite, saponite and phillipsite). Saponite-celadonite is a transition mineral and its abundance and occurrence is related to those of both its end-member minerals. Nontronite and chlorite/smectite were only identified by XRD-analyses and therefore no microprobe data or information on the occurrence in thin sections can be reported.

#### *Celadonite*

Celadonite is the most abundant alteration product in basalts from 0.12 – 4.6 Ma and is restricted to off-axis samples (>0.015 Ma) where it is associated with iron oxyhydroxides. Analyses are shown in Table 2.

Celadonite is a dioctahedral mineral of the mica group, of ideal composition  $K(Mg,Fe)^{2+}(Fe,Al)^{3+}(OH)_2[Si_4O_{10}]$ . Celadonite replaces primary minerals (Fig.3.3) (locally partially replacing plagioclase, more commonly partially or completely replacing olivine) and fills vesicles and veins. Celadonite shows various colors in thin section, although in contrast to the work of Alt (1993) and Laverne et al. (1996), the different colors do not always appear to be associated with different compositions. For example, an intense green color, often observed at the center of yellow-orange celadonite clots commonly originates from a micro-porous clump of celadonite crystals. The color appears to result from refraction in the empty pores existing between the microparticles of celadonite. In other cases the same appearance reflects a transition from celadonite to saponite (Fig.3.2).

In comparison to samples from the Troodos ophiolite (Gillis, 1987) and ODP samples from Leg 168 (0-3.5 Ma, Juan de Fuca Ridge) (Hunter et al., 1998; Hunter et al., 1999; Marescotti et al., 2000; Porter et al., 2000), Leg 148 Hole 896A (5.9 Ma, south of Costa Rica rift) (Laverne et al., 1996) and Leg 176 Hole 735B (11.5 Ma South West Indian Ridge) (Alt and Bach, 2001), celadonites from EXCO basalts are characterized by high Fe-contents (Fig.4). Results from ODP samples show a similar behaviour for “iddingsite” which is in fact a mixture of celadonite, saponite and iron oxyhydroxide (Laverne et al., 1996). Stoichiometric calculations show the EXCO “celadonite” analyses to have greater than 4 cations in octahedral coordination, suggesting that the celadonites are interlayered with other phases. Other grains showing both lower Fe-contents and lower octahedral totals come from celadonite intergrown with saponite, whereas grains with high Fe and low K-contents suggests mixtures with iron oxyhydroxide.

In contrast to ODP samples, the interlayer composition of the celadonite structure is dominated by K, with substitution by Na (Fig.5). Decreasing K-contents and increasing Na-contents also mark the transition to saponite.

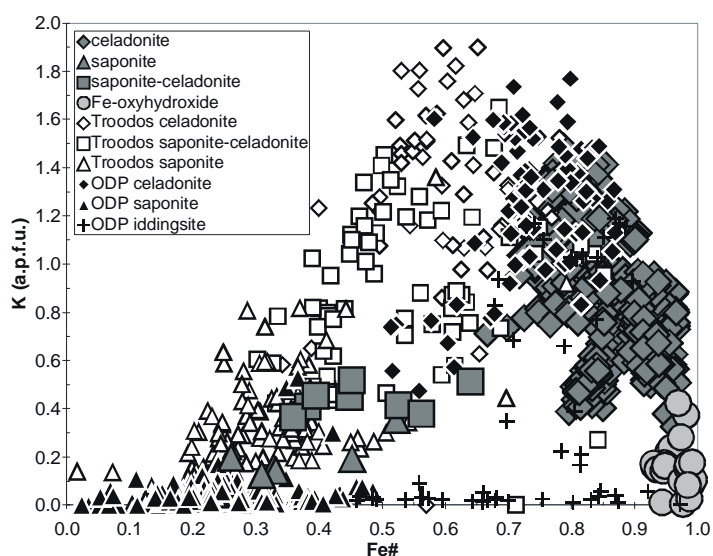


Figure 4. Results of electron microprobe analyses of clay minerals. Interlayer K plotted against Fe#. Units are moles per  $O_{20}(OH)_4$  from the calculated formulae in Table 2. Shown for comparison are clays from the Troodos ophiolite (Gillis, 1987) and ODP samples (Laverne et al., 1996; Hunter et al., 1998; Hunter et al., 1999; Marescotti et al., 2000; Porter et al., 2000; Alt and Bach, 2001).

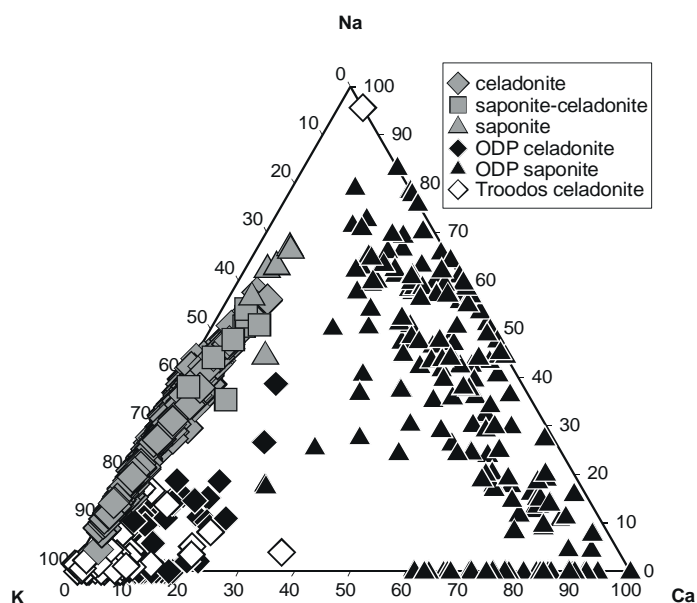


Figure 5. Proportions of cations (stoichiometric proportions) in interlayer sites of EXCO clay minerals. Troodos saponites show no systematics and so are not plotted for clarity.

### Saponite

Saponite becomes an ubiquitous phase in samples  $\geq 2.92$  Ma and is always associated with celadonite or saponite-celadonite (Fig.3.2). Petrographic evidence suggests that it either replaces or overprints the latter phases, suggesting that saponite forms later than celadonite under either different redox conditions, water/rock ratios or at higher temperatures. Saponites are characterized by a lower Fe and K, and higher Mg content than celadonite. There is a considerable Fe-Mg substitution in our saponites and saponite-celadonite mixtures, a feature which has also been reported from ODP samples (Fig.6). Furthermore EXCO saponites contain nearly no Al in the octahedral position resulting in the interlayer is richer in Na (Fig.5). A comparison with saponites from ODP holes demonstrate that Ca plays only a subordinate role in EXCO saponites, implying that the fluids circulating in this area are particularly Ca-poor.

Sample 9DS8 (2.92 Ma) exhibits two types of saponite (Table 2), a low and high Fe type. Andrews (1980) reported that saponites occurring in oxidative environments are Mg-rich and relatively Fe-poor. Those in non-oxidative environments are Fe-rich with a somewhat lower Mg content. These observations suggest a polyphase generation of saponites in sample 9DS8.

Mixed compositions of celadonite in Hole 896A are indicating combinations of saponite and celadonite (Teagle et al., 1996). We also identified an illite/smectite mixed layer, occurring as a physical mixture between saponite and celadonite, replacing or dissolving celadonite (Fig.3.2).

### Phillipsite

Phillipsite is the volumetrically most abundant alteration product in rocks older than 4.6 Ma and is restricted to glassy rinds in basalts older than 1 Ma. It commonly fills fractures created by glass dissolution (Fig.3.4) and has a distinctive  $K_2O$  content and  $SiO_2/Al_2O_3$  ratio (Table 4) compared to those reported, for example, from the Troodos ophiolite (Gillis, 1987). The relatively high  $K_2O$  content in our phillipsites compared to Troodos phillipsites is probably the result of the interplay between K and Ca in the circulating fluids. In

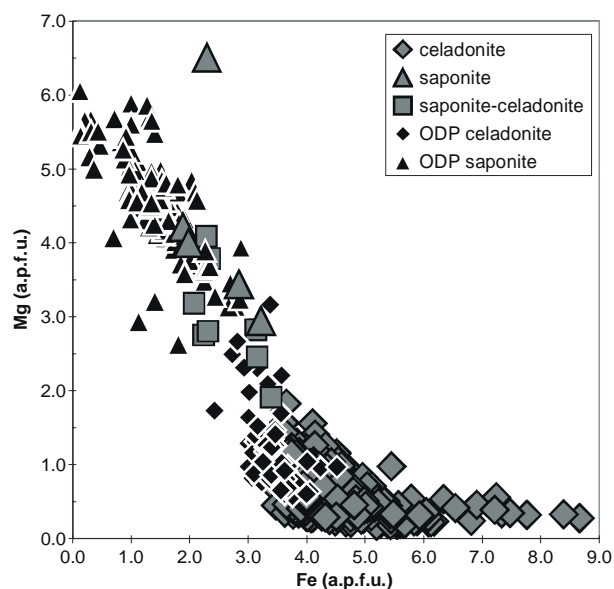


Figure 6. Results of electron microprobe analyses of clay minerals demonstrating Mg-Fe substitution in saponite and saponite-celadonite. Units are moles per  $O_{20}(OH)_4$  from the calculated formulae in Table 2.

view of the exchange of K, Na and Ca in the zeolite structure, a limited Ca availability (as suggested by the saponite chemistry, see above) implies that, to maintain charge balance, the zeolites will incorporate more alkalis. Phillipsites from Hole 896A show smaller portions of alkalis. In the case of the area studied here, it seems that the phillipsites preferentially take up K. Dissolution of glass and alteration of plagioclase probably makes large amounts of Si and Al available for the formation of the abundant phillipsites in rocks older than 6 Ma.

#### 4.4. Geochemical fluxes

Compositions of fresh glass and immediately adjacent alteration haloes from the same rock were compared to quantify the chemical fluxes that result from low temperature alteration (Table 3). By comparing parts of the same rock, we exclude all variations in chemistry which result from magma genesis (there is a large variation in magma composition between sampling sites related to the petrogenetic processes at the ridge axis, see Grevemeyer et al., 2002). A comparison of oxidation haloes and “fresh” rock interiors was not made because even the rock interior has undergone a slight alteration and therefore does not wholly reflect the initial pristine magmatic composition (Staudigel et al., 1996).

The calculation of chemical flux is based on the method of Gresens (1967) which was later modified by Grant (1986). The concentration of a component in the altered rock is compared to that in the original through a mass change term

$$C_i^A = M^O/M^A(C_i^O + \Delta C_i)$$

Dredge Ma	29DS2 1.16	36DS7 4.6	42DS10 6.84	42DS10 6.84	43DS13 8.64	43DS13 8.64
mineral	phillipsite	phillipsite	phillipsite	phillipsite	phillipsite	phillipsite
SiO <sub>2</sub>	53.9	60.3	60.3	49.2	59.3	55.5
TiO <sub>2</sub>	0.14	0.01	0.03	0.28	0.04	0.18
Al <sub>2</sub> O <sub>3</sub>	17.3	21.1	21.2	19.1	20.6	18.4
FeO	2.3	0.12	0.18	2.2	0.49	2.7
MnO	0.14	0.09	0.02	0.26	0.05	0.31
MgO	0.26	0.03	0.05	0.44	0.05	0.31
CaO	2.4	0.12	0.07	0.29	0.09	0.19
Na <sub>2</sub> O	5.0	4.0	3.6	4.4	3.7	5.0
K <sub>2</sub> O	5.7	6.2	6.6	5.2	6.1	6.7
P <sub>2</sub> O <sub>5</sub>	0.07	0.03	0.01	0.07	0.04	0.11
Cr <sub>2</sub> O <sub>3</sub>	0.05	0.03	0.01	0.02	0.01	0.04
total	87.2	92.0	92.1	81.4	90.6	89.5
Number of ions on the basis of 32 oxygens						
Si	11.336	11.609	11.605	10.987	11.614	11.350
Al	4.276	4.789	4.810	5.014	4.753	4.438
Ti	0.022	0.002	0.005	0.047	0.007	0.028
Fe	0.405	0.020	0.029	0.416	0.083	0.464
Mn	0.025	0.014	0.004	0.049	0.008	0.054
Mg	0.083	0.009	0.013	0.146	0.016	0.096
P	0.013	0.004	0.002	0.013	0.007	0.019
Cr	0.008	0.004	0.002	0.003	0.002	0.006
Ca	5.033	0.024	0.015	0.069	0.019	0.042
Na	1.023	1.491	1.366	1.922	1.420	1.996
K	1.532	1.525	1.624	1.467	1.540	1.754
total	23.755	19.493	19.475	20.133	19.470	20.247
standard deviation						
n	1	10	53	1	48	21
SiO <sub>2</sub>		1.87	2.45		3.16	2.64
TiO <sub>2</sub>		0.02	0.06		0.06	0.13
Al <sub>2</sub> O <sub>3</sub>		0.87	0.96		1.46	1.11
FeO		0.08	0.28		0.81	1.24
MnO		0.16	0.06		0.09	0.27
MgO		0.02	0.06		0.08	0.32
CaO		0.05	0.06		0.16	0.23
Na <sub>2</sub> O		1.23	1.25		1.10	0.37
K <sub>2</sub> O		0.43	0.87		1.17	0.62
P <sub>2</sub> O <sub>5</sub>		0.03	0.02		0.13	0.06
Cr <sub>2</sub> O <sub>3</sub>		0.02	0.02		0.02	0.03
total		2.10	1.84		3.43	3.71

**Table 4.** Average electron microprobe analyses and calculated formulae for phillipsite from EXCO rocks (wt%), n = number of analyses. Standard deviation is given in wt%.

where  $C_i^A$  = concentration of component  $i$  in the altered rock;  $M^O$  = mass of the original, fresh rock;  $M^A$  = mass of the altered rock;  $C_i^O$  = concentration of component  $i$  in the original rock; and  $\Delta C_i$  = change in concentration of component  $i$ . Results for elements from individual samples are plotted as  $C_i^A$  vs.  $C_i^O$ , where all data points lie along an arc of a circle centered on the origin (Fig.7). By evaluating which points group together, it is possible to evaluate which elements are appropriate for calculation of the mass change term ( $M^O/M^A$ ), which is then used to calculate elemental gains and losses (results are shown in Table 5).

Samples of all ages are enriched in  $K_2O$ , Rb, Cs, Ba and U, however, only the older off-axis samples show significant gains in these elements in their oxidation haloes (Fig.8). The degree of enrichment generally increases with age, MgO, Li, Cr, Ni, Cu, Ga, Pb and Th show minor gains and losses with no apparent systematics with age. The high Ni and Pb value in 9DS2, 9DS8 and 43DS13 might be the result of an analytical problem. Zn is enriched in all samples from the ridge axis, but shows no systematic behaviour in older samples either. All other elements appear to be behaving essentially as immobile elements.

In the following we compare our results with those from DSDP/ODP holes to show the significance of our results for more general, globally-relevant mass balance calculations. DSDP sites 417 and 418 penetrate 365 m / 217 m into 118 Ma old basement. Alteration in Hole 417A is probably the most intense of any DSDP/ODP basement core, with highly oxidized, alkali-enriched and Mg-depleted rocks (Alt and Honnorez, 1984). The calculated geochemical fluxes at these sites show the crust to be taking up Cs over Rb and K, with characteristic K/Rb and Rb/Cs ratios of 510/65 (Staudigel et al., 1996), similar to our results (average of 404/53).

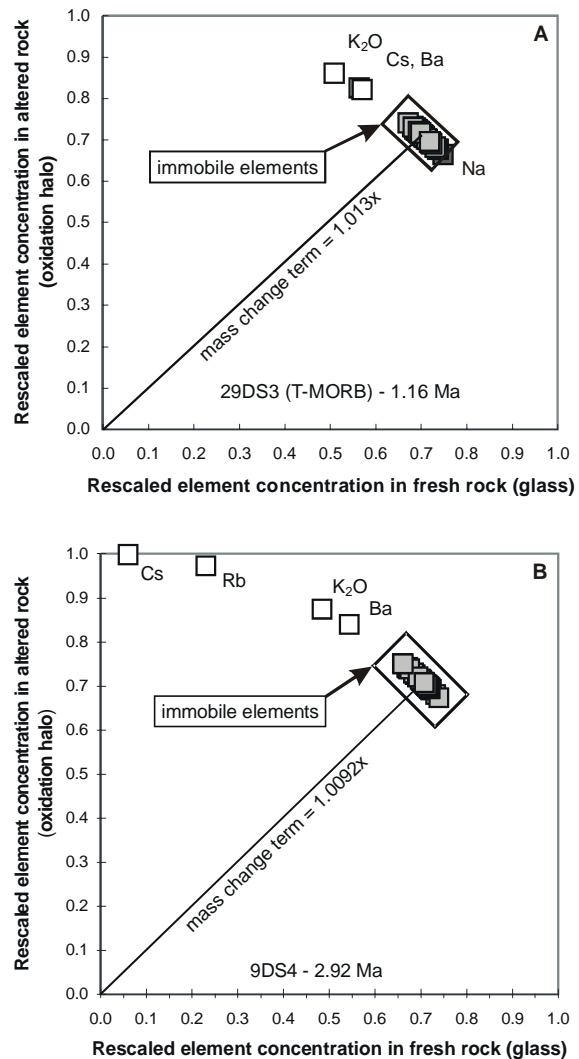


Figure 7. Examples of plots of the concentration data for glass-altered rock pairs for sample 29DS3 (1.16 Ma) (A) and 9DS4 (2.92 Ma) (B), rescaled to allow evaluation of which elements may be considered “relatively immobile” during the alteration process. The concentration data have been standardized so that the sums of squares equal 1, thereby resulting in all data points lying along the arc of a unit circle (Humphris et al., 1998). Mobile elements are labeled on the diagram.

Dredge	Ma	alt	SiO <sub>2</sub>	TiO <sub>2</sub>	Al <sub>2</sub> O <sub>3</sub>	Fe <sub>2</sub> O <sub>3</sub>	MnO	MgO	CaO	Na <sub>2</sub> O	K <sub>2</sub> O	P <sub>2</sub> O <sub>5</sub>	Li	Sc	V	Cr	Co	Ni	Cu	Zn	Ga	Rb	Sr	Y	Zr	Nb	Cs
21DS4	0.000	0.3 %	1%	-7%	3%	-4%	-11%	2%	7%	-10%	15%	-2%	-9%	3%	8%	14%	6%	7%	10%	<b>54%</b>	5%	<b>29%</b>	5%	-4%	-13%	5%	<b>21%</b>
18DS9	0.015	0.0 %	1%	-7%	2%	-1%	-6%	-1%	2%	1%	<b>16%</b>	3%	<b>-22%</b>	2%	2%	3%	2%	8%	7%	<b>14%</b>	1%	-8%	1%	0%	-2%	-1%	-4%
20DS3	0.015	0.5 %	8%	-1%	10%	4%	6%	7%	11%	9%	1%	12%	-9%	9%	12%	16%	8%	-4%	1%	<b>850%</b>	13%	-2%	3%	0%	-1%	-1%	-6%
22DS2	0.120	3.0 %	-5%	3%	<b>-10%</b>	7%	-6%	<b>-14%</b>	-5%	-4%	<b>122%</b>	n.d.	-7%	5%	3%	<b>-14%</b>	-3%	<b>-19%</b>	<b>-29%</b>	-2%	-4%	<b>314%</b>	8%	0%	3%	-1%	<b>1921%</b>
28DS1	0.650	2.7 %	8%	-8%	5%	9%	-2%	<b>28%</b>	7%	8%	<b>57%</b>	<b>62%</b>	<b>-14%</b>	2%	9%	<b>19%</b>	-6%	<b>-15%</b>	<b>-11%</b>	1%	<b>17%</b>	1%	5%	0%	-2%	5%	<b>-55%</b>
28DS3	0.650	2.5 %	-2%	<b>-16%</b>	-6%	0%	1%	<b>15%</b>	-4%	-9%	6%	<b>41%</b>	<b>12%</b>	3%	3%	4%	6%	0%	-2%	-5%	1%	8%	3%	0%	-1%	1%	<b>68%</b>
29DS2	1.160	2.7 %	1%	-2%	1%	7%	<b>51%</b>	4%	5%	-4%	<b>20%</b>	-4%	<b>-55%</b>	7%	11%	<b>19%</b>	1%	1%	-5%	<b>26%</b>	<b>17%</b>	<b>190%</b>	<b>24%</b>	8%	4%	4%	<b>1016%</b>
29DS3	1.160	2.0 %	-5%	-9%	-5%	6%	3%	-5%	-3%	<b>-12%</b>	<b>67%</b>	0%	4%	1%	0%	-9%	-1%	-1%	-1%	-8%	-8%	9%	1%	2%	-5%	-3%	<b>44%</b>
35DS2	2.560	3.3 %	2%	-10%	5%	2%	1%	6%	3%	3%	<b>61%</b>	<b>17%</b>	7%	1%	5%	9%	-5%	<b>-14%</b>	2%	<b>-16%</b>	<b>18%</b>	<b>94%</b>	4%	0%	5%	7%	<b>122%</b>
9DS2	2.920	4.5 %	7%	4%	7%	7%	3%	4%	7%	-5%	<b>17%</b>	2%	<b>-17%</b>	-3%	-1%	<b>407%</b>	1%	<b>3734%</b>	1%	<b>-57%</b>	13%	10%	1%	6%	9%	0%	10%
9DS4	2.920	3.0 %	-3%	-4%	1%	-1%	9%	-4%	2%	-8%	<b>80%</b>	10%	10%	5%	6%	6%	-5%	-5%	13%	-10%	3%	<b>321%</b>	9%	-2%	1%	2%	<b>1571%</b>
9DS8	2.920	4.0 %	1%	-8%	4%	-2%	5%	2%	-1%	-3%	<b>70%</b>	10%	12%	-3%	0%	1%	<b>32%</b>	<b>30%</b>	11%	<b>49%</b>	-2%	<b>61%</b>	0%	-4%	7%	4%	<b>163%</b>
36DS8	4.600	4.0 %	-2%	-6%	4%	0%	2%	<b>-26%</b>	3%	5%	<b>84%</b>	<b>112%</b>	<b>50%</b>	-5%	-4%	-7%	-5%	<b>-13%</b>	-5%	6%	-3%	<b>139%</b>	3%	-1%	-1%	4%	<b>185%</b>
42DS10	6.840	7.0 %	-7%	-11%	-5%	-8%	-5%	-6%	-5%	<b>14%</b>	<b>28%</b>	4%	6%	-3%	-6%	-9%	-6%	-9%	<b>-21%</b>	<b>-19%</b>	<b>-17%</b>	<b>44%</b>	-7%	3%	-7%	-9%	<b>68%</b>
43DS13	8.640	7.0 %	-3%	-7%	-1%	-2%	-2%	-4%	-1%	<b>-12%</b>	<b>52%</b>	-2%	-7%	-2%	1%	3%	<b>23%</b>	<b>44%</b>	<b>54%</b>	<b>28%</b>	7%	<b>433%</b>	<b>-15%</b>	3%	<b>26%</b>	<b>24%</b>	<b>328%</b>

Dredge	Ma	alt	Ba	La	Ce	Pr	Nd	Sm	Eu	Gd	Tb	Dy	Ho	Er	Tm	Yb	Lu	Hf	Ta	Pb	Th	U	Mass change term
21DS4	0.000	0.3 %	12%	4%	4%	4%	3%	3%	3%	1%	0%	-1%	-4%	-6%	-8%	-10%	-12%	-15%	3%	0%	<b>-36%</b>	<b>-39%</b>	0.9764
18DS9	0.015	0.0 %	-3%	0%	0%	-1%	0%	1%	0%	-1%	0%	0%	-1%	0%	-1%	0%	0%	1%	0%	-2%	-1%	6%	0.9772
20DS3	0.015	0.5 %	<b>259%</b>	-4%	-6%	-4%	-4%	-4%	-4%	-5%	-4%	-6%	-5%	-3%	-4%	-6%	-6%	-8%	-9%	-12%	-7%	4%	0.9138
22DS2	0.120	3.0 %	4%	4%	2%	2%	2%	0%	0%	0%	0%	0%	0%	0%	1%	1%	0%	1%	-4%	<b>-14%</b>	-2%	<b>38%</b>	1.0418
28DS1	0.650	2.7 %	<b>14%</b>	2%	-3%	-1%	-3%	-3%	-3%	-3%	-2%	-4%	-2%	-2%	-4%	-4%	-2%	-4%	-1%	<b>17%</b>	5%	<b>71%</b>	0.8978
28DS3	0.650	2.5 %	<b>697%</b>	2%	1%	0%	0%	0%	0%	0%	0%	0%	0%	0%	0%	0%	-1%	-3%	1%	<b>19%</b>	-7%	<b>-20%</b>	0.9945
29DS2	1.160	2.7 %	<b>36%</b>	1%	-2%	-1%	-1%	-2%	-4%	-4%	-3%	-4%	-4%	-2%	-4%	-4%	-6%	-5%	-3%	9%	0%	<b>46%</b>	0.9593
29DS3	1.160	2.0 %	<b>42%</b>	2%	4%	3%	2%	5%	4%	5%	3%	4%	4%	3%	5%	3%	6%	2%	1%	-6%	-5%	-4%	1.0145
35DS2	2.560	3.3 %	<b>71%</b>	<b>14%</b>	-5%	-2%	-2%	-3%	-5%	-3%	-3%	-4%	-3%	-2%	-3%	-1%	-3%	-1%	-4%	<b>26%</b>	<b>33%</b>	<b>262%</b>	0.9663
9DS2	2.920	4.5 %	<b>16%</b>	-3%	-6%	-6%	-5%	-6%	-5%	-6%	-6%	-5%	-4%	-2%	-2%	-3%	-3%	-1%	-3%	-10%	<b>27%</b>	<b>91%</b>	0.9277
9DS4	2.920	3.0 %	<b>54%</b>	-1%	-1%	-2%	-3%	-4%	-3%	-4%	-4%	-4%	-4%	-3%	-3%	-3%	-3%	-1%	-2%	3%	-1%	13%	1.0066
9DS8	2.920	4.0 %	<b>46%</b>	12%	7%	-2%	-3%	-6%	-7%	-7%	-6%	-6%	-6%	-4%	-4%	-4%	-5%	2%	-4%	<b>516%</b>	13%	<b>83%</b>	0.9833
36DS8	4.600	4.0 %	<b>133%</b>	<b>12%</b>	0%	2%	1%	0%	0%	1%	1%	1%	0%	1%	0%	1%	1%	-3%	<b>15%</b>	4%	4%	<b>214%</b>	1.0123
42DS10	6.840	7.0 %	-8%	5%	2%	6%	7%	7%	10%	9%	9%	10%	7%	7%	7%	8%	9%	4%	6%	-2%	-3%	1%	1.0695
43DS13	8.640	7.0 %	<b>601%</b>	<b>51%</b>	10%	11%	9%	2%	-4%	0%	-1%	-2%	0%	0%	0%	-1%	-2%	2%	-1%	<b>310%</b>	<b>41%</b>	<b>264%</b>	1.0197

**Table 5.** Relative gains (+) and losses (-) of elements in alteration haloes or bulk rock relative to their respective glass rims. Elements which are believed to be mobile are marked bold, alt = alteration of individual sample in percent estimated from thin section.

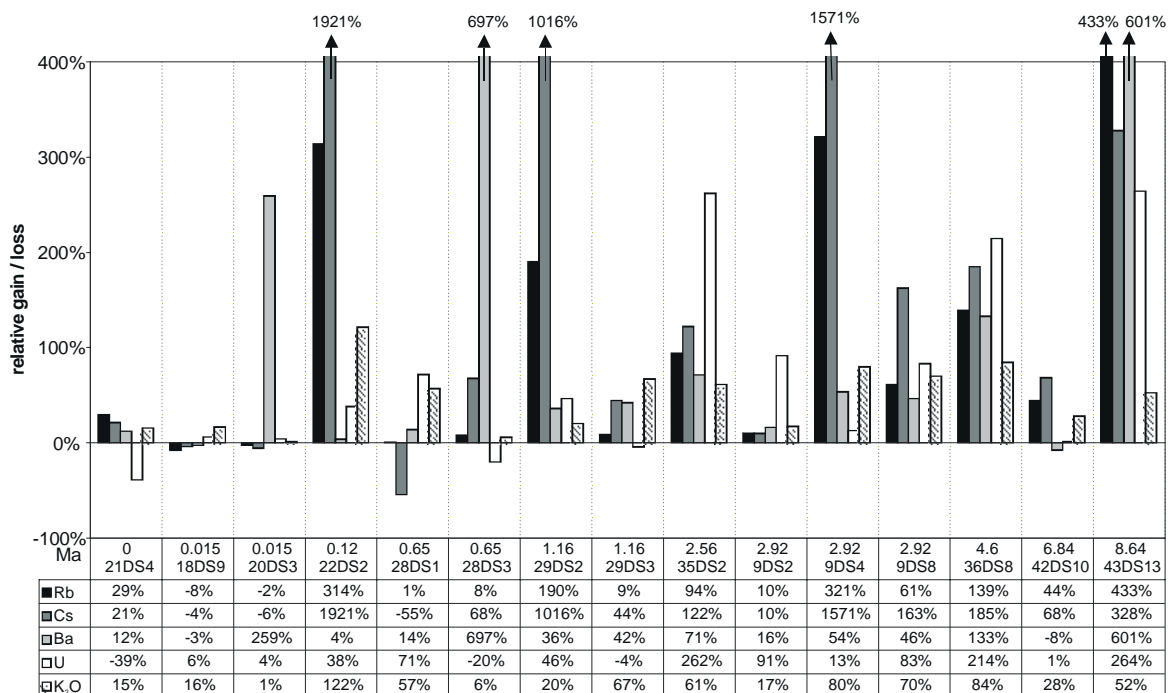


Figure 8. Gain/loss diagram for trace elements during the alteration process (comparison between fresh glass and oxidation haloes / bulk rock (relative %)).

When we compare the geochemical flux, using the same calculation for global flux as Staudigel et al. (1996) for our off-axis ( $\geq 0.12$  Ma) EXCO samples, 417/418 flux for  $K_2O$  is about 10 times higher than EXCO flux (Table 6). Similar to the EXCO samples, the 417/418 cores are enriched in U. Uranium uptake in these cores is connected to the precipitation of carbonate coupled with the possibility of U redistribution under oxidising conditions whereas U uptake in the EXCO samples could be controlled by iron oxyhydroxides. The uptake of REE in the crust is related to the precipitation of Fe-Mn oxide particles.

Hole 896A (290 m thick volcanic section) and 504B (571.5 m volcanic section) in 5.9 Ma old crust show similar fluxes to those in the EXCO area. Chemical changes include increased Mg, K, Rb, B, Cs, Li,  $CO_2$  and  $H_2O$  contents, as well as local uptake of  $P_2O_5$  (Alt et al., 1996b). In Hole 504B here is a downward decrease of

	EXCO				EXCO	EXCO	504B <sup>b</sup>	417/418 <sup>c</sup>	
	$S_i$ ridge-axis fresh (ppm)	$S_A$ ridge-axis altered (ppm)	$S_i$ off-axis fresh (ppm)	$S_A$ off-axis altered (ppm)	ridge axis <sup>a</sup>	off-axis <sup>a</sup>	600 m VZ <sup>a</sup>	<sup>a</sup>	
Rb	1.40	1.49	1.12	1.52	5.9	103	81		$\times 10^6$ mol/yr
Cs	0.019	0.02	0.02	0.09	0.03	3.0	1.5		$\times 10^6$ mol/yr
Ba	13.2	24.9	10.0	24.1	497	597			$\times 10^6$ mol/yr
U	0.10	0.09	0.07	0.13	-0.2	1.5	0.9		$\times 10^6$ mol/yr
$K_2O$	1222	1358	983	1527	8.3	33.5	34.5	332	$\times 10^9$ mol/yr

**Table 6.** Comparison of geochemical fluxes derived for EXCO samples with Hole 504B and Hole 417/418. Negative values indicate flux into the ocean, positive values indicate flux into the crust.

<sup>a</sup> Flux (mol/yr) =  $[(S_A - S_i)(g/kg) * \text{crustal production rate } (3.45 \times 10^6 \text{ m}^2/\text{yr}) * \text{density } (2800 \text{ kg/m}^3)] / \text{molecular weight (g/mol)}$  (Bach et al., 2003).

<sup>b</sup> Data for flux calculation taken from: Bach et al. (2003, Table 4). VZ = volcanic zone.

<sup>c</sup> Data for flux calculation taken from: Staudigel et al. (1996, Table 6).

K<sub>2</sub>O contents, suggesting a decreasing influence of seawater with depth. The geochemical flux for EXCO mobile elements is similar to those calculated for 504B, only the magnitude for Cs and U is about 2 / 1.6 times higher. As in our study, there is no or little change in REE in Hole 896A (Teagle et al., 1996). The permeability of the upper ~200 m of basement in both holes is sufficient to support circulation in ridge flank basement (Fisher et al., 1990; Fisher et al., 1994; Becker, 1996).

If we consider the permeability of the ocean crust on ridge flanks and compare the results of calculated fluxes from the upper volcanic section of drill sites with our dredged samples we see a very similar picture. This suggests that dredged samples from the seafloor provide a representative picture of the alteration occurring within the upper hundreds of meters of this crust.

## **5. Discussion**

Low temperature alteration of the ocean crust as it ages is controlled by local and regional variations in lithology and primary porosity; the type, thickness, and lateral extent of sediment cover; and the seafloor topography (Fisher, 1998; Marescotti et al., 2000). In the EXCO area, sediment thickness increases only slowly with distance from the ridge axis, reaching 30m on 7 Ma old crust (Hauschild et al., 2003). Data from seismic observations show a large increase in velocity in Layer 2 rocks with age (Grevemeyer and Weigel, 1997). Heat flow values are low close to the ridge and show a fast recovery to almost lithospheric conductive cooling values at a very young age of 9.3 Ma (Villinger et al., 2002). Sediment pore fluids extracted along the EXCO transect show lower values of K and Ca compared to seawater (Mottl and Wheat, 2000). The different secondary mineral assemblages in the EXCO rocks provide a record of changing conditions during the first 9 Ma of crustal aging. Although all samples were in contact with seawater, their alteration characteristics from both oxidative and non-oxidative conditions. We attribute this to strong similarities in the chemical environment on the micro-environment of a single pillow (open or sealed cracks leading to more oxidizing or reducing conditions, respectively) or macro-scale of the upper crust as a whole (more or less sediment covered leading to weaker or stronger exchange with the oxidising ocean water respectively).

### ***5.1. Evolution of low temperature alteration***

Three alteration types, which probably reflect separate stages in the progressive alteration, occur in the uppermost crust. We stress that these stages are not strictly sequential and that the inferred conditions probably overlapped and may even be coeval.

- 1) ***Dissolution of glass.*** Incipient alteration is characterized by partial replacement of glass by palagonite (devitrified glass). Alteration is very minor at the ridge axis but increases significantly off-axis, especially in rocks from the oldest locations (6.84 and 8.64 Ma) where palagonite is more abundant (10 %). Whereas palagonite is found in all samples, smectite and phillipsite only occurs off-axis, indicating formation at more advanced stage of alteration (e.g. Stroncik and Schmincke, 2002). Comparison of fresh glass with palagonite shows that K, Ti, Fe and H<sub>2</sub>O are gained and Si, Mn, Mg, Ca and Na are depleted as glass alters. Smectite acts as a sink for a significant portion of the elements liberated by palagonisation (Staudigel and Hart, 1983) whereas phillipsite probably competed with the palagonite for the available dissolved K. Other studies report significant losses in Mg, Si, Al, Ca, Na, P and Mn during the palagonitization of volcanic glass (e.g. Staudigel and Hart, 1983; Singer and Banin, 1990).
- 2) ***Precipitation of iron oxyhydroxide.*** Iron oxyhydroxides are found in oxidation haloes, disseminated in the groundmass and as Fe-staining on outer surfaces and along fractures. Depositional sequences show that iron oxyhydroxides predate celadonite at the ridge axis, whereas off-axis these phases can also be coeval (Fig.3.5). The axial samples are likely too young for seawater/rock interaction to provide the necessary high concentrations of alkali and Si to enable the precipitation of celadonite (Andrews, 1980). Iron oxyhydroxides are often mixed up with celadonite as reported in Hole 896A (Teagle et al., 1996). In ODP holes 1023-1032 drilled during Leg 168 the formation of iron oxyhydroxide associated with celadonite occurred during an early oxidative alteration period (Hunter et al., 1999). Pichler et al. (1999) also reported this stage as one of the first alteration stages for oceanic crustal rocks in general.
- 3) ***Formation of alteration haloes and secondary minerals (celadonite, saponite-celadonite, saponite and phillipsite).*** Concentric alteration haloes adjacent to fractures and veins did not develop until 0.12 Ma. The haloes are characterized by the occurrence of clay minerals and iron oxyhydroxides in fractures, voids and the groundmass. Secondary minerals only occur off-axis and replace interstitial glass (phillipsite), primary minerals (celadonite) and Fe-oxyhydroxides (celadonite, saponite) in veins, vesicles and voids. Alteration haloes with Fe-oxyhydroxides and celadonite develop at a relatively early stage, under oxidizing conditions at low temperature (<50°C) (e.g. Alt et al., 1992; Alt, 1993; Marescotti et al., 2000). The EXCO samples were in contact with seawater and therefore temperatures should be around 2°C. Saponite-celadonite and saponite were precipitated subsequent to celadonite, indicating a change towards more reducing conditions within these lavas at the seafloor. This is a typical sequence in dredged (Pichler et al., 1999) and drilled volcanics (e.g. Alt, 1999). Zeolite probably formed in response to an increase in pH of the circulating fluid resulting from the consumption of H<sup>+</sup> related to the breakdown of plagioclase (Laverne et al., 1996).

## 5.2. Fluid circulation in the crust

Basement temperatures for the EXCO area are lower than those expected for conductive cooling of the lithosphere but are typical for young oceanic crust covered by a discontinuous thin veneer of pelagic sediment. Basement temperatures inferred from the heat flow data and pore fluid chemistry are significantly lower than those inferred for the eastern flank of the Juan de Fuca Ridge. These low temperatures are consistent with the alteration characteristics for rocks recovered from exposed basement highs. This suggests that if these topographic features act as discharge zones, the venting fluids are cool and likely strongly seawater-dominated. This conclusion is supported by data for the seamount located close to the sampling locality 36DS (4.6 Ma) which stands approximately 800 m above the surrounding sedimented seafloor. A heat flow value of 618 mW/m<sup>2</sup>, 275% of the expected conductive heat loss, suggests that this seamount is an outflow point for circulating fluids (Villinger et al., 2002). The rock samples collected close to this suspected discharge site exhibit no extraordinary alteration features, in agreement with the suspected temperature at the sediment-basement interface of only about 14°C and the supposedly extremely focussed nature of the discharge (Villinger et al., 2002).

The secondary mineral and altered bulk rock compositions can provide direct information about the compositions of the circulating fluids. Pore fluid data from sediments taken immediately above the magmatic basement in the area studied show that the fluids circulating in this basement have lower K and Ca than Pacific seawater (Mottl and Wheat, 2000). As shown by the pore water chemistry most of the pore fluids are diffusing upward (Devey et al., 2000), suggesting that their chemistry provide a clue to the basement fluids and therefore their depletion in K and Ca are because of celadonite formation. The EXCO samples show that K is taken up by celadonite formation in the volcanic basement and EXCO celadonites have lower K-contents than celadonites from other parts of the world (Fig.4), and are lower in Ca than, for example, the Troodos and ODP celadonites (Fig.5). The high abundance of celadonite compared to saponite suggests that much of the alteration occurred under oxidizing conditions, which implies high seawater/rock ratios (e.g. Alt et al., 1992). This conclusion is supported by the high absolute iron contents of celadonite and their close association with iron oxyhydroxides. The Fe necessary for iron oxyhydroxide formation is available from the breakdown of olivine and the reactions occurring during the penetration of seawater through the rock (e.g. dissolution of glass). The transition from iron oxyhydroxide and celadonite to Mg-rich and then Fe-rich saponites results from a progressively more reducing nature of the circulating fluids (e.g. Marescotti et al., 2000) (Fig.9). Subsequent increasing sediment thickness and the local formation of alteration rinds leads progressively to a more limited exchange of the circulating fluids with the open ocean, the fluids become more reducing and saponite becomes a stable phase.

These links between fluid chemistry and alteration mineralogy open up the possibility of using successive alteration mineral parageneses to track evolving pore fluid composition during progressive alteration.

### 5.3. Geochemical fluxes

#### 5.3.1. $K_2O$ , $P_2O_5$ , $Rb$ and $Cs$

The EXCO samples demonstrate that, with the exception of  $K_2O$ , all major elements are essentially immobile during alteration except during the breakdown of glass to palagonite. High  $K_2O$ -contents of the altered EXCO rocks

are due to the presence of celadonite and typical of basalts altered at low temperature by seawater-derived fluids (e.g. Alt and Honnorez, 1984). Depending on local conditions, the magnitude of the flux is varying with age, but is significantly higher off-axis (e.g. comparing ridge axis and off-axis geochemical flux for  $K_2O$ , off-axis flux is about 4 times higher, Table 6). Phosphorus enrichment in a few of the samples could be associated with the formation of secondary hydrous ferric oxides, which formed from the breakdown of olivine and titanomagnetite (Böhlke et al., 1981)

The gain of  $K_2O$  and local uptake of  $P_2O_5$  is also reported for rocks from the volcanic section of Hole 896A and 504B (Alt et al., 1996b), as well as DSDP 417/418 (Staudigel et al., 1996). The geochemical  $K_2O$  flux for the EXCO area is about the same as in Hole 504B, but only tenth part of DSDP 418/418 (Table 6). The reported enrichment of Fe in volcanics in 896A and 504B is not shown by the EXCO samples, probably the result of the minor pervasive concentration of secondary minerals in the groundmass and the focused precipitation in fractures.

The EXCO samples are systematically enriched in Rb and Cs. Although the enrichments of these two elements are broadly correlated, the quantities of secondary minerals and therefore the intensity of alteration in off-axis samples is too small to allow the calibration of the Rb or Cs enrichments as an alteration index. The concentrations of these elements can easily be increased during alteration because they are readily supplied by seawater (Hart et al., 1974). Also they are incorporated in, or absorbed on, secondary clay minerals (Hart et al.,

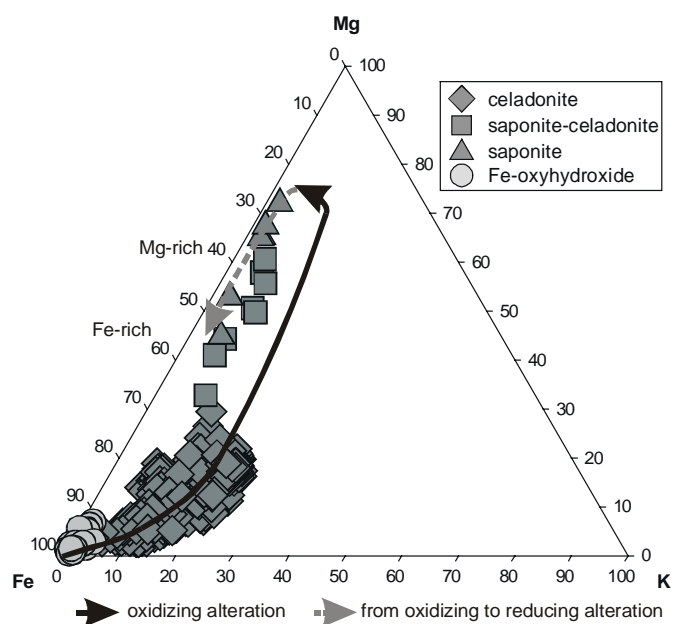


Figure 9. Plot of EXCO clay minerals with the hypothesized evolution from oxidizing to reducing alteration (cation proportions) (Marescotti et al., 2000).

1974), leading to increases in their concentrations in the altered off-axis samples (Table 3 and 5). The very high enrichment of Cs in a few samples (more than 1000%) is in good agreement with the Rb enrichment. An increase in the sensitivity to alteration in the order  $K > Rb > Cs$  and a consistent enrichment during the alteration in the order  $Cs > Rb > K$ , as reported in other dredged volcanics (Pichler et al., 1999), can not be recognized in the EXCO samples. The geochemical flux for Cs is about 2 times higher than in Hole 504B, Rb shows only a slightly more enriched flux.

When comparing the magnitude of flux for the mobile elements with Hole 504B, the geochemical flux in the EXCO samples is only slightly higher, but significantly lower than those reported for DSDP 418/418 (Table 6).

### 5.3.2. *Ba and U*

Ba and U are both enriched in the alteration haloes. The enrichment of Ba in altered rocks is due to its uptake into secondary minerals (clays and zeolites) at low temperature (Mottl, 1983). Studies from ODP Leg 157 Site 953 (off Gran Canaria) show high Ba concentrations in some phillipsites (Utzmann et al., 2002). However, Ba is not enriched in 42DS (6.84 Ma), where phillipsite is the main alteration product in veins, and there is no correlation between Ba enrichment and enrichment in alkali elements or the prevalence of secondary minerals. We conclude from these observations that the Ba enrichment is primarily associated with the presence of phillipsite and that the very heterogeneous distribution of phillipsite in the groundmass makes a representative bulk rock sampling of this alteration product difficult. This is in contrast to the alkali elements which are associated with the much more homogeneously disseminated celadonite.

The enrichment of U appears to be broadly connected to the enrichment in Rb and K and so associated with the formation of celadonite during the most oxidative phase of alteration. Strong U enrichments have also been reported for the oxidatively-altered rocks of Hole 735B (Bach et al., 2001) and Hole 504B (Bach et al., 2003) as well as an U uptake connected to the precipitation of carbonate (Staudigel et al., 1996).

### 5.2.3. *Global importance*

There might appear at first inspection to be several reasons why a comparison of our results from the EXCO area with those from Leg 168 near the Juan de Fuca ridge might not be appropriate, such as the differences in sediment thicknesses and the expected temperatures at the sediment-basement interface. Nevertheless, the EXCO alteration sequence is similar to that seen at the Juan de Fuca Ridge, where Fe-oxyhydroxide+celadonite, saponite and phillipsite were sequentially deposited over a time period of 0 – 3.5 Ma (Hunter et al., 1999). The EXCO sequence shows similar stages for the precipitation of secondary minerals and element flux for initial low

temperature alteration under seawater-dominated conditions. A major difference between the EXCO and Juan de Fuca transects is that the Juan de Fuca volcanics have undergone a more pervasive reducing stage due to the overlying sediments and therefore limited seawater recharge. It is interesting to compare conditions inferred for the EXCO basaltic outcrops to those for Baby Bare, a basaltic outcrop on 3.5 Ma old crust located ~ 100 km east of the Endeavor Segment of the Juan de Fuca Ridge. There, warm fluids (25°C) that emanated from the seafloor are interpreted to have reacted at higher temperatures (62-64°C) within the crust. Spring waters are enriched in Mn, Co, Ni, and Zn, indicating that the ocean crust is a source for these elements (Wheat et al., 2000; Wheat et al., 2002). EXCO samples show that these elements are immobile, indicating that the chemical flux documented for the eastern flank of the Juan de Fuca are not representative of those away from continental margins.

The enrichments of Rb, Cs, Ba, U and K during alteration and the sequence of secondary minerals in our study are similar to those found in studies of drilled rocks of Leg 118 Hole 735 (Hart et al., 1999) and Leg 176 Hole 735B (Bach et al., 2001). Enrichments in Rb, Cs, K, U and P in gabbros from the uppermost 40 meter below sea floor (mbsf) and in rocks from 500 – 600 mbsf, respectively, are reported in these two studies. Thus it appears that, although our samples are dredged from the surface of the basaltic oceanic crust, the alteration-induced chemical changes we have documented are applicable to the low-temperature alteration of deeper parts of the basaltic or gabbroic crust.

It has been suggested, from comparisons of up to 57 Ma old basalts with either fresh precursors from the ridge axis or their palagonitized margins, that strong enrichments in REE can occur in weathered dredged basalts (Ludden and Thompson, 1979). These changes are not observed for our samples, presumably because alteration was not intense enough to mobilize REE.

Using the estimated percentages of alteration given in Table 3 and the chemical differences between altered and fresh parts of the same sample presented in Table 5 it is possible to estimate the compositional changes which will have occurred in MOR basalt within 9 Ma. As this is the least extreme but most ubiquitous alteration to be expected on the seafloor, these compositional changes will have affected ALL submarine basalts. As can be seen from Figure 8, these chemical (as opposed to mineralogical) changes have in fact been fully completed by the time the basalts are 120 kyr old. The elements are enriched significantly, after this time it is only the percentage alteration of the sample which varies with time. Table 7 shows the chemical effects of this type of seafloor weathering on two of the most commonly-used average basalt compositions – namely N-MORB from Hofmann (1988) and Sun and McDonough (1989). We expect that ALL ocean ridge basalts, with the exception of those < 120 kyr, will have suffered AT LEAST this amount of pervasive alteration. With increasing age and sediment cover it is to be expected that the exchange with seawater will cease, at which point the elements

scavenged by the rocks from seawater as shown in Table 7 will be sealed within the crust. Using a total crustal production rate of  $3.45 \times 10^6 \text{ m}^2/\text{yr}$  (Bach et al., 2003), a density for the basaltic crust of  $2800 \text{ kg/m}^3$  and a depth of 600 m to which this type of low-temperature alteration takes place (as reported in the volcanic section of Hole 504B, Alt et al., 1996a), we calculate that the crust absorbs at least  $1.3 \times 10^7 \text{ g Cs}$ ,  $3.8 \times 10^8 \text{ g Rb}$ ,  $3.5 \times 10^9 \text{ g Ba}$ ,  $1.6 \times 10^7 \text{ g U}$  and  $9.5 \times 10^{10} \text{ g K}$  per year from the oceans. Our calculated extraction of K from the ocean into the crust represents only 0.1 % of the river input ( $0.74 \cdot 10^{14} \text{ g/year}$ ) (Thompson, 1983) into the ocean. The explanation for this imbalance is that we calculate only the pervasive uptake of K in the groundmass, ignoring the amount of K taken up by secondary minerals in veins. As the altered part of the rock contains voids and veins filled with secondary minerals, the total uptake of K into the crust will be much higher. The volume of rock being altered is so miniscule relative to the volume of the oceans that this scavenging has no noticeable effect ( $< 0.0001\%$  change) on the composition of the oceans. The composition of the oceanic crust, on the other hand, is affected significantly.

	Hofmann (1988)		Sun & McDonough (1989)	
	N-MORB	altered <sup>a</sup>	N-MORB	altered <sup>a</sup>
SiO <sub>2</sub>	50.45	50.43		
TiO <sub>2</sub>	1.615	1.611	Ti 7600	7582
Al <sub>2</sub> O <sub>3</sub>	15.255	15.255		
Fe <sub>2</sub> O <sub>3</sub>	10.426	10.429		
MgO	7.576	7.571		
CaO	11.303	11.304		
Na <sub>2</sub> O	2.679	2.678		
K	883.7	901.5	600	612
P			510	514
Li			4.3	4.3
Sc	41.37	41.37		
Co	47.07	47.15		
Ni	149.5	149.7		
Cu	74.4	74.5		
Rb	1.262	1.335	0.56	0.59
Sr	113.2	113.2	90	90
Y	35.82	35.84	28	28
Zr	104.24	104.43	74	74
Nb	3.507	3.512	2.33	2.33
Cs	0.01408	0.01618	0.007	0.008
Ba	13.87	14.71	6.3	6.7
La	3.895	3.913	2.5	2.5
Ce	12.001	12.008	7.5	7.5
Pr	2.074	2.076	1.32	1.32
Nd	11.179	11.185	7.3	7.3
Sm	3.752	3.752	2.63	2.63
Eu	1.335	1.335	1.02	1.02
Gd	5.077	5.076	3.68	3.68
Tb	0.885	0.885	0.67	0.67
Dy	6.304	6.303	4.55	4.55
Ho	1.342	1.342	1.01	1.01
Er	4.143	4.143	2.97	2.97
Tm	0.621	0.621	0.456	0.456
Yb	3.900	3.900	3.05	3.05
Lu	0.589	0.589	0.455	0.455
Hf	2.974	2.974	2.05	2.05
Ta	0.192	0.192	0.132	0.132
Pb	0.489	0.507	0.30	0.31
Th	0.1871	0.1879	0.12	0.12
U	0.0711	0.0739	0.047	0.049

**Table 7.** The calculated effects from pervasive seafloor weathering for rocks  $>120$  kyr of two of the most commonly-used average basalt compositions (Hofmann, 1988; Sun and McDonough, 1989). Rb, Cs, Ba, U and K are expected to be mobile during alteration, other elements show only minor changes and are given for completeness. Altered composition is calculated on the basis of Table 5 (rocks from 0.12 – 8.64 Ma).

$$^a \text{Altered composition: } C_i + C_i \cdot \left( \sum_{i=1}^n \frac{E_i \cdot S_i}{100 \cdot n} \right) / 100$$

$C_i$  = Element concentration in N-MORB.

$E_i$  = Gain or loss of element concentration in percent from EXCO rocks (from Table 5).

$S_i$  = Altered sample in percent from EXCO rocks (from Table 5).

## 6. Summary & conclusions

The EXCO sampling transect documents changing conditions in the uppermost oceanic crust with age over the time period 0-9 Ma. Secondary mineral assemblages and chemical fluxes documented for discrete crustal ages provide key constraints concerning the timing of alteration stages. Samples from the ridge axis contain no secondary minerals and nearly no chemical change (<1 % alteration). Secondary minerals develop surprisingly very early, between 0.015 and 0.12 Ma. The 0.12 Ma old sample contains, with the exception of phillipsite, all identified secondary minerals. The first occurrence of phillipsite is found at 1.16 Ma. Over the following 8 Ma no other new minerals join the alteration assemblage and based on local parameters, only the redox conditions of the fluids circulating through the rocks and the intensity of the alteration appear to change. The dominant secondary minerals in our studied samples are celadonite (0.12 – 4.6 Ma) and phillipsite in rocks older than 6 Ma.

The transition from oxidizing to more reducing alteration conditions is consistently evident in crust  $\geq 2.92$  Ma, reflecting the continued evolution of the fluid as it becomes isolated from the open ocean through the formation of alteration rinds and sealing of fractures with secondary minerals and, away from basement exposures, by the progressive thickening of the sediment blanket. Alteration begins with the palagonisation of glass and the formation of Fe-oxyhydroxides. During the next stage of alteration, K bearing minerals (iron oxyhydroxide-celadonite) become the dominate phases which require substantial supplies of Fe and K from very low temperature seawater-dominated fluids. Iron that is necessary for the precipitation of iron oxyhydroxide is available from the breakdown of olivine and the reactions occurring during the penetration of seawater through the rock (e.g. dissolution of glass) or from reactions of the fluid with the deeper basement.

The onset of saponite formation at  $\sim 2.92$  Ma marks a change from seawater-dominated circulating fluids to more reducing fluids, a change from Mg to Fe-rich saponite compositions also reflects ever more reducing fluids. Phillipsite joins the secondary mineral assemblage at 1.16 Ma, always associated with glass dissolution and is the dominant secondary phase in crust  $>6$  Ma.

The uptake of  $K_2O$ , Rb, Cs, Ba and U in altered basalts indicate oxidizing conditions and high water/rock ratios, and occurs within a few million years of crustal formation. The geochemical flux is considerable higher off-axis, but the gain and loss of elements in the off-axis appears only to be influenced by local parameters such as basement topography and the reaction of the circulating fluids within the rock and not upon time. The geochemical flux is only slightly higher than those calculated for Hole 504B, but significantly lower (one tenth) than in DSDP 417/418, probably the most intense of any DSDP/ODP basement core. The seawater - ocean crust exchange relative to the volume of the ocean is so small that there is no effect on the composition of seawater,

but considerable changes in bulk chemical properties of altered ocean crust occur. This means that the average composition of the upper oceanic crust cannot be taken as that of N-MORB using compiled literature values but that a correction factor for alteration must be taken into account.

### **Acknowledgements**

The authors wish to thank Captain Papenhagen and his crew for the excellent support during the SO145/2 sampling work. Andreas Kronz (Univ. Göttingen), Burkhard Schulz-Dobrick (Univ. Mainz) and Anette von der Handt (MPI Mainz) are thanked for assistance with the microprobe analyses, Dieter Garbe-Schönberg (Univ. Kiel) kindly provided ICP-MS analyses and Karsten Haase XRF analyses. Jan Scholten (Univ. Kiel) is thanked for able assistance with the XRD measurements. This study was supported by BMBF grant 03G0145A.

file	21DS1 glass repeat						BHVO-1.D 0.495					accuracy	BIR-1HA.D		0.201		accuracy	
Sample	21DS1 glass	21DS1 glass rep1	21DS1 glass rep2	21DS1 glass rep3	21DS1 average	SD (%)	BHVO-1 20282	BHVO-1 20414	BHVO-1 average	BHVO-1 SD(%)	BHVO-1 standard	deviation ave-std	BIR-1 19808	BIR-1 20413	BIR-1 average	BIR-1 SD(%)	BIR-1 standard	deviation ave-std
Li	6.4	6.4	6.1	5.7	6.2	5.3%	4.6	4.6	4.6	0.8%	4.6	-0.3%	3.0	3.1	3.1	2.8%	3.6	-15.0%
Sc	43.1	43.1	40.8	38.5	41.4	5.3%	33.1	30.4	31.8	6.0%	31.8	0.0%	43.6	43.9	43.7	0.5%	44.0	-0.6%
V	320	320	307	294	311	4.1%	358	311	334	10.0%	317	5.4%	341	341	341	0.0%	310	10.1%
Cr	245	245	235	225	238	4.1%	304	286	295	4.1%	289	2.1%	413	380	397	5.8%	370	7.2%
Co	38.6	38.6	37.3	36.0	37.6	3.3%	46.9	43.4	45.2	5.6%	45.0	0.3%	51.5	51.0	51.2	0.7%	52.0	-1.5%
Ni	65.2	65.2	62.8	60.5	63.4	3.6%	122	124	123	1.2%	121	1.5%	164	164	164	0.0%	170	-3.5%
Cu	63.3	63.3	60.8	59.0	61.6	3.3%	143	132	138	5.3%	136	1.2%	117	113	115	2.6%	125	-7.8%
Zn	140	140	135	134	137	2.4%	108	106	107	1.2%	105	1.7%	65.4	62.6	64.0	3.1%	70.0	-8.6%
Ga	15.3	15.3	15.2	15.0	15.2	1.0%	25.1	27.1	26.1	5.4%	21.0	24.5%	16.9	14.4	15.6	11.5%	16.0	-2.3%
Rb	1.19	1.19	1.22	1.19	1.20	1.1%	10.0	9.1	9.6	6.5%	11.0	-13.0%	0.20	0.20	0.20	1.7%		
Sr	122	122	123	123	122	0.5%	446	391	419	9.4%	403	3.8%	114	111	112	2.2%	110	2.0%
Y	32.0	32.0	32.0	31.7	31.9	0.4%	26.5	24.1	25.3	6.9%	28.0	-9.6%	14.9	14.9	14.9	0.2%	16.0	-6.9%
Zr	103	103	102	101	102	0.8%	194	166	180	10.7%	179	0.6%	14.2	14.5	14.4	1.6%	18.0	-20.1%
Nb	2.7	2.7	2.6	2.6	2.7	0.9%	19.2	16.8	18.0	9.5%	19.0	-5.4%	0.52	0.51	0.52	1.0%	0.60	-13.9%
Cs	0.02	0.02	0.02	0.02	0.02	4.0%	0.10	0.11	0.11	0.9%	0.13	-19.1%	0.00	0.01	0.01	11.4%		
Ba	11.2	11.2	11.3	11.2	11.2	0.2%	147	131	139	8.3%	139	-0.2%	6.8	6.7	6.8	2.0%	7.0	-3.5%
La	3.7	3.7	3.6	3.6	3.6	0.7%	16.9	15.2	16.0	7.5%	16.0	0.2%	0.63	0.63	0.63	0.2%	0.63	-0.1%
Ce	11.7	11.7	11.6	11.5	11.6	0.8%	40.6	37.7	39.2	5.2%	39.0	0.5%	1.87	1.94	1.91	2.6%	2.0	-4.7%
Pr	2.0	2.0	2.0	2.0	2.0	0.9%	5.9	5.4	5.7	6.0%	6.0	-5.6%	0.38	0.39	0.39	1.8%		
Nd	10.8	10.8	10.8	10.7	10.8	0.6%	26.8	24.3	25.6	6.9%	25.0	2.4%	2.4	2.4	2.4	0.2%	2.5	-3.4%
Sm	3.8	3.8	3.8	3.8	3.8	0.6%	6.8	6.2	6.5	5.6%	6.2	4.9%	1.12	1.16	1.14	2.5%	1.10	3.8%
Eu	1.34	1.34	1.35	1.33	1.34	0.5%	2.23	2.07	2.15	5.4%	2.06	4.3%	0.53	0.54	0.54	1.3%	0.55	-2.4%
Gd	5.0	5.0	4.9	4.9	4.9	0.8%	6.7	6.2	6.5	5.7%	6.4	0.9%	1.85	1.87	1.86	0.8%	1.8	3.5%
Tb	0.89	0.89	0.90	0.89	0.89	0.3%	1.03	0.93	0.98	7.0%	0.96	2.0%	0.37	0.37	0.37	0.4%		
Dy	6.1	6.1	6.1	6.0	6.0	0.4%	5.8	5.4	5.6	5.4%	5.2	7.7%	2.6	2.7	2.7	1.3%	4.0	-33.3%
Ho	1.28	1.28	1.28	1.28	1.28	0.1%	1.08	0.99	1.04	6.2%	0.99	5.0%	0.59	0.59	0.59	0.1%		
Er	3.6	3.8	3.8	3.8	3.7	2.7%	2.7	2.5	2.6	7.5%	2.4	7.5%	1.72	1.71	1.72	0.7%		
Tm	0.53	0.53	0.54	0.54	0.53	1.0%	0.36	0.34	0.35	4.3%	0.33	5.5%	0.26	0.25	0.26	0.6%		
Yb	3.4	3.4	3.5	3.5	3.5	1.6%	2.2	2.0	2.1	5.0%	2.0	5.5%	1.71	1.68	1.69	1.1%	1.70	-0.3%
Lu	0.51	0.51	0.53	0.52	0.52	1.4%	0.30	0.27	0.29	6.6%	0.29	-1.3%	0.26	0.25	0.25	0.6%	0.26	-2.3%
Hf	2.8	2.8	2.9	2.8	2.8	0.9%	5.0	4.7	4.8	4.5%	4.4	10.0%	0.62	0.62	0.62	0.4%	0.60	3.9%
Ta	0.19	0.19	0.19	0.19	0.19	0.1%	1.25	1.13	1.19	7.4%	1.20	-0.8%	0.04	0.04	0.04	0.3%		
Pb	1.26	1.26	1.28	1.31	1.28	1.9%	2.2	2.1	2.2	4.3%	2.6	-17.2%	3.2	3.0	3.1	4.4%	3.0	3.6%
Th	0.18	0.18	0.18	0.19	0.18	1.6%	1.38	1.24	1.31	7.2%	1.10	19.3%	0.03	0.03	0.03	4.2%		
U	0.06	0.06	0.06	0.07	0.06	5.3%	0.47	0.43	0.45	5.9%			0.01	0.01	0.01	1.3%		

Appendix 1. Data quality control information derived from the analysis of sample repeats, standard reference material and blanks for trace elements by ICP-MS.

file	BHVO-2 repeat									accuracy	141.D	155.D	156.D	173.D	174.D	186	187	BHVO-2			accuracy
Sample	BHVO-2	BHVO-2 rep1	BHVO-2 rep2	BHVO-2 rep3	BHVO-2 average	BHVO-2 SD(%)	BHVO-2 standard	accuracy deviation ave-std		BHVO-2	BHVO-2	BHVO-2	BHVO-2	BHVO-2	BHVO-2a	BHVO-2b	BHVO-2 average	BHVO-2 SD(%)	BHVO-2 standard	accuracy deviation ave-std	
Li	3.6	3.7	3.9	4.0	3.8	5.2%	5.0	-23.6%		3.6	3.6	3.4	3.3	3.4	4.6	4.5	3.8	11.8%	5.0	-24.3%	
Sc	28.9	30.9	31.9	32.5	31.1	5.1%	32.0	-2.9%		28.9	29.5	28.2	27.5	28.6	31.9	32.0	30.1	6.0%	32.0	-6.0%	
V	304	323	331	335	323	4.3%	317	2.0%		306	314	300	287	302	320	321	313	4.6%	317	-1.3%	
Cr	281	294	305	306	297	3.9%	280	5.9%		281	287	274	271	278	268	269	283	4.8%	280	1.1%	
Co	40.5	41.8	42.3	43.1	41.9	2.6%	45.0	-6.8%		40.7	41.3	39.3	37.9	39.4	42.5	42.6	41.0	4.0%	45.0	-8.8%	
Ni	105	108	110	110	108	2.2%	119	-9.2%		105	108	101	102	103	111	113	107	3.7%	119	-10.3%	
Cu	111	114	116	116	114	2.3%	127	-9.9%		111	113	108	107	109	116	117	113	3.2%	127	-11.2%	
Zn	88.7	92.7	94.4	94.8	92.6	3.0%	103	-10.1%		92.5	112	87.1	93.1	124	101	90.1	97.3	11.5%	103	-5.5%	
Ga	21.6	22.5	22.8	22.8	22.4	2.5%	21.7	3.4%		21.7	22.2	21.2	20.5	21.2	25.5	25.6	22.5	7.3%	21.7	3.8%	
Rb	8.6	8.8	9.0	9.0	8.9	2.1%	9.8	-9.7%		8.64	8.86	8.46	8.22	8.47	8.88	8.91	8.71	2.9%	9.80	-11.1%	
Sr	389	398	402	401	398	1.5%	389	2.2%		388	398	378	368	379	388	387	389	2.8%	389	0.0%	
Y	23.0	23.5	23.7	23.7	23.5	1.5%	26.0	-9.8%		23.1	23.6	22.6	21.9	22.6	23.8	23.7	23.2	2.7%	26.0	-10.8%	
Zr	169	171	175	173	172	1.5%	172	-0.2%		169	173	166	160	166	165	164	168	2.7%	172	-2.3%	
Nb	16.6	16.8	16.9	16.8	16.8	0.7%	18.0	-6.7%		16.8	17.0	16.2	15.8	16.2	16.7	16.6	16.6	2.2%	18.0	-7.9%	
Cs	0.09	0.09	0.09	0.09	0.09	0.9%				0.09	0.10	0.09	0.08	0.09	0.11	0.11	0.09	8.7%			
Ba	130	130	130	129	130	0.4%	130	-0.1%		131	133	126	122	126	129	129	129	2.3%	130	-0.9%	
La	14.7	14.5	14.5	14.5	14.5	0.5%	15.0	-3.0%		14.8	15.0	14.3	13.8	14.2	14.8	14.8	14.5	2.4%	15.0	-3.1%	
Ce	35.5	35.1	35.1	34.8	35.1	0.8%	38.0	-7.5%		35.5	36.1	34.5	33.3	34.1	37.0	36.9	35.3	3.1%	38.0	-7.2%	
Pr	5.1	5.1	5.1	5.1	5.1	0.8%				5.1	5.2	5.0	4.9	5.0	5.3	5.3	5.1	2.8%			
Nd	23.6	23.4	23.4	23.2	23.4	0.7%	25.0	-6.6%		23.7	24.1	23.1	22.2	22.7	24.1	24.1	23.4	2.5%	25.0	-6.4%	
Sm	6.0	5.9	5.9	5.9	5.9	1.0%	6.2	-4.6%		6.0	6.1	5.8	5.6	5.7	6.2	6.2	5.9	2.9%	6.2	-4.2%	
Eu	1.97	1.95	1.95	1.93	1.95	0.8%				1.97	2.0	1.93	1.86	1.90	2.0	2.0	1.96	2.8%			
Gd	5.9	5.8	5.8	5.7	5.8	1.3%	6.3	-7.7%		6.0	6.0	5.8	5.6	5.7	6.2	6.2	5.9	3.3%	6.3	-6.7%	
Tb	0.92	0.90	0.89	0.88	0.90	1.8%	0.90	-0.2%		0.92	0.94	0.89	0.86	0.88	0.94	0.93	0.90	2.9%	0.90	0.5%	
Dy	5.2	5.1	5.1	5.0	5.1	1.5%				5.2	5.3	5.1	4.9	5.0	5.4	5.4	5.2	3.2%			
Ho	0.96	0.95	0.95	0.93	0.95	1.5%	1.04	-8.9%		0.98	0.99	0.94	0.91	0.93	0.98	0.98	0.95	2.7%	1.04	-8.3%	
Er	2.4	2.4	2.4	2.4	2.4	1.3%				2.4	2.5	2.4	2.3	2.3	2.4	2.4	2.4	2.3%			
Tm	0.32	0.32	0.31	0.31	0.32	2.0%				0.32	0.33	0.31	0.30	0.31	0.32	0.33	0.32	2.7%			
Yb	1.9	1.9	1.9	1.9	1.9	1.8%	2.0	-5.2%		1.95	1.98	1.91	1.82	1.88	1.95	1.96	1.91	2.6%	2.0	-4.4%	
Lu	0.27	0.26	0.26	0.26	0.26	2.2%	0.28	-6.2%		0.27	0.28	0.26	0.25	0.26	0.27	0.27	0.26	2.5%	0.28	-5.6%	
Hf	4.5	4.3	4.3	4.2	4.3	2.2%	4.1	5.8%		4.5	4.5	4.4	4.1	4.3	4.4	4.5	4.4	2.7%	4.1	6.4%	
Ta	1.11	1.09	1.07	1.05	1.08	2.2%	1.40	-22.7%		1.12	1.14	1.09	1.05	1.08	1.10	1.10	1.09	2.4%	1.40	-22.1%	
Pb	1.78	1.79	1.77	1.78	1.78	0.4%				1.45	1.71	1.42	1.53	1.39	1.44	1.31	1.58	12.0%			
Th	1.22	1.23	1.22	1.22	1.22	0.4%	1.20	1.8%		1.23	1.24	1.19	1.15	1.18	1.16	1.16	1.20	2.7%	1.20	-0.1%	
U	0.41	0.41	0.41	0.41	0.41	0.6%				0.42	0.43	0.41	0.39	0.40	0.53	0.39	0.42	9.2%			

Appendix 1. (continued)

file	138.D	139.D	169.D	170.D	171.D	172.D	184	185			WASH4D	WASH5.D	
Sample	blank	blank	blank	blank	blank	blank	Blank1	Blank2	blank average	System-blank	wash4	wash5	wash average
Li	0.00	0.01	0.01	0.00	0.00	0.00	-0.03	-0.03	0.00	0.00	0.00	0.00	0.00
Sc	0.02	0.03	0.03	0.02	0.03	0.02	0.00	0.00	0.02	0.00	0.12	0.15	0.13
V	-0.05	0.13	0.01	-0.02	-0.03	-0.05	0.00	-0.02	0.00	0.00	0.08	-0.05	0.02
Cr	0.11	0.26	0.13	0.14	0.09	0.06	0.06	0.05	0.11	0.00	0.18	0.03	0.11
Co	0.03	0.05	0.02	0.05	0.03	0.03	0.01	0.02	0.03	0.00	0.02	0.00	0.01
Ni	0.03	0.11	0.05	0.10	0.06	0.02	0.01	0.00	0.04	0.00	0.06	-0.01	0.03
Cu	0.03	0.11	0.04	0.08	0.09	0.02	0.00	0.02	0.15	0.00	0.05	0.00	0.02
Zn	2.90	1.96	1.10	6.70	3.78	3.47	1.00	3.68	3.07	0.00	0.03	-0.02	0.01
Ga	0.00	0.02	0.01	0.00	0.00	0.00	0.02	0.02	0.01	0.02	0.02	0.01	0.01
Rb	0.00	0.00	0.00	0.00	0.00	0.00	0.00	0.00	0.00	0.00	0.00	0.00	0.00
Sr	0.01	0.11	0.06	0.04	0.04	0.01	0.00	-0.02	0.03	0.00	0.10	0.00	0.05
Y	0.01	0.01	0.00	0.00	0.02	0.00	0.01	0.00	0.01	0.00	0.01	0.00	0.01
Zr	0.18	0.09	0.02	0.02	0.11	0.01	0.11	0.00	0.07	0.00	0.05	0.00	0.03
Nb	0.00	0.01	0.00	0.00	0.00	0.00	0.00	0.00	0.00	0.00	0.00	0.00	0.00
Cs	0.00	0.00	0.00	0.00	0.00	0.00	0.00	0.00	0.00	0.00	0.00	0.00	0.00
Ba	0.03	0.04	0.03	0.04	0.03	0.02	0.02	0.00	0.03	0.00	0.02	0.00	0.01
La	0.00	0.00	0.00	0.00	0.00	0.00	0.00	0.00	0.00	0.00	0.00	0.00	0.00
Ce	0.00	0.01	0.00	0.00	0.00	0.00	0.00	0.00	0.00	0.00	0.01	0.00	0.00
Pr	0.00	0.00	0.00	0.00	0.00	0.00	0.00	0.00	0.00	0.00	0.00	0.00	0.00
Nd	0.00	0.00	0.00	0.00	0.00	0.00	0.00	0.00	0.00	0.00	0.00	0.00	0.00
Sm	0.00	0.00	0.00	0.00	0.00	0.00	0.00	0.00	0.00	0.00	0.00	0.00	0.00
Eu	0.00	0.00	0.00	0.00	0.00	0.00	0.00	0.00	0.00	0.00	0.00	0.00	0.00
Gd	0.00	0.00	0.00	0.00	0.00	0.00	0.00	0.00	0.00	0.00	0.00	0.00	0.00
Tb	0.00	0.00	0.00	0.00	0.00	0.00	0.00	0.00	0.00	0.00	0.00	0.00	0.00
Dy	0.00	0.00	0.00	0.00	0.00	0.00	0.00	0.00	0.00	0.00	0.00	0.00	0.00
Ho	0.00	0.00	0.00	0.00	0.00	0.00	0.00	0.00	0.00	0.00	0.00	0.00	0.00
Er	0.00	0.00	0.00	0.00	0.00	0.00	0.00	0.00	0.00	0.00	0.00	0.00	0.00
Tm	0.00	0.00	0.00	0.00	0.00	0.00	0.00	0.00	0.00	0.00	0.00	0.00	0.00
Yb	0.00	0.00	0.00	0.00	0.00	0.00	0.00	0.00	0.00	0.00	0.00	0.00	0.00
Lu	0.00	0.00	0.00	0.00	0.00	0.00	0.00	0.00	0.00	0.00	0.00	0.00	0.00
Hf	0.01	0.00	0.00	0.00	0.00	0.00	0.00	0.00	0.00	0.00	0.00	0.00	0.00
Ta	0.00	0.00	0.00	0.00	0.00	0.00	0.00	0.00	0.00	0.00	0.00	0.00	0.00
Pb	0.02	0.02	0.01	0.03	0.05	0.01	0.00	0.01	0.02	0.00	0.00	0.00	0.00
Th	0.00	0.00	0.00	0.00	0.00	0.00	0.00	0.00	0.00	0.00	0.00	0.00	0.00
U	0.00	0.00	0.00	0.00	0.00	0.00	0.00	0.00	0.00	0.00	0.00	0.00	0.00

Appendix 1. (continued)

sample	standard deviation														
	21DS4	18DS9	20DS3	22DS2	28DS1	28DS3	29DS2	29DS3	35DS2	9DS2	9DS4	9DS8	36DS8	42DS10	43DS13
Ma	0	0,015	0,015	0,12	0,65	0,65	1,16	1,16	2,56	2,92	2,92	2,92	4,6	6,84	8,64
n	10	10	5	25	10	10	10	10	9	11	9	10	7	7	10
SiO <sub>2</sub>	0,25	0,24	0,07	0,22	0,23	0,23	0,16	0,06	0,16	0,23	0,28	0,20	0,32	0,54	0,21
TiO <sub>2</sub>	0,05	0,02	0,03	0,04	0,02	0,03	0,02	0,04	0,06	0,03	0,05	0,05	0,03	0,05	0,04
Al <sub>2</sub> O <sub>3</sub>	0,14	0,07	0,19	0,09	0,06	0,08	0,07	0,11	0,09	0,08	0,10	0,11	0,09	0,13	0,11
FeO	0,15	0,10	0,13	0,07	0,06	0,07	0,11	0,06	0,08	0,13	0,13	0,11	0,09	0,13	0,09
MnO	0,01	0,02	0,02	0,02	0,02	0,03	0,03	0,01	0,02	0,03	0,02	0,01	0,02	0,02	0,02
MgO	0,11	0,08	0,10	0,07	0,07	0,09	0,04	0,05	0,15	0,09	0,11	0,10	0,10	0,16	0,05
CaO	0,17	0,13	0,08	0,10	0,09	0,07	0,09	0,11	0,08	0,06	0,15	0,12	0,08	0,08	0,08
Na <sub>2</sub> O	0,06	0,07	0,07	0,07	0,04	0,05	0,09	0,03	0,06	0,07	0,11	0,09	0,06	0,09	0,05
K <sub>2</sub> O	0,01	0,01	0,01	0,01	0,01	0,01	0,02	0,01	0,01	0,02	0,01	0,01	0,01	0,02	0,01
P <sub>2</sub> O <sub>5</sub>	0,04	0,03	0,04	n.d.	0,02	0,02	0,04	0,04	0,03	0,02	0,03	0,02	0,02	0,02	0,02
Cr <sub>2</sub> O <sub>3</sub>	0,01	0,02	0,02	0,02	0,01	0,02	0,02	0,01	0,03	0,01	0,02	0,02	0,02	0,03	0,01

Appendix 2. Standard deviation of microprobe analyses together with the number of individual spots measured and used to calculate the mean values.

sample	BHVO-1						accuracy deviation ave-std
	BHVO-1 1	BHVO-1 2	BHVO-1 2	BHVO-1 average	BHVO-1 SD(%)	BHVO-1 standard	
SiO <sub>2</sub>	50,0	49,9	49,8	49,9	0,2%	49,9	-0,1%
TiO <sub>2</sub>	2,8	2,8	2,8	2,8	0,2%	2,7	1,6%
Al <sub>2</sub> O <sub>3</sub>	13,7	13,6	13,6	13,6	0,5%	13,8	-1,1%
Fe <sub>2</sub> O <sub>3</sub>	12,0	12,2	12,3	12,2	1,4%	12,2	-0,5%
MnO	0,16	0,16	0,17	0,16	3,5%	0,17	-3,9%
MgO	7,3	7,2	7,2	7,2	1,1%	7,2	0,0%
CaO	11,5	11,4	11,4	11,4	0,7%	11,4	0,1%
Na <sub>2</sub> O	2,5	2,5	2,4	2,5	1,0%	2,3	9,1%
K <sub>2</sub> O	0,54	0,53	0,54	0,54	1,1%	0,52	3,2%
P <sub>2</sub> O <sub>5</sub>	0,29	0,28	0,29	0,29	2,0%	0,27	5,0%
total	100,8	100,4	100,5	100,5	0,2%	100,5	0,0%

Appendix 3. Data quality control information derived from the analysis of standard reference material for major elements by XRF.

## References

- Alt, J.C., 1993. Low-temperature alteration of basalts from the Hawaiian Arch, Leg 136. Proceedings of the Ocean Drilling Program, Scientific Results, 136: 133-146.
- Alt, J.C., 1999. Very Low Grade Metamorphism of Basic Igneous Rocks. In: M. Frey and D. Robinson (Editors), Low Grade Metamorphism. Blackwell Scientific, pp. 169-201.
- Alt, J.C. and Bach, W., 2001. Data Report: Low-Grade Hydrothermal Alteration of Uplifted Lower Oceanic Crust, Hole 735B: Mineralogy and Isotope Geochemistry. Proceedings of the Ocean Drilling Program, Scientific Results, 176: 1-24 (Online).
- Alt, J.C., France-Lanord, C., Floyd, P.A., Castillo, P. and Galy, A., 1992. Low-temperature hydrothermal alteration of Jurassic ocean crust, Site 801. Proceedings of the Ocean Drilling Program, Scientific Results, 129: 415-427.
- Alt, J.C. and Honnorez, J., 1984. Alteration of the upper oceanic crust, DSDP Site 417: Mineralogy and chemistry. Contributions to Mineralogy and Petrology, 87: 149-169.
- Alt, J.C., Laverne, C., Vanko, D.A., Tartarotti, P., Teagle, D.A.H., Bach, W., Zuleger, E., Erzinger, J., Honnorez, J., Pezard, P.A., Becker, K., Salisbury, M.H. and Wilkens, R.H., 1996a. Hydrothermal alteration of a section of upper oceanic crust in the eastern equatorial Pacific: a synthesis of results from Site 504 (DSDP Legs 69, 70, and 83, and ODP Legs 111, 137, 140, and 148). In: J.C. Alt, H. Kinoshita and L.B. Stokking (Editors), Proceedings of the Ocean Drilling Program; Scientific Results. Ocean Drilling Program, College Station, TX, pp. 417-434.
- Alt, J.C., Teagle, D.A.H., Laverne, C., Vanko, D.A., Bach, W., Honnorez, J., Becker, K., Ayadi, M. and Pezard, P.A., 1996b. Ridge flank alteration of upper ocean crust in the eastern Pacific; synthesis of results for volcanic rocks of holes 504B and 896A. Proceedings of the Ocean Drilling Program, Scientific Results, 148: 435-450.
- Andrews, A.J., 1980. Saponite and celadonite in layer 2 basalts, DSDP Leg 37. Contributions to Mineralogy and Petrology, 73(4): 323-340.
- Bach, W., Alt, J.C., Nio, Y., Humphris, S.E., Erzinger, J. and Dick, H.J.B., 2001. The geochemical consequences of late-stage low-grade alteration of lower ocean crust at the SW Indian Ridge; results from ODP Hole 735B (Leg 176). Geochimica et Cosmochimica Acta, 65(19): 3267-3287.

- Bach, W., Peucker-Ehrenbrink, B., Hart, S.R. and Blusztajn, J.S., 2003. Geochemistry of hydrothermally altered oceanic crust: DSDP/ODP Hole 504B - Implications for seawater-crust exchange budgets and Sr- and Pb-isotopic evolution of the mantle. *Geochemistry, Geophysics, Geosystems*, G<sup>3</sup>, an electronic journal of the earth sciences, 4(3): (29).
- Becker, K., 1996. Permeability measurements in Hole 896A and implications for the lateral variability of upper crustal permeability at sites 504 and 896. In: J.C. Alt, H. Kinoshita and L.B. Stokking (Editors), *Proceedings of the Ocean Drilling Program; Scientific results*. Ocean Drilling Program, College Station, TX, pp. 353-363.
- Böhlke, J.K., Honnorez, J., Honnorez-Guerstein, B.M., Muehlenbachs, K. and Petersen, N., 1981. Heterogeneous Alteration of the Upper Oceanic Crust: Correlation of Rock Chemistry, Magnetic Properties, and O Isotope Ratios with Alteration Patterns in Basalts from Site 396B, DSDP. *Journal of Geophysical Research*, 86(B9): 7935-7950.
- Buatier, M.D., Monnin, C., Früh-Green, G.L. and Karpoff, A.-M., 2001. Fluid-sediment interactions related to hydrothermal circulation in the Eastern Flank of the Juan de Fuca Ridge. *Chemical Geology*, 175: 343-360.
- Carlson, R.L., 1998. Seismic velocities in the uppermost oceanic crust: Age dependence and the fate of layer 2A. *Journal of Geophysical Research*, 103(4): 7069-7077.
- Cormier, M.H., Scheirer, D.S. and MacDonald, K.C., 1996. Evolution of the East Pacific Rise at 16-19S since 5 Ma; bisection of overlapping spreading centers by new, rapidly propagating ridge segments. *Marine Geophysical Researches*, 18(1): 53-84.
- DeMets, C., Gordon, R.G., Argus, D.F. and Stein, S., 1994. Effect of recent revisions to the Geomagnetic Reversal Time Scale on estimates of current plate motions. *Geophysical Research Letters*, 21: 2191-2194.
- Devey, C.W., Bond, Z., Dunk, R., Gharib, J., Junge, G., Lackschewitz, K., Lear, C., Mottl, M., Pracht, J., Rudnicki, M., Scholz, C., Schramm, B., Severmann, S. and Wheat, G., 2000. Report and preliminary results of Sonne cruise SO145/2 (EXCO-II), Talcahuano (Chile) - Arica (Chile). 164, *Berichte aus dem Fachbereich Geowissenschaften Universität Bremen*.
- Elderfield, H., Wheat, C.G., Mottl, M.J., Monnin, C. and Spiro, B., 1999. Fluid and geochemical transport through oceanic crust: A transect across the eastern flank of the Juan de Fuca Ridge. *Earth and Planetary Science Letters*, 172: 151-165.

- Fisher, A.T., 1998. Permeability within basaltic oceanic crust. *Reviews of Geophysics*, 36(2): 143-182.
- Fisher, A.T., Becker, K. and Narasimhan, R.N., 1994. Off-axis hydrothermal circulation: Parametric tests of a refined model of processes at Deep Sea Drilling Project/Ocean Drilling Program Site 504. *Journal of Geophysical Research*, 99: 3097-3123.
- Fisher, A.T., Becker, K., Narasimhan, T.N., Langseth, M.G. and Mottl, M.J., 1990. Passive off-axis convection through the southern flank of the Costa Rica Rift. *Journal of Geophysical Research*, 95: 9343-9370.
- Garbe-Schönberg, D., 1993. Simultaneous determination of 37 trace elements in 28 international rock standards by ICP/MS. *Geostandards Newsletter*, 17: 81-97.
- Gillis, K.M., 1987. Multistage alteration of the extrusive sequence, Troodos ophiolite, Cyprus. Ph.D. Thesis, Dalhousie University, Halifax, 387 pp.
- Govindaraju, K., 1994. 1994 compilation of working values and descriptions for 383 geostandards. *Geostandards Newsletter*, 118: 1-158.
- Grant, J.A., 1986. The Isocon Diagram - a simple solution to Gresens' Equation for metasomatic alteration. *Economic Geology*, 81: 1976-1982.
- Gresens, R.L., 1967. Composition-volume relationships of metasomatism. *Chemical Geology*, 2: 47-65.
- Grevemeyer, I., Kaul, N., Villinger, H. and Weigel, W., 1999. Hydrothermal activity and the evolution of the seismic properties of upper oceanic crust. *Journal of Geophysical Research*, 104(B3): 5069-5079.
- Grevemeyer, I., Schramm, B., Devey, C.W., Jochum, B., Wilson, D.S., Hauschild, J., Aric, K., Villinger, H. and Weigel, W., 2002. A multibeam-sonar, magnetic and geochemical flow-line survey at 14°14's on the southern East Pacific Rise - insights into the fourth dimension of ridge crest segmentation. *Earth and Planetary Science Letters*, 199(3-4): 359-372.
- Grevemeyer, I. and Weigel, W., 1996. Seismic velocities of the uppermost igneous crust versus age. *Geophysical Journal International*, 124(2): 631-635.
- Grevemeyer, I. and Weigel, W., 1997. Increase of seismic velocities in upper oceanic crust: The "superfast" spreading East Pacific Rise at 14°14'S. *Geophysical Research Letters*, 24: 217-220.
- Hart, R.A., 1973. Geochemical and Geophysical Implications of the Reaction between Seawater and the Oceanic Crust. *Nature*, 243: 76-78.
- Hart, R.A., Erlank, A.J. and Kable, E.J.D., 1974. Sea floor basalt alteration: some chemical and Sr isotopic effects. *Contributions to Mineralogy and Petrology*, 44: 219-230.

- Hart, S.R., Blusztajn, J., Dick, H.J.B., Meyer, P.S. and Muehlenbachs, K., 1999. The fingerprint of seawater circulation in a 500-meter section of ocean crust gabbros. *Geochimica et Cosmochimica Acta*, 63(23-24): 4059-4080.
- Hauschild, J., Grevemeyer, I., Kaul, N. and Villinger, H., 2003. Asymmetric sedimentation on young ocean floor at the East Pacific Rise, 15°S. *Marine Geology*, 193(1-2): 49-59.
- Hékinian, R., 1973. Petrology of rocks from the northeastern Indian Ocean basins and the Ninety East Ridge. *Eos, Transactions, American Geophysical Union*, 54(11): 1006-1008.
- Hofmann, A.W., 1988. Chemical differentiation of the Earth: The relationship between mantle, continental crust, and oceanic crust. *Earth and Planetary Science Letters*, 90: 297-314.
- Humphris, S.E., Alt, J.C., Teagle, D.A.H. and Honnorez, J.J., 1998. Geochemical changes during hydrothermal alteration of basement in the stockwork beneath the active TAG hydrothermal mound. In: P.M. Herzig, S.E. Humphris, D.J. Miller and R.A. Zierenberg (Editors), *Proceedings of the Ocean Drilling Program; Scientific Results*. Ocean Drilling Program, College Station, TX, pp. 255-276.
- Hunter, A.G., Kempton, P.D. and Greenwood, P., 1999. Low-temperature fluid-rock interaction; an isotopic and mineralogical perspective of upper crustal evolution, eastern flank of the Juan de Fuca Ridge (JdFR), ODP Leg 168. *Chemical Geology*, 155(1-2): 3-28.
- Hunter, A.G. and ODP Leg 168 Scientific Party, 1998. Petrological investigations of low temperature hydrothermal alteration of the upper crust, Juan de Fuca Ridge, ODP Leg 168. In: R.A. Mills and K. Harrison (Editors), *Modern ocean floor processes and the geological record*. Geological Society Special Publications, pp. 99-125.
- Jochum, K.P., Dingwell, D.B., Rocholl, A., Stoll, B. and Hofmann, A.W., 2000. The preparation and preliminary characterisation of eight geological MPI-DING reference glasses for in-situ microanalysis. *Geostandards Newsletter*, 24(1): 87-133.
- Laverne, C., Agrinier, P., Hermitte, D. and Bohn, M., 2001. Chemical fluxes during hydrothermal alteration of a 1200-m long section of dikes in the oceanic crust, DSDP/ODP Hole 504B. *Chemical Geology*, 181: 73-98.
- Laverne, C., Belarouchi, A. and Honnorez, J., 1996. Alteration mineralogy and chemistry of the upper oceanic crust from Hole 896A, Costa Rica Rift. *Proceedings of the Ocean Drilling Program, Scientific Results*, 148: 151-170.

- Lonsdale, P., 1989. Segmentation of the Pacific-Nazca spreading center, 1°N-20°S. *Journal of Geophysical Research*, 94: 12197-12225.
- Ludden, J.N. and Thompson, G., 1978. Behaviour of rare earth elements during submarine weathering of tholeiitic basalt. *Nature*, 274: 147-149.
- Ludden, J.N. and Thompson, G., 1979. An evaluation of the behavior of the rare earth elements during the weathering of sea-floor basalt. *Earth and Planetary Science Letters*, 43: 85-92.
- Marescotti, P., Vanko, D.A. and Cabella, R., 2000. From oxidizing to reducing alteration: Mineralogical variations in pillow basalts from the east flank, Juan de Fuca Ridge. *Proceedings of the Ocean Drilling Program, Scientific Results*, 168: 119-136.
- Mottl, M.J., 1983. Hydrothermal processes at seafloor spreading centers: Application of basalt-seawater experimental results. In: P.A. Rona, K. Boström, L. Laubier and K.L. Smith (Editors), *Hydrothermal Processes at Seafloor Spreading Centers*. Plenum, New York, pp. 199-224.
- Mottl, M.J., 2003. Partitioning of Energy and Mass Fluxes between Mid-ocean Ridge Axes and Flanks at High and Low Temperature. In: P.E. Halbach, V. Tunnicliffe and J.R. Hein (Editors), *Dahlem Workshop Report 89, Energy and Mass Transfer in Marine Hydrothermal Systems*. Dahlem University Press, Berlin, pp. 271-286.
- Mottl, M.J. and Wheat, C.G., 1994. Hydrothermal circulation through mid-ocean ridge flanks: Fluxes of heat and magnesium. *Geochimica et Cosmochimica Acta*, 58(10): 2225-2237.
- Mottl, M.J. and Wheat, C.G., 2000. Hydrothermal Fluxes on Mid-Ocean Ridge Flanks: EXCO II on the Eastern Flank of the East Pacific Rise near 14°S. *Eos Trans. AGU*, 81(48): F458 Fall Meeting.
- Pichler, T., Ridley, W.I. and Nelson, E., 1999. Low-temperature alteration of dredged volcanics from the Southern Chile Ridge: Additional information about early stage of seafloor weathering. *Marine Geology*, 159: 155-177.
- Porter, S., Vanko, D.A. and Ghazi, A.M., 2000. Major and trace element compositions of secondary clays in basalts altered at low temperature, Eastern flank of the Juan de Fuca Ridge. *Proceedings of the Ocean Drilling Program, Scientific Results*, 168: 149-157.
- Singer, A. and Banin, A., 1990. Characteristics and mode of formation of palagonite; a review. *Sciences Geologiques*, 88: 173-181.
- Staudigel, H. and Hart, S.R., 1983. Alteration of basaltic glass: Mechanisms and significance for the oceanic crust-seawater budget. *Geochim. Cosmochim. Acta*, 47: 337-350.

- Staudigel, H., Hart, S.R. and Richardson, S., 1981. Alteration of the oceanic crust: Processes and timing. *Earth and Planetary Science Letters*, 52: 311-327.
- Staudigel, H., Plank, T., White, B. and Schmincke, H.-U., 1996. Geochemical fluxes during seafloor alteration of the basaltic upper oceanic crust: DSDP Sites 417 and 418. In: G.E. Bebout, D.W. Scholl, S.H. Kirby and J.P. Platt (Editors), *Subduction top to bottom. Geophysical Monograph*, pp. 19-38.
- Stein, C.A. and Stein, S., 1994. Constraints on hydrothermal heat flux through the oceanic lithosphere from global heat flow. *Journal of Geophysical Research*, 99: 3081-3095.
- Stroncik, N.A. and Schmincke, H.-U., 2002. Palagonite - a review. *International Journal of Earth Sciences (Geologische Rundschau)*, 91(4): 680-697.
- Sun, S.S. and McDonough, W.F., 1989. Chemical and isotopic systematics of oceanic basalts: Implications for mantle composition and processes. In: A.D. Saunders and M.J. Norry (Editors), *Magmatism in the Ocean Basins. Geological Society Special Publication*, pp. 313-345.
- Teagle, D.A.H., Alt, J.C., Bach, W., Halliday, A.N. and Erzinger, J., 1996. Alteration of upper ocean crust in a ridge-flank hydrothermal upflow zone: Mineral, chemical, and isotopic constraints from Hole 896A. *Proceedings of the Ocean Drilling Program, Scientific Results*, 148: 119-150.
- Teagle, D.A.H., Alt, J.C. and Halliday, A.N., 1998. Tracing the evolution of hydrothermal fluids in the upper oceanic crust: Sr-isotopic constraints from DSDP/ODP Holes 504B and 896A. In: R.A. Mills and K. Harrison (Editors), *Modern ocean floor processes and the geological record. Geological Society Special Publications*, pp. 81-97.
- Thompson, G., 1973. A geochemical study of the low-temperature interaction of sea-water and oceanic igneous rocks. *Eos, Transactions, American Geophysical Union*, 54(11): 1015-1019.
- Thompson, G., 1983. Hydrothermal fluxes in the ocean. *Chemical Oceanography*, 8: 271-337.
- Utzmann, A., Hansteen, T.H. and Schmincke, H.U., 2002. Trace element mobility during sub-seafloor alteration of basaltic glass from Ocean Drilling Program Site 953 (off Gran Canaria). *International Journal of Earth Sciences (Geologische Rundschau)*, 91(4): 661-679.
- Villinger, H., Grevemeyer, I., Kaul, N., Hauschild, J. and Pfender, M., 2002. Hydrothermal heat flux through aged oceanic crust: where does the heat escape ? *Earth and Planetary Science Letters*, 202(1): 159-170.
- Weigel, W., Grevemeyer, I., Kaul, N., Villinger, H., Lüdmann, T. and Wong, H.K., 1996. Aging of oceanic crust at the southern East Pacific Rise. *EOS Trans. AGU*, 77(50): 504.

- Wheat, C.G., Elderfield, H., Mottl, M.J. and Monnin, C., 2000. Chemical composition of basement fluids within an oceanic ridge flank: Implications for along-strike and across-strike hydrothermal circulation. *Journal of Geophysical Research*, 105(B6): 13437-13447.
- Wheat, G.C., Mottl, M.J. and Rudnicki, M., 2002. Trace element and REE composition of a low-temperature ridge flank hydrothermal spring. *Geochimica et Cosmochimica Acta*, 66(21): 3696-3705.
- Wilkens, R.H., Fryer, G.J. and Karsten, J., 1991. Evolution of porosity and seismic structure of upper oceanic crust: Importance of aspect ratios. *Journal of Geophysical Research*, 96: 17891-17995.
- Wilson, S.A., 1997. Data compilation for USGS reference material BHVO-2, Hawaiian Basalt, U.S. Geological Survey Open-File Report.

**Colored atlas of low temperature alteration features  
in basalts**

Burkhard Schramm



# Colored atlas of low temperature alteration features in basalts

Burkhard Schramm\*

\**Fachbereich Geowissenschaften, Universität Bremen, Klagenfurter Str., 28359 Bremen, Germany*

## 1. Introduction

The study of low temperature alteration in magmatic rocks is focused on chemical and mineralogical investigations, but only in rare cases do these investigations provide pertinent photomicrographs as a helpful tool for the identification of secondary minerals. For identifying secondary minerals under the microscope, fundamental knowledge about the mineralogical alteration features in thin sections are necessary. However, most atlases about rocks and minerals in thin section provide mainly information about primary minerals or the structure of unaltered rocks [e.g. *MacKenzie and Adams, 2001; MacKenzie and Guilford, 1980*]. The best information is available from an atlas with an intense focusing on “normal” or higher degree of alteration, but with only limited illustrations about low temperature alteration [*Delvigne, 1998*]. This low temperature alteration atlas provides an descriptive overview about the identified secondary minerals and the alteration features (oxidation haloes, void / vein filling) in basalts, as well as the problems occurring when identifying secondary minerals under the microscope. The aim is to provide self-contained photomicrographs of distinct alteration products that people can use as a base for the work with low temperature altered basalts.

All illustrations are digital photomicrographs made with a Nikon Coolpix 800 under either a Leica polarizing microscope from thin sections or a Leica binocular from hand pieces. Used magnifications under the microscope are 40x, 100x and 400x. To provide high quality and realistic colors, contrast and brightness were post processes with a computer program (Adobe Photoshop 5.5). This uniformity provides a better homogeneity of colors in all pictures. The pictures were taken either in plane-polarized light (PPL) or under crossed polars (XPL), in some cases the same field of view is shown under both conditions.

## 2. Preliminary work

The atlas is based on a study focused on alteration of basalts from the Southern East Pacific Rise [*Schramm et al., submitted*]. The sampling program was located in an area concentrated between 14-16°S, extending from the spreading axis out to 9 Ma old crust. Rock samples were recovered by dredging on topographic highs or

close to seamounts (35DS and 36DS) and show generally an increasing degree of alteration with distance from the spreading axis and therefore with time. The occurrence of all alteration features like oxidation haloes or secondary minerals were confirmed by X-ray diffraction, X-ray fluorescence and microprobe analysis. Detailed information about the magmatic and chemical evolution of these rocks are given elsewhere [Schramm and Devey, submitted; Schramm *et al.*, submitted].

### **3. Problems**

Secondary minerals can be easily distinguished from primary minerals in thin sections, e.g. by their irregular shape or their replacing character. Nevertheless, the identification of different kinds of secondary minerals yields many problems. Clays can be identified as secondary minerals, but without microprobe analyses or additional information from XRD-analyses it is not possible to determine particular clay minerals. Colors and the homogeneous or heterogeneous distribution in voids and veins or the replacement of primary minerals can be taken as an helpful tool to minimize these problems. Nevertheless, clays can be confused with palagonite or Fe-oxhydroxide and sometimes clay minerals only cover/overprint primary minerals, so microprobe analyses of clay-looking minerals in thin section can still yield analyses of primary minerals like plagioclase or pyroxene. Moreover, different colors do not always represent different compositions.

In the following the alteration features of the rocks are illustrated in photomicrographs, with a characterization of the identification problems and how to minimize or solve these problems.

### **4. Photomicrographs**

All illustrations are shown with their sample number, age and a short description. The location of the alteration features are indicated by a box in the overview photomicrograph of each thin section. All descriptions are based on thin section observations.

#### **4.1 Glass / palagonite (Pic.1-4)**

The dissolution of glass is characterized by partial replacement with palagonite. Fresh glass was identified by its homogeneous yellow-beige appearance under PPL (**1, 3, 4**) and opaque appearance under XPL (**2**). For this reason it can be easily differentiated from the heterogeneous brown-gold-orange colored palagonite. Palagonite is focused at the outer rim of the sample (**2, 3, 13, 14**) and along small cracks and shows a concentric alignment with changing shades of colors towards the center, reflecting different degrees of palagonization, best visible

under XPL (**2, 14**). The occasional occurrence of dark brown variolites at the glassy margin which form around small crystal seeds like plagioclase, increases towards the rock interior (**3, 4**).

#### **4.2 Alteration haloes (Pic.5-8)**

Many samples are characterized by the presence of oxidation haloes. These haloes can be identified as dark gray or brownish bands in the rock at the outer rim of the sample (**5, 6**) or associated along fractures (**5, 7, 8**). They form by contact with the circulating fluids and represent the most altered areas in these low temperature altered rocks. The haloes are related to fluid conduits such as fractures or other surfaces. These areas are characterized by higher amounts of secondary minerals, giving this part of the rock a darker color in contrast to the generally less altered rock interior (**5-8**). In some cases, when many small fractures are present, the least altered rock interiors can have a patchy occurrence, probably reflecting higher porosity and/or permeability (**7, 8**).

Black haloes represent a transition zone from the glassy margin to the oxidation haloes and consist of increasing amounts of variolites, best illustrated in thin section 22DS1, 35DS4 and 43DS13 (see Appendix).

#### **4.3 Void filling (Pic.9-12)**

The occurrence of voids (cavities or vesicles) in all EXCO rocks is only up to 3 % but many samples from other parts of the ocean can have higher vesicularity. Voids can be present throughout the whole rock, but predominantly towards the glassy margin, especially when pillows are present. Most of the voids in the least altered part of the rock (mainly the rock interior) remain open, whereas voids in the oxidation halo are lined or filled with secondary minerals (**9-12**). The size can be up to 4 mm, but most voids are below 1 mm. Due to the small size, most void filling material can only be identified under the microscope. Secondary minerals are Fe-oxyhydroxide (**21, 22**), clays (celadonite (**9, 26-30**), saponite (**27-30**)) and phillipsite (**10-12**), depending on redox conditions or degree of alteration. They always grow towards the void center. Depositional sequences in many thin sections show that Fe-oxyhydroxides precipitates first and celadonite predate saponite and phillipsite. A possible sequence of clay minerals is shown in Fig.1. Additional, all phases can be coeval and mixtures especially between phillipsite and clay minerals occur (**41, 42**). Other void filling material can be infiltrated sediment, foraminifera or pieces of Mn-crusts (**10**).

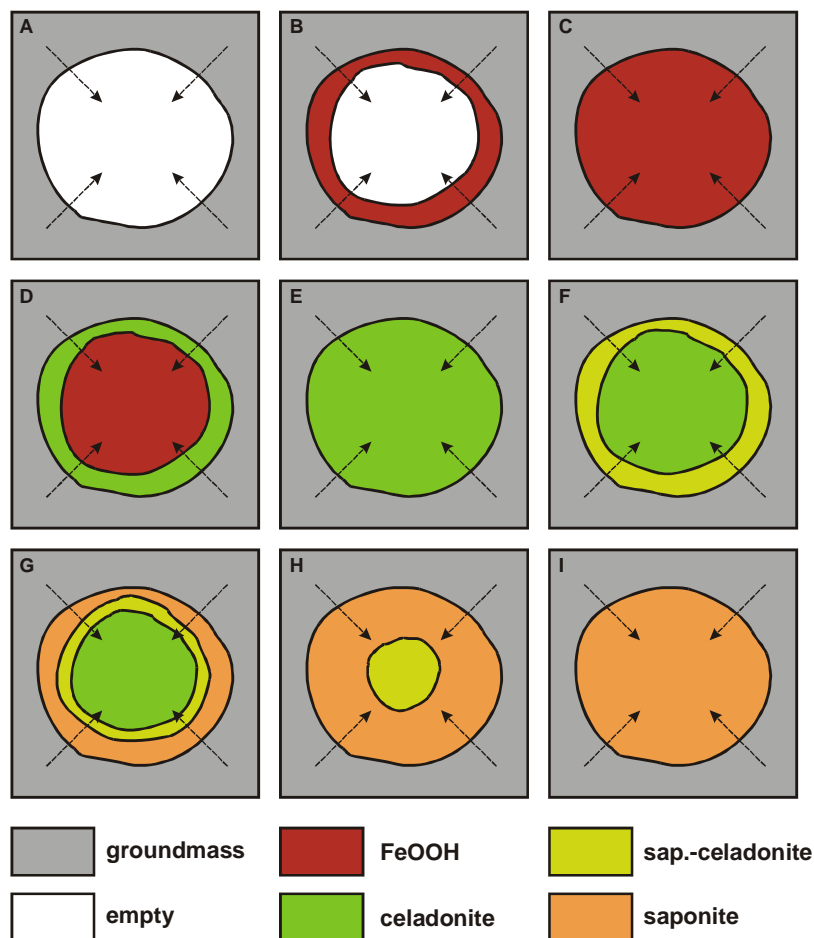


Figure 1. Possible depositional sequence of clayey void filling material. The disappearing minerals (e.g. FeOOH between C and E) are being replaced progressively. Arrows indicate direction of infiltration. A. Open void in a basaltic groundmass. B. Void lined with FeOOH (22). C. Void completely filled with FeOOH (21). D. Void filled with FeOOH and lined with celadonite (23, 24, 26). E. Celadonite completely replacing or covering FeOOH (9). F. Redox change towards more oxidizing conditions indicating by the partial replacement of celadonite by saponite, resulting in a mixture of saponite-celadonite at the inner wall of the void. G. More oxidizing conditions cause the increased precipitation of saponite towards the void center (27-30). H. All celadonite is replaced or covered by saponite and saponite-celadonite. I. Void completely filled with saponite. Not all voids in the rocks are completely filled with clay minerals, they can also be filled or lined with other secondary minerals (e.g. phillipsite) or remain open.

#### 4.4 Vein filling (Pic.13-20)

Veins are filled by the same secondary minerals as voids. In rare cases palagonite also fills veins and mixtures between phillipsite and clay minerals are more common (18, 37-39). At the glassy margin many veins are bounded by palagonite and are lined or filled with phillipsite (13, 14) or a mixture of phillipsite and clay minerals. In some cases groundmass particles and trace amounts of sediment can also be present (16). At the oxidation halo veins can also be filled with celadonite and Fe-oxyhydroxide (15). Sometimes, where veins are connecting oxidation haloes and the rock interior (15), celadonite shows a change in its composition with high

Fe and low Mg content located on the outer margin of the oxidation halo towards decreasing Fe and increasing Mg content at the border between oxidation halo and the less altered rock interior, where most veins remain open.

#### **4.5 Secondary Minerals**

##### **4.5.1 FeOOH (Pic.21, 22)**

Fe-oxyhydroxides are the first secondary minerals that precipitate in the rocks and are found in oxidation haloes lining or filling voids and veins (**21**), disseminated in the groundmass and as Fe-staining on outer surfaces and along fractures. In thin section Fe-oxyhydroxides can have a very homogeneous appearance, but they also occur as irregular distributed spotted minerals which could be needles of goethite (**22**). Their red brown appearance is a good criteria for the distinction from celadonite (**23, 24, 26**). However, mixtures can also occur and it is not always possible to distinguish between these two phases.

##### **4.5.2 Celadonite and saponite (Pic.23-32)**

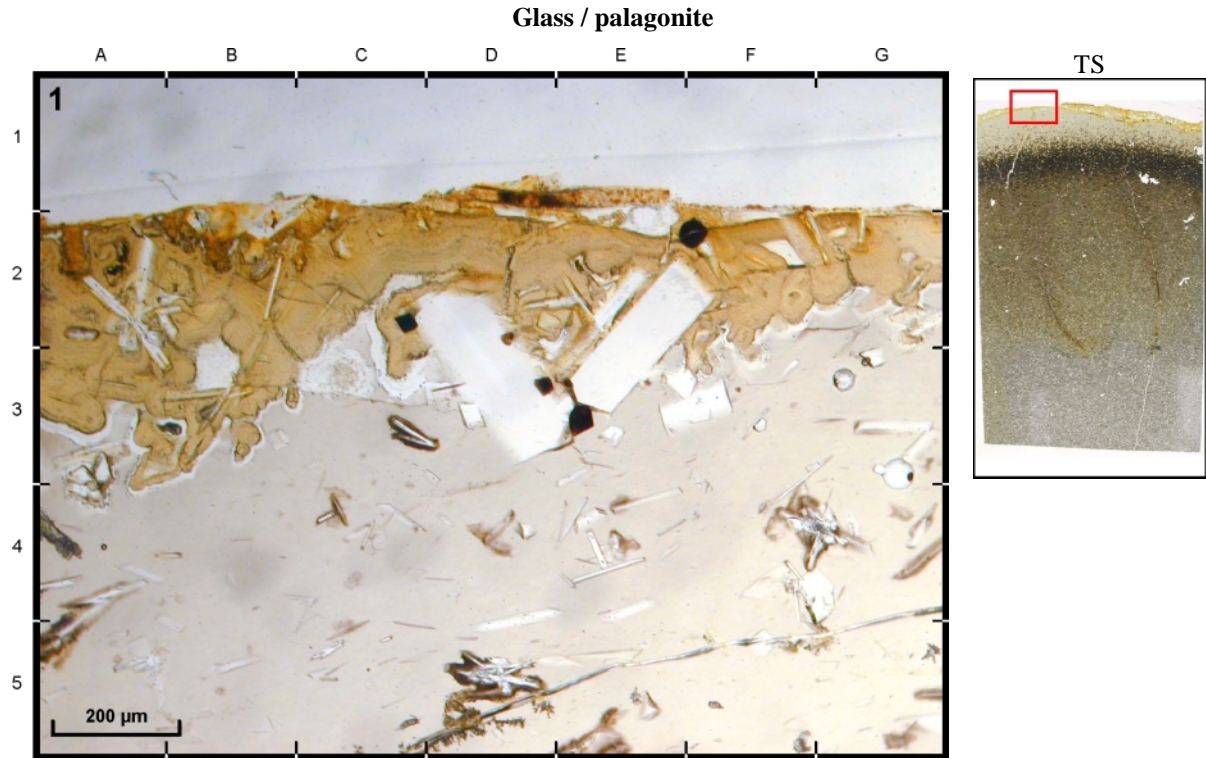
Celadonite is a dioctahedral mineral of the mica group, of ideal composition  $K(Mg,Fe)^{2+}(Fe,Al)^{3+}(OH)_2[Si_4O_{10}]$  [Jackson, 1997]. The composition of the celadonite shown here, is characterized by higher amounts of Fe in the octahedral position [Schramm *et al.*, submitted]. Celadonite occurs predominantly in oxidation haloes, replacing primary minerals (locally partially replacing plagioclase, more commonly partially or completely replacing or overprinting olivine or pyroxene, **23, 24, 31, 32**) and Fe-oxyhydroxide (**26**) and fills vesicles and veins. It occurs in shades of yellow (**23, 24**), orange (**31, 32**) and green (**27-30**), and it appears reddish brown at high Fe content (**15**) and can easily be confused with Fe-oxyhydroxide. The very often occurring orange color is the result of a contamination with Fe-oxyhydroxide. Nevertheless, the different colors do not always appear to be associated with different compositions. For example, an intense green color, often observed at the center of yellow-orange saponite and celadonite clots commonly originates from a micro-porous clump of celadonite crystals (**27-30**). The color appears to result from refraction in the empty pores existing between the microparticles of celadonite. In other cases the same appearance reflects a transition from celadonite to saponite. Based of the limited resolution of the optical microscope it is not always possible to distinguish between these two possibilities. The only indications are the very low totals of microprobe analyses in the microporous celadonite regions (totals < 20%) which can be used to distinguish these two similarly-colored mineral occurrences.

In terms of physical appearance and optical properties celadonite can also be easily confused with palagonite and saponite. In contrast to the heterogeneous and concentric alignment of palagonite under XPL, celadonite exhibits a fine grained laminar texture (**28, 30**). In some cases, where celadonite occurs in voids it is replaced at the outer rim by saponite, indicated by a color change to the more orange saponite (**27, 29**). Nevertheless, celadonite can also occur in a similar color, making the interpretation more difficult. Celadonite is also replacing olivine at intramineral fissures and progressing to complete replacement of olivine where only the pseudomorph gives a clue to the nature of the primary mineral (**32**). It also covers plagioclase and pyroxene so that the appearance under the optical microscope looks like celadonite (**23, 31**). No pseudomorph of the primary mineral is visible, but analyses with the microprobe still yields the composition of the primary mineral.

Saponite is a trioctahedral member of the smectite group with an ideal structural formula of  $(\text{Ca}, \text{Na})^{\text{X}}_{0.66}(\text{Mg})^{\text{VI}}_6(\text{Si}_{7.34}\text{Al}_{0.66})^{\text{IV}}_{8.0}\text{O}_{20}(\text{OH})_4$  where IV, VI and X represent tetrahedral, octahedral and exchangeable interlayer sites [Deer *et al.*, 1962]. In this study it is characterized by a lower Fe and K, and higher Mg content than celadonite [Schramm *et al.*, submitted]. In thin section it appears yellow-orange, fills voids and is always associated with the replacement or overprinting of celadonite or saponite-celadonite (**27-30**, a transition mineral, its abundance and occurrence is related to those of both its end-member minerals), suggesting that saponite forms later than celadonite under either different redox conditions, water/rock ratios or at higher temperatures. In the rocks studied here it never occurs in veins nor it is associated with the replacement of primary minerals.

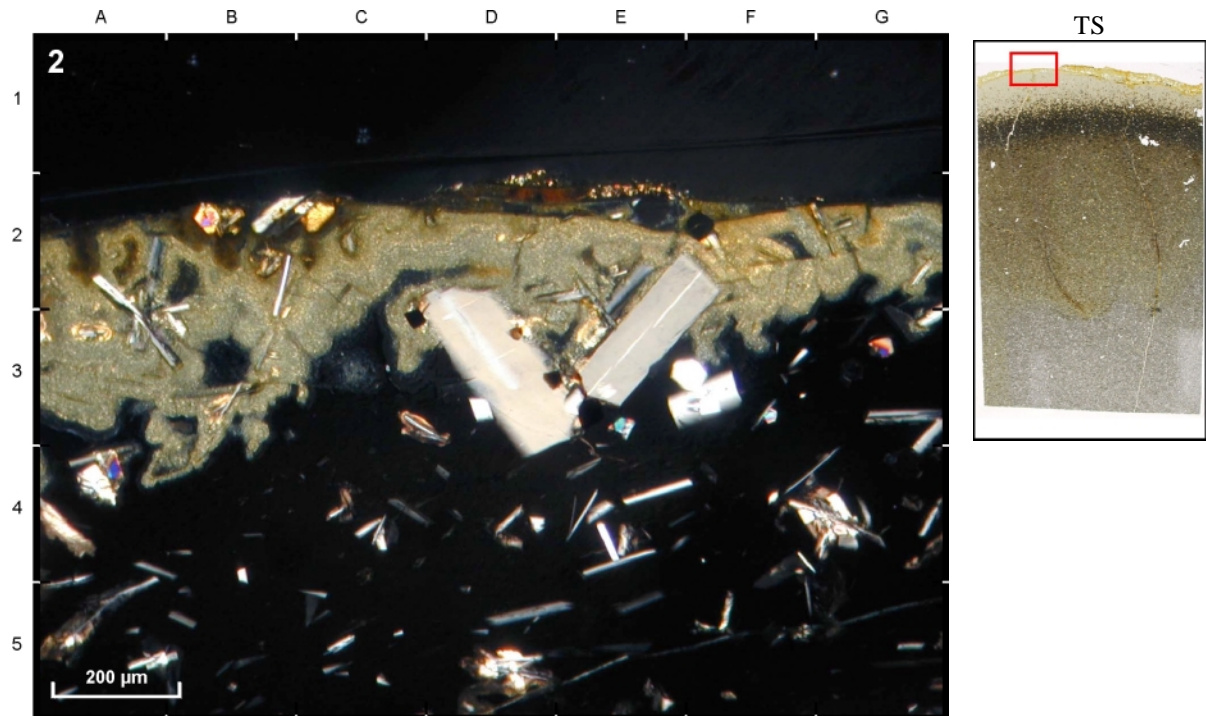
#### 4.5.3 Phillipsite (Pic.33-42)

Phillipsite is a monoclinic zeolite mineral with the formula  $(\frac{1}{2}\text{Ca}, \text{Na}, \text{K})_3(\text{Al}_3\text{Si}_5\text{O}_{16})6\text{H}_2\text{O}$  [Deer *et al.*, 1977]. In this study it is characterized by higher amounts of  $\text{K}_2\text{O}$  (~6 wt %) [Schramm *et al.*, submitted]. It is restricted to glassy rinds and commonly occurs in fractures and veins left by the dissolution of glass growing towards the center (**20, 35-38**) until the vein is completely filled (**13, 14, 19, 33, 34**). Only trace amounts of phillipsite occur in voids (**10-12**), lining the inner wall always associated with the occurrence of glass or palagonite. Phillipsite can be easily identified by its white complex fibrous crystals (**39, 40**), only when occurring together with clay minerals can an identification be difficult due the heterogeneous overprinting with clay minerals (**37-39, 41, 42**). In this case the two phases occur as an irregular gray-brown material. Microprobe analyses of these mixed phases yield a phillipsite composition with an advanced Fe-content, reflecting the incorporation of clay minerals.



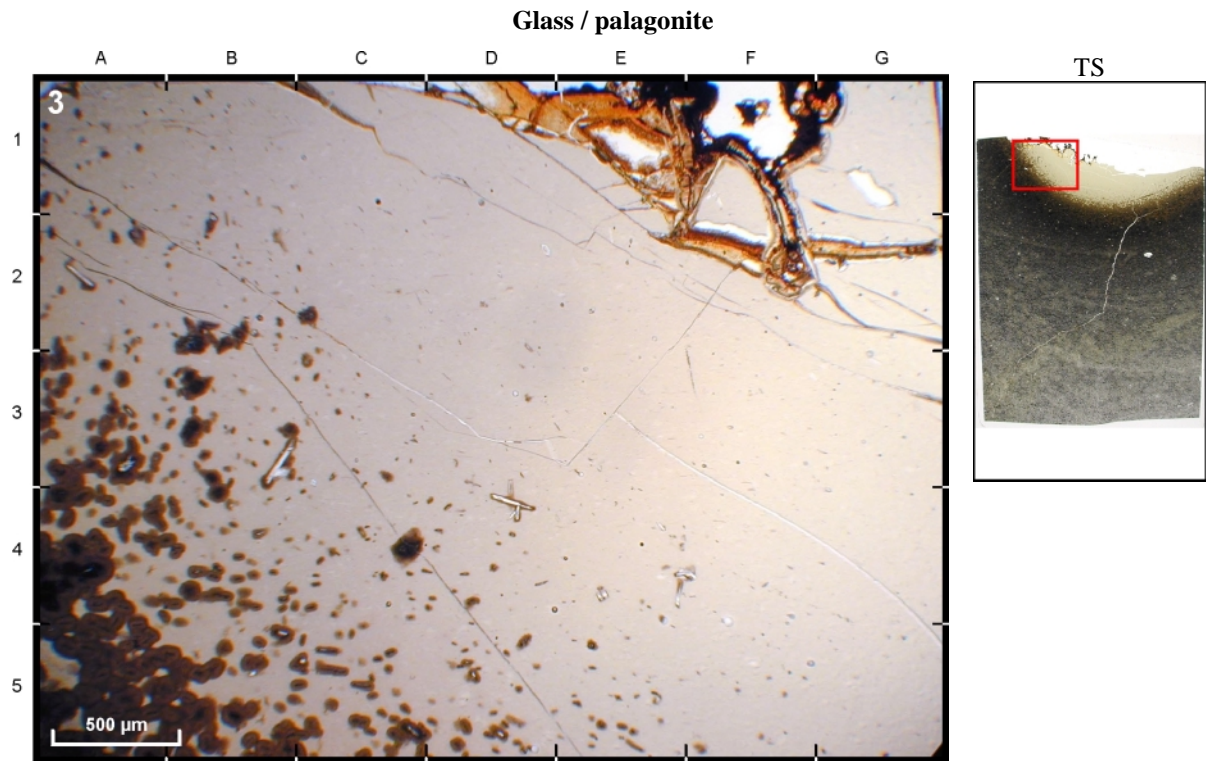
**35DS4 - 2-56 Ma - Glass and palagonite - PPL**

Glass with palagonization and plagioclase along the outer rim. Note the small contamination with clay minerals along the outer surface (B1, DE1), distinguishable by the spotted presence and brighter orange color. Spinel occurs as dark brown mineral at C2 and DE3.



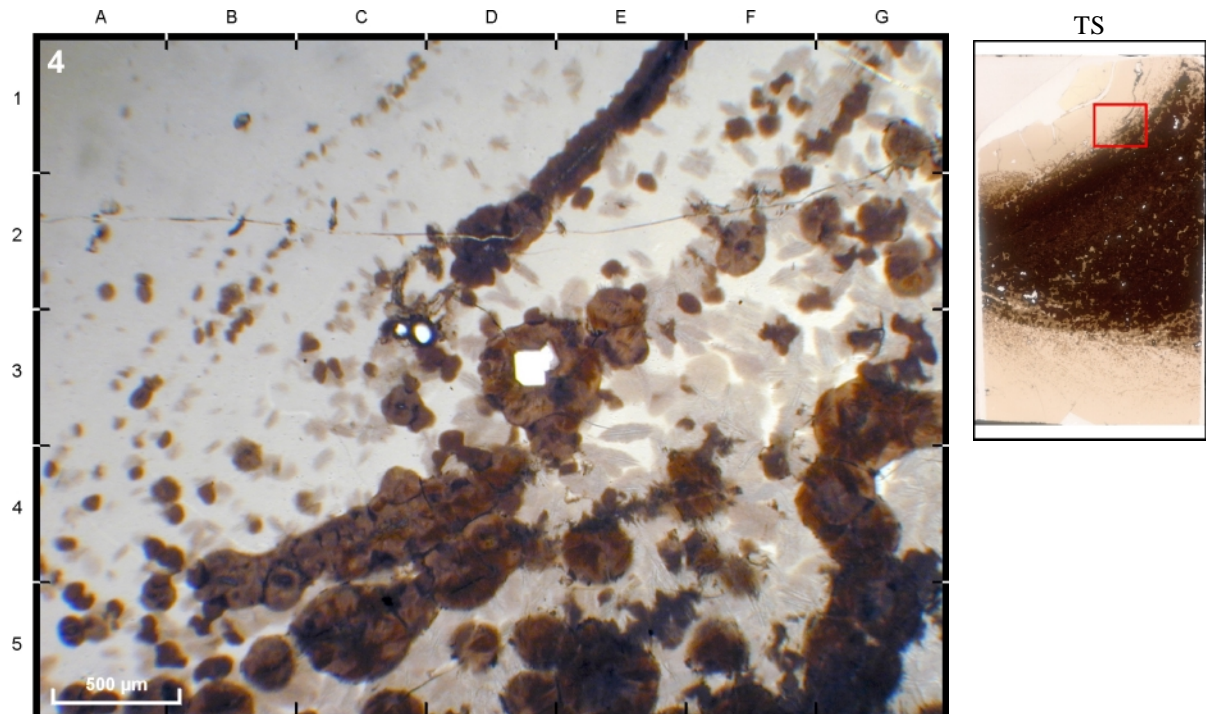
**35DS4 - 2-56 Ma - Glass and palagonite - XPL**

Glass is easily identified by its opaque appearance, palagonite shows a brown-gold-orange irregular dotted occurrence and can therefore be distinguished from the contamination with clay minerals (best visible in DE1-2).



**22DS1 - 0.12 Ma - Glass - PPL**

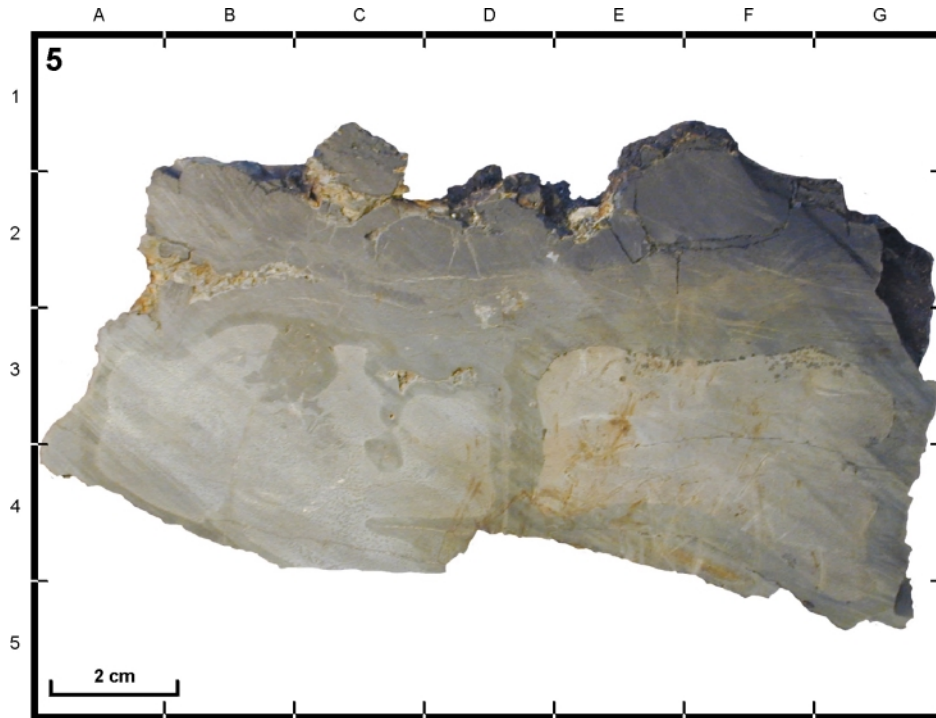
Fresh glass at the outer rim. Note the increasing amount of variolites towards A5, the palagonization along small cracks (FG2) and the presence of Mn-coating at the margin (EF1). Elongate crystals at A2, B3 and D4 are plagioclase.



**36DS8 - 4.6 Ma - Glass & variolites - PPL**

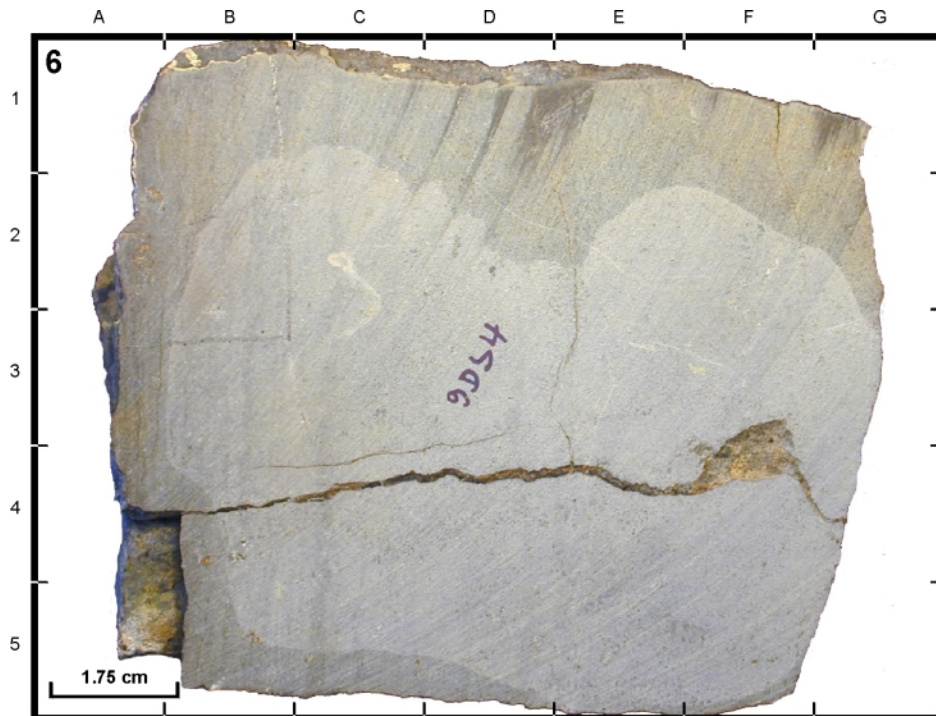
Fresh glass with increasing amounts of variolites towards the center (G5). Variolites form around small crystal seeds like plagioclase (D3), are more resistant to alteration and can remain as small dots on the rock surface after all glass is removed by alteration.

**Alteration haloes**



**29DS2 - 1.16 Ma - Alteration halo**

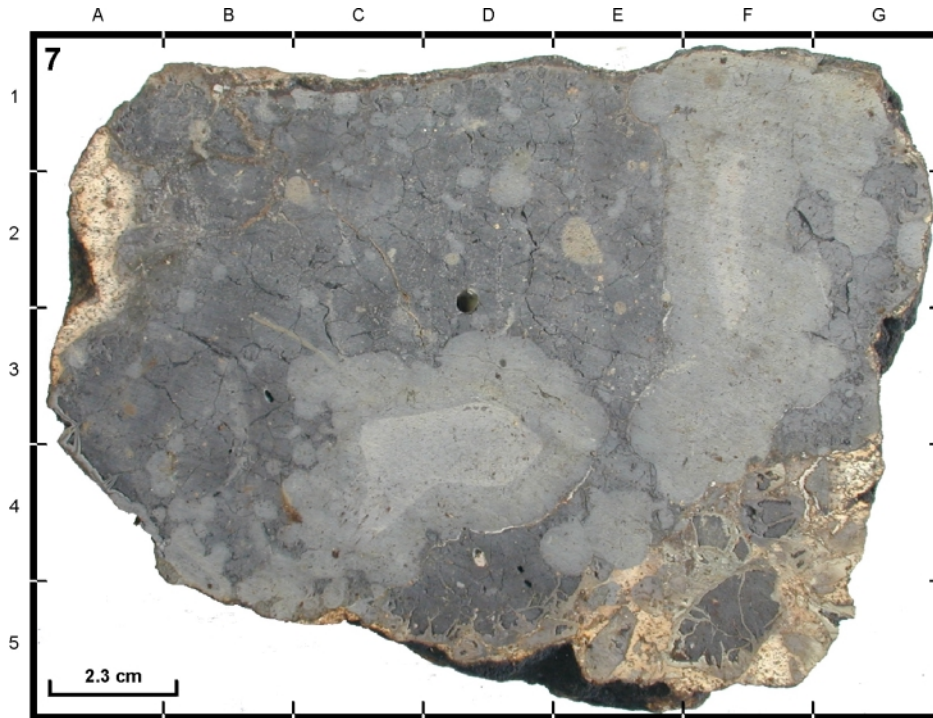
The gray halo is concentrated along the surface of the rock (top) and fractures which are pathways for the circulating fluids. The two areas of the brighter colored rock interior are separated by a halo along a small fracture (D3-4). Note the darker color of the oxidation halo towards the top of the sample, indicating increasing amounts of circulating fluids.



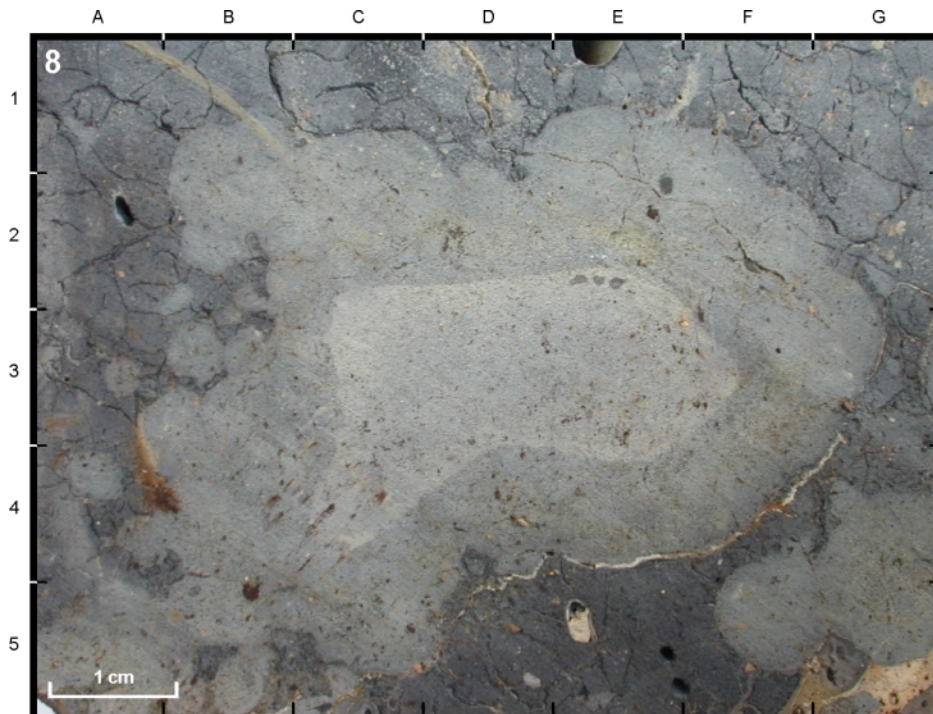
**9DS4 - 2.92 Ma - Alteration halo**

Halo concentrated along the outer rim of the rock. The minor occurrence of fresh glass indicates that the left side was the top of the sample.

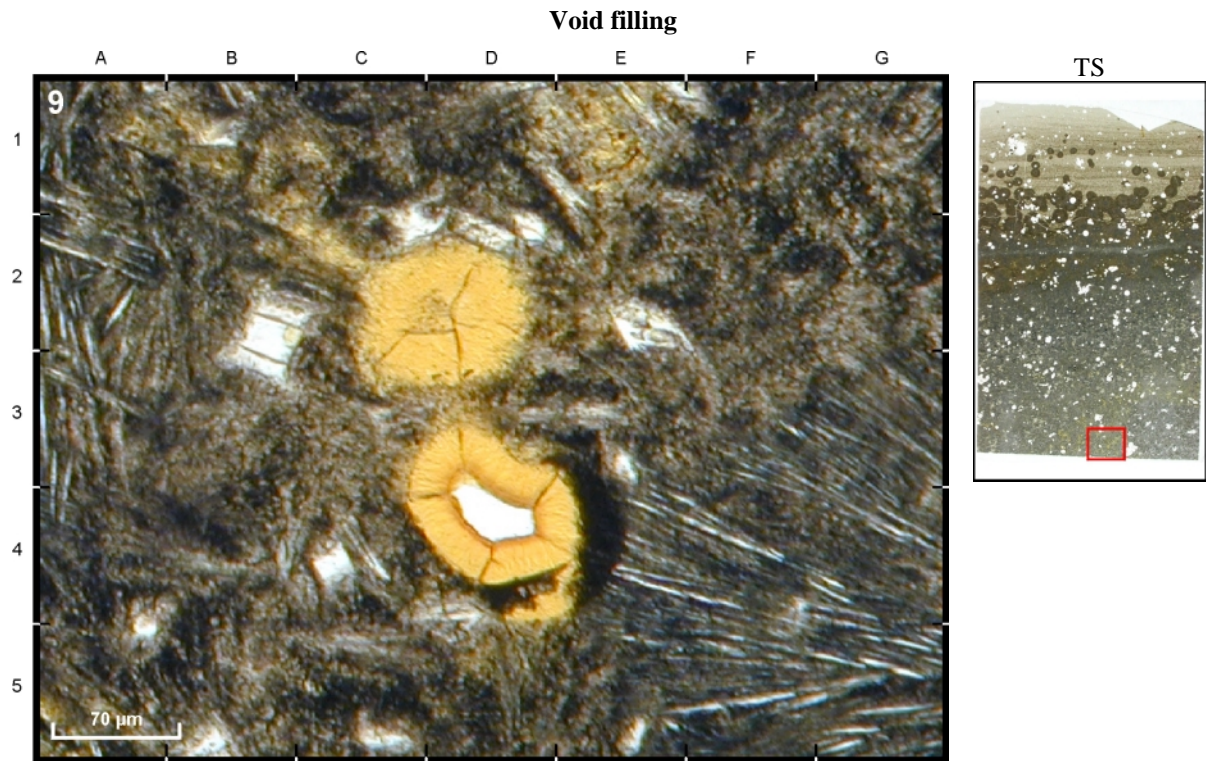
## Alteration haloes

**43DS3 - 8.64 Ma - Alteration halo**

Patchy occurrence of the least altered rock interior (lighter gray areas), probably an effect of higher amounts of small fractures and therefore higher porosity and/or permeability. Beige colored cemented sediments are visible at A1-3, a brecciation cemented by sediments at the area around F5.

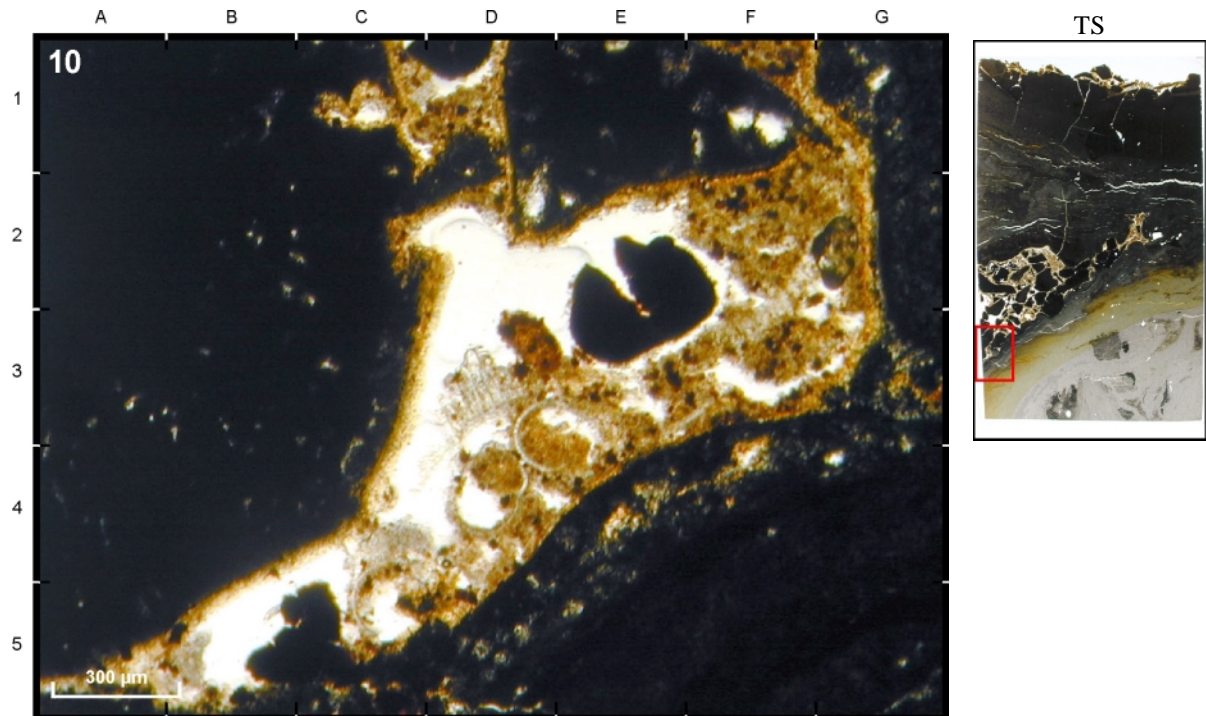
**43DS3 - 8.64 Ma - Alteration halo**

Close up of the above picture (CD3-4) illustrating the least altered part of the rock interior in the center, indicated by the brightest gray color. Note the decreasing amount of small fractures towards the center and therefore decreasing water rock interactions. The halo possesses a darker color and a dark gray appearance for the rest of the sample.



**28DS1 - 0.65 Ma - Void filling - PPL**

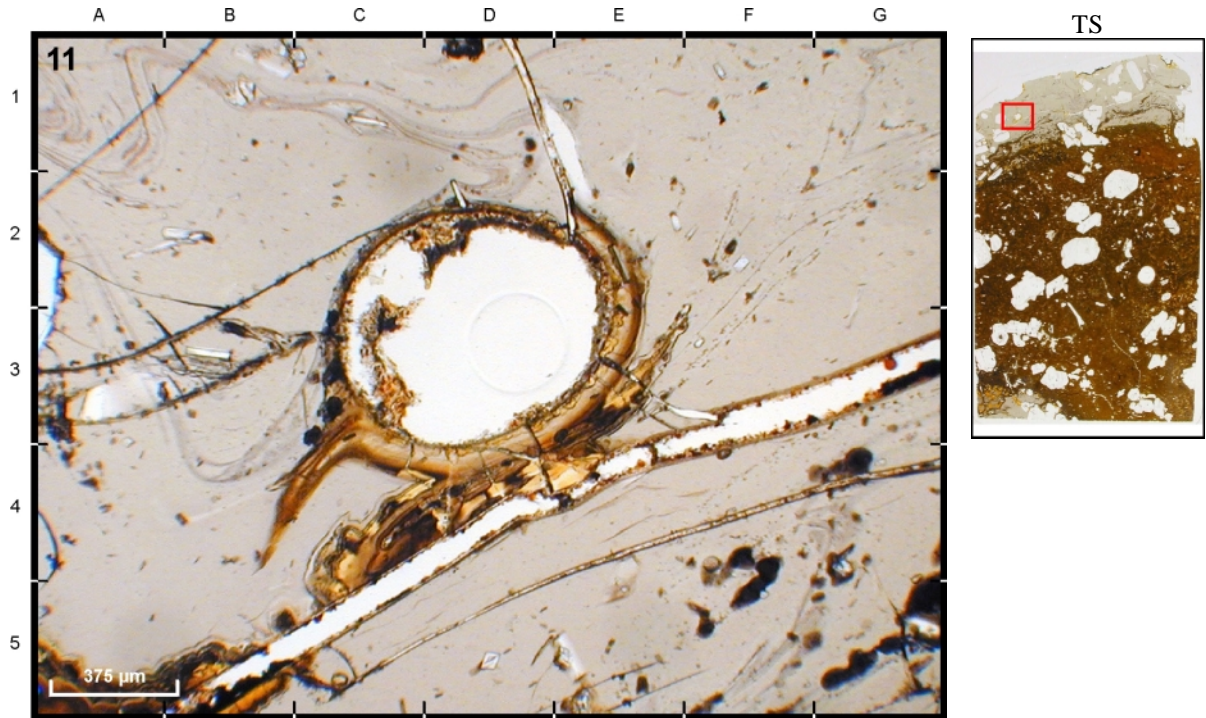
Voids located in the oxidation halo, partly (D3-4) and totally (CD2) filled by celadonite. Celadonite is also distributed within the groundmass (e.g. E1). White primary minerals (e.g. B2, C4) are olivine, elongated crystals in the groundmass are plagioclase.



**29DS2 - 1.16 Ma - Void filling - PPL**

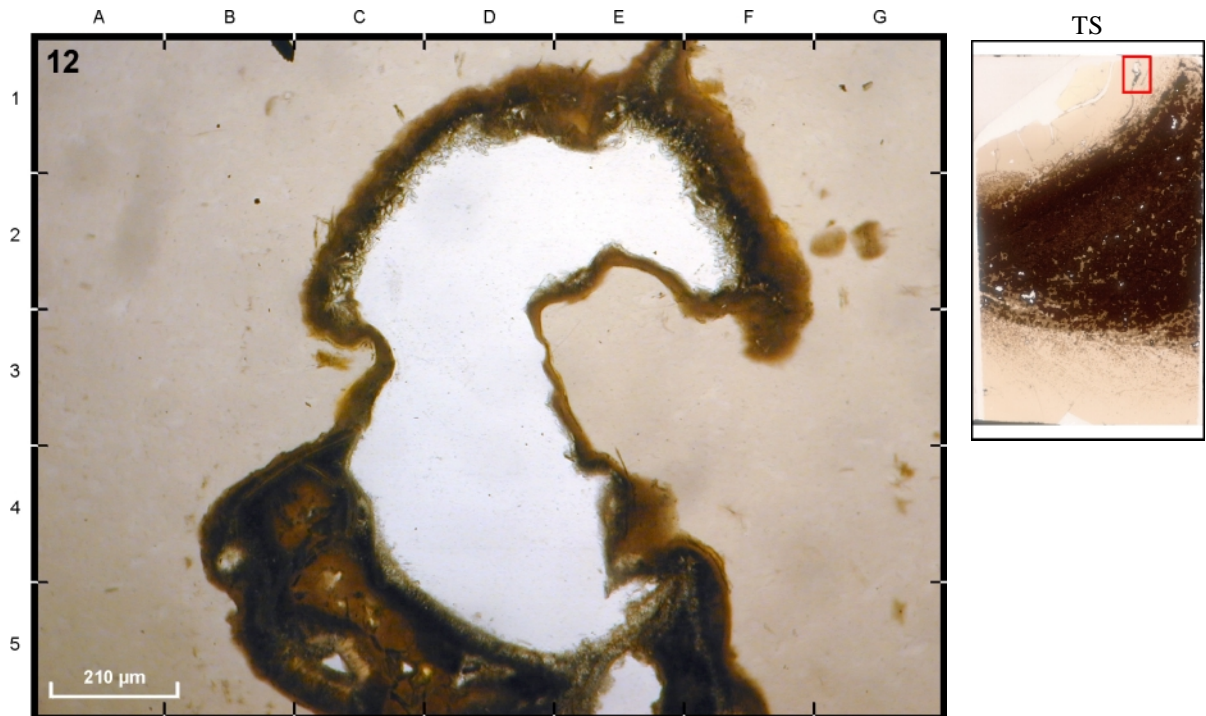
Void at the outer rim of the sample in a basaltic groundmass, lined with sediment and partly filled with clay minerals (F2), phillipsite (D3), foraminifera (DE3-4) and fragments of manganese crust (E2).

**Void filling**



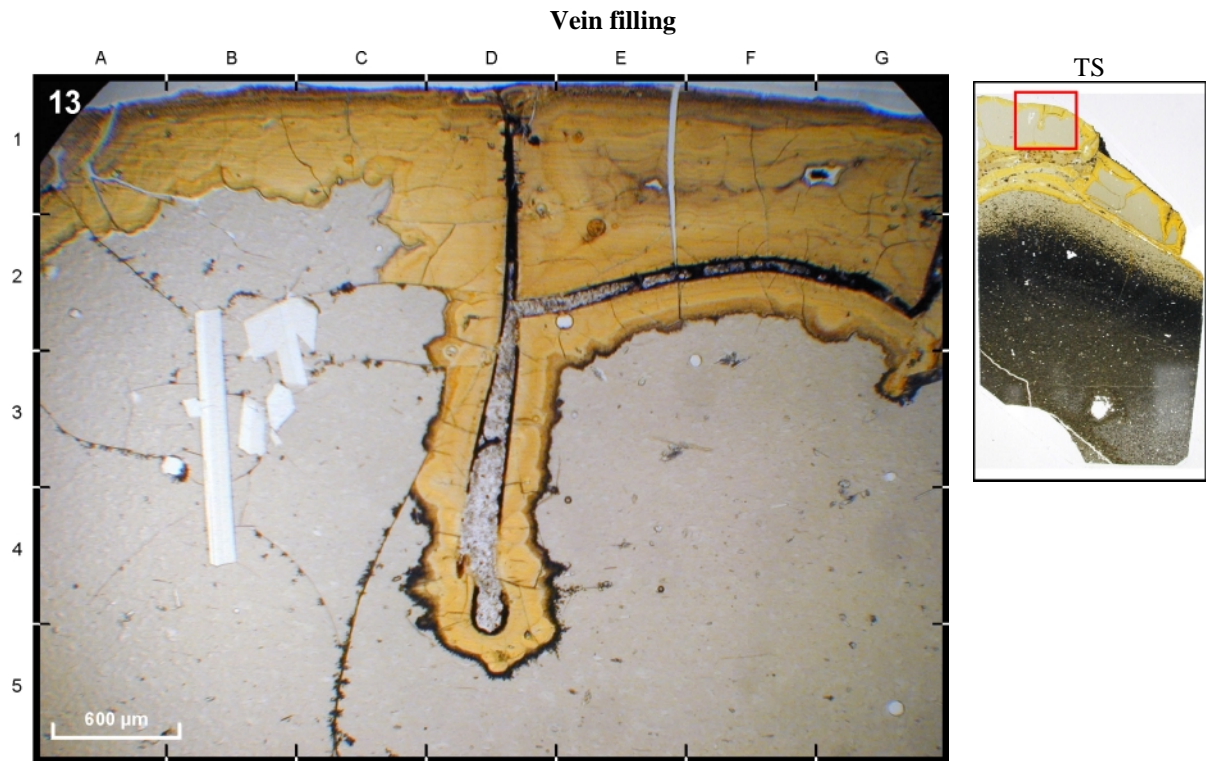
**36DS7 - 4.6 Ma - Void filling - PPL**

Open void in a glassy matrix lined on the inner side with small amounts of phillipsite and clay minerals. The tiny fibrous crystals of phillipsite are growing from the palagonitized area around the void.



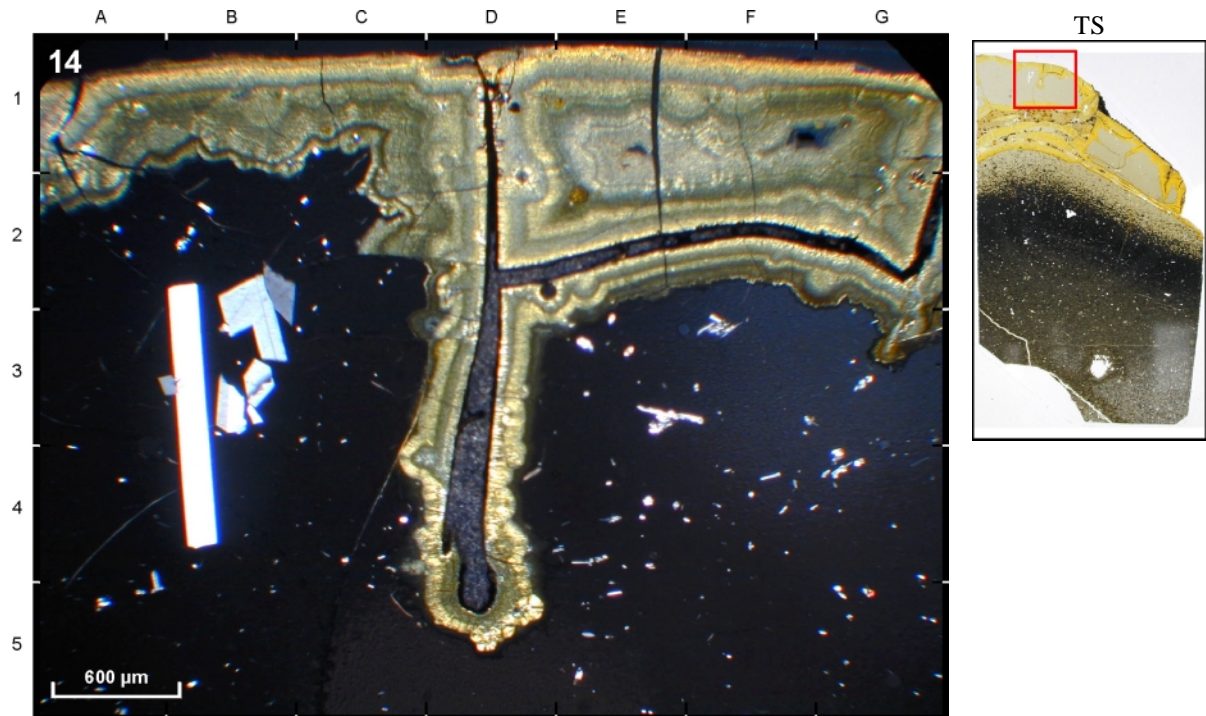
**36DS8 - 4.6 Ma - Void filling - PPL**

Open void in a glassy matrix lined with small amounts of fibrous crystals of phillipsite (best visible in C1, D1). Analyses show that the dark brown area around the void consists of a mixture of palagonite, groundmass and plagioclase.



**43DS13 - 8.64 Ma - Vein filling - PPL**

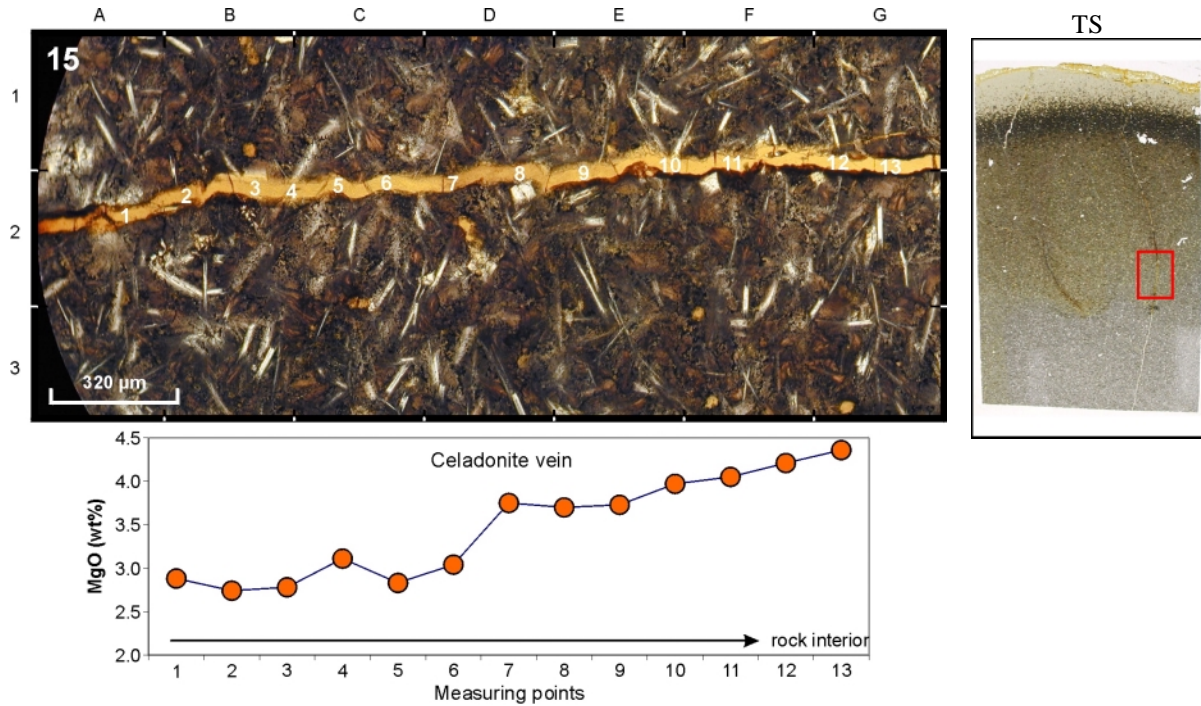
Vein in a glassy matrix at the outer rim of the sample, bounded by palagonite (orange area) and filled with phillipsite created by glass dissolution. Primary minerals in the left side of the picture are plagioclase.



**43DS13 - 8.64 Ma - Vein filling - XPL**

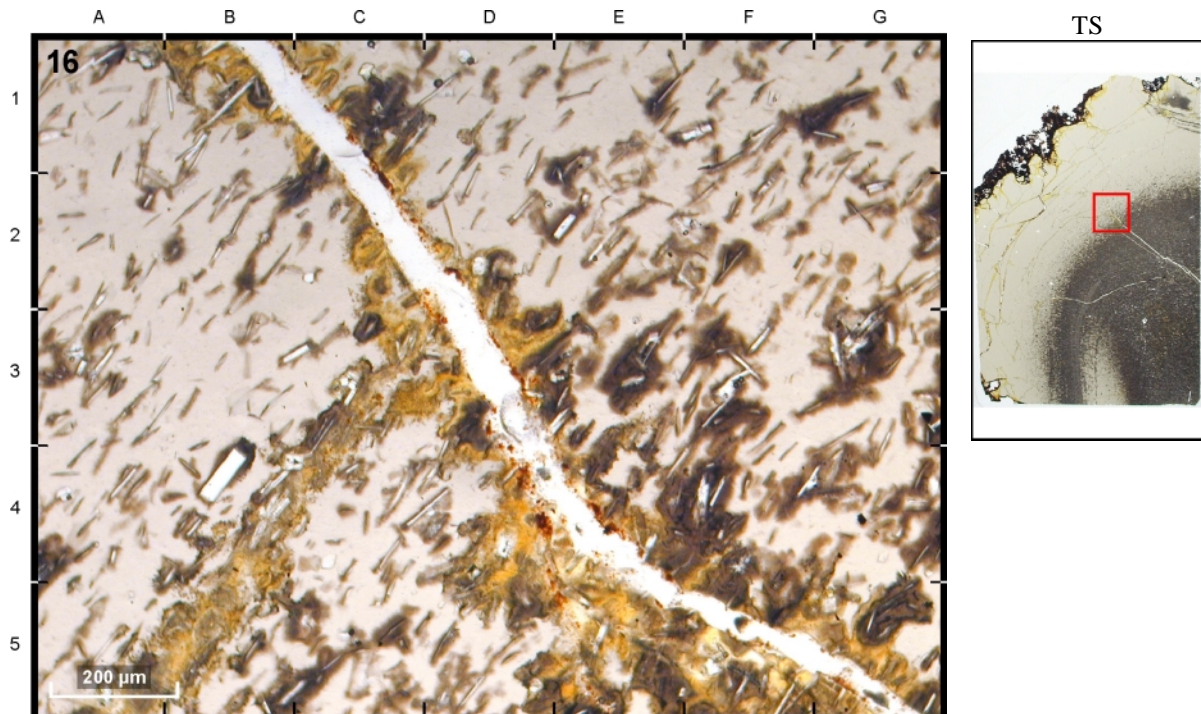
Phillipsite appears as dark gray crystals, whereas palagonite shows a concentric alignment along the vein and the margin with changing shades of colors. Primary minerals at the opaque fresh glass are plagioclase.

**Vein filling**



**35DS4 - 2.56 Ma - Vein filling - PPL**

Section of a celadonite filled vein from the oxidation halo with decreasing FeO and increasing MgO content towards the rock interior (right side). The decreasing influence of FeOOH is best visible in the thin section, where the rock interior shows a more grayish color than the brown colored oxidation halo. The color of the vein filling celadonite is only changing slightly from orange (A2) to a brighter orange (G2).



**35DS2 - 2.56 Ma - Vein filling - PPL**

Open vein in a glassy matrix from the outer rim of the sample, partly filled with small groundmass particles (e.g. G5). The orange area around the vein is covered by palagonite, not celadonite.

**Vein filling**



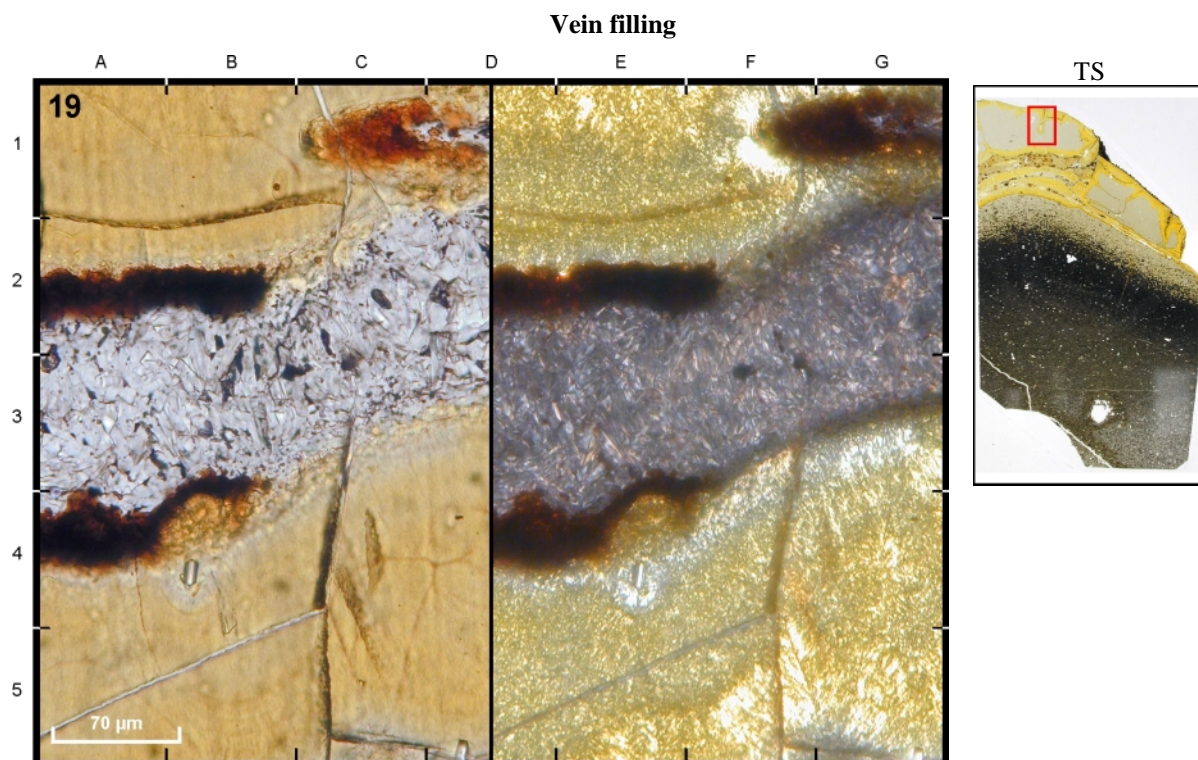
**22DS1 - 0.12 Ma - Vein filling - PPL**

Open void in the rock interior, partly lined with patchy distributed celadonite (D3, C4) and FeOOH (red-brown particle in C5).



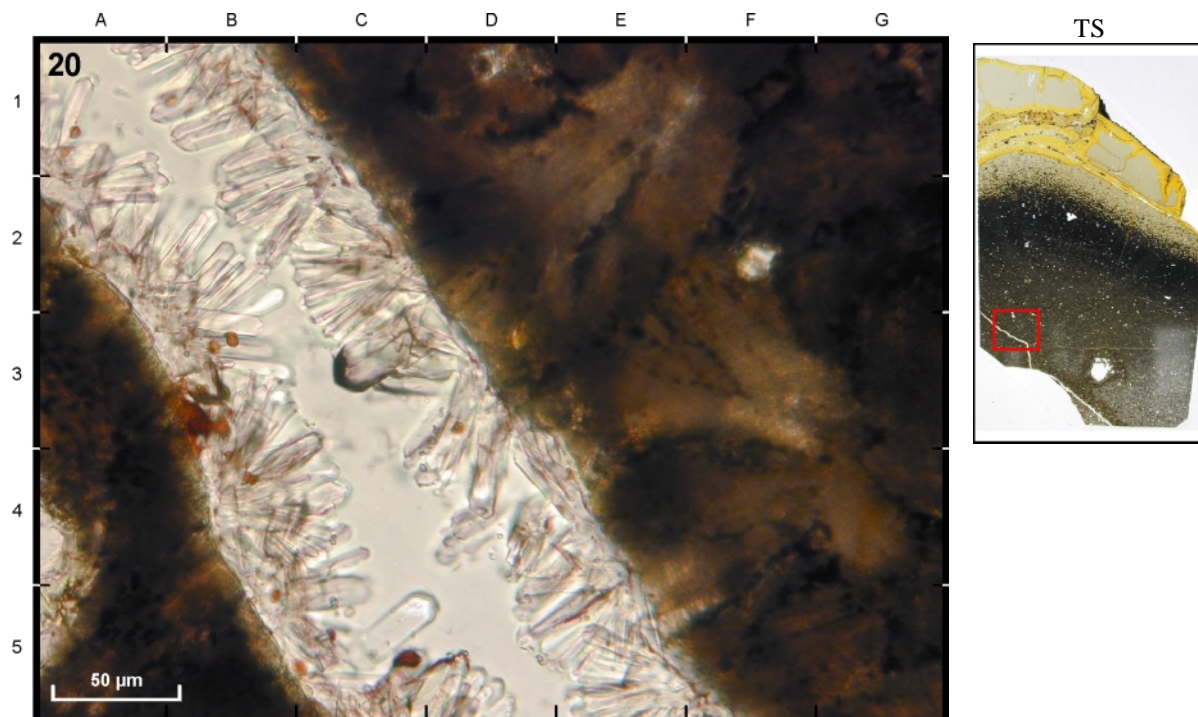
**42DS10 - 6.84 Ma - Vein filling - PPL**

Vein in a glassy matrix, filled with a mixture of celadonite (orange patches) and phillipsite. The vein is surrounded by palagonite, brown and dark brown areas are altered groundmass, plagioclase occurs as white elongated crystals (EF2, AB5).



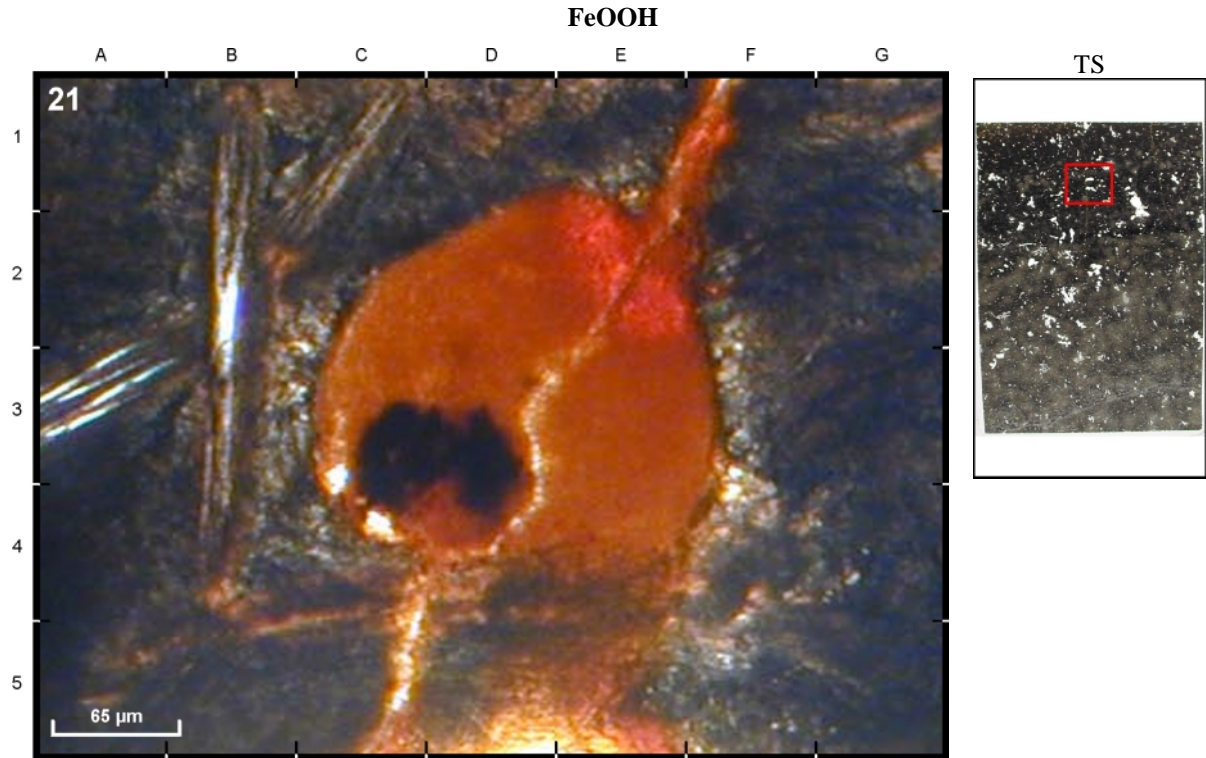
**43DS13 - 8.64 Ma - Vein filling phillipsite - PPL (left), XPL (right)**

Vein bounded by palagonite at the outer rim of the sample, filled with fibrous crystals of phillipsite. Clays are visible in C1 (PPL) and G1 (XPL). The dark area between palagonite and phillipsite consists of a mixture of altered glass / palagonite / clays.



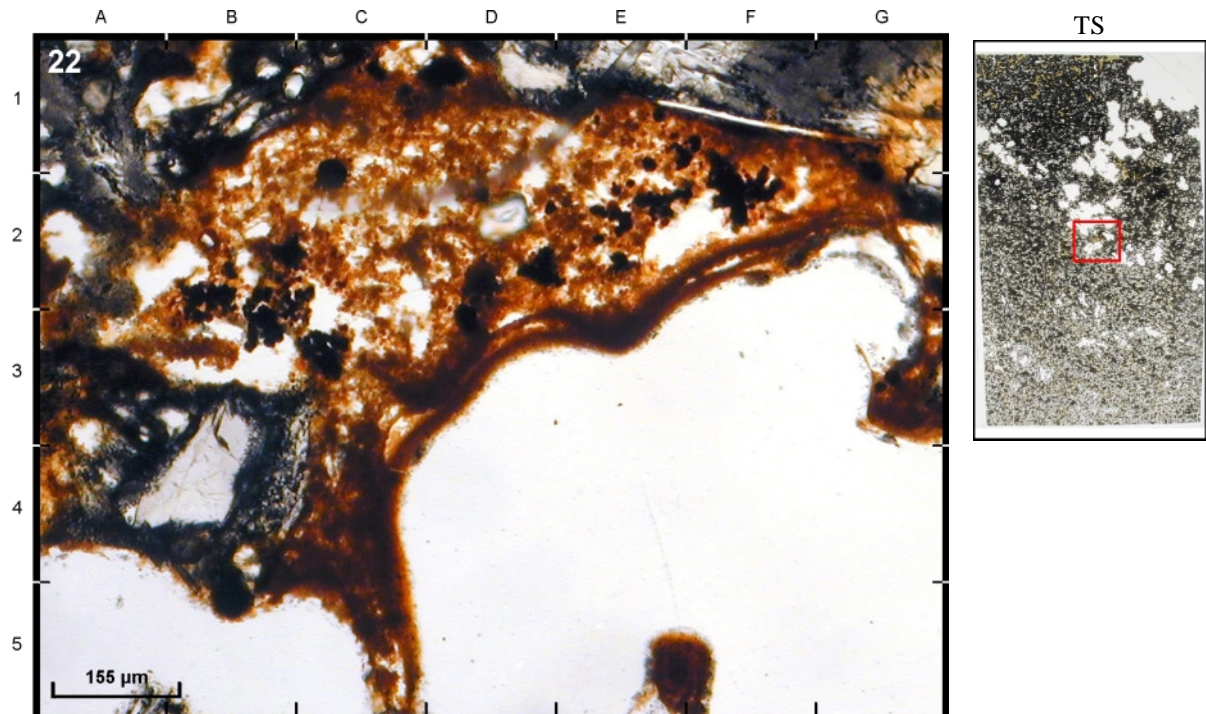
**43DS13 - 8.64 Ma - Vein filling phillipsite - PPL**

Vein in an oxidation halo partly filled with fibrous crystals of phillipsite, growing from the inner wall of the vein towards the center. The sparsely occurring small red-brown spots within the phillipsite are clays, probably celadonite.



**20DS3 - 0.15 Ma - Void filling FeOOH - PPL**

Void filling reddish brown secondary mineral, distributed within the partially weathered rock (DE5), identified as FeOOH.



**21DS4 - 0.00 Ma - Void filling FeOOH - PPL**

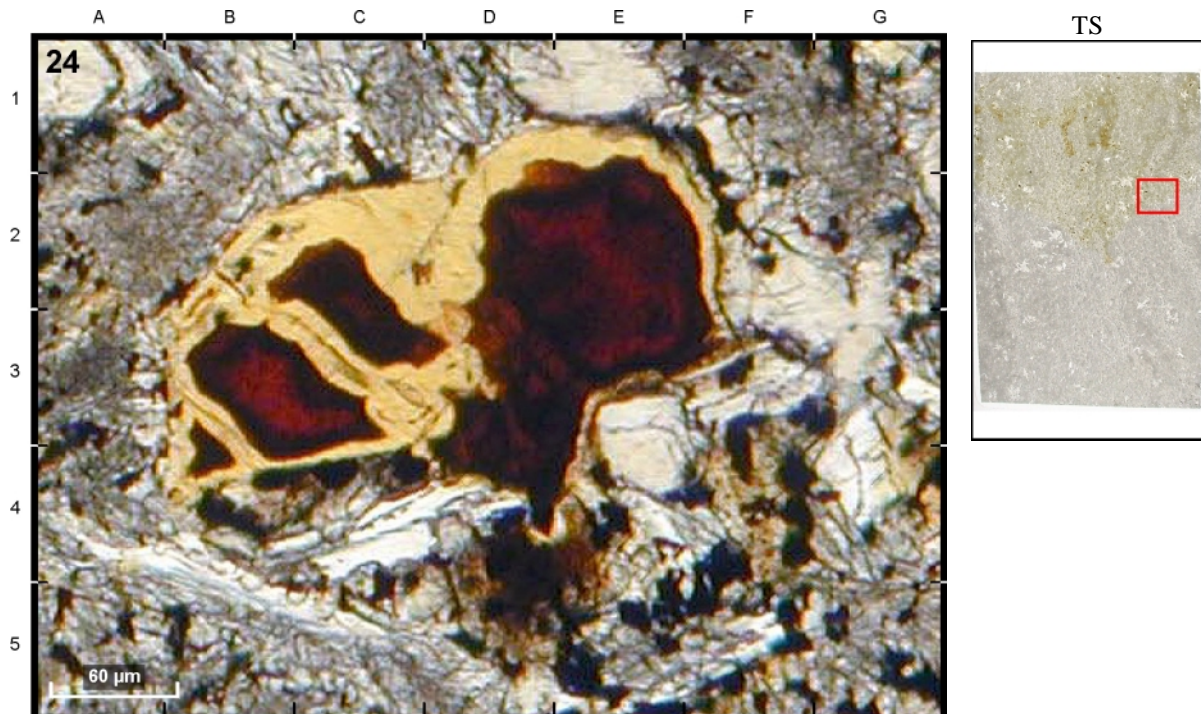
Randomly distributed void filling FeOOH. Some small spots could be needles of goethite. However, due to the empty pores between individual spots microprobe analyses yields totals lower than 50% and can therefore not confirm the presence of goethite.

**Celadonite & saponite**



**9DS4 - 2.92 Ma - Celadonite and FeOOH - PPL**

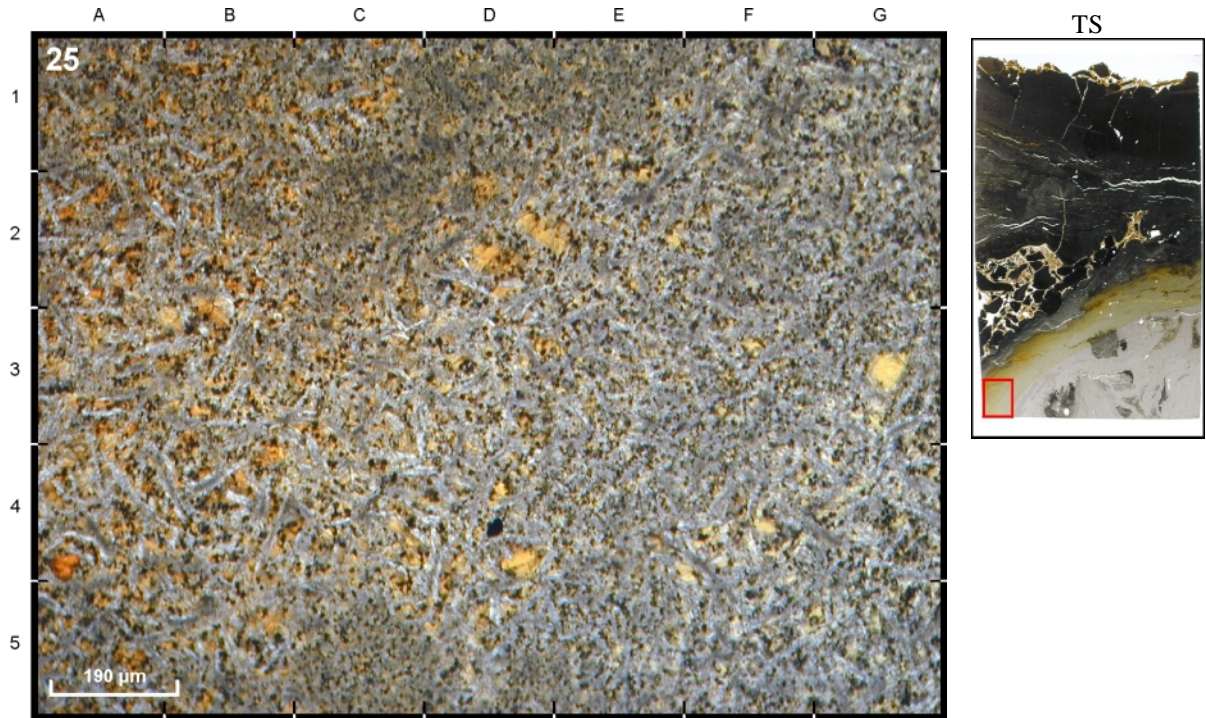
Celadonite and FeOOH replacing primary minerals (D3). Parts of the altered primary mineral in C4-5 are replaced (C4) or only covered (C5) by celadonite (identified as pyroxene). The difference can only be identified by microprobe analyses. The original shape of the pyroxene can only be supposed.



**9DS4 - 2.92 Ma - Celadonite and FeOOH - PPL**

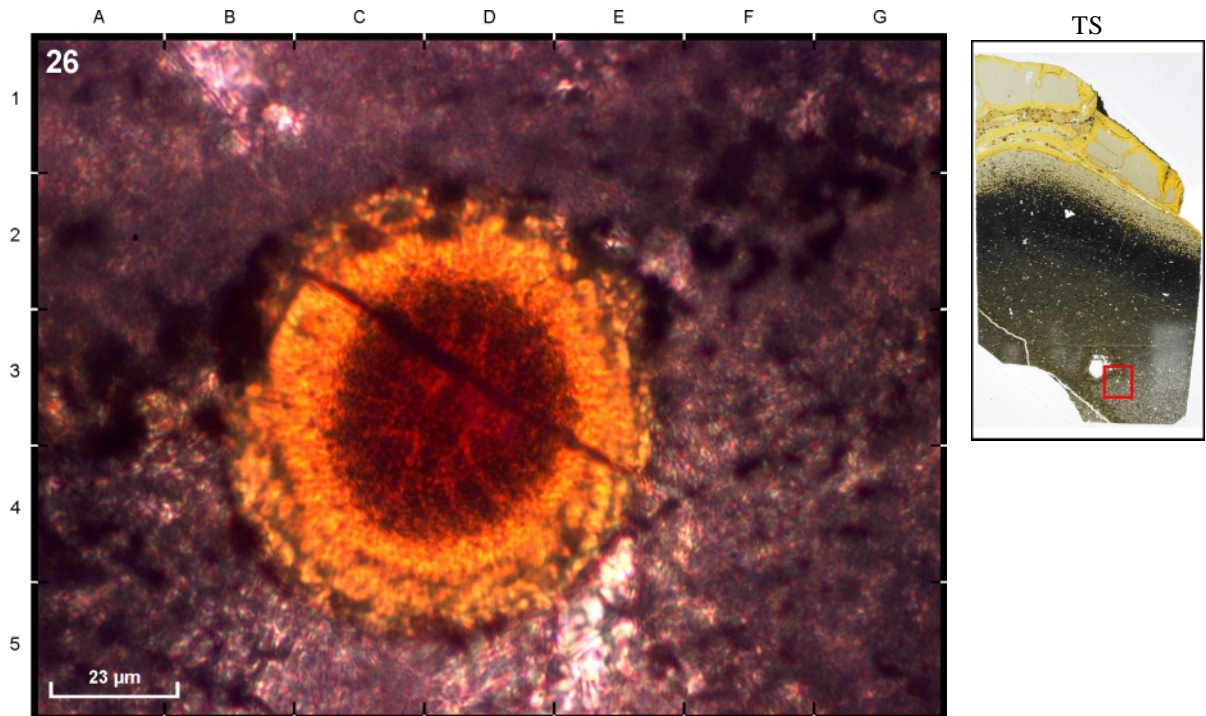
Close up of section D2-3 of the above picture. Celadonite (yellow) and FeOOH (red-brown) replacing a cluster of primary minerals with FeOOH in the center and celadonite towards the rim.

**Celadonite & saponite**



**29DS2 - 1.16 Ma - Celadonite - PPL**

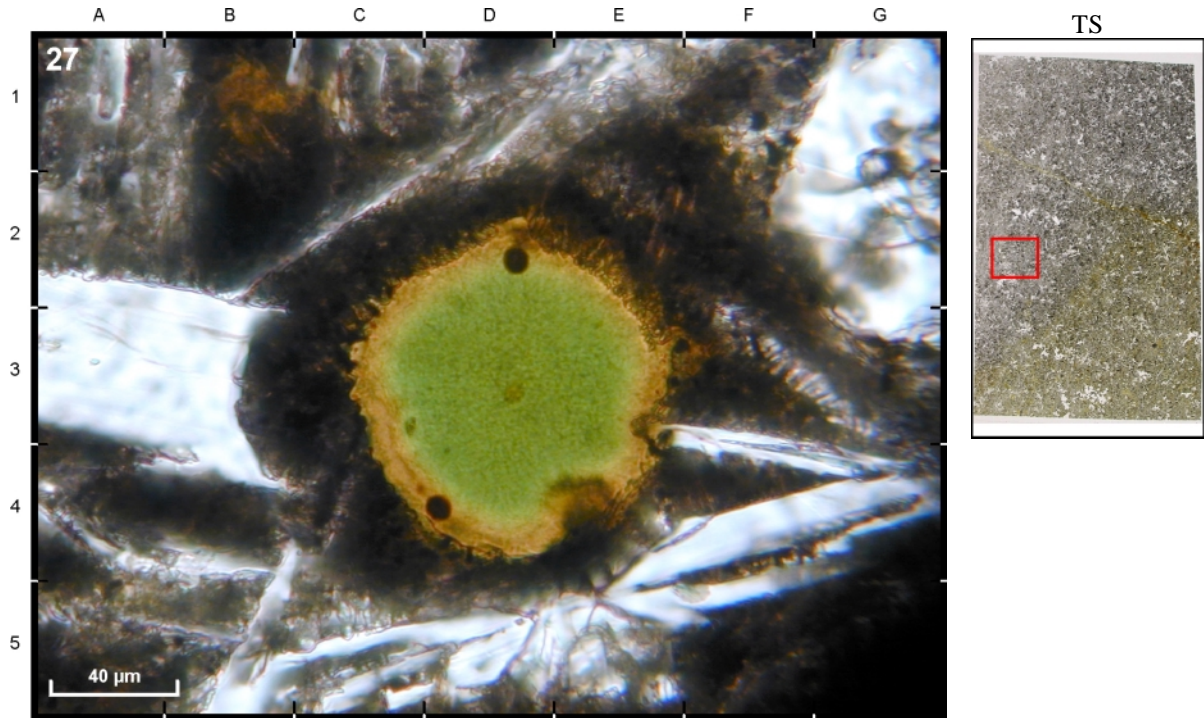
Part of an oxidation halo, showing celadonite filling voids (e.g.G3), replacing primary minerals (e.g.D4) and disseminated within the groundmass.



**43DS13 - 8.64 Ma - Celadonite, FeOOH - PPL**

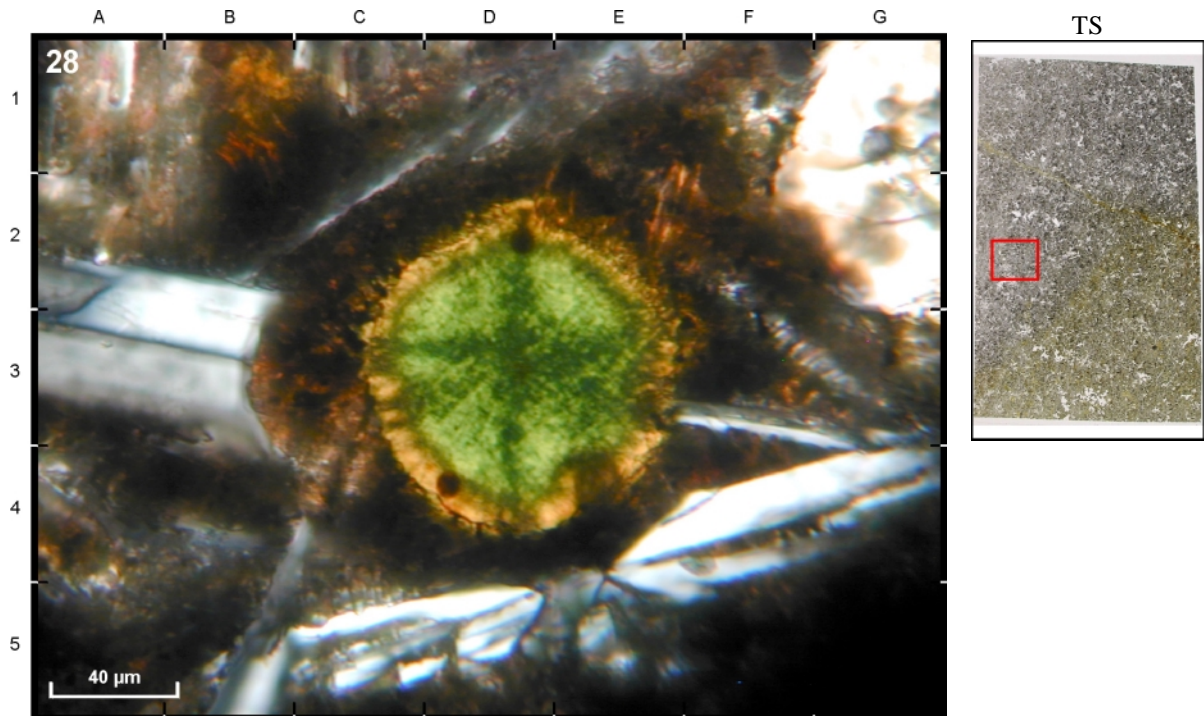
The vesicle is filled by FeOOH (brown) and later replaced or covered at the outer rim by celadonite (orange). Continuing alteration would have caused the FeOOH to be totally replaced by celadonite.

**Celadonite & saponite**



**9DS8 - 2.92 Ma - Void filling celadonite and saponite - PPL**

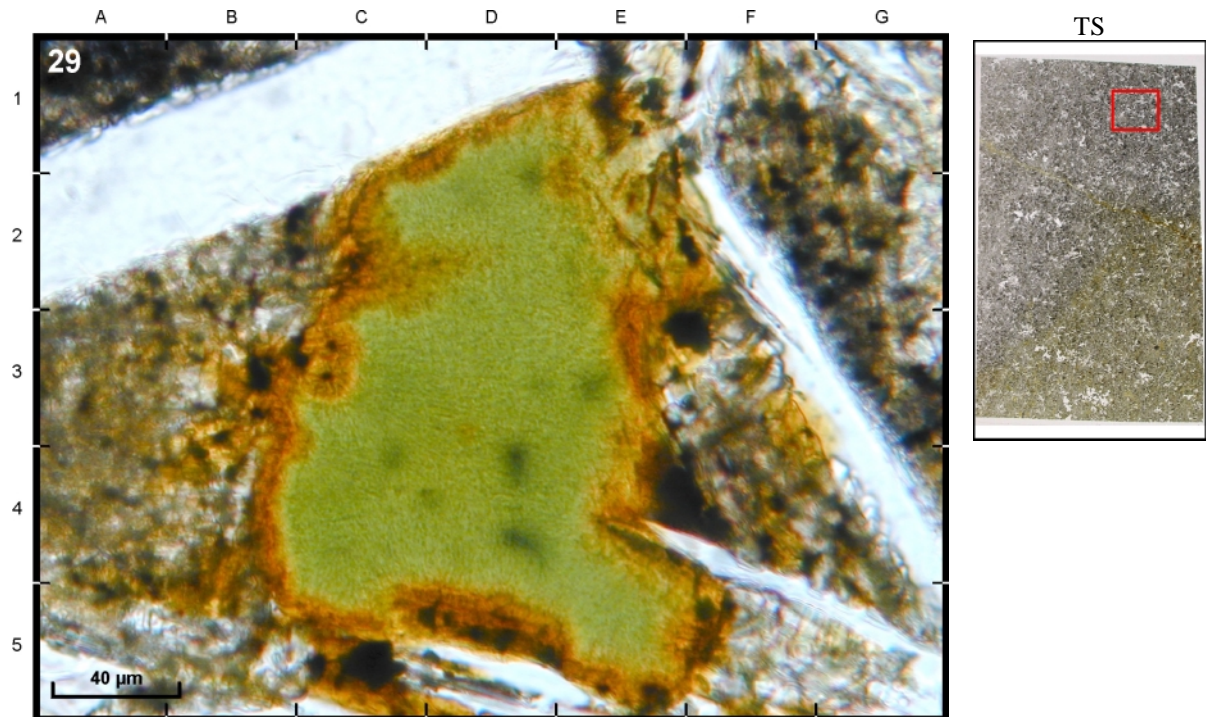
The vesicle is filled by celadonite (green) and later replaced at the outer rim by saponite (orange), indicating a redox change towards more reducing conditions. The yellow-green transition zone is characterized by a mixture of saponite and celadonite. More reducing conditions would have caused the celadonite to be totally replaced by saponite. Image taken from [Schramm *et al.*, submitted].



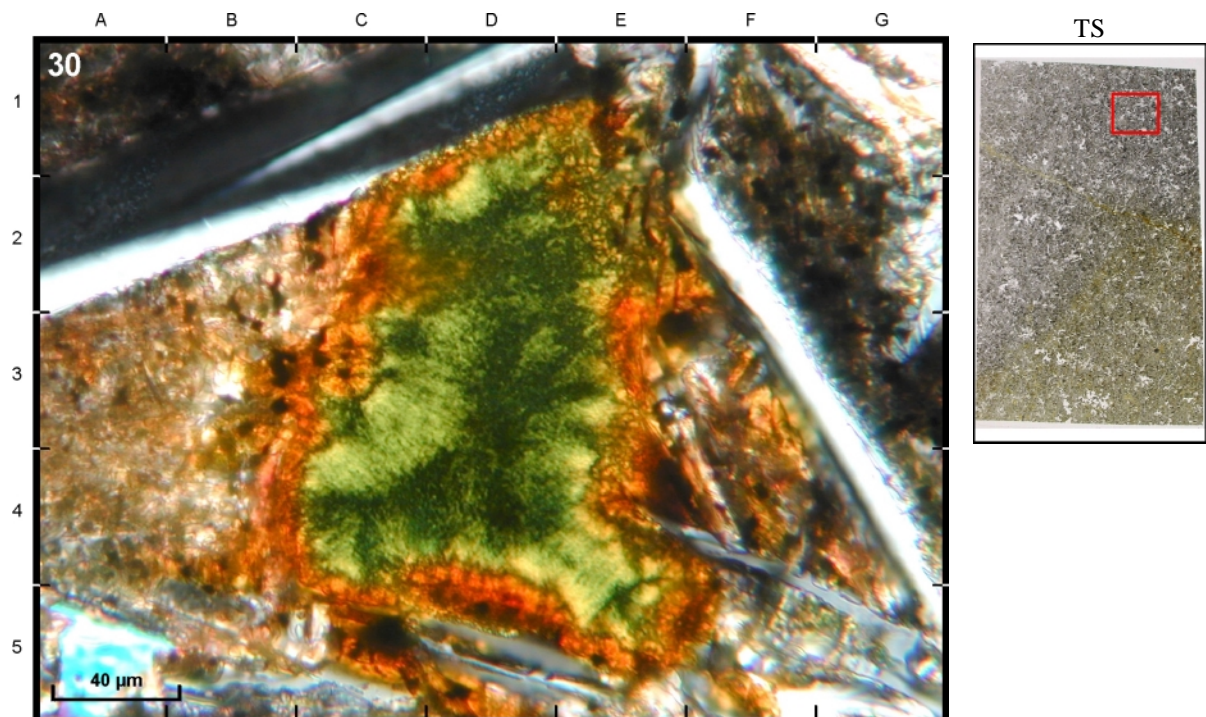
**9DS8 - 2.92 Ma - Celadonite, saponite-celadonite, saponite - XPL**

The clays seem preferentially orientated to the center. The dark areas of the green colored celadonite originate from a micro-porous clump of celadonite crystals and refraction in the empty pores existing between the microparticles of celadonite.

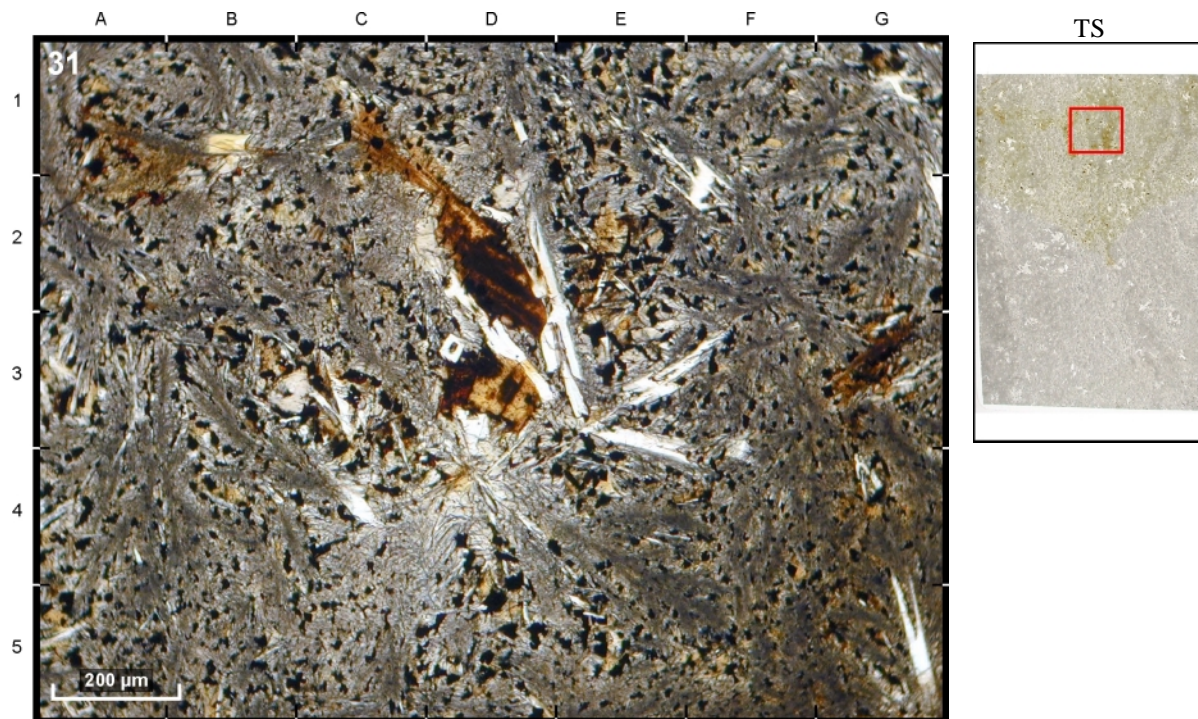
## Celadonite &amp; saponite

**9DS8 - 2.92 Ma - Void filling celadonite and saponite - PPL**

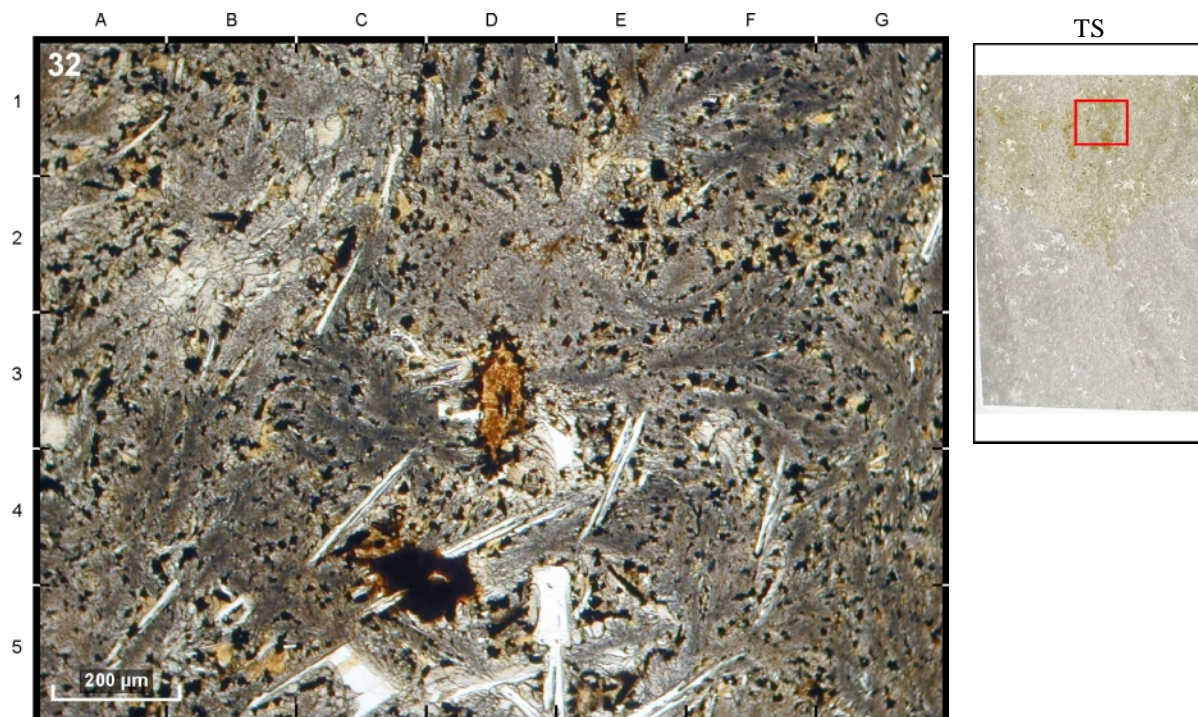
The void is filled by celadonite (green) and later replaced at the outer rim by saponite (orange), indicating a redox change towards more reducing conditions. The yellow-green transition zone is characterized by a mixture of saponite and celadonite. More reducing conditions would have caused the celadonite to be totally replaced by saponite.

**9DS8 - 2.92 Ma - Celadonite, saponite-celadonite, saponite - XPL**

The clays seem preferentially orientated to the center. The dark areas of the green colored celadonite originate from a micro-porous clump of celadonite crystals and refraction in the empty pores existing between the microparticles of celadonite.

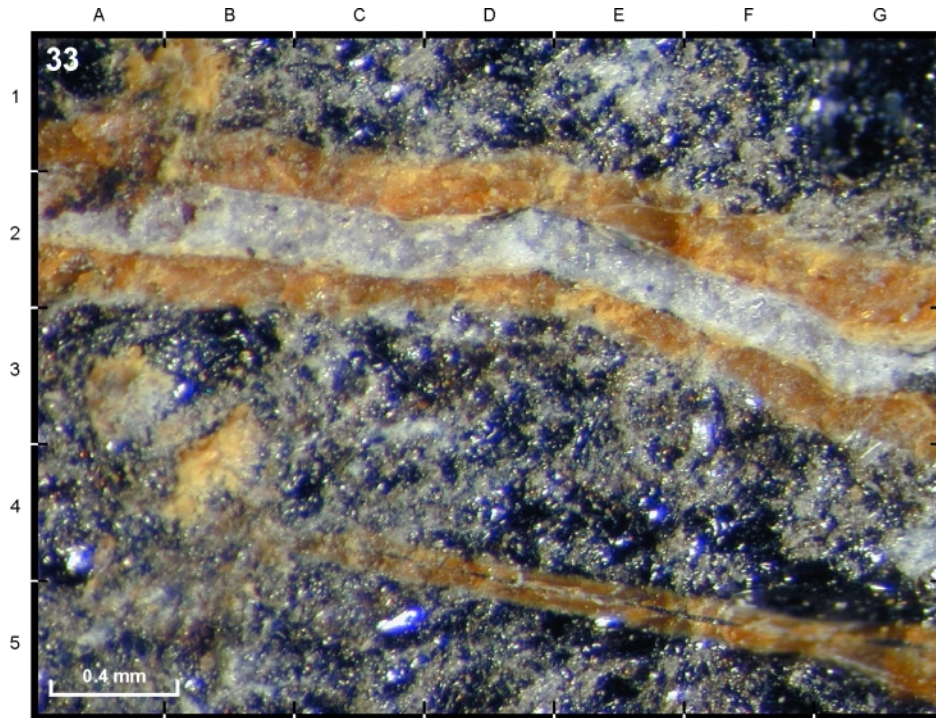
**Celadonite & saponite****9DS4 - 2.92 Ma - Celadonite - PPL**

Celadonite and FeOOH replacing primary minerals (D3,D2), probably olivine in an oxidation halo. Pyroxene, completely covered by celadonite is visible in E2. Even under XPL the pyroxene can not be identified by its color or shape, only the microprobe analyses is identifying the mineral as pyroxene, only covered by celadonite.

**9DS4 - 2.92 Ma - Celadonite - PPL**

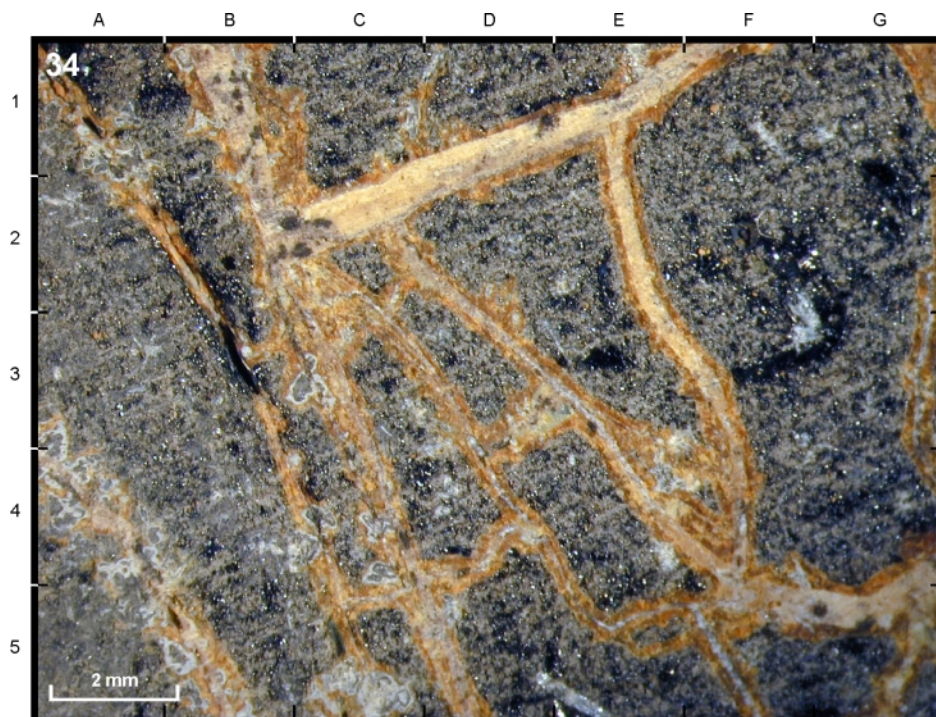
An euhedral crystal of olivine, completely altered by celadonite (D3) located in an oxidation halo. The problem of identifying replaced or covered primary minerals is obvious in B5. The yellow-brown colored grains are pyroxene (left) and plagioclase (right), covered by celadonite. Analyses still evidence the primary mineral composition.

**Phillipsite**



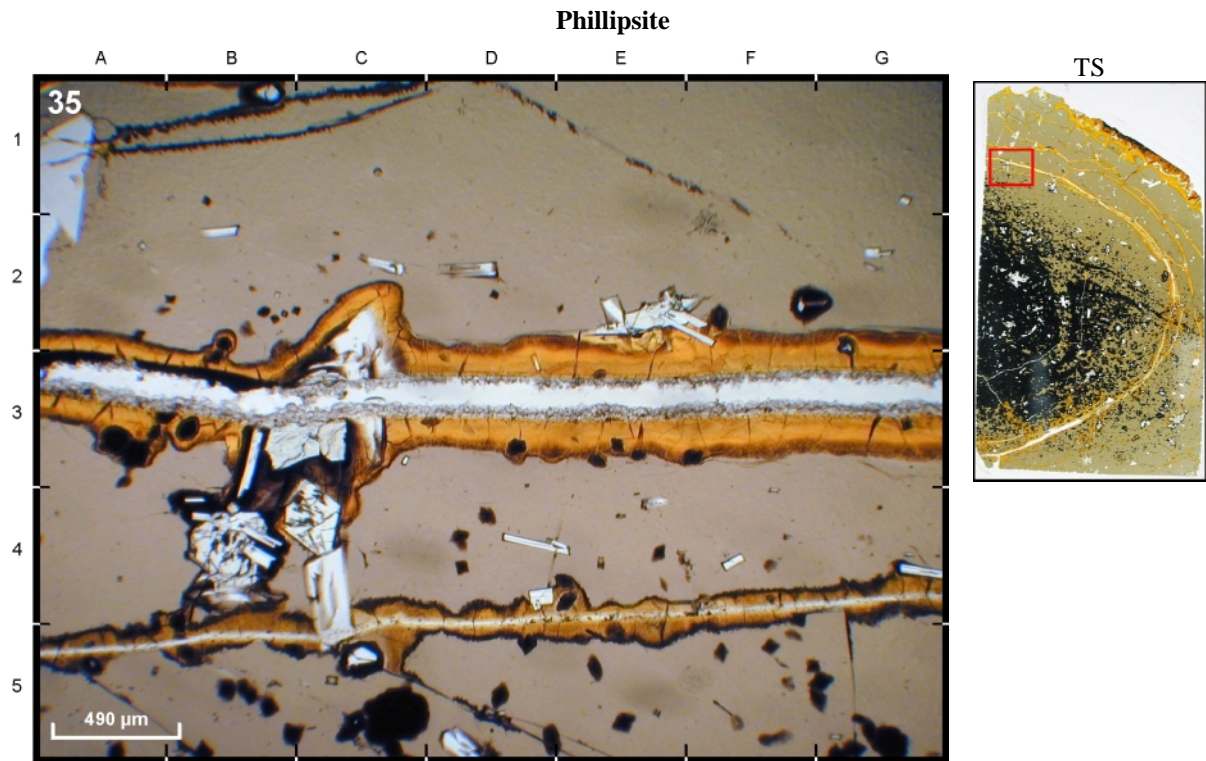
**42DS2 - 6.84 Ma - Phillipsite**

Veins in a glassy matrix, completely filled by phillipsite (white crystals) and bounded by palagonite (orange). Picture taken through a binocular. Image taken from [Schramm *et al.*, submitted].



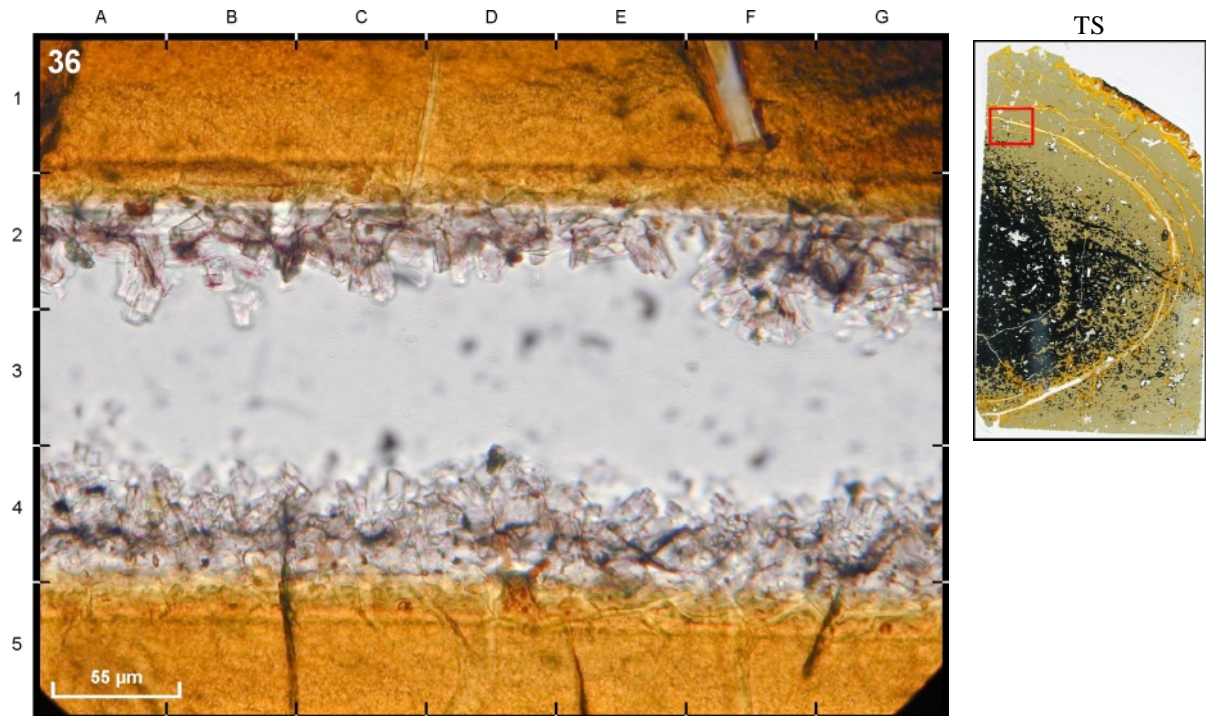
**42DS9 - 6.84 Ma - Phillipsite**

Veins in a basaltic groundmass completely filled by phillipsite or a mixture of clays and phillipsite (yellow-orange material at C2 - F1 and E1 - F3), bounded by orange palagonite. Picture taken through a binocular.



**42DS10 - 6.84 Ma - Phillipsite - PPL**

Open vein in a glassy matrix bounded by palagonite, lined with phillipsite. The smaller vein remains open or is partly filled with palagonite or trace amounts of phillipsite.



**42DS10 - 6.84 Ma - Phillipsite - PPL**

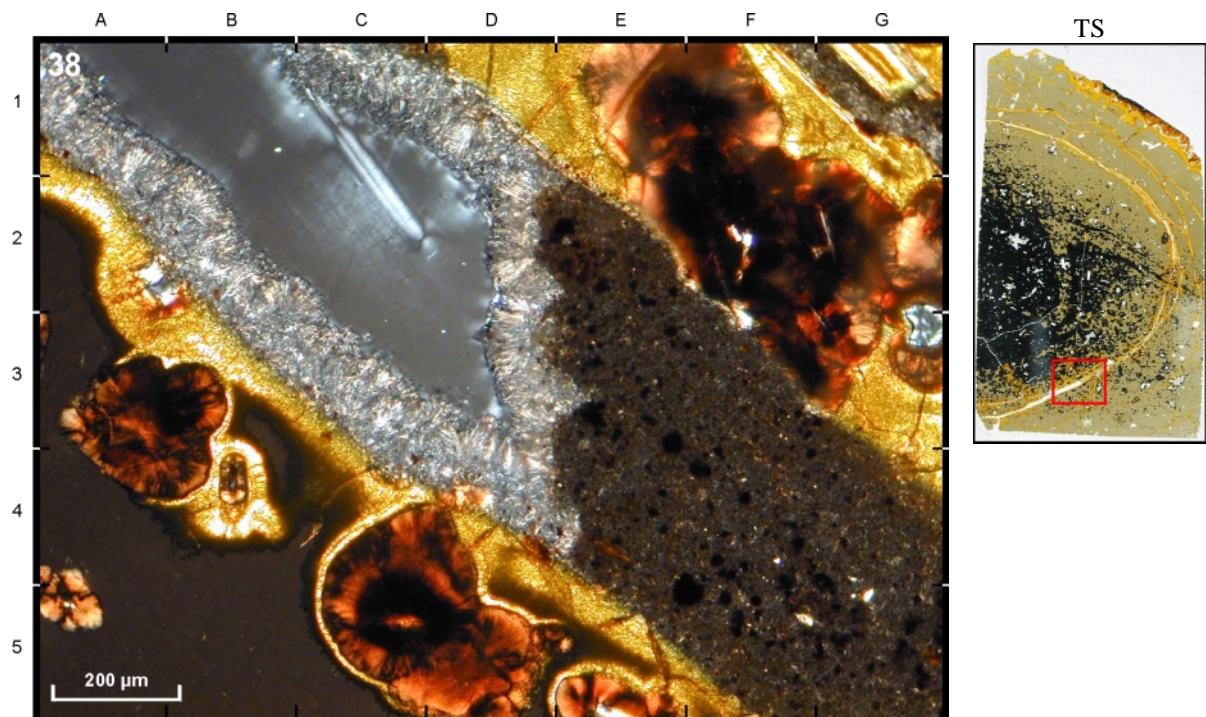
Close up of section D3 from the above picture. Formation of phillipsite at the inner wall of the vein created by glass dissolution, bounded by palagonite. Continuing alteration would have caused the vein to be completely filled with phillipsite. Image taken from [Schramm *et al.*, submitted].

**Phillipsite**



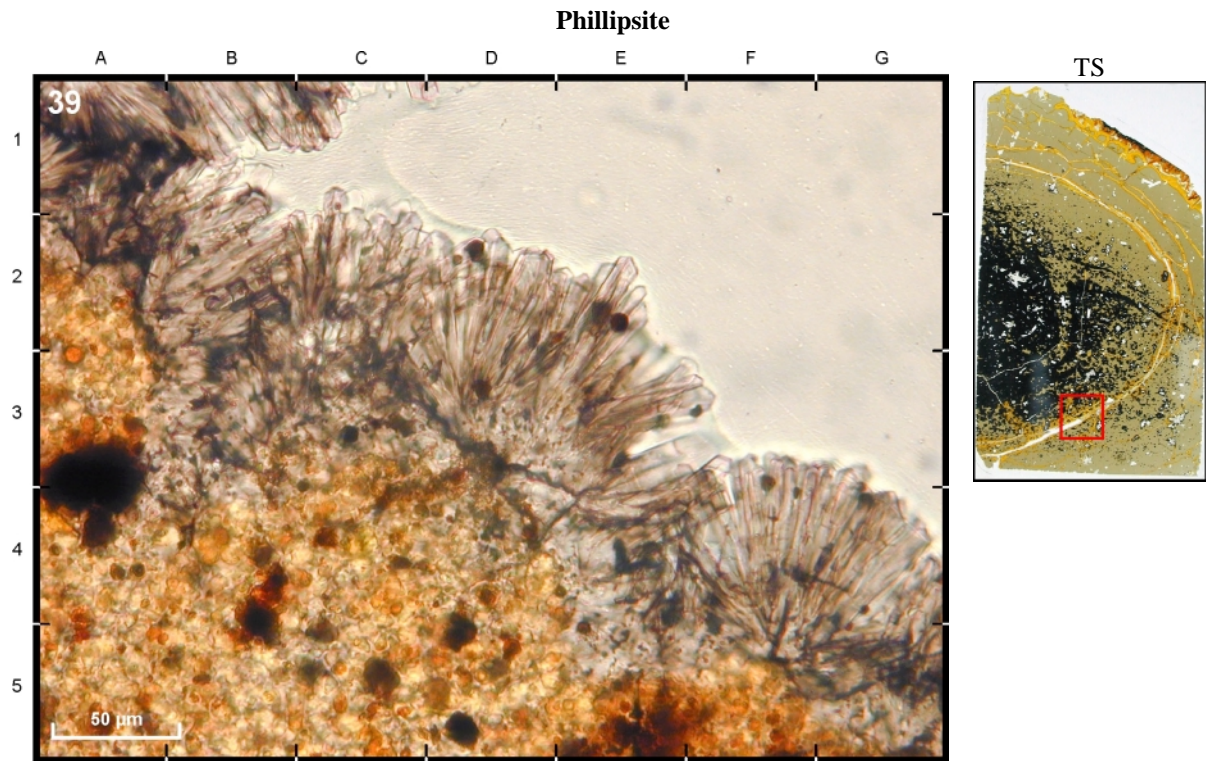
**42DS10 - 6.84 Ma - Phillipsite - PPL**

Vein in a glassy matrix, lined with phillipsite (upper left corner) or filled with a mixture of clay and phillipsite (brown spotted crystals). The vein is bounded by palagonite (orange) and groundmass material (variolites) / altered glass (dark areas).



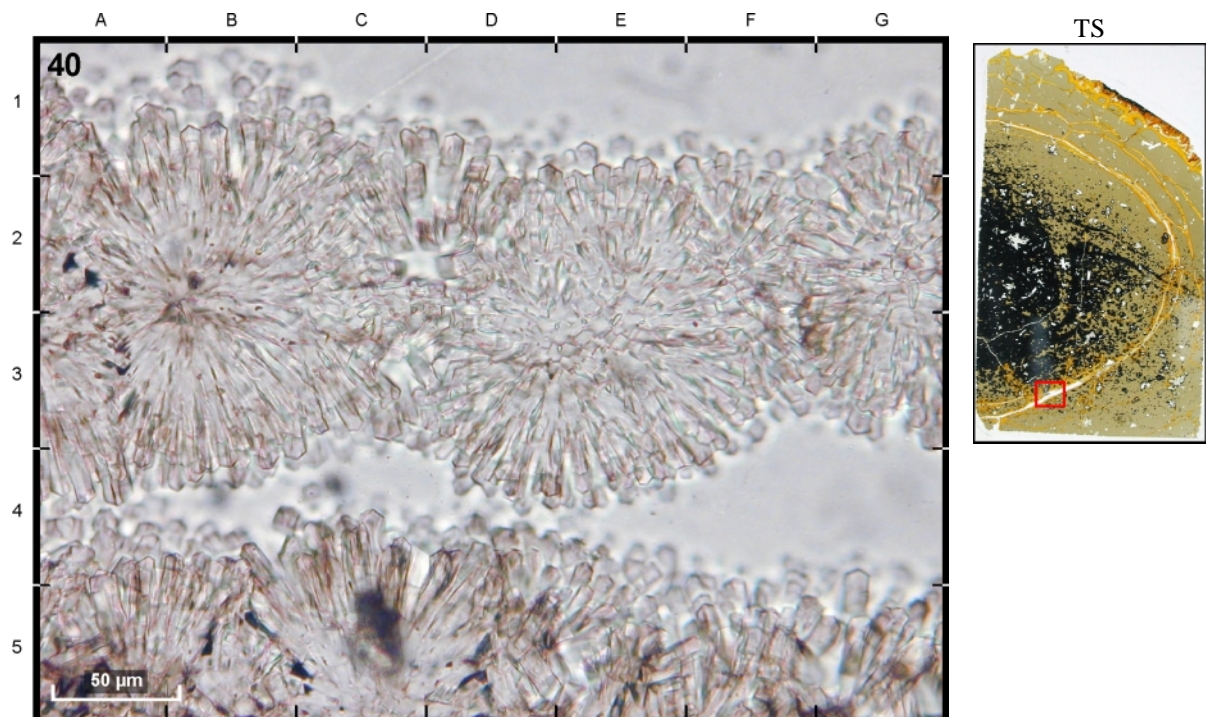
**42DS10 - 6.84 Ma - Phillipsite - XPL**

Under XPL phillipsite appears in about the same color, whereas the phillipsite / clay mixture shows a darker color, different from the appearance of celadonite under XPL (green or orange, definitely brighter).



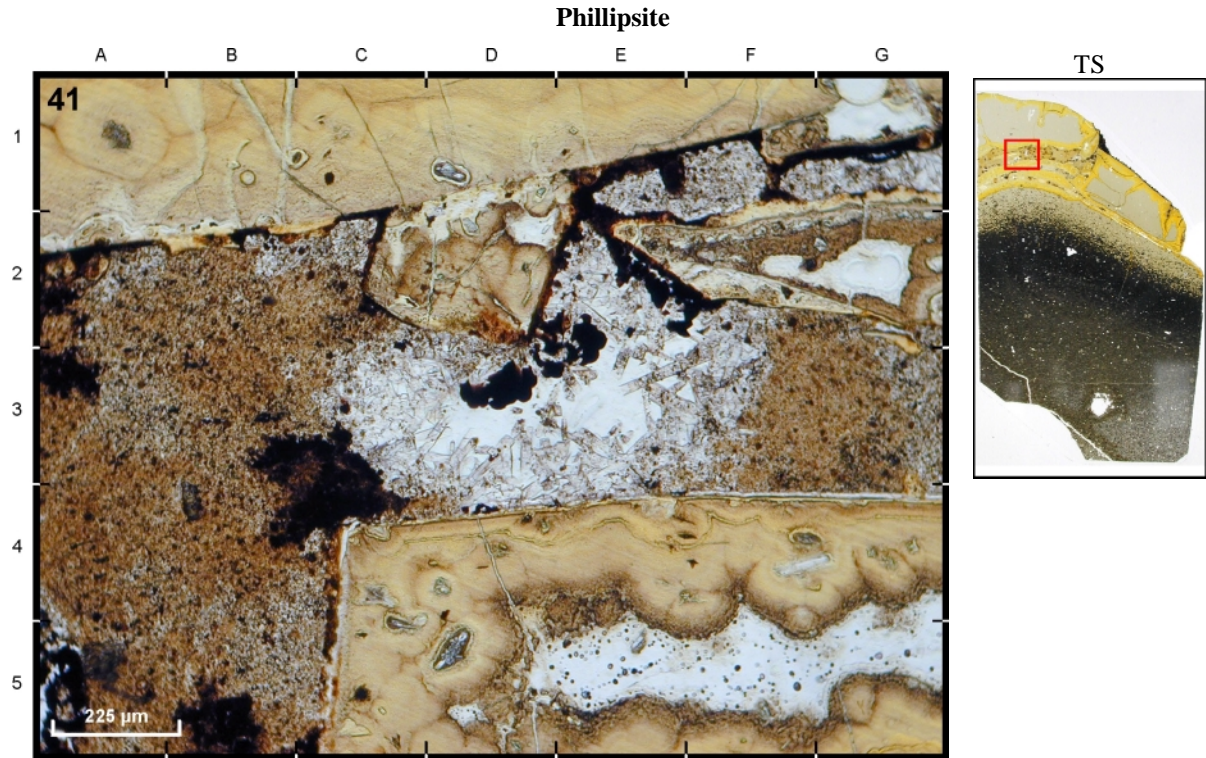
**42DS10 - 6.84 Ma - Phillipsite - PPL**

Phillipsite growing from the inner wall of a vein in contact with a mixture of palagonite / clays and phillipsite.



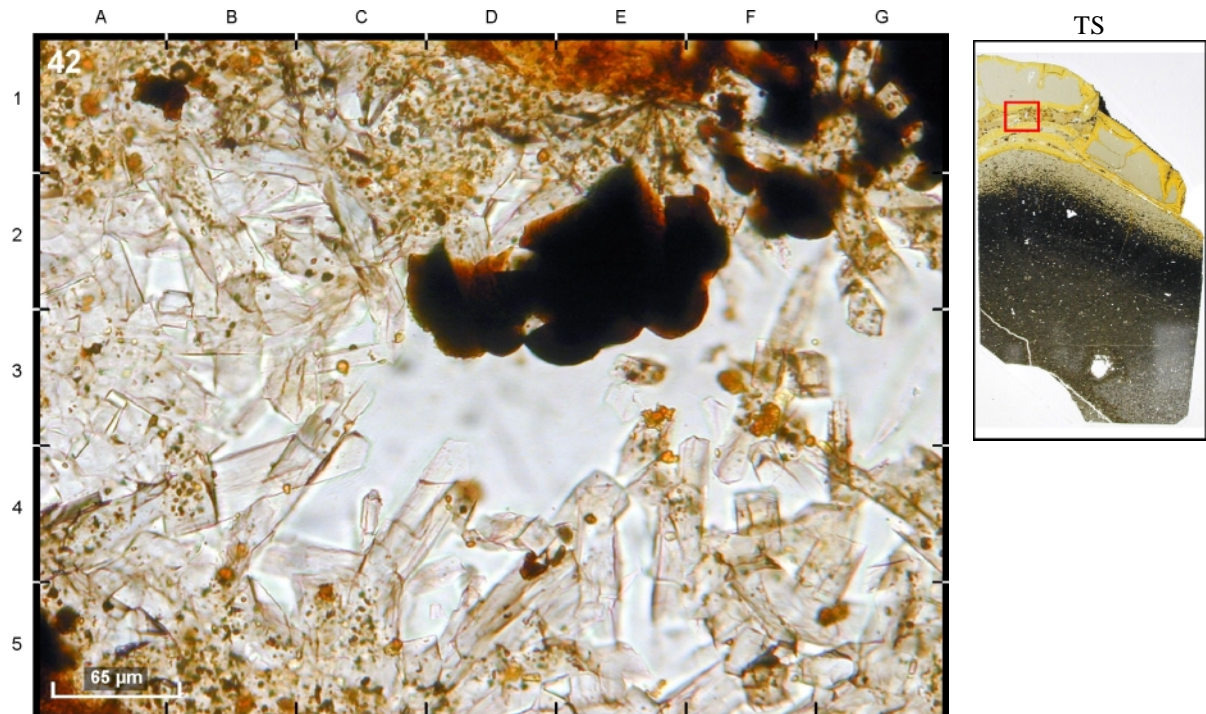
**42DS10 - 6.84 Ma - Phillipsite - PPL**

Vein filling fibrous fan-shaped growing crystals of phillipsite. Image taken from [Schramm *et al.*, submitted].



**43DS13 - 8.64 Ma - Phillipsite and clays - PPL**

Phillipsite (fibrous crystals), and a mixture of phillipsite and clays (brown spotted particles) filling a vein in a glassy matrix bounded by palagonite (yellow-orange areas) at the glassy margin of the sample.

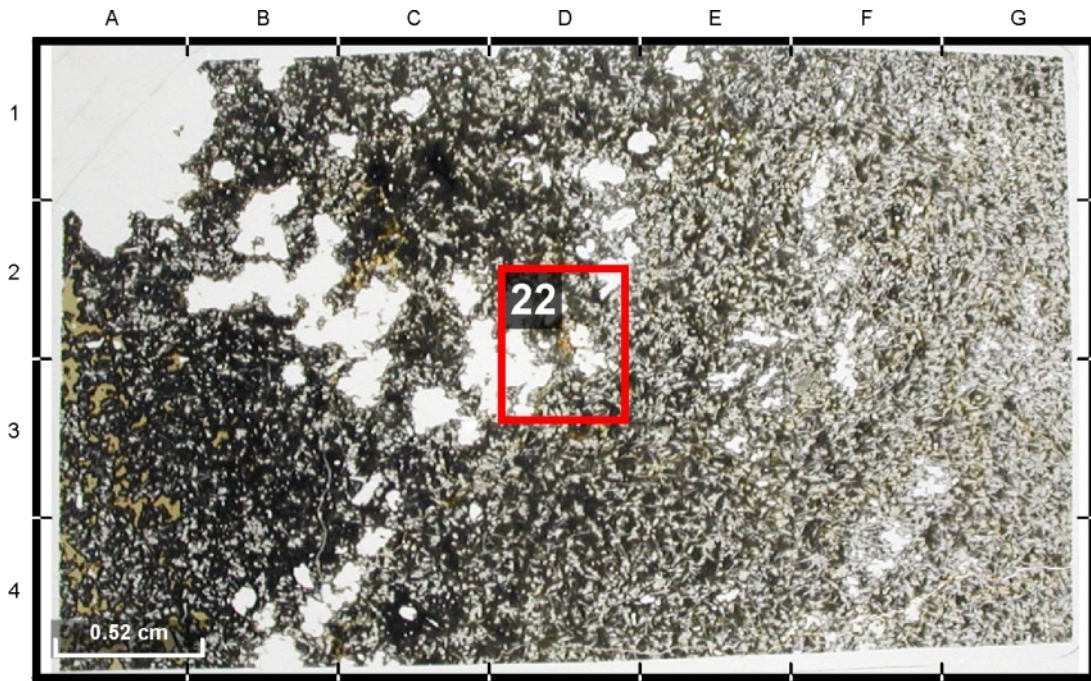


**43DS13 - 8.64 Ma - Phillipsite and clays - PPL**

Close up of the above picture (DE3) illustrating fibrous crystals of phillipsite with decreasing amounts of clay minerals towards the open center of the vein.

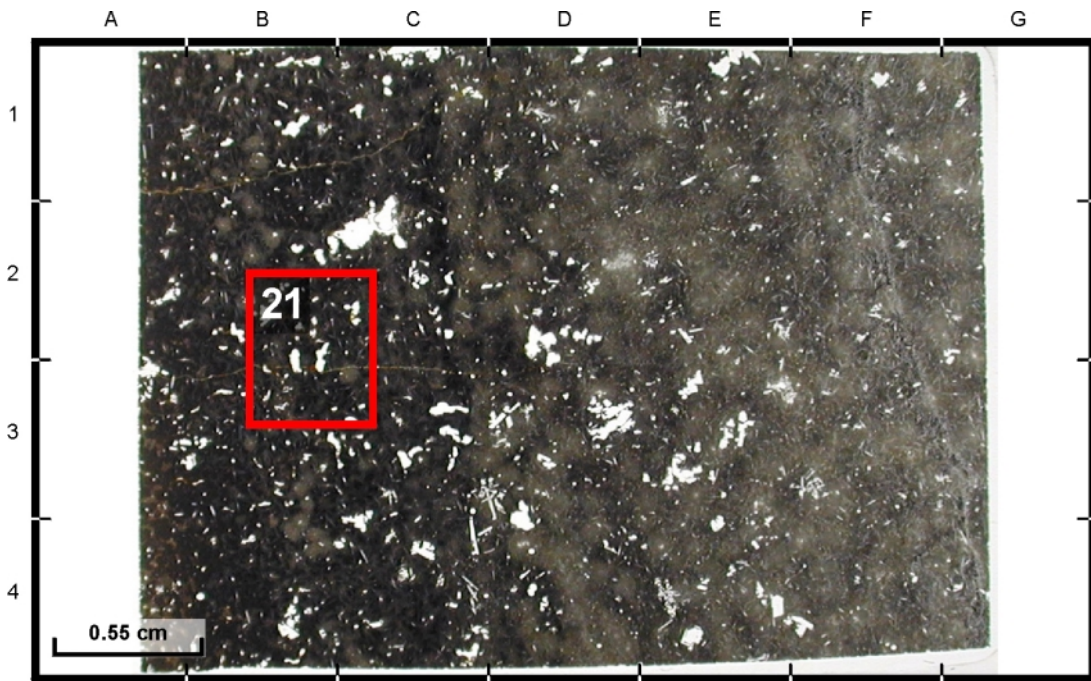
### Appendix – Thin sections

An overview of the position of all photomicrographs in the thin sections.



**21DS4 - Ridge axis 0.0 Ma**

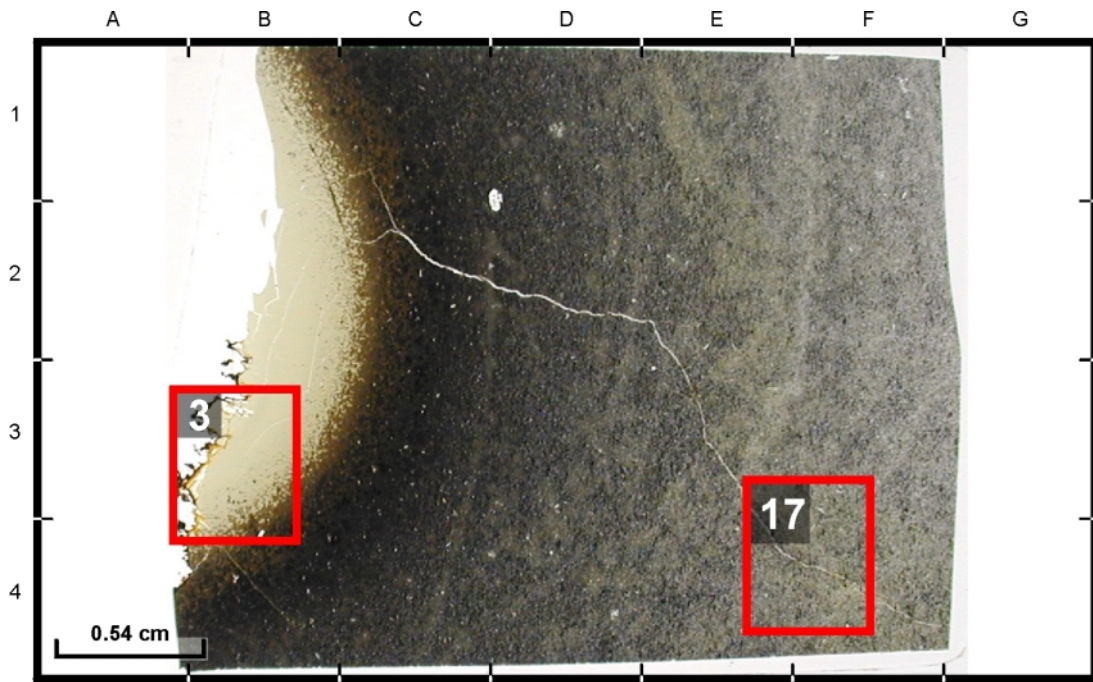
22: Void filling FeOOH. PPL.



**20DS3 - Ridge axis 0.015 Ma**

21: Void filling FeOOH, probably needles of goethite. PPL.

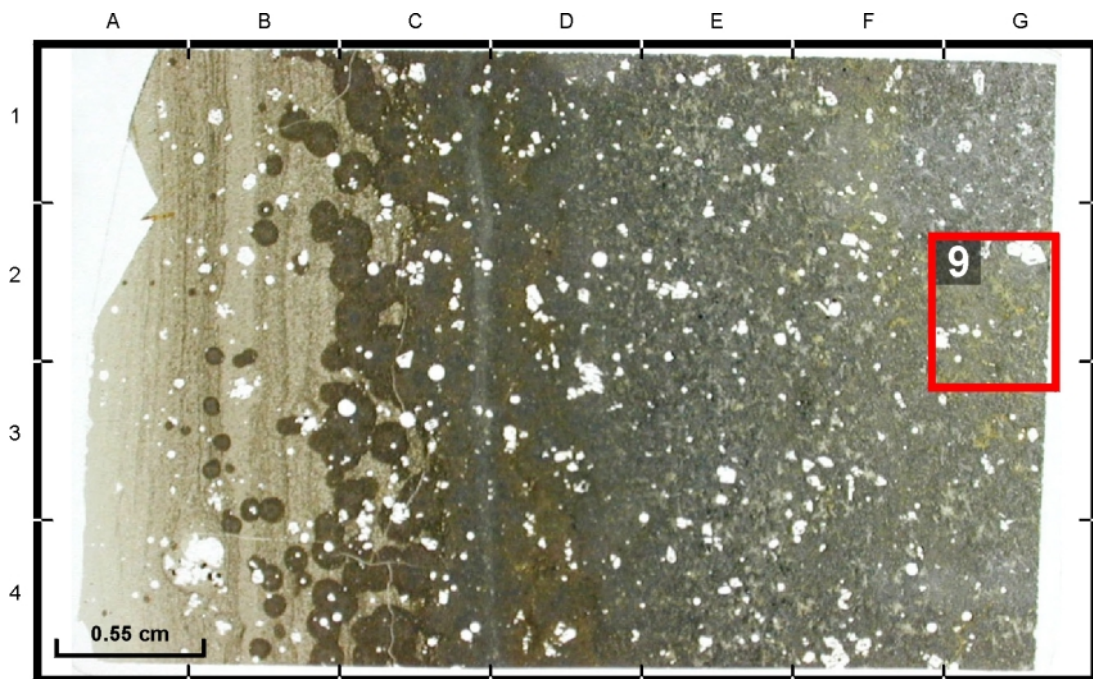
**Thin sections**



**22DS1 - 0.15 Ma**

- 3: Fresh glass and variolites at the outer rim of the sample. PPL.
- 17: Open vein in the least altered part of the rock, lined with celadonite and FeOOH. PPL.

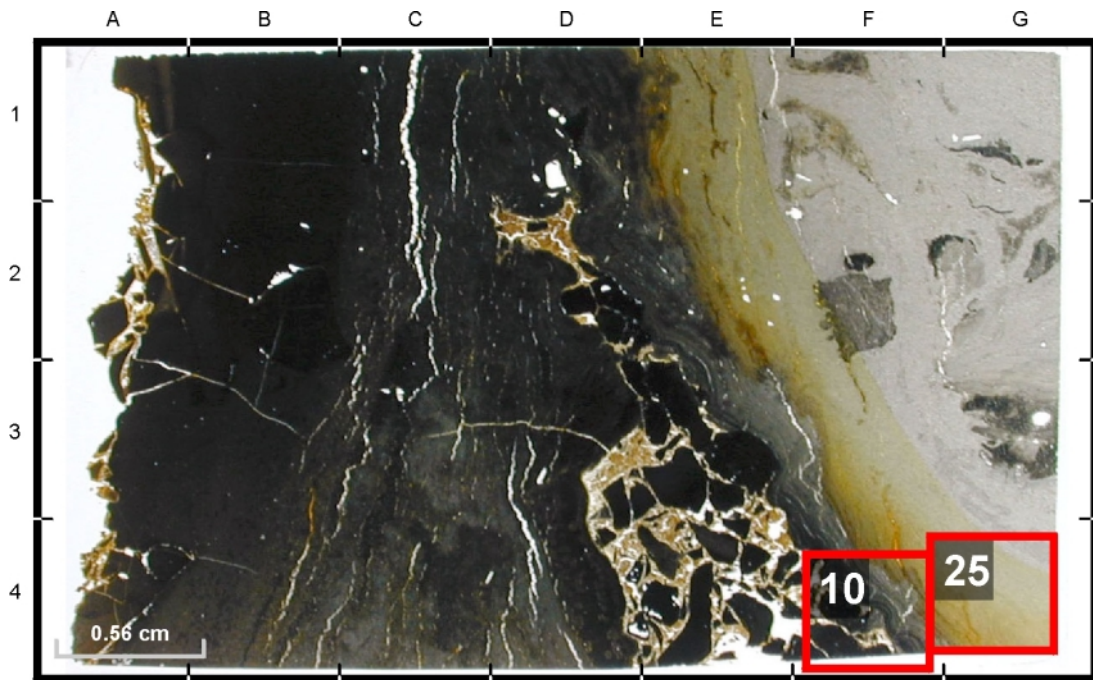
The black halo represents a transition zone from the glassy margin to the oxidation halo (C1-B4).



**28DS1 - 0.65 Ma**

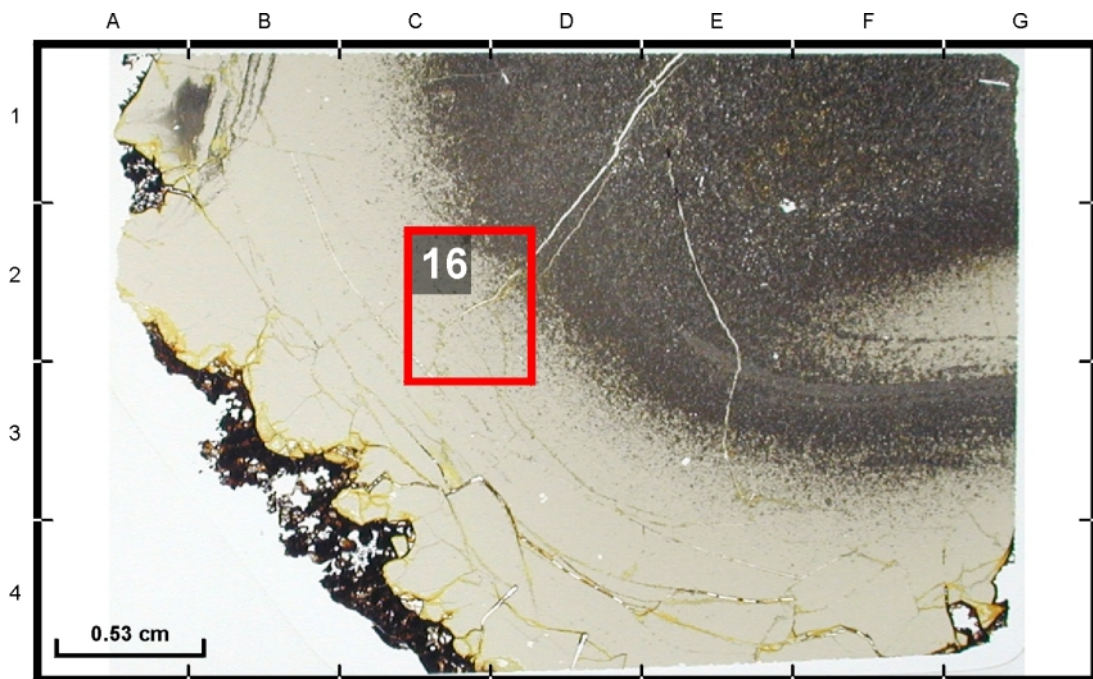
- 9: Voids located at the oxidation halo, lined or completely filled with celadonite. PPL.

Thin sections



29DS2 - 1.16 Ma

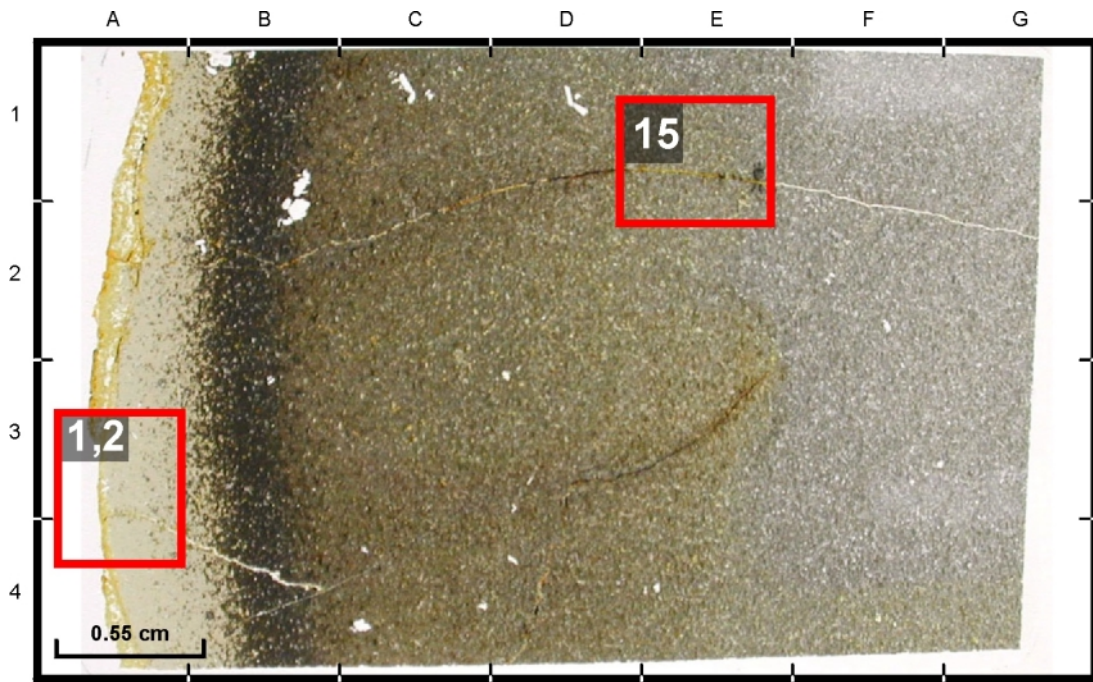
- 10: Void in a basaltic groundmass, partly filled with sediment, clays, phillipsite and foraminifera. PPL.
- 25: Disseminated celadonite in the groundmass of an oxidation halo. PPL.



35DS2 - 2.56 Ma

- 16: Open vein in a glassy matrix, partly bounded by palagonite. PPL.

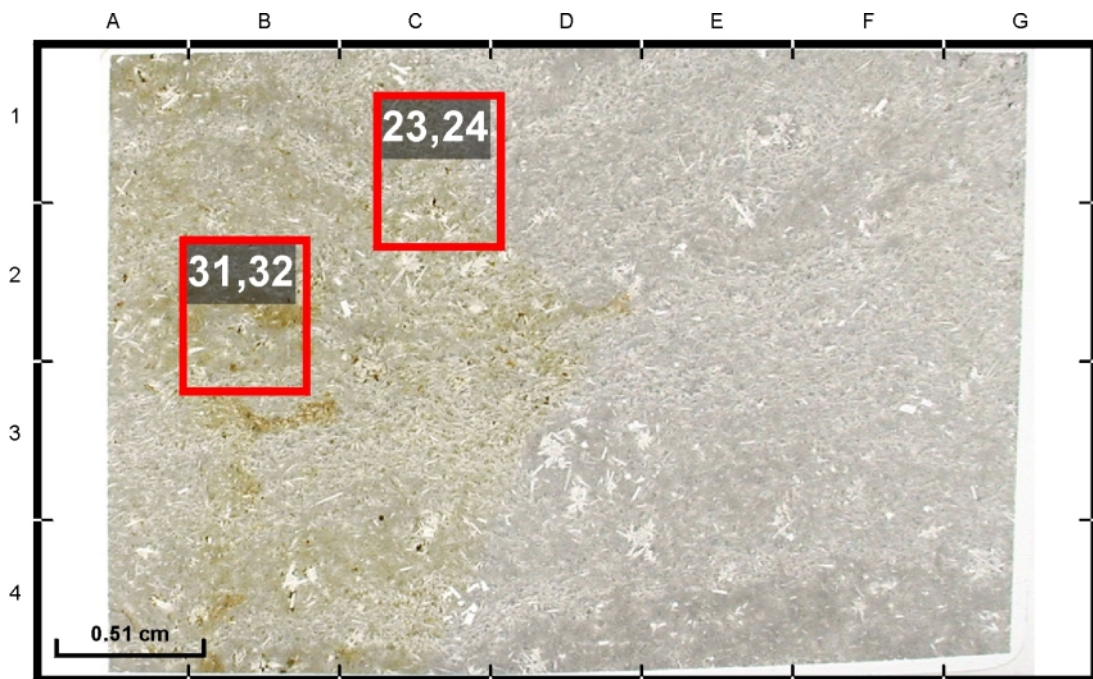
**Thin sections**



**35DS4 - 2.56 Ma**

- 1: Fresh glass with palagonite at the outer rim of the sample. PPL.
- 2: Same field of view as Pic.1 under XPL.
- 15: Vein filling celadonite at the border of oxidation halo and rock interior, with decreasing contamination of FeOOH towards the rock interior. PPL.

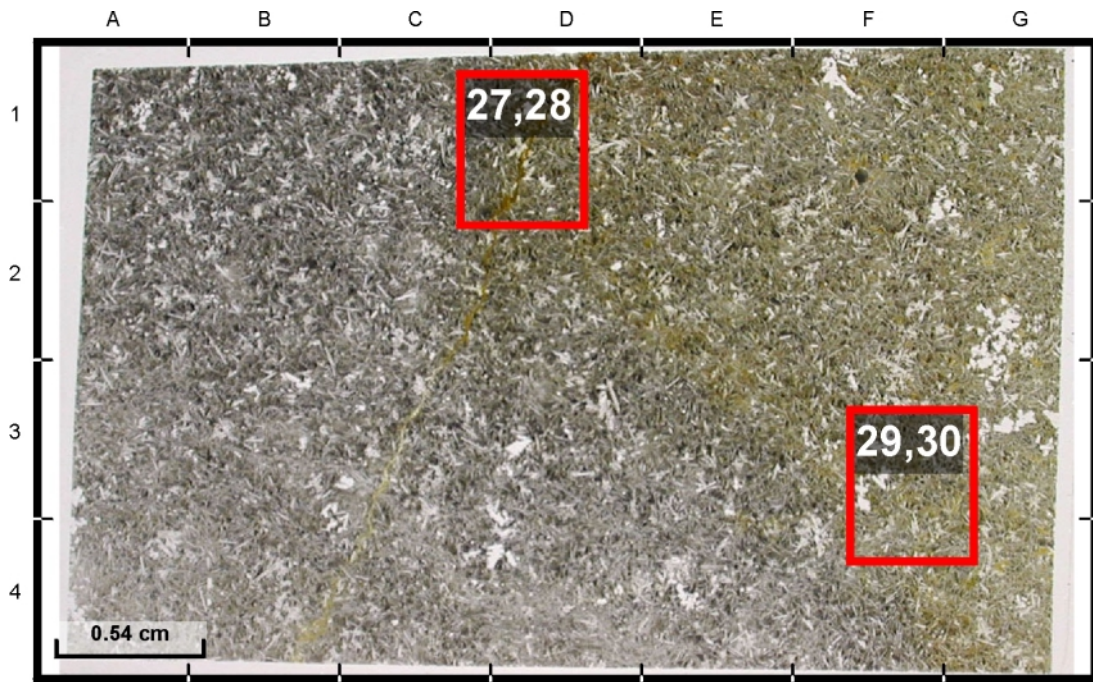
The black halo represents a transition zone from the glassy margin to the oxidation halo (B1-B4).



**9DS4 - 2.92 Ma**

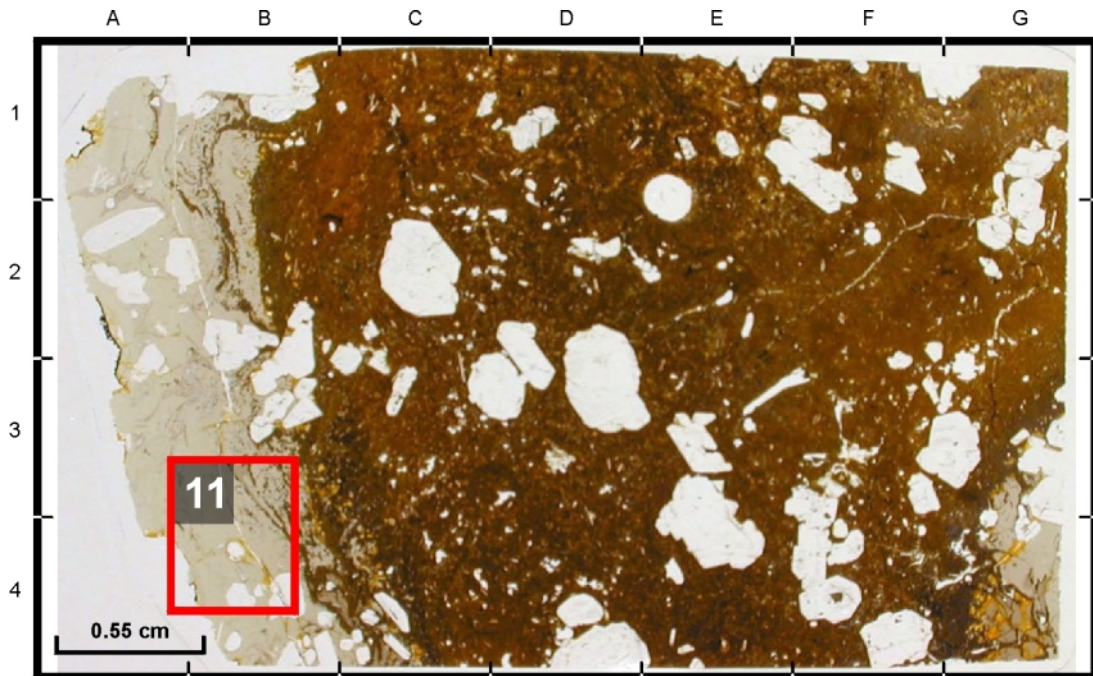
- 23: Celadonite and FeOOH replacing and covering primary minerals in an oxidation halo. PPL.
- 24: Close up of Pic.23. PPL.
- 31: Celadonite and FeOOH replacing and covering primary minerals in an oxidation halo. PPL.
- 32: An euhedral crystal of olivine, completely altered by celadonite, located in an oxidation halo. PPL.

Thin sections



9DS8 - 2.92 Ma

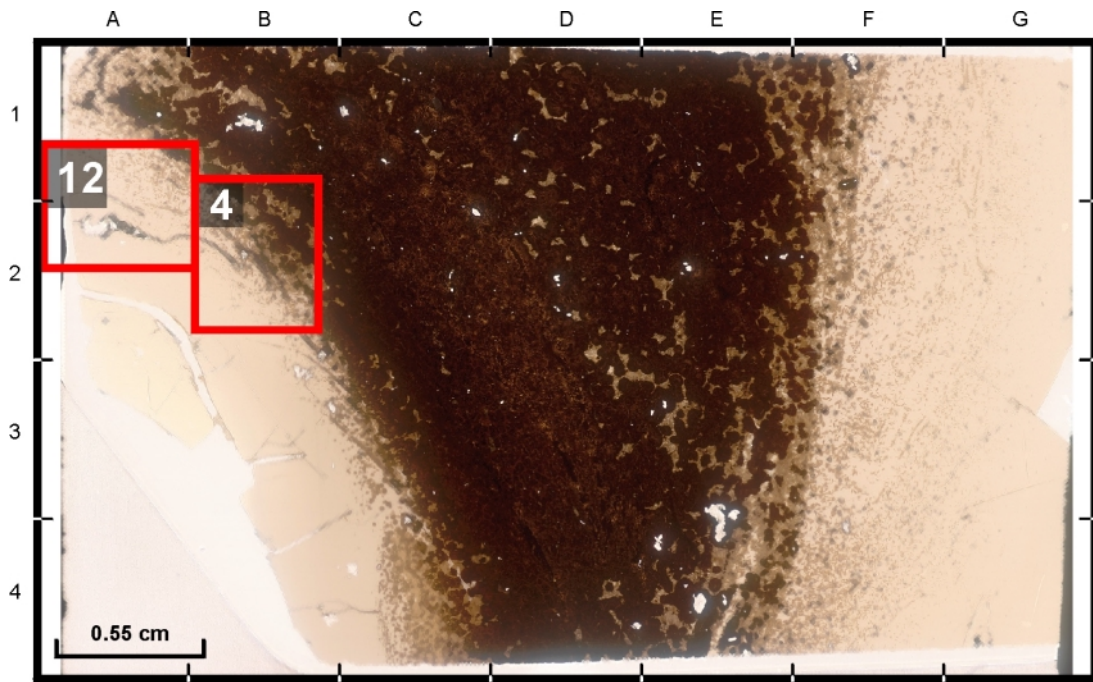
- 27: Void filling celadonite, replaced at the outer rim by saponite. PPL.
- 28: Same field of view as Pic.27 under XPL.
- 29: Void filling celadonite, replaced at the outer rim by saponite. PPL.
- 30: Same field of view as Pic.29. under XPL.



36DS7 - 4.6 Ma

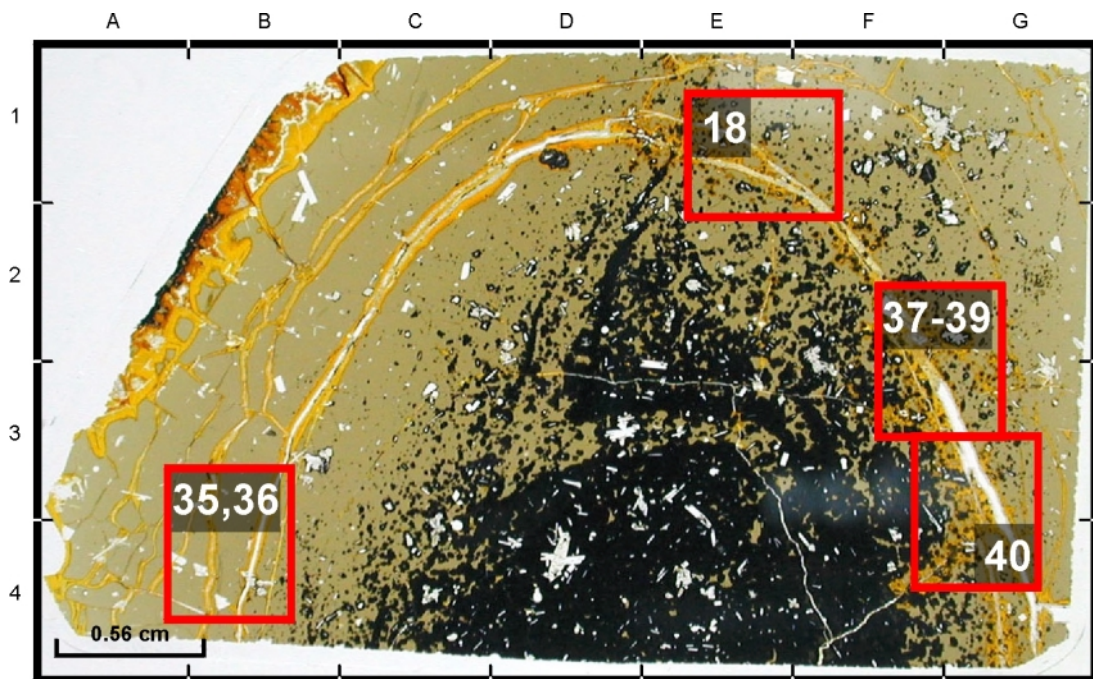
- 11: Open void in a glassy matrix, lined with trace amounts of phillipsite and clays, bounded by palagonite. PPL.

Thin sections



36DS8 - 4.6 Ma

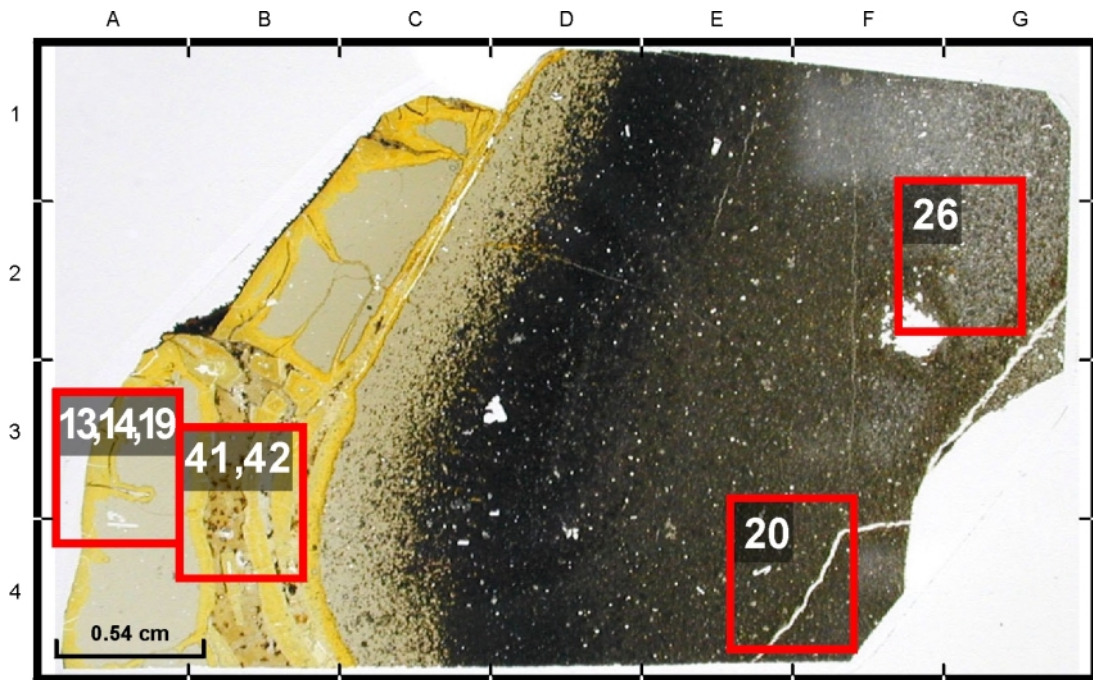
- 4: Fresh glass with increasing amounts of variolites. PPL.
- 12: Open void in a glassy matrix, lined with trace amounts of phillipsite. PPL.



42DS10 - 6.84 Ma

- 18: Vein in a glassy matrix, filled with a mixture of celadonite and phillipsite, bounded by palagonite. PPL.
- 35: Open vein in a glassy matrix, bounded by palagonite and lined with phillipsite. PPL.
- 36: Close up of Pic.35. PPL.
- 37,38: Vein in a glassy matrix, lined with phillipsite or completely filled with celadonite/phillipsite. PPL & XPL.
- 39: Fibrous crystals of phillipsite in contact with a mixture of celadonite and phillipsite. PPL.
- 40: Fibrous fan shaped growing crystals of phillipsite. PPL.

## Thin sections



43DS13 - 8.64 Ma

- 13: Vein in a glassy matrix, bounded by palagonite and filled with phillipsite. PPL.
- 14: Same field of view as Pic.13 under XPL.
- 19: Close up of Pic.13 & 14. PPL & XPL.
- 20: Open vein in an oxidation halo, lined with fibrous crystals of phillipsite. PPL.
- 26: Vesicle filled by FeOOH and celadonite. PPL.
- 41: Vein in a glassy matrix, bounded by palagonite and filled with phillipsite and a mixture of phillipsite & celadonite. PPL.
- 42: Close up of Pic.42. Fibrous crystals of phillipsite. PPL.

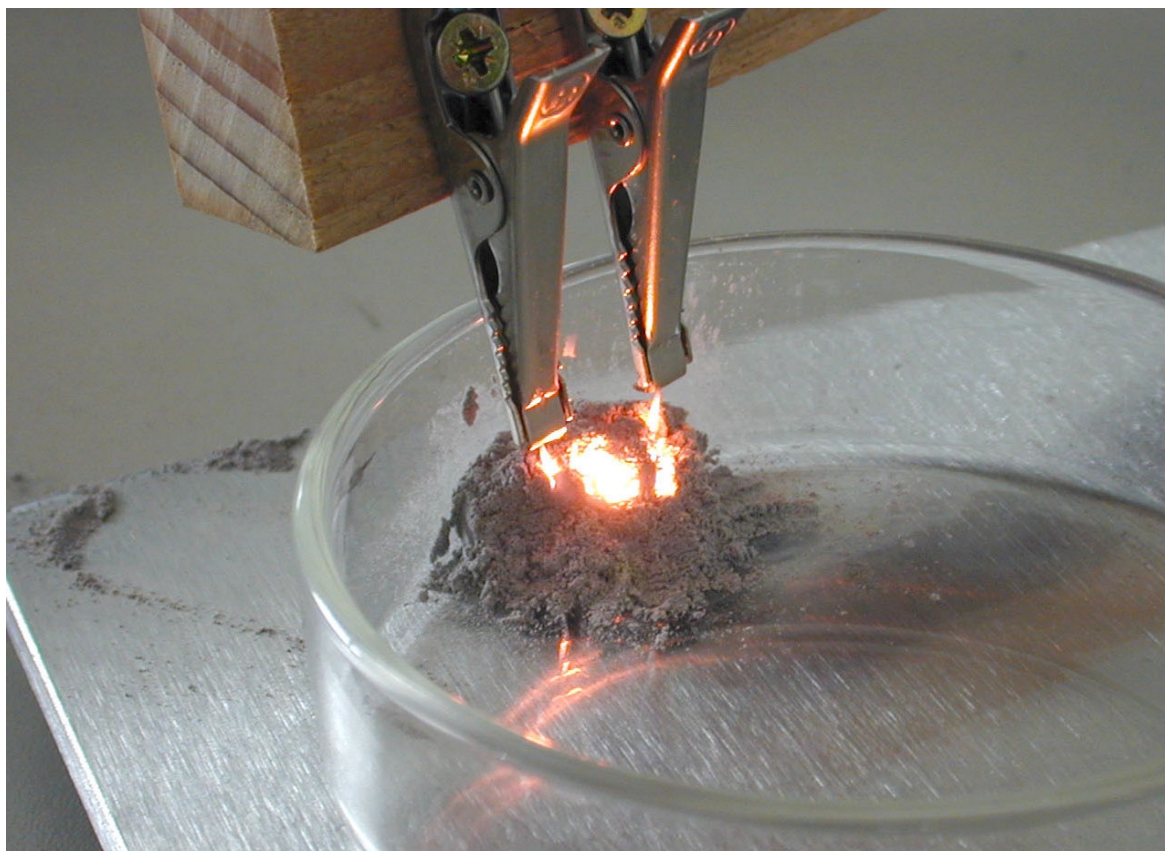
The black halo represents a transition zone from the glassy margin to the oxidation halo (E1-D4).

**References**

- Deer, W. A., Howie, R. A. and Zussman, J., Rock Forming Minerals, 3 Sheet silicates. Longmans, London, 270 pp, 1962.
- Deer, W. A., Howie, R. A. and Zussman, J., An Introduction to the Rock Forming Minerals, London, 528 pp, 1977.
- Delvigne, J. E., Atlas of Micromorphology of Mineral Alteration and Weathering. Mineralogical Association of Canada, Ottawa, Ontario, Canada, 495 pp, 1998.
- Jackson, J. A., Glossary of Geology. American Geological Institute, 769 pp, 1997.
- MacKenzie, W. S. and Adams, A. E., A Colour Atlas of Rocks and Minerals in Thin Section. Manson Publishing Ltd, 192 pp, 2001.
- MacKenzie, W. S. and Guilford, C., Atlas of rock-forming minerals in thin section. Longman, London, 98 pp, 1980.
- Schramm, B. and Devey, C. W., The fourth dimension in spreading axis activity: Magmatic evolution along the Southern East Pacific Rise at 14°S during the last 9 Ma. *Earth and Planetary Science Letters*, submitted.
- Schramm, B., Devey, C. W., Gillis, K. M. and Lackschewitz, K., Quantitative assessment of chemical and mineralogical changes due to progressive low temperature alteration of East Pacific Rise basalts from 0-9 Ma. *Chemical Geology*, submitted.

# **Producing melts of crystalline basaltic groundmass for analysis with the electron microprobe**

Burkhard Schramm and Colin W. Devey



*Submitted to European Journal Of Mineralogy, 3 September 2003*

## **Producing melts of crystalline basaltic groundmass for analysis with the electron microprobe**

Burkhard Schramm<sup>1\*</sup> and Colin W. Devey<sup>1</sup>

<sup>1</sup> *Fachbereich Geowissenschaften, Universität Bremen, Klagenfurter Str., 28359 Bremen, Germany*

\* *Corresponding author. Phone: +49-421-2187766; Fax: +49-421-218 9460;*

*E-mail: [bschramm@uni-bremen.de](mailto:bschramm@uni-bremen.de)*

*Submitted to European Journal Of Mineralogy, 3 September 2003*

### **Abstract**

Analyses of natural glass reflect the pristine magmatic composition of mid-ocean ridge basalts (MORB). Glass can remain fresh for many Ma and reflect the composition before the magma starts to crystallize. For samples without fresh glass, analyses have to be carried out on the groundmass. Unfortunately, the groundmass is always effected by alteration and does not reflect the pristine magmatic composition. In addition, microprobe analyses of the groundmass are difficult to perform quantitatively due to the presence of crystallites. If all glass is altered to secondary phases, an effective and simple technique to get reliable and reproducible analyses of the pristine magmatic composition is melting of the freshest available rock powder with a platinum wire. The results show totals less than the expected natural glass composition, but all element analyses are within the analytical error of the microprobe. By accurate preparation of the rock powder and carefully working during the melting procedure, the fused rock powder will produce high quality glass that can easily analyzed by microprobe. Special care has to be taken with crystalline samples containing large amounts of titanomagnetite. The results will have higher amounts of Ti and Fe, still within analytical error, but if possible powdered groundmass from crystalline samples should be avoided.

Keywords: volcanic glass, wire-loop, electron microprobe.

## Introduction

Chemical analyses of glass from mid-ocean ridge basalt provide important information about their geochemical composition. Due to the rapid cooling of magma upon contact with seawater, basalts from the ridge axis form a glass crust with a thickness of up to a few centimeters. As the crust moves off-axis, alteration will change the chemistry and mineralogy of the rocks, including the groundmass (e.g. Alt, 1999; Bach et al., 2003; Schramm et al., submitted). Glass is more resistant to alteration than primary minerals or groundmass material and will be altered to palagonite and / or clay minerals or remain unchanged, independent of the age of the sample. The oldest volcanic glass in the oceans was recovered in the Western Pacific during Ocean Drilling Program Leg 185 Site 801C (170 Ma) (Fisk & Kelley, 2002), providing information over the composition from the time of eruption. In addition, it can be very important as a precursor for a comparison of fresh and altered parts of the rock.

Unfortunately not all recovered samples from MOR contain glass, especially more altered or older samples show only minor or no amounts of fresh glass due to intense alteration by circulating fluids. For reconstruction of mass balances or an alteration history, it is often necessary to determine compositional changes which have occurred between the pristine magma and the altered bulk rock by comparing the freshest and most altered part of the rock. If all glass is altered to secondary phases, the freshest part has to be taken from the groundmass, but even this part can be altered to a minor extent. Therefore the results will be different to those derived from a comparison to the glass composition. Microprobe analyses of groundmass most probably comprise mixed analyses of small amounts of minerals (e.g. plagioclase, olivine, pyroxene) and therefore are not conducive to this type of study. To avoid these problems, methods were invented to produce artificial glass in the laboratory. The first technique was described by Riboud & Muan (1962) and was later modified by Donaldson et al. (1975). The method comprises an effective way for melting groundmass to glass beads using a platinum wire (0.2 mm) and was described as the wire-loop technique (Donaldson, 1979). Samples were quenched in water and experiments were run for 0.05 – 168 hours in a gas mixing furnace, where  $P_{O_2}$  was controlled by mixing of  $CO_2$  and  $H_2$  gases. Temperatures were 10 – 60° C above liquidus temperature. Other experiments were done using a platinum foil with a thickness of 0.1 mm or platinum wire with a diameter of 0.35 mm that was pressed into a foil (Borisov & Palme, 1997). This paper presents a successful and quick method for melting groundmass powder to glass using a platinum wire without a closed sample container under normal atmosphere pressure. Microprobe analyses of the fused glass yield comparable results to their natural composition. The simplified method and the shorter running time reduces the complexity of melting groundmass powder to glass.

## Experiment

### *Running procedure*

The experiment has been carried out using a “RFT transformer TST 280/6” with a power output of 6 ampere at the University of Hannover, Germany. The experimental setup is shown in Fig.1. The powdered starting material was filled into a small ceramic container (5 cm long, 2 cm wide, 1 cm high). A 0.2 – 0.3 mm thick platinum wire was attached between the clips and dipped into the powdered groundmass. The platinum wire is heated electrically until the melting procedure starts and the powder begins to glow (Fig.1). A time of 10 seconds is enough to produce small glass beads around the wire. Afterwards the power can be turned off and the wire can be lifted out of the groundmass. Due to the small diameter of the wire, the heat achievement is only low, so the rest of the powdered groundmass and the container will only take up a small part of the heat and the glass beads around the wire will be cool down in about 1 minute.



Figure 1. Melting of powdered groundmass using an electrically heated platinum wire in a ceramic container.

### *Material and Methods*

All samples are basalts, dredged from the East Pacific Rise between 14°S and 16°S, during the EXCO (Exchange between Crust and Ocean) cruises. All rocks show a similar mineralogy, containing small amounts of vesicles (3 %), are plagioclase-phyric (1-5 %) with minor olivine (1-2 %) and pyroxene (<1%). Only sample 22DS is more crystalline and contains higher amounts of magnetite. Detailed geochemical and mineralogical results are reported elsewhere (Grevemeyer et al., 2002; Schramm et al., submitted).

Sample preparation was done with a representative, homogeneous, least altered piece from the groundmass, crushed in a steel mortar and powdered with an agate mortar. Even the freshest groundmass is affected by alteration, but during the melting procedure secondary minerals (e.g. clays that comprise high amounts of water) will be vaporized. To provide a consistent melting procedure, the powdered groundmass was sieved to a grain size of 150 µm. Sieving can theoretically lead to a mineral separation, although the procedure used here shows no indication of mineral separating. The quantity of powder necessary is dependent on the size of the sample container and the wire. For the experiments reported here a quantity of three gram was sufficient.

Natural and experimental glass chips were carefully separated and washed in an ultrasonic bath to provide material for the determination of magmatic composition. The natural glass chips appear unaltered both in thin section and at high magnification (1200x) under the microprobe. Analyses were determined by a five-spectrometer JEOL JXA 8900 RL electron microprobe (University of Göttingen). Analytical conditions were 15kV accelerating voltage and 11-13 nA sample current. The electron beam was slightly defocused (10  $\mu\text{m}$  diameter) to avoid the volatilization of alkalis. The raw major element data from each measured spot were corrected to the KL2-G MPI-DING reference glass (Jochum et al., 2000).

## Results

Analyses of natural glass and glasses derived from melted powders from the groundmass, together with the standard deviation, are given in Table 1. The natural glass samples yield totals of ~100 %, implying that little or no extraneous water has been incorporated as a result of incipient alteration. Analyses of the experimental glass yields totals between 97 and 98 % which is probably the result of surface effects during the melting procedure. Electron microscope images (8500x magnification) of the fused glass show more vesicles and a more irregular surface than fresh natural volcanic glass (Fig.2). Such surface irregularities generally will lead to poorer analytical results and are presumably the cause of the lower totals for the fused groundmass samples. We suggest that vesicles result primarily from the outgassing during the melting process of absorbed water in the samples. The surface irregularities appear to have mainly angular shapes and we conclude that they are crystal remains which have survived the melting process. As long as they are regularly distributed and their size is well below the microprobe spot size, their presence should not affect the accuracy of the analysis. Only in the case of sample 22DS we have probably mineral effects from the groundmass which have been inherited in the melt: The melted groundmass glass is  $\text{TiO}_2$ - and FeO-richer than the natural glass. The analyses are in agreement with the higher amount of titanomagnetite throughout the groundmass, visible in thin sections. This can be explained by (a) mineral fractionation in the crushed sample before melting or (b) preferential solubility of titanomagnetites in the melted powder around the platinum filament.

Contamination problems are reported for Fe-containing systems, where Fe rapidly alloys with Pt when using tubes or crucibles for holding melted silicates (Donaldson et al., 1975). The thin platinum wire provides a very small contact area to sample volume ratio and therefore reduces the problem of the reaction of Fe with Pt to a minimum. A comparison of the averaged results from experimental fused glass and their natural glass compositions shows that most of the gains or losses of elements lie within the analytical error of the microprobe

sample	SiO <sub>2</sub>	TiO <sub>2</sub>	Al <sub>2</sub> O <sub>3</sub>	FeO	MnO	MgO	CaO	Na <sub>2</sub> O	K <sub>2</sub> O	P <sub>2</sub> O <sub>5</sub>	Cr <sub>2</sub> O <sub>3</sub>	Total	n
20DS4 nat	50.6	1.7	14.1	11.0	0.20	7.5	11.7	2.7	0.10	0.12	0.04	99.7	7
20DS4 exp	49.9	1.5	13.1	10.7	0.19	7.9	11.7	2.4	0.10	0.12	0.04	97.5	20
SD% exp	2%	28%	30%	22%	24%	32%	6%	27%	31%	46%	98%		
diff %	-1%	-10%	-8%	-2%	-4%	5%	0%	-12%	-8%	-1%	3%	-2%	
18DS5 nat	50.3	1.8	13.9	11.3	0.22	7.1	11.3	2.9	0.13	0.13	0.02	99.1	7
18DS5 exp	49.7	1.7	13.6	11.1	0.19	7.2	11.2	2.7	0.11	0.14	0.02	97.6	10
SD% exp	2%	4%	2%	2%	19%	2%	1%	3%	15%	34%	77%		
diff %	-1%	-5%	-2%	-2%	-14%	1%	-1%	-8%	-16%	11%	11%	-2%	
18DS7 nat	51.1	1.9	13.9	11.4	0.22	7.2	11.5	2.9	0.11	0.13	0.03	100.5	10
18DS7 exp	49.8	1.6	13.8	10.7	0.18	6.8	11.2	2.7	0.11	0.16	0.03	97.1	10
SD% exp	2%	9%	9%	6%	20%	9%	3%	8%	18%	23%	100%		
diff %	-3%	-12%	-1%	-6%	-16%	-6%	-2%	-7%	-5%	17%	-17%	-3%	
36DS8 nat	49.6	1.1	15.6	9.4	0.17	9.1	12.7	2.4	0.04	0.06	0.07	100.2	7
36DS8 exp	48.1	1.0	15.2	8.9	0.16	8.9	12.4	2.3	0.03	0.05	0.04	97.0	10
SD% exp	2%	5%	2%	2%	15%	3%	1%	5%	30%	36%	69%		
diff %	-3%	-10%	-3%	-5%	-2%	-3%	-2%	-6%	-20%	-3%	-34%	-3%	
21DS1 nat	50.9	1.8	14.4	10.7	0.20	7.5	11.7	2.9	0.11	0.15	0.03	100.4	10
21DS1 exp	49.4	1.6	14.1	10.4	0.20	7.4	11.3	2.8	0.12	0.14	0.07	97.6	10
SD% exp	2%	2%	2%	2%	11%	3%	2%	4%	12%	31%	47%		
diff %	-3%	-9%	-2%	-3%	1%	-1%	-3%	-6%	8%	-2%	97%	-3%	
21DS1 nat	50.9	1.8	14.4	10.7	0.20	7.5	11.7	2.9	0.11	0.15	0.03	100.4	10
21DS1.1 exp	49.6	1.8	13.7	10.7	0.19	6.9	11.2	2.8	0.13	0.19	0.03	97.3	39
SD% exp	2%	9%	3%	8%	16%	6%	3%	5%	17%	20%	93%		
diff %	-2%	2%	-5%	1%	-3%	-8%	-5%	-5%	17%	29%	0%	-3%	
22DS2 nat	49.8	1.7	14.0	11.0	0.19	7.3	11.1	2.7	0.12	n.d.	0.04	98.0	25
22DS2 exp	48.9	2.2	13.1	12.1	0.21	7.1	11.0	2.6	0.11	0.19	0.02	97.5	60
SD% exp	4%	33%	23%	23%	24%	24%	6%	19%	28%	36%	95%		
diff %	-2%	28%	-7%	10%	6%	-4%	0%	-4%	-9%	n.d.	-39%	0%	

Table 1. Electron microprobe analyses (wt%) of natural glassy MORB pieces (nat) and fused powdered groundmass (exp). Note the higher difference between natural and artificial glass analyses of sample 22DS2 (see text for discussion). Standard deviation (SD) of the experimental analyses is given in %; n = number of analyses.

(Fig.3). Single sample analyses also show only small changes in most of the elements. Due to the generally low concentration of Cr<sub>2</sub>O<sub>3</sub>, this element shows the highest deviation in a single sample from the natural glass composition (up to 97 %). K<sub>2</sub>O and P<sub>2</sub>O<sub>5</sub> also show high differences (29 % to -17 %), but still within standard deviation. The only element that shows a significant loss in a few samples is TiO<sub>2</sub> (-9 % to -12 %). The loss of Fe and Na during experiments is dependent on sample amount, diameter of the platinum wire and running time, with longer times resulting in higher losses (Corrigan & Gibb, 1979; Donaldson & Gibb, 1979). In our experiments the melting time is very short (~10 seconds) and the loss of Fe is small and also within analytical error.

Analyses of the fused glass of sample 22DS2 are used to discuss the dependence of chemical variation and tectonic segmentation along a segment of the East Pacific Rise (Grevemeyer et al., 2002).

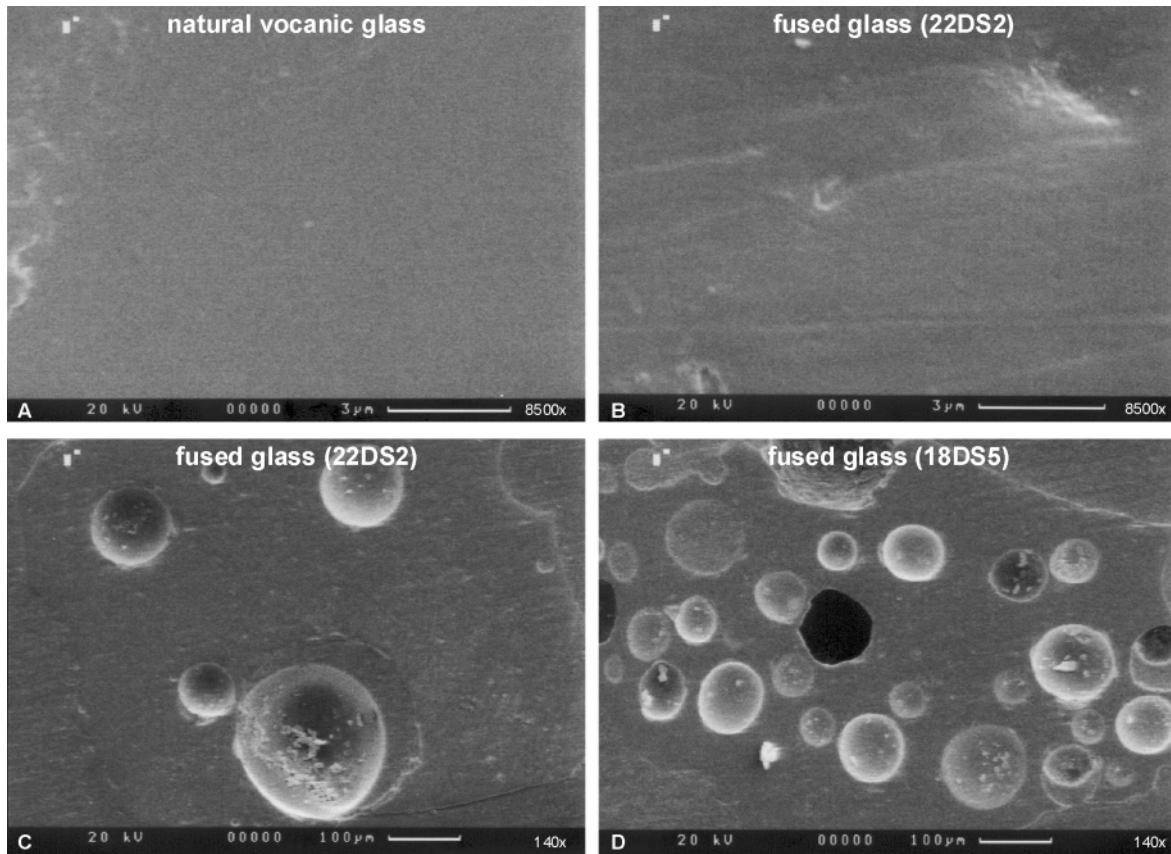


Figure 2. Natural and fused glass surface images taken by an electron microscope. A. Natural volcanic glass with a very smooth and homogeneous surface (8500x magnification). B. The fused glass shows surface irregularities with some uneven patches, leading to lower totals when analyzing with the electron microscope (8500x). C and D. Images with lower magnification (140x) of the synthesized glass show the presence of microbubbles, resulting primarily from the outgassing during the melting process of absorbed water.

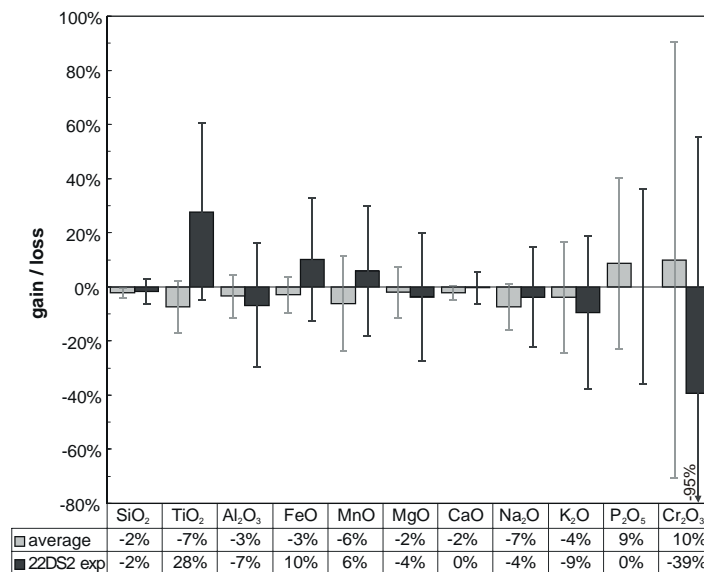


Figure 3. Gain and loss (%) of the major elements from experimental glass beads to their natural glass composition. Note the relatively high increase of TiO<sub>2</sub> and FeO in sample 22DS2, due to the higher amount of titanomagnetite in the powdered crystalline groundmass. Average = average of all samples given in Table 1. Small bars indicate the standard deviation.

## Summary

Fusing of rock powder to glass beads is a very efficient method to get glass analyses from samples without natural glass. It is a simple and reliable technique that yields reproducible results with element losses within analytical error. Special attention should be paid to powdered groundmass from crystalline rocks. Differential melting behaviour of minerals such as titanomagnetite will affect the glass composition, resulting in higher amounts of specific elements (e.g. Ti and Fe).

## Acknowledgments

The authors wish to thank Jasper Berndt and Francois Holtz (University of Hannover) for assistance during the experiment and Andreas Kronz (University of Göttingen) for assistance with the electron microprobe analyses. This study was supported by BMBF grant 03G0145A.

## References

- Alt, J.C., (1999). Hydrothermal alteration and mineralization of oceanic crust; mineralogy, geochemistry, and processes. In: C.T. Barrie & M.D. Hannington (Editors), *Volcanic-associated massive sulfide deposits; processes and examples in modern and ancient settings - Reviews in Economic Geology*. Society of Economic Geologists, pp. 133-155.
- Bach, W., Peucker-Ehrenbrink, B., Hart, S.R., Blusztajn, J.S., (2003). Geochemistry of hydrothermally altered oceanic crust: DSDP/ODP Hole 504B - Implications for seawater-crust exchange budgets and Sr- and Pb-isotopic evolution of the mantle. *Geochemistry, Geophysics, Geosystems, G<sup>3</sup>, an electronic journal of the earth sciences*, **4**(3): (29).
- Borisov, A. & Palme, H., (1997). Experimental determination of the solubility of platinum in silicate melts. *Geochimica et Cosmochimica Acta*, **61**(20): 4349-4357.
- Corrigan, G. & Gibb, F.G.F., (1979). The loss of Fe and Na from a basaltic melt during experiments using the wire-loop method. *Mineralogical magazine*, **43**: 121-126.
- Donaldson, C.H., (1979). Composition changes in a basalt melt contained in a wire loop of Pt (sub 80) Rh (sub 20) ; effects of temperature, time, and oxygen fugacity. *Mineralogical Magazine*, **43**(325): 115-119.

- Donaldson, C.H. & Gibb, F.G.F., (1979). Changes in sample composition during experiments using the "wire-loop" technique. *Mineralogical Magazine*, **43**(325): 115.
- Donaldson, C.H., Williams, R.J., Lofgren, G., (1975). A sample holding technique for study of crystal growth in silicate melts. *American Mineralogist*, **60**: 324-326.
- Fisk, M. & Kelley, K.A., (2002). Probing the Pacific's oldest MORB glass; mantle chemistry and melting conditions during the birth of the Pacific Plate. *Earth and Planetary Science Letters*, **202**(3-4): 741-752.
- Grevemeyer, I., Schramm, B., Devey, C.W., Jochum, B., Wilson, D.S., Hauschild, J., Aric, K., Villinger, H., Weigel, W., (2002). A multibeam-sonar, magnetic and geochemical flow-line survey at 14°14's on the southern East Pacific Rise - insights into the fourth dimension of ridge crest segmentation. *Earth and Planetary Science Letters*, **199**(3-4): 359-372.
- Jochum, K.P., Dingwell, D.B., Rocholl, A., Stoll, B., Hofmann, A.W., (2000). The preparation and preliminary characterisation of eight geological MPI-DING reference glasses for in-situ microanalysis. *Geostandards Newsletter*, **24**(1): 87-133.
- Riboud, P.V. & Muan, A., (1962). Phase equilibria in a part of the system "FeO"-MnO-SiO<sub>2</sub>. *Transactions of the Society of Mining Engineers of American Institute of Mining, Metallurgical and Petroleum Engineers, (AIME)*, **224**: 27-33.
- Schramm, B., Devey, C.W., Gillis, K.M., Lackschewitz, K., (submitted). Quantitative assessment of chemical and mineralogical changes due to progressive low temperature alteration of East Pacific Rise basalts from 0-9 Ma. *Chemical Geology*.

## Conclusions

### Geochemistry

- Magmatic evolution in the EXCO area has remained stable throughout the last 8.64 Ma and shows no correlation with spreading rate or off-axis discordant zones produced by fossil overlapping spreading centers.
- The backtracked data to the present day ridge axis shows that there are no variations in the magmatic composition with time.
- Significant and systematic variations of the geochemistry of basalts along the ridge axis is a striking feature with homogeneous and high MgO occurring in the north and more heterogeneous and low MgO in the south, separated by a magmatic boundary at 14°24'S. Small-scale spatial variations in chemistry are a robust feature along the SEPR.
- The observed magmatic boundary does not coincide with the left-stepping deval at 14°30'S, therefore magmatic boundaries along the SEPR can be independent of ridge axis discontinuities.
- The presence of off-axis volcanism can be identified by its trace element depleted signatures. The age of these samples implies the presence of an off-axis magmatic system characterized by stability on the several million year scale.

### Alteration

- The EXCO sampling transect documents an increasing alteration stage and a slight change in redox conditions with distance from the spreading axis and therefore with time. Fresh rocks were dredged at the ridge axis, whereas off-axis basalts contain features of seawater-generated low temperature alteration.
- Fe-oxyhydroxides and celadonite (main alteration component in 0.12 – 4.6 Ma old rocks) are the first alteration products, partly replaced or dissolved by saponite under more reducing conditions. Phillipsite is more abundant in rocks older than 4.6 Ma.
- The geochemical flux in the altered basalts indicates oxidizing conditions and high water/rock ratios. In contrast to the mineralogical changes, the gain and loss of elements appears to be affected only by local parameters such as basement topography and reaction of circulating fluids within the rock but not by time.

- The seawater-ocean crust exchange affected the bulk chemical properties of the upper ocean crust even at ages  $< 9$  Ma. Therefore the average composition of the upper oceanic crust cannot be taken as that of N-MORB using compiled literature values but a correction factor for alteration must be taken into account.